Integrin $\alpha v\beta 3$ expression in Cardiovascular PET/CT Imaging: Correlation with Myocardial Blood Flow

Matthieu Dietz

THESE de DOCTORAT DE
L'UNIVERSITE CLAUDE BERNARD LYON 1

Ecole Doctorale N° 205
Interdisciplinaire Sciences-Santé (EDISS)

Discipline :
Recherche clinique, innovation technologique

Soutenue publiquement le 19/12/2023, par :
Matthieu DIETZ

Integrin $\alpha_v\beta_3$ expression in Cardiovascular PET/CT Imaging: Correlation with Myocardial Blood Flow

---

Devant le jury composé de :

Denis AGOSTINI	Professeur, Université de Caen	Rapporteur
Pierre-Yves MARIE	Professeur, Université de Lorraine	Rapporteur
Emmanuelle CANET-SOULAS	Professeure, Université Lyon 1	Examinatrice
Nathalie PREVOT-BITOT	Maître de Conférences, Université Jean Monnet Saint-Etienne	Examinatrice
Nathan MEWTON	Professeur, Université Lyon 1	Directeur de thèse
John O. PRIOR	Professeur, Université de Lausanne	Co-directeur de thèse
Fabien HYAFIL	Professeur, Université Paris Cité	Invité
Dominique LE GULUDEC	Professeure Emérite, Université Paris Cité	Invitée

Université Claude Bernard Lyon 1

UNIVERSITE CLAUDE BERNARD LYON I

Président de l'Université	Frédéric FLEURY
Président du Conseil Académique et de la Commission Recherche	Hamda BEN HADID
Vice-Président du Conseil d'Administration	Didier REVEL
Vice-Présidente de la Commission Formation	Céline BROCHIER
Vice-Président Relations Hospitalo-Universitaires	Jean François MORNEX
Directeur général des services	Pierre ROLLAND

SECTEUR SANTE

Doyen de l'UFR de Médecine Lyon-Est	Gilles RODE
Doyen de l'UFR de Médecine et de Maïeutique Lyon Sud - Charles Mérieux	Philippe PAPAREL
Doyen de l'Institut des Sciences Pharmaceutiques et Biologiques (ISPB)	Claude DUSSART
Doyen de l'UFR d'Odontologie	Jean-Christophe MAURIN
Directeur de l'Institut des Sciences & Techniques de Réadaptation (ISTR)	Jacques LUAUTÉ
Présidente du Comité de Coordination des Études Médicales	Carole BURILLON

SECTEUR SCIENCES ET TECHNOLOGIE

Directrice de l'UFR Biosciences	Kathrin GIESELER
Directeur de l'UFR Faculté des Sciences	Bruno ANDRIOLETTI
Directeur de l'UFR Sciences & Techniques des Activités Physiques et Sportives (STAPS)	Guillaume BODET
Directeur de Polytech Lyon	Emmanuel PERRIN
Directeur de l'Institut Universitaire de Technologie Lyon 1 (IUT)	Michel MASSENZIO
Directeur de l'Institut des Science Financière & Assurances (ISFA)	Nicolas LEBOISNE

Université Claude Bernard Lyon 1

Directeur de l'Observatoire de Lyon	Bruno GUIDERDONI
Directeur de l'Institut National Supérieur du Professorat & de l'Éducation (INSPÉ)	Pierre CHAREYRON
Directrice du Département-composante Génie Électrique & des Procédés (GEP)	Rosaria FERRIGNO
Directrice du Département-composante Informatique	Saida BOUAZAK BRONDEL
Directeur du Département-composante Mécanique	Marc BUFFAT

TITRE EN ANGLAIS

Integrin $\alpha_v\beta_3$ expression in Cardiovascular PET/CT Imaging: Correlation with Myocardial Blood Flow

RESUME EN ANGLAIS

Angiogenesis, which is the creation of new microvasculature, is a natural phenomenon that can take place in cases of prolonged tissue ischemia. It has a significant role in enhancing tissue perfusion and blood circulation following instances like a heart attack. The research on molecular imaging of angiogenesis in the cardiovascular system is an evolving field. This specialized imaging aims to non-invasively observe the molecular signals connected with the angiogenic process, such as the expression of integrin $\alpha_v\beta_3$. When used alongside physiological perfusion imaging, it has the potential to forecast and assess clinical outcomes for conditions such as ischemic heart disease.

MOTS-CLES EN ANGLAIS

Myocardial angiogenesis - integrin $\alpha_v\beta_3$ - Molecular imaging - PET

TITRE EN FRANCAIS

Expression de l'intégrine $\alpha_v\beta_3$ dans l'imagerie cardio-vasculaire par TEP/TDM : corrélations avec les flux sanguins myocardiques

RESUME EN FRANCAIS

La néoangiogenèse, qui correspond à la création de nouveaux microvaisseaux, est un phénomène naturel pouvant survenir en cas d'ischémie tissulaire prolongée. Elle joue un rôle significatif dans l'amélioration de la perfusion tissulaire et de la circulation sanguine à la suite d'incidents tels qu'une crise cardiaque. La recherche sur l'imagerie moléculaire de l'angiogenèse dans le système cardiovasculaire est un domaine en développement. Cette imagerie spécialisée vise à observer de manière non-invasive les signaux moléculaires liés au processus angiogénique, tels que l'expression de l'intégrine αvβ3. Lorsqu'elle est utilisée en conjonction avec l'imagerie de la perfusion physiologique, elle a le potentiel de prédire et d'évaluer des conséquences cliniques pour des affections telles que la maladie cardiaque ischémique.

MOTS-CLES EN FRANCAIS

Angiogenèse myocardique - intégrine $\alpha v\beta_3$ - Imagerie moléculaire - TEP (Tomographie par Émission de Positons)

INTITULE ET ADRESSE DU LABORATOIRE

Laboratoire CarMeN, Equipe IRIS, INSERM U1060, Université Lyon 1, INRAe U1397; Hospices Civils de Lyon, site OPeRA-B13, Groupement Hospitalier Est, 54 Boulevard Pinel, 69500 Bron, France.

To my family,

You must see the bigger picture.

And for that, you need sophisticated tools.

Table of Contents

PART I

Preface

Chapter 1

French summary

Bien que les intégrines aient été initialement identifiées comme des récepteurs extracellulaires impliqués dans l'adhérence entre les cellules et la matrice extracellulaire, on reconnaît maintenant qu'elles ont un rôle physiologique beaucoup plus large. Ces récepteurs médient des signaux cytosoliques qui influencent la croissance, la prolifération, la survie et les mouvements cellulaires. Les intégrines sont impliquées à la fois dans les processus physiologiques normaux et dans les états pathologiques, ce qui rend cette famille de récepteurs attrayante pour le ciblage diagnostique. Les récepteurs d'intégrine jouent un rôle relativement non spécifique et étendu, car ils assument également la fonction de mécanosenseurs. Cela implique qu'ils induisent à la fois des changements intracellulaires et extracellulaires pour assurer la survie et l'homéostasie en fonction des stimuli physiques de la matrice extracellulaire (1-3).

La matrice extracellulaire est une structure essentielle qui fournit la composition adéquate pour maintenir un environnement physiologiquement acceptable qui nourrit les cellules et maintient l'homéostasie. Les forces mécaniques et les changements de l'environnement sont communiqués entre les cellules et la matrice extracellulaire par l'intermédiaire des récepteurs d'intégrine. Diverses cascades en aval, telles que la libération de facteurs de croissance ou d'autres formes de signalisation, entraînent des adaptations cellulaires telles que la prolifération, une survie accrue, la formation de fibres de stress plus épaisses et l'angiogenèse. Ainsi, les protéines membranaires d'intégrine peuvent être régulées à la hausse au cours de certains processus pathologiques, dont la néoangiogenèse est un exemple important. La néoangiogenèse est notamment une exigence essentielle pour la croissance tumorale, car les tumeurs ne peuvent pas dépasser une certaine taille à moins d'établir un accès accru à la circulation sanguine (1-5).

Les techniques de médecine nucléaire comprennent la tomographie par émission de positons (TEP) et la tomographie d'émission monophotonique (TEMP), qui marquent les molécules avec des isotopes radioactifs (radiotraceurs ou radiopharmaceutiques) pour suivre le déplacement de ces molécules. L'imagerie nucléaire fournit des informations fonctionnelles. Ces techniques nucléaires peuvent être combinées avec des technologies d'imagerie fournissant des informations anatomiques telles que l'imagerie par résonance magnétique (IRM) ou la tomodensitométrie (TDM). L'IRM utilise des champs magnétiques et des ondes radio pour générer des images détaillées des organes et des structures à l'intérieur du corps. La TDM reconstruit un grand nombre d'images en coupe de rayons X en une image tridimensionnelle de

l'anatomie du corps. L'imagerie isotopique joue un rôle essentiel dans la pathologie cardiovasculaire, que ce soit pour le diagnostic, la prise de décision et le suivi thérapeutique, ainsi que pour l'évaluation du prognostic. Dans les années 1970 et 1980, les caméras TEP étaient principalement utilisées comme des outils de recherche pour mieux comprendre les caractéristiques métaboliques du cerveau et du cœur. Cependant, c'est dans le domaine de l'oncologie qu'elles ont véritablement pris leur essor au milieu des années 1990, devenant ainsi un instrument incontournable pour les explorations de routine. Il est intéressant de noter que malgré son utilisation précoce comme outil de recherche pour comprendre les particularités métaboliques du cœur dans les années 1970 et 1980, l'intégration du TEP dans la pratique clinique quotidienne pour cet organe a été retardée jusqu'à la fin des années 2000. Les photons détectés par les caméras TEP sont plus énergétiques (511 keV) par rapport aux photons détectés par les caméras de scintigraphie conventionnelle. De plus, ces photons sont émis en coïncidence, c'est-à-dire que deux photons sont émis en opposition à 180 degrés, ce qui nécessite une géométrie de détection circulaire.

Le tripeptide arginine, glycine et acide aspartique (RGD) est un motif essentiel utilisé lors de la communication intercellulaire en raison de sa grande affinité pour les intégrines. Actuellement, la séquence RGD est utilisée dans des recherches translationnelles pour cibler spécifiquement l'intégrine $\alpha_v\beta_3$ et visualiser les phénomènes de néoangiogenèse de manière non-invasive.

Les intégrines sont composées de deux sous-unités de glycoprotéines transmembranaires (unités α et β) et font partie des récepteurs les plus importants qui influencent les communications intra et extracellulaires. La même molécule d'intégrine démontre différentes spécificités de liaison aux ligands selon le type de cellule sur lequel elle se trouve. Cela indique que des facteurs spécifiques à la cellule modulent l'activité de liaison des intégrines aux ligands. Il existe trois sous-unités β différentes qui forment des dimères avec différents types de sous-unités α. La sous-unité β1 forme des complexes avec au moins douze sous-unités α, l'unité β2 avec quatre sous-unités α et l'unité β3 se trouve dans de nombreux types de cellules, y compris les plaquettes sanguines et les protéines de la matrice telle que le fibrinogène. Au total, huit intégrines ont été identifiées pour reconnaître la séquence RGD, à savoir $\alpha_v\beta_1$, $\alpha_v\beta_3$, $\alpha_v\beta_5$, $\alpha_v\beta_6$, $\alpha_v\beta_8$, $\alpha_5\beta_1$, $\alpha_8\beta_1$ et $\alpha_{II}\beta_3$, et ces intégrines jouent un rôle prépondérant dans la pathogenèse du cancer et les pathologies impliquant la matrice extracellulaire. En particulier, $\alpha_v\beta_1$ et $\alpha_v\beta_3$ favorisent les facteurs de croissance, la

différenciation des cellules souches néoplasiques et sont des facteurs pronostiques de la chimiosensibilité chez les patients atteints de cancer (6). L'affinité de liaison de la séquence RGD avec l'intégrine $\alpha_v\beta_3$ a été la plus documentée.

Non seulement les intégrines (en particulier $\alpha_v\beta_3$) sont impliquées dans le développement et la progression des tumeurs, mais elles jouent également un rôle dans l'inflammation et le remodelage. Cependant, contrairement à la tumorigenèse, ces processus peuvent être pathologiques ou faire partie de la réparation normale. L'intégrine $\alpha_v\beta_3$ participe au processus normal de régulation des réponses des macrophages pendant l'inflammation, mais des preuves suggèrent également qu'elle pourrait être impliquée dans le maintien de la pathologie inflammatoire chronique. Étant donné que les intégrines modulent et médiatisent l'adhérence cellulaire, la mobilité et les interactions avec la matrice extracellulaire, ces récepteurs sont fortement impliqués dans tous les types de remodelage tissulaire (7-11).

La pharmacocinétique d'une traceur radiomarqué est un facteur décisif pour sa capacité à détecter des pathologies à l'intérieur du corps. L'objectif de l'application d'un radiotraceur est défini par sa pharmacocinétique inhérente. La pharmacocinétique et la demi-vie physique de l'isotope radioactif peut déterminer la pertinence d'une imagerie précoce ($\leq$ 60 minutes) ou d'une imagerie retardée (plusieurs heures après l'administration). La voie et le degré d'excrétion peuvent également avoir un impact sur l'utilisation pratique pour détecter des pathologies de manière non-invasive. La présence accrue d'un traceur dans certains tissus (par exemple, le cœur, qui est le sujet principal de cette thèse) peut être considérée comme préjudiciable pour l'imagerie d'une pathologie tissulaire ciblée (par exemple, une lésion de l'aorte), car la présence accrue du traceur entraînera un signal de fond qui interférerait avec la distinction adéquate du tissu d'intérêt. Dans certains cas, cependant, cette distribution tissulaire et la persistance du traceur dans le tissu peuvent être bénéfiques (par exemple, présence dans le cerveau), si le tissu d'intérêt est une zone avec des barrières empêchant normalement une accumulation élevée. Il est important de souligner les facteurs qui influencent le choix de l'agent d'imagerie nucléaire pour une investigation spécifique. Le radiotraceur devrait présenter une forte affinité pour le récepteur de l'intégrine présent dans le mécanisme spécifique de la maladie (principalement en ce qui concerne l'intégrine $\alpha_v\beta_3$ dans les applications pertinentes envisagées pour l'investigation). Pour l'imagerie TEMP, les radioisotopes indium-111 (par exemple, [111In]In-RAFT-RGD) et technétium-99m sont les plus largement disponibles. Pour l'imagerie TEP, en plus du fluor-18, des radiométaux tels que le cuivre-64, le zirconium-89 et le gallium-68 sont

utilisés. Si une approche diagnostique-thérapeutique de radiothérapie alpha/bêta (également appelée théranostique) est souhaitée, des recherches ont identifié des paires de radioisotopes théranostiques appropriées, comme le gallium-68 pour le diagnostic combiné au lutétium-177 pour la thérapie. La demi-vie étendue du zirconium-89 (78,4 heures) pourrait offrir des avantages supplémentaires pour les applications d'imagerie in vivo qui nécessitent un temps de balayage prolongé (en raison d'une pharmacocinétique in vivo plus lente, par exemple, pour les macromolécules) ou si un temps de production plus long est indiqué pour le marquage radiolabelé du vecteur.

L'utilisation du gallium-68 est répandue en raison de sa facilité d'utilisation et de la bonne disponibilité de ce radioisotope grâce à un générateur de ^{68}Ge/^{68}Ga. D'autres facteurs à prendre en compte sont le rendement radiochimique obtenu lors du marquage du traceur avec le radioisotope spécifique de choix, ainsi que le temps de la radiosynthèse (qui influence l'exposition aux radiations). Ce radio-émetteur est celui qui a été utilisé dans les travaux de cette these. Cette thèse se concentre sur l'exploration de la néo-angiogenèse en utilisant une technique d'imagerie TEP basée sur un traceur radiomarqué marqué au gallium-68, ligand des intégrines $\alpha_v\beta_3$: le ^{68}Ga-NODAGA-RGD.

Le ^{68}Ga-NODAGA-RGD est un radiopharmaceutique qui se lie aux intégrines $\alpha_v\beta_3$ grâce à son motif RGD. Il est composé d'un motif RGD similaire aux ligands des intégrines $\alpha_v\beta_3$ et d'un chélateur NODAGA, qui n'a pas d'activité propre mais permet la liaison de l'isotope radioactif ^{68}Ga. Les études ont montré que le taux de fixation du ^{68}Ga-DOTA-RGD et du ^{68}Ga-NODAGA-RGD était similaire, voire meilleur, que celui du ^{18}F-galacto-RGD, tout en délivrant une dose au patient plus favorable en raison de sa demi-vie plus courte (68 minutes contre 110 minutes pour le ^{18}F).

Les maladies cardiovasculaires restent la principale cause de décès dans le monde et sont à elles seules responsables de 30 % des décès. Dans ce groupe, les pathologies coronariennes occupent la place numéro un. Pour les prévenir, les diagnostiquer et les traiter, il est essentiel d'utiliser des modalités d'imagerie non-invasives qui combinent rapidité, adaptabilité et accessibilité, comme la TEP qui trouve de nombreuses applications cardiovasculaires. Cette thèse met en évidence l'utilisation prometteuse du ^{68}Ga-NODAGA-RGD en tant que traceur spécifique pour l'imagerie de la néo-angiogenèse, ce qui pourrait permettre une meilleure évaluation et un meilleur suivi des patients atteints de pathologies

coronariennes, en particulier dans le contexte de la réparation du muscle cardiaque après une lésion ischémique.

Cette thèse débute par une partie d'introduction intégrant un travail de revue sur les applications cardiovasculaires des radiotraceurs ciblant l'intégrine $\alpha_v\beta_3$ en imagerie TEP (12) (chapitre 2).

La deuxième partie de cette thèse se concentre sur le myocarde infarcie, avec l'étude principale portant sur l'imagerie de l'intégrine $\alpha_v\beta_3$ en imagerie TEP après un infarctus du myocarde de type STEMI (chapitre 3).

Après un infarctus du myocarde, une série complexe et bien coordonnée de processus est déclenchée pour initier la réparation cardiaque. Initialement, une phase pro-inflammatoire avec une inflammation intense et une infiltration de cellules immunitaires aide à éliminer l'infarctus des cellules mortes dans les premiers jours suivant la reperfusion. Cette phase est suivie d'une phase réparatrice et prolifération, qui comprend la résolution de l'inflammation, la prolifération des fibroblastes cardiaques, la formation de cicatrices et la néovascularisation au cours des jours suivants, avec un pic autour du septième jour après l'infarctus du myocarde. La néoangiogenèse est considérée comme une partie importante de ce processus de réparation (13,14). On sait depuis des décennies que l'intégrine $\alpha_v\beta_3$ joue un rôle majeur dans la néoangiogenèse, et elle est notamment surexprimée dans les états de néoangiogenèse dans le myocarde après une lésion (15-18). De plus, des études précliniques et cliniques ont révélé que les fibroblastes cardiaques et les macrophages activés expriment l'intégrine $\alpha_v\beta_3$ lors de la chimiotaxie et de la margination (19-20). Cette expression de l'intégrine $\alpha_v\beta_3$ pourrait être bénéfique pour favoriser la cicatrisation cardiaque et la réparation après un infarctus du myocarde (20). Le peptide RGD (H-Arg-Gly-Asp-NH2 ; arginine-glycine-aspartic acid) conjugué à NODAGA (1,4,7-triazacyclononane-1,4-bis[acetic acid]-7-[2-glutaric acid]) marqué au ^{68}Ga est un traceur de TEP avec une forte affinité de liaison à l'intégrine $\alpha_v\beta_3$. Le rubidium-82 (^{82}Rb) est un traceur de perfusion TEP largement utilisé en pratique clinique, qui peut mesurer avec précision la perfusion myocardique au repos et sous stress en unités absolues (21). Nous avons émis l'hypothèse que la captation myocardique du ^{68}Ga-NODAGA-RGD est augmentée pendant le pic présumé de la phase proliférative après un infarctus aigu du myocarde avec élévation du segment ST (STEMI) et réduite au cours des phases ultérieures de la guérison de l'infarctus. Dans cette étude sur des survivants d'un infarctus aigu de type STEMI, nous

avons cherché à évaluer l'expression basale de l'intégrine $\alpha_v\beta_3$ dans le myocarde entre 4 et 10 jours après l'infarctus du myocarde, ainsi que les variations temporelles à 1 mois et 3 mois, en corrélation avec les flux sanguins myocardiques de repos et sous stress.

Cette étude a été approuvée par la Commission d'éthique du canton de Vaud (protocole CER-VD # 429/14) et enregistrée sur Clinical-Trials.gov (NCT03809689). Tous les participants ont donné leur consentement éclairé par écrit. Nous avons recruté prospectivement 20 survivants d'un infarctus du myocarde de type STEMI et les avons invités à passer une TEP-TDM ^{82}Rb au repos et sous stress pharmacologique, ainsi qu'une TEP/TDM au ^{68}Ga-NODAGA-RGD entre 4 et 10 jours après l'infarctus du myocarde. Les participants ont ensuite été invités à revenir pour une deuxième série de TEP-TDM au ^{82}Rb et au ^{68}Ga-NODAGA-RGD au repos et sous stress à 1 mois après l'infarctus du myocarde et enfin pour une troisième série à 3 mois.

Le chapitre 4 porte quant à lui sur une étude réalisée dans le centre de Turku en Finlande, évaluant le débit sanguin myocardique et la captation du ^{68}Ga-NODAGA-RGD en TEP chez 31 patients, 7,7 ± 3,8 jours après une intervention coronaire percutanée primaire pour un infarctus du myocarde de type STEMI. Une échocardiographie transthoracique a été réalisée le jour de la TEP et lors du suivi à 6 mois. L'objectif de cette étude était d'évaluer de manière prospective les facteurs déterminants de la captation myocardique du ^{68}Ga-NODAGA-RGD et son lien avec la fonction ventriculaire gauche chez les patients après un infarctus du myocarde. Cette approche s'avère complémentaire à l'étude principale de ce manuscrit (chapitre 3), qui se concentre principalement sur l'évolution naturelle du signal ^{68}Ga-NODAGA-RGD dans le myocarde après un infarctus du myocarde.

La troisième partie de cette thèse porte sur l'imagerie de l'intégrine $\alpha_v\beta_3$ en imagerie TEP dans l'athérosclérose. Les stratégies d'explorations restent actuellement basées sur une dualité entre anatomie (visualisation de la lésion avec le coroscanner) et fonctionnalité (le retentissement fonctionnel de la lésion : ischémie, réserve coronaire). Ce paradigme a ses limites. Notamment, il a été démontré que plus de la moitié des infarctus surviennent sur des plaques non sténosantes. Il est logique de s'intéresser à une troisième voie, le repérage des plaques instables. L'avènement des nouvelles TEP digitales couplées à des scanners haut de gamme permet désormais de coupler l'anatomie et l'étude de la vulnérabilité de la plaque par des mécanismes directs ou indirects traçant l'activité de l'athérosclérose. A l'heure actuelle, le traceur le plus documenté est le fluorure de sodium marqué au ^{18}F (^{18}F-Na), qui se fixe sur les microcalcifications secondaires aux modifications inflammatoires de la plaque et de la matrice

extracellulaire (22). Commercialement disponible, il bénéficie d'une absence de fixation physiologique du myocarde et donc d'un excellent rapport signal/bruit. Cette hyperfixation sur les microcalcifications actives pourrait être diminuée par un traitement médical préventif, ce qui ouvre la porte à utiliser le ^{18}F-Na comme marqueur d'évaluation thérapeutique (23).
La possibilité de détecter la plaque instable pourrait permettre de fournir de nouvelles connaissances pathologiques et permettre l'évaluation de nouvelles cibles pour de futures approches diagnostiques et thérapeutiques.

La présence accrue de l'intégrine $\alpha_v\beta_3$ indique un athérome instable (susceptible de se détacher) et par conséquent un risque plus élevé de complications. La principale conséquence de ces changements pathologiques est l'augmentation de la néo-angiogenèse et l'accumulation de macrophages (positifs pour l'intégrine $\alpha_v\beta_3$) (24–28). Des agents basés sur le peptide RGD, tant en SPECT qu'en TEP, ont été utilisés pour l'identification de l'athérome instable en ciblant l'expression des intégrines $\alpha_V\beta_3$ et $\alpha_V\beta_5$. La plupart des traceurs étaient sélectifs pour $\alpha_V\beta_3$, mais le radiotraceur ^{68}Ga-DOTA-RGD se liait à la fois à $\alpha_V\beta_3$ et $\alpha_V\beta_5$, ce qui pourrait permettre une surveillance plus étendue de la maladie en fonction des mécanismes sous-jacents. En utilisant des souris recombinantes LDLR−/−ApoB100/100, l'autoradiographie a démontré la liaison de ces traceurs aux intégrines, montrant des perspectives prometteuses pour des applications futures visant à mesurer l'état inflammatoire de l'athérome. De son côté, le ^{18}F-RGD-K5 est hautement sélectif pour $\alpha_V\beta_3$ uniquement. Il présente également une élimination rapide et une toxicité moindre.

Jusqu'à present et avant le travail de cette thèse, seuls le ^{68}Ga-NOTA-RGD et ^{18}F-galacto-RGD ont été évalués chez l'homme pour l'imagerie des lésions athéroscléreuses. Malgré les bons résultats des découvertes existantes, il est important de souligner que les études d'imagerie publiées étaient limitées à de petites populations de patients, à savoir (i) une étude portant sur dix patients pour ^{18}F-galacto-RGD TEP-TDM et (ii) deux études ex vivo. A noter qu'étant donné que la taille des lésions athéroscléreuses est considérablement plus petite que celle des tumeurs, il y a un débat sur la faisabilité de ces traceurs pour détecter la plaque athéroscléreuse en raison des limites de résolution spatiale des caméras TEP disponibles (29–32).

Nous présentons ici une étude retrospective portant sur l'analyse du signal ^{68}Ga-NODAGA-RGD dans la paroi artérielle des gros vaisseux dans une cohorte de 44 patients oncologiques (chapitre 5) (33). Le chapitre 6 présente une étude annexe qui explore une

approche théranostique potentielle dans le domaine de l'athérosclérose (34). Cette approche repose sur l'utilisation d'une même molécule pour le diagnostic et la thérapie ultérieure, en changeant seulement l'isotope associé. À titre d'illustration, cette étude s'appuie sur une cohorte de 19 patients ayant montré des signes de régression de l'inflammation coronarienne après une thérapie ciblée des récepteurs peptidiques par radionucléides (PRRT). La thérapie ciblait spécifiquement le sous-type de récepteur de la somatostatine-2 (SST2) avec le Lutétium-177 DOTA-0-Tyr3-Octréotate (^{177}Lu-DOTATATE).

La quatrième section de cette thèse se focalise sur la TEP au rubidium, un examen qui joue un rôle essentiel dans l'étude principale concernant l'imagerie de l'intégrine $\alpha_v\beta_3$ en TEP après un infarctus du myocarde de type STEMI. La réserve coronaire est la capacité du réseau coronaire à augmenter son débit afin de couvrir une augmentation potentielle de la consommation myocardique d'oxygène. Elle est étudiée au moyen d'un test pharmacologique vasodilatateur (adénosine, dipyridamole, regadénoson). Les vasodilatateurs, en diminuant les résistances artériolaires, induisent une augmentation du débit coronaire pouvant aller jusqu'à 400-500 % chez le sujet normal. L'augmentation insuffisante du débit coronaire voire la diminution du débit en aval d'une sténose, apparaît alors par contraste sous la forme d'une hypoperfusion du territoire concerné par opposition aux territoires normaux, qui, eux, augmentent cette perfusion. L'étude de la perfusion myocardique par TEP peut se faire de manière quantitative par l'estimation du débit sanguin myocardique en mL/min/g au stress et au repos, permettant de déduire la réserve de flux myocardique qui se définit par le ratio des débits sanguins myocardiques de stress et de repos. Cette quantification a des intérêts diagnostique et pronostique, avec des performances accrues par rapport aux analyses semi-quantitatives (35).

Le chapitre 7 présente une étude prospective sur la valeur pronostique des paramètres quantitatifs en TEP au Rubidium (36). Cette étude inclut le paramètre régional de la capacité de perfusion myocardique, qui est un indice quantitatif combinant la réserve de perfusion myocardique et les flux de stress pour chaque pixel du myocarde. Cette analyse est réalisée en utilisant la nouvelle technologie des photomultiplicateurs au silicium (SiPM) avec des doses réduites de radiotraceur, permettant de délivrer moins d'1 mSv pour un patient de 70 kg pour la totalité de l'examen (repos, stress et scanner de repérage).

Dans une optique de recherche innovante, le chapitre 8 explore l'utilisation de l'Intelligence Artificielle (IA) pour étudier la perfusion myocardique en TEP au Rubidium dans le but de prédire les événements cardiaques majeurs indésirables (MACE). Un processus général de validation des modèles d'IA a été employé pour évaluer et comparer les performances des modèles globaux, segmentaires, radiomiques et des Réseaux de Neurones Convolutifs (CNN) exploitant différentes caractéristiques de la perfusion myocardique, en utilisant un ensemble de données comprenant 234 patients.

Les maladies des petits vaisseaux (SVD) jouent un rôle crucial dans l'ischémie cardiaque et cérébrale, mais peu d'informations sont disponibles sur les éventuelles interrelations entre les deux. Le chapitre 8 présente une étude d'évaluation de l'interrelation entre les SVD cardiaques et cérébrales en utilisant la TEP au Rubidium-82 pour le cœur et l'IRM pour le cerveau. Nous avons évalué rétrospectivement 370 patients, dont 38 présentaient une SVD cardiaque pure et 176 avaient une perfusion myocardique normale. Tous ont subi à la fois une TEP cardiaque au Rubidium-82 et une IRM cérébrale à 1,5T ou 3T. Le débit sanguin myocardique du ventricule gauche (LV-MBF) et la réserve de débit (LV-MFR) ont été enregistrés à partir de la TEP au Rubidium-82, tandis que le score de Fazekas, le volume des lésions de la substance blanche (WMab), le volume des lésions de la substance grise profonde (GMab) et la morphométrie cérébrale à l'aide du logiciel prototype MorphoBox ont été dérivés de l'IRM. Les groupes ont été comparés avec le test de Kruskal-Wallis, et le coefficient de corrélation de Pearson a été utilisé pour évaluer les éventuelles interrelations entre les marqueurs de SVD cardiaques et cérébraux. Toujours dans l'étude de la perfusion myocardique en TEP-TDM, le chapitre 9 se concentre quant à lui sur une étude de la dosimétrie pédiatrique de la TEP-TDM au ^{82}Rb. Nous fournissons ici des données originales prospectivement incluses de dosimétrie chez les enfants, confirmant sa sécurité et recommandant son inclusion dans la carte de dosage pédiatrique de l'association européenne de médecine nucléaire. Enfin, le chapitre 10 de cette partie se concentre sur l'utilisation de l'Intelligence Artificielle pour prédire les événements cardiaques majeurs en se basant sur des images de la perfusion myocardique. Il a été développé un pipeline d'évaluation des modèles d'Intelligence Artificielle, démontrant que les modèles régionaux d'Intelligence Artificielle surpassent significativement le modèle global traditionnel dans la prédiction d'événements cardiaques majeurs, avec un modèle de Réseau de Neurones Convolutifs obtenant le meilleur résultat. Notre étude montre que des modèles d'Intelligence Artificielle offrent un potentiel prometteur pour améliorer l'évaluation personnalisée du risque d'événements cardiaques majeurs liés aux maladies cardiovasculaires.

Enfin, la cinquième partie de la thèse se concentre sur des études annexes visant à documenter la recherche (37, 38). Le chapitre 11 présente une étude comparant la TEP au ^{68}Ga-NODAGA-RGD à la TEP au ^{18}F-FDG chez des patients atteints de cancers de l'œsophage ou de la jonction œsogastrique. Dans le chapitre 12, une comparaison similaire est effectuée dans le contexte de la polyarthrite rhumatoïde. Cette dernière partie ouvre de nombreuses perspectives et voies de recherche dans ce domaine.

Cette thèse a été réalisée au sein du service de médecine nucléaire du CHUV (Centre Hospitalier Universitaire Vaudois) à Lausanne, dans le cadre d'un projet coordonné par le co-directeur de thèse, le Professeur John Prior. Le travail a été effectué en collaboration avec l'Hôpital Cardiologique de Lyon et le laboratoire de recherche CARMEN de l'Université Lyon 1, sous la direction du Professeur Nathan Mewton, directeur de thèse. Des collaborations scientifiques ont également eu lieu avec l'Université de Turku en Finlande, en collaboration avec les Professeurs Antti Saraste et Johanni Knuuti.

References

1. Schwartz MA. Integrins and extracellular matrix in mechanotransduction. Cold Spring Harb Perspect Biol. 2010;2(12):a005066.
2. Stupack DG, Cheresh DA. Integrins and Angiogenesis. Curr Top Dev Biol. 2004;64:207–38.
3. Zanotelli MR, Reinhart-King CA. Mechanical forces in tumor angiogenesis. Adv Exp Med Biol. 2018;1092:91–112.
4. Harris AL. Hypoxia – a key regulatory factor in tumour growth. Nat Rev Cancer. 2002;2:38–47.
5. Cameliet P, Jain RK. Molecular mechanisms and clinical applica- tions of angiogenesis. Nature. 2011;473:298–307.
6. Niebler M, Reuning U, Reichart F, Notni J, Wester HJ, Schwaiger M, et al. Exploring the role of RGD-recognizing integrins in can- cer. Cancers. 2017;9(9):116.
7. Sinanan AC, Machell JR, Wynne-Hughes GT, Hunt NP, Lewis MP. Alpha v beta 3 and alpha v beta 5 integrins and their role in muscle precursor cell adhesion. Biol Cell. 2008;100(8):465–77.

8. Antonov AS, Antonova GN, Munn DH, Mivechi N, Lucas R, Catravas JD, et al. αVβ3 Integrin regulates macrophage inflam- matory response vis PI3 kinase/Akt-dependent NK-kB activation. J Cell Physciol. 2011;226(2):469–76.
9. Ward PA. Inflammation and αVβ3 integrin. Am J Respir Crit Care Med. 2012;185(1):5–6.
10. Hsueh WA, Law RE, Yuns S. Integrins, adhesion and cardiac remodelling. Hypertenstion. 1998;31:176–80.
11. Prowse ABJ, Chong F, Gray PP, Munro TP. Stem cell integrins: implications for ex-vivo culture and cellular therapies. Stem Cell Res. 2011;6(1):1–12.
12. Dietz M, Kamani CH, Dunet V, Fournier S, Rubimbura V, Testart Dardel N, Schaefer A, Jreige M, Boughdad S, Nicod Lalonde M, Schaefer N, Mewton N, Prior JO, Treglia G. Overview of the RGD-Based PET Agents Use in Patients With Cardiovascular Diseases: A Systematic Review. Front Med (Lausanne). 2022 6;9:887508. doi: 10.3389/fmed.2022.887508.
13. Prabhu SD, Frangogiannis NG. The Biological Basis for Cardiac Repair After Myocardial Infarction: From Inflammation to Fibrosis. *Circ Res*. 2016;119:91-112.
14. Khurana R, Simons M, Martin JF, Zachary IC. Role of angiogenesis in cardiovascular disease: a critical appraisal. *Circulation*. 2005;112:1813-1824.
15. Meoli DF, Sadeghi MM, Krassilnikova S, et al. Noninvasive imaging of myocardial angiogenesis following experimental myocardial infarction. *J Clin Invest*. 2004;113:1684-1691.
16. Higuchi T, Bengel FM, Seidl S, et al. Assessment of alphavbeta3 integrin expression after myocardial infarction by positron emission tomography. *Cardiovasc Res*. 2008;78:395-403.
17. Brooks PC, Clark RA, Cheresh DA. Requirement of vascular integrin alpha v beta 3 for angiogenesis. *Science*. 1994;264:569-571.
18. van den Borne SWM, Isobe S, Verjans JW, et al. Molecular imaging of interstitial alterations in remodeling myocardium after myocardial infarction. *J Am Coll Cardiol*. 2008;52:2017-2028.

19. Ebenhan T, Kleynhans J, Zeevaart JR, Jeong JM, Sathekge M. Non-oncological applications of RGD-based single-photon emission tomography and positron emission tomography agents. *Eur J Nucl Med Mol Imaging*. 2021;48:1414-1433.

20. Jenkins WSA, Vesey AT, Stirrat C, et al. Cardiac $\alpha_V \beta_3$ integrin expression following acute myocardial infarction in humans. *Heart*. 2017;103:607-615.

21. Gould KL, Johnson NP, Bateman TM, et al. Anatomic Versus Physiologic Assessment of Coronary Artery Disease: Role of Coronary Flow Reserve, Fractional Flow Reserve, and Positron Emission Tomography Imaging in Revascularization Decision-Making. *J Am Coll Cardiol*. 2013;62:1639-1653.

22. Kwiecinski J, Tzolos E, Adamson PD, Cadet S, Moss AJ, Joshi N, Williams MC, van Beek EJR, Dey D, Berman DS, Newby DE, Slomka PJ, Dweck MR. Coronary 18F-Sodium Fluoride Uptake Predicts Outcomes in Patients With Coronary Artery Disease. J Am Coll Cardiol. 2020 Jun 23;75(24):3061-3074. doi: 10.1016/j.jacc.2020.04.046.

23. Dietz M, Chironi G, Faraggi M. Reduced 18F-sodium fluoride activity in coronary plaques after statin therapy. Eur Heart J Cardiovasc Imaging. 2021;22:e133. doi: 10.1093/ehjci/jeab016.

24. Kim LT, Yamada KM. The regulation of expression of integrin receptors. Proc Soc Exp Biol Med. 1997;214:123–31.

25. Ikari Y, Yee KO, Schwart SM. Role of $\alpha 5\beta 1$ and $\alpha V\beta 3$ integrins on smooth muscle cell migration in fibrin gels. Thromb Haemost. 2000;84:701–5.

26. Davenpeck KL, Marcinkiewiz C, Wang D, Niculescu R, Shi Y, et al. Regional differences in integrin expression: role of $\alpha 5\beta 1$ in regulating smooth cell muscle functions. Circ Res. 2001;88:352– 8. 1180. Moiseeva EP. Adhesion receptors of vascular smooth muscle cells and their functions. Cardiovasc Res. 2001;52:372–86.

27. Al-Fakhari N, Wilhelm J, Hahn M, Heidt M, Herlein FW, et al. Increased expression of disintegrin-metalloproteinases ADAM-15 and ADAM-9 following upregulation of integrins $\alpha 5\beta 1$ and $\alpha V\beta 3$ in atherosclerosis. J Cell Biochem. 2003;89:808–23.

28. Lee SJ, Paeng JC. Nuclear molecular imaging for vulnerable ath- erosclerotic plaques. Korean J Radiol. 2015;16:955–66.

29. J, Laitinen L, Luoto P, Ivenson P, Wilson I, et al. ^{68}Ga- DOTA-RGD peptide: biodistribution and binding into atheroscle- rotic plaques in mice. Eur J Nucl Med Mol Imaging. 2009;36: 2058–67.

30. Laitinen I, Saraste A, Weidl E, Poethko T, Weber AW, et al. Evaluation of αVβ3-integrin targeted positron emission tomogra- phy tracer ^{18}F-Galacto-RGD for imaging of vascular inflamma- tion in atherosclerotic mice. Circ Cardiovasc Imaging. 2009;2: 331–8.
31. Razavian M, Marfatia R, Mongue-Din H, Tavakoli S, Sinusas AJ, et al. Intergin-targeted imaging of inflammation in vascular re- modeling. Atheroscler Tromb Vasc Biol. 2011;31:2820–6.
32. Paeng JC, Lee YS, Lee JS, Jeong JM, Kim KB, et al. Feasibility and kinetic characteristics of 68Ga-NOTA-RGD PET for in vivo atherosclerosis imaging. Ann Nucl Med. 2013;27:847–54.
33. Dietz M, Kamani CH, Deshayes E, Dunet V, Mitsakis P, Coukos G, Nicod Lalonde M, Schaefer N, Prior JO. Imaging angiogenesis in atherosclerosis in large arteries with 68Ga-NODAGA-RGD PET/CT: relationship with clinical atherosclerotic cardiovascular disease. EJNMMI Res. 2021 Aug 14;11(1):71. doi: 10.1186/s13550-021-00815-5.
34. Dietz, M., et al. "Cardiac theranostics: A possible role of 177Lu-DOTATATE therapy in coronary atherosclerotic plaque inflammation." Médecine Nucléaire 46.4 (2022): 201-203.
35. Herzog BA, Husmann L, Valenta I, Gaemperli O, Siegrist PT, Tay FM, Burkhard N, Wyss CA, Kaufmann PA. Long-term prognostic value of 13N-ammonia myocardial perfusion positron emission tomography added value of coronary flow reserve. J Am Coll Cardiol. 2009 Jul 7;54(2):150-6. doi: 10.1016/j.jacc.2009.02.069.
36. Dietz M, Kamani CH, Allenbach G, Rubimbura V, Fournier S, Dunet V, Treglia G, Nicod Lalonde M, Schaefer N, Eeckhout E, Muller O, Prior JO. Comparison of the prognostic value of impaired stress myocardial blood flow, myocardial flow reserve, and myocardial flow capacity on low-dose Rubidium-82 SiPM PET/CT. J Nucl Cardiol. 2023 Aug;30(4):1385-1395. doi: 10.1007/s12350-022-03155-6.
37. Dietz M, Dunet V, Mantziari S, Pomoni A, Dias Correia R, Testart Dardel N, Boughdad S, Nicod Lalonde M, Treglia G, Schafer M, Schaefer N, Prior JO. Comparison of integrin αvβ3 expression with 68Ga-NODAGA-RGD PET/CT and glucose metabolism with 18F-FDG PET/CT in esophageal or gastroesophageal junction cancers. Eur J Hybrid Imaging. 2023 Feb 1;7(1):3. doi: 10.1186/s41824-023-00162-9.

38. Dietz, M.; Nicod Lalonde, M.; Omoumi, P.; Testart Dardel, N.; Hügle, T.; Prior, J.O. Imaging of αvβ3 integrin expression in rheumatoid arthritis with [68Ga]Ga-NODAGA-RGDyk PET/CT in comparison to [18F]FDG PET/CT. Med. Nucl. 2021, 45, 293–295.

Chapter 2

Overview of the RGD-Based PET Agents Use in Patients With Cardiovascular Diseases: A Systematic Review

Front. Med. 2022 9:887508. doi: 10.3389/fmed.2022.887508

Matthieu Dietz, Christel H. Kamani, Vincent Dunet, Stephane Fournier, Vladimir Rubimbura, Nathalie Testart Dardel, Ana Schaefer, Mario Jreige, Sarah Boughdad, Marie Nicod Lalonde, Niklaus Schaefer, Nathan Mewton, John O. Prior, and Giorgio Treglia

Abstract

Studies using arginine–glycine–aspartate (RGD)-PET agents in cardiovascular diseases have been recently published. The aim of this systematic review was to perform an updated, evidence-based summary about the role of RGD-based PET agents in patients with cardiovascular diseases to better address future research in this setting. Original articles within the field of interest reporting the role of RGD-based PET agents in patients with cardiovascular diseases were eligible for inclusion in this systematic review. A systematic literature search of PubMed/MEDLINE and Cochrane library databases was performed until October 26, 2021. Literature shows an increasing role of RGD-based PET agents in patients with cardiovascular diseases. Overall, two main topics emerged: the infarcted myocardium and atherosclerosis. The existing studies support that $\alpha_v\beta_3$ integrin expression in the infarcted myocardium is well evident in RGD PET/CT scans. RGD-based PET radiotracers accumulate at the site of infarction as early as 3 days and seem to be peaking at 1–3 weeks post myocardial infarction before decreasing, but only 1 study assessed serial changes of myocardial RGD-based PET uptake after ischemic events. RGD-based PET uptake in large vessels showed correlation with CT plaque burden, and increased signal was found in patients with prior cardiovascular events. In human atherosclerotic carotid plaques, increased PET signal was observed in stenotic compared with non-stenotic areas based on MR or CT angiography data. Histopathological analysis found a co-localization between tracer accumulation and areas of $\alpha_v\beta_3$ expression. Promising applications using RGD-based PET agents are emerging, such as prediction of remodeling processes in the infarcted myocardium or detection of active atherosclerosis, with potentially significant clinical impact.

Introduction

Ischemic heart disease is the leading cause of death worldwide (1). Understanding cellular alterations involved in atherosclerotic plaque instability, as well as reparative mechanisms following myocardial infarction (MI) is important for both preventive and therapeutic intervention.

Positron emission tomography (PET) is an in vivo medical imaging technique that enables quantification of radiotracer uptake in the entire body at a cellular level.

Integrin $\alpha_v\beta_3$ is a transmembrane receptor mediating cell adhesion that influences cell growth, proliferation, survival, and migration. The peptide motif arginine–glycine–aspartate, abbreviated by "RGD" in the one-letter code, has been identified in 1984 as a minimal amino acid sequence that some integrins recognize in their natural ligands (2). In 1991 a group from Germany reported a strong and selective binding of cyclic pentapeptides containing the RGD sequence to $\alpha_v\beta_3$ integrin (3). The past 20 years have witnessed a remarkable expansion on cyclic peptides containing the RGD sequence since it was found that $\alpha_v\beta_3$ integrin plays a major role in angiogenesis, further enhanced by the first successful clinical applications of the PET radiopharmaceutical ^{18}F-Galacto-RGD (4-8).

The integrin-mediated cell adhesion/migration imaging with RGD PET was found to be involved in a wide range of pathophysiological processes, not only related to angiogenesis. Increased $\alpha_v\beta_3$ expression has been observed in some cancer cells as well as in cells involved in extracellular matrix remodeling such as fibroblasts and activated macrophages (8-9). However, the clinical relevance of such biomarker is not well understood (8). Although most studies using RGD-PET agents focused predominantly on tumorigenesis, a greater focus on non-oncological applications such as cardiovascular diseases is of interest (9). In fact, in the development of atherosclerosis, expression of integrin $\alpha_v\beta_3$ has been found in endothelial cells as well as in CD68-positive macrophages, which are known as key factors in plaque instability (10-12). Moreover, $\alpha_v\beta_3$ integrin expression seems to appear central to the coordination of myocardial repair following MI. $\alpha_v\beta_3$ integrin is indeed upregulated in states of angiogenesis within the infarcted myocardium and could be expressed by activated myofibroblasts and macrophages during margination and chemotaxis (13-14).

Some recent studies using RGD-PET agents in cardiovascular diseases have been published. The aim of this systematic review is to perform an updated evidence-based summary about the role of RGD-based PET agents in patients with cardiovascular diseases to better address further research in this setting.

Methods

The reporting of this systematic review conforms to the updated "Preferred Reporting Items for a Systematic Review and Meta-Analysis" (PRISMA) statement, an established guidance to identify, select, appraise, and synthesize studies in systematic reviews (15).

Search strategy

A comprehensive computer literature search of PubMed/MEDLINE, and Cochrane library databases was performed by two authors (MD and GT) to identify published articles that investigated the role of RGD-based PET agents in patients with cardiovascular diseases. A combination of the following terms was used for the search algorithm: ((integrin) OR (angiogenesis) OR (RGD) OR (NODAGA)) AND ((PET) OR (positron)) AND ((myocard*) OR (cardi*) OR (heart) OR (cardiovascular) OR (CAD)). The search was carried out from inception to October 26, 2021. To expand the search, references of the retrieved articles were also screened for additional studies.

Study selection

Original articles within the field of interest reporting the role of RGD-based PET agents in patients with cardiovascular diseases were eligible for inclusion. The exclusion criteria were as follow: (a) original preclinical studies in the field of interest (b) articles outside of the field of interest of this review; (c) case reports and small case series (less than 5 patients); (d) review articles, comments, letters, editorials, and conference proceedings. No language or date restrictions were used. The titles and abstracts of the recovered articles were reviewed independently by two researchers (MD and GT) according to the inclusion and exclusion criteria. Articles which appeared evidently ineligible according to these eligibility criteria were rejected. The full-length version of the remaining articles was independently reviewed by two researchers (MD and GT) to evaluate their eligibility for inclusion. Any disagreements over articles eligibility were resolved by consensus.

Quality assessment

The quality assessment was performed according to the NIH Quality assessment tool for Observational Cohort and Cross-Sectional Studies (https://www.nhlbi.nih.gov/health-topics/study-quality-assessment-tools).

Results

Literature Search

The review question was the role of RGD-based PET agents in patients with cardiovascular diseases. The literature search results using a systematic approach are reported in Figure 1. The comprehensive computer literature search from PubMed/MEDLINE and Cochrane library database revealed 325 records. Reviewing titles and abstracts, 319 records were excluded: 253 because they were not in the field of interest of this review; 34 reviews, editorials, letters, or comments; 31 preclinical studies, and 1 case report. Six articles were selected and retrieved in full-text version. One additional study was found screening the references of the selected articles. Finally, 7 articles (198 patients) including data on the role of RGD-based PET agents in patients with cardiovascular diseases were included in the systematic review (16-22). The characteristics of the studies selected for the systematic review are presented in Tables 1-5.

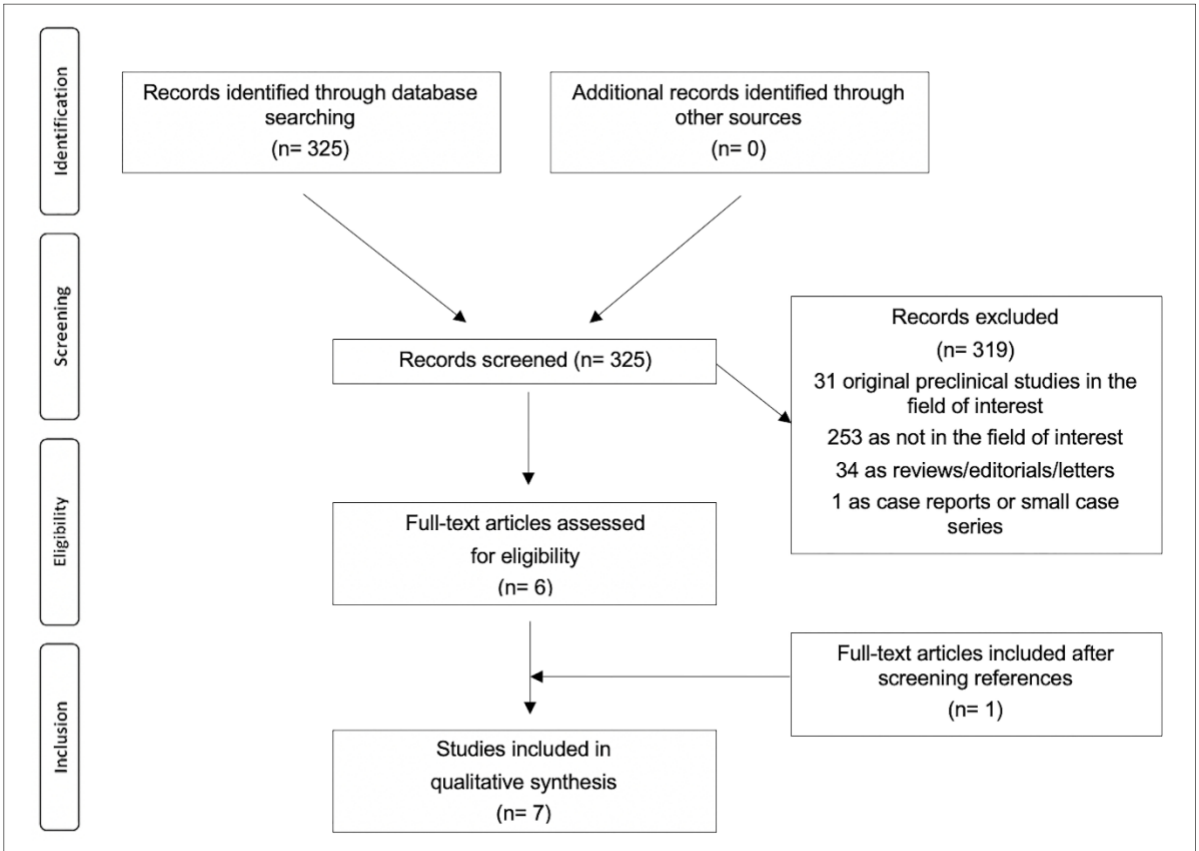

FIGURE 1 | Flowchart of the literature search.

Qualitative Synthesis (Systematic Review)

Basic Study and Patient Characteristics

Through the comprehensive computer literature search, 7 full-text articles including data on the role of RGD-based PET agents in patients with cardiovascular diseases were selected (Table 1) (16–22). All the selected articles were published in the last nine years. Korea, the United Kingdom, China, Germany, and Switzerland were represented. All the studies were monocentric, 86% were prospective and 14% were retrospective. 2 out of the 7 studies (29%) focused only on the infarcted myocardium, one study focused on the infarcted myocardium and stroke (14%), one study focused only on stroke (14%), and the remaining 3 studies (43%) focused on atherosclerosis. Included patients had high rates of cardiovascular diseases: 130 out of the 198 patients (66%) had previous MI or stroke or were scheduled for carotid endarterectomy. The number of patients performing PET with RGD-based PET agents in cardiovascular studies ranged from 10 to 46. The mean age of the included patients ranged from 6.1 to 68.5 years; the female percentage was variable from 0% to 50%.

The quality of all the selected studies is judged as moderate according to the NIH quality assessment tools.

Technical Aspects

The included studies had heterogeneous technical aspects (Table 2). Five different radiotracers were used, the most frequent being ^{18}F-Galacto-RGD and ^{18}F-fluciclatide. The hybrid imaging modality was PET/CT for all the studies (no PET/MR study recorded). The radiopharmaceutical injected activity varied among the included studies (Table 2). The mean time interval between radiotracer injection and image acquisition varied among the included studies, from 20 to 120 minutes. Fasting was not requested before radiolabelled RGD-based injection. The PET image analysis was performed by using qualitative (visual) analysis and additional semi-quantitative analysis through the calculation of standardized uptake values (SUV) in most studies (6 out of the 7 studies: 86%). All reported values were corrected for mean radiotracer activities in the normal myocardium, and/or the normal brain, the blood, the liver, the most frequent being the blood pool activity.

Main findings for studies focused on the infarcted myocardium

29 out of the 56 (52%) MI patients in studies focused on the infarcted myocardium had ST-elevation MI (STEMI), 6 out of the 56 (11%) MI patients had non-ST-elevation MI (NSTEMI), and this information was not available in the 21 remaining patients (38%). The main outcome measurements of RGD-based tracer accumulation in the infarcted myocardium are listed in Table 3 and include correlation between RGD uptake and MI size, characterization of RGD uptake pattern, histological correlates, and the temporal expression of RGD uptake. The time

interval between MI and RGD-based PET/CT varied from 3 days to 2 years, most patients undergoing RGD-based PET/CT within 3 months after the MI attack. Importantly, 63 out of the 73 RGD-based PET acquisitions (86%) displayed positive radiotracer uptake in the infarcted zones. Other modalities used to outline the infarcted zones were ^{99m}Tc-MIBI, cardiac MRI and [^{13}N]NH3 PET.

The MI size was determined by ^{99m}Tc-MIBI cardiac perfusion imaging (measurements of the maximum diameters of the infarcted regions), cardiac MRI (measurements in g/m^2) or [^{13}N]NH3 perfusion PET (% of left ventricle). 2 out of the 3 studies found correlation between RGD uptake and MI size but the remaining third study did not find any correlation.

Concerning the correlation between perfusion and RGD uptake, Makowski et al. found a per-segment negative correlation between tracer uptake of [^{18}F]Galacto-RGD and blood flow, as measured by [^{13}N]NH3 (20). Interestingly, Sun et al. found ^{68}Ga-PRGD2 uptake to be located at or immediately around the area of infarction outlined by matched ^{99m}Tc-MIBI perfusion images and ^{18}F-FDG metabolism images (16). This finding supports a potential increased $\alpha_v\beta_3$ expression also in non-viable tissue, as defined by regional reductions in ^{18}F-FDG uptake in proportion to regional reductions in myocardial perfusion.

Only 1 out of the 3 studies reported histopathological analysis in an exploratory analysis for two patients, finding positive staining for $\alpha_v\beta_3$ integrin, largely in regions that co-localized to vascular endothelial cells. Lower numbers of CD68-positive inflammatory cells and smooth muscle actin-positive myofibroblasts co-registered also with $\alpha_v\beta_3$ integrin expression were found in their exploratory analysis (18). One out of the 3 studies studied the temporal expression of the RGD uptake using serial assessments, with 17 out of the 21 patients agreeing to return for a second RGD PET/CT 76±19 days post-MI and found a reduced RGD uptake intensity as compared with earlier imaging 14±7 days post-MI (18).

The study from Jenkins et al was also the only study that assessed the correlation between RGD uptake and functional recovery. Interestingly, they found an association between increased $\alpha_v\beta_3$ expression and improvement of wall motion (18).

A representative example of RGD PET/CT imaging in the infarcted myocardium is illustrated in Figure 2.

TABLE 1 | Basic study and patient characteristics of the included studies.

References	Country	Study design		Study focus	Number of patients	MI patients	Stroke patients or patients scheduled for carotid endarterectomy	Average age (range)	Male/ Female
Choi et al. (22)	Korea	Prospective	Monocentric	Stroke	10	NR	10	6.1 (2–14)*	5/5†
Sun et al. (16)	China	Prospective	Monocentric	MI	39	23	16	MI Patients: 61 (45–82) Stroke Patients: 56 (33–80)	30/9
Beer et al. (17)	Germany	Prospective	Monocentric	Atherosclerosis	10	NR	10	68.5 (55–79)	NR
Jenkins et al. (19)	United Kingdom	Prospective	Monocentric	MI	37	21	NR	64 ± 10 (NR)	27/10
Jenkins et al. (19)	United Kingdom	Prospective	Monocentric	Atherosclerosis	46	24	NR	66 ± 10 (NR)	34/12
Makowski et al. (20)	Germany	Prospective	Monocentric	MI	12	12	NR	53 ± 12 (NR)	12/0
Dietz et al. (21)	Switzerland	Retrospective	Monocentric	Atherosclerosis	44	5	5	60 (NR)	24/20

MI, myocardial infarction; NR, not reported.
**Age 1–14 years in the method section.*
†Male/Female 6/4 in the method section.

Main findings for studies focused on atherosclerosis

The arterial segments assessed were internal and common carotid arteries, ascending aorta, aortic arch, descending aorta, abdominal aorta, and iliac arteries. One study focused only on internal and common carotid arteries and another study focused only on thoracic aorta for in vivo imaging (17, 19). No study assessed the coronary arteries. The main outcome measurements of RGD-based tracer accumulation in atherosclerosis are listed in Table 4 and include clinical, morphological, and histological correlates. The median intensity of tracer uptake as determined by TBR measurements ranged from 1.31 (IQR 1.62–2.04) to 1.84 (IQR 1.62–2.04), but these data were available only in 2 out of 3 studies (19, 21). Only one study included a binary visual analysis and found a positive signal in carotid plaques on PET using ^{68}Ga-NOTA-PRGD2 in only half of the patients (5 out of 10 patients) (17).

Two studies focused on clinical correlates and found correlation with prior cardiovascular or cerebrovascular events as well as with history of hypercholesterolemia (19, 21).

Morphological imaging was included in all studies. Two studies focused on CT plaque burden in large vessels and found correlation with CT calcium scoring and/or the indexed plaque volume (19, 21). One study included further exploration using ultrasound and MR angiography and found a higher tracer accumulation in areas of the carotids with medium- or high-grade stenosis compared with areas with none/low-grade stenosis (17).

Finally, 2 out of the 3 studies reported histopathological analysis and found a co-localization between tracer accumulation and areas of $\alpha_v\beta_3$ expression (17, 19).

A representative example of RGD PET/CT imaging in atherosclerosis is illustrated in Figure 3.

TABLE 2 | Technical aspects of RGD-based PET/CT in the included studies.

References	PET/CT scanner	Tracers used	Mean injected activity (range)	Mean time interval between radiotracer injection and image acquisition	PET/CT image analysis	
					Semi-quantative	Reference
Choi et al. (22)	NR	^{68}Ga-NOTA-RGD	111	20 min	Lesion to control ratios	Normal brain
Sun et al. (16)	Siemens Biograph 64 TruepointTrueV	^{68}Ga-NOTA-PRGD2	1.85 MBq/kg	30 min	SUV_{peak}; SUV ratios	Normal myocardium; normal brain
Beer et al. (17)	Siemens Biograph Sensation 16	^{18}F-Galacto-RGD	188 ± 16 (NR) MBq	90 min	SUV_{mean}; TBR	Common carotid artery
Jenkins et al. (19)	Siemens Biograph mCT	^{18}F-fluciclatide	229 ± 12 (NR) MBq	40 min	SUV_{mean}; SUV_{max}; TBR	Superior vena cava
Jenkins et al. (19)	Siemens Biograph mCT	^{18}F-fluciclatide	229 (NR) MBq	40 min	SUV_{mean}; SUV_{max}; TBR	Superior vena cava
Makowski et al. (20)	Siemens Biograph Sensation 16	^{18}F-Galacto-RGD	188 ± 19 (NR) MBq	120 min	SUVs; SUV ratios	Normal myocardium, blood, liver
Dietz et al. (21)	GE Discovery 690 TOF; Siemens Biograph Vision 600	^{68}Ga-NODAGA-RGD	190 (NR) MBq	63 min	SUV_{max}; SUV_{mean}; TBR	Inferior and superior vena cava

NR, not reported; SUV, standardized uptake value; TBR, target-to-background ratio.

TABLE 3 | Summary of PET findings for studies focused on the infarcted myocardium.

References	MI type	RGD-based tracer accumulation				RGD-based tracer changes according to time after the event	Correlation between RGD uptake and MI size	Other modalities used to determine the infarcted zones	Uptake pattern	Histological correlates
		Days after MI	Positive number	SUV values	Negative number					
Sun et al. (16)	NR (one NSTEMI patient specified among the negative patients)	3 days−2 years	20/23	SUV_{peak} 1.94 ± 0.48, SUV ratios 2.33 ± 1.04, with peak uptake 1 week after MI	3	No serial assessment. Peak uptake 1 week after MI. Plateau within 4–75 days after MI	Yes ($r = 0.748$, $P = 0.001$)	^{99m}Tc-MIBI/cardiac ^{18}F-FDG PET/CT	Patchy form, within the area of infarction or immediately around	NR
Jenkins et al. (19)	STEMI	14 ± 7 days ($n = 21$)	21	TBR_{mean} 1.34 ± 0.22	0	Reduced intensity on second PET/CT scans	No ($r = 0.03$, $P = 0.90$)	Cardiac MRI	Within the area of infarction	Viable myocardium with widespread positive staining for $\alpha_v\beta_3$ integrin (exploratory analysis for two patients)
		76 ± 19 days ($n = 17$)	17	TBR_{mean} 1.20 ± 0.21	0					
Makowski et al. (20)	7 STEMI/5 NSTEMI	31 ± 14 days	5	Lesion/blood 1.15 ± 0.06; lesion/liver 0.61 ± 0.18	7	NR	Yes (moderate, $r = 0.73$, $P = 0.016$)	Cardiac MRI/[^{13}N]NH3 PET	Within the area of infarction or immediately around	NR

NR, not reported; MI, myocardial infarction; STEMI, ST-elevation myocardial infarction; NSTEMI, Non-ST-elevation myocardial infarction.
r = Pearson correlation analysis.

TABLE 4 | Summary of PET findings for studies focused on atherosclerosis.

References	Arterial segment	RGD-based tracer accumulation			Clinical correlates	Morphological imaging correlates	Histological correlates
		Values; median (IQR)	Positive number	Negative number			
Beer et al. (17)	Internal and common carotid arteries	NR	In 5 patients (50%)	In 5 patients (50%)	NR	Higher tracer accumulation in areas of the carotids with medium- or high-grade stenosis compared with areas with none/low-grade stenosis (stenosis classified by using ultrasound and MR angiography, $P = 0.04$).	$\alpha_v\beta_3$ expression ($r = 0.787$, $P = 0.026$)
Jenkins et al. (19)	Ascending aorta, aortic arch, and descending thoracic aorta (for *in vivo* imaging)	SUV_{mean} 2.73 (2.35–3.05) SUVmax 3.65 (3.04–4.01) TBR 1.31 (1.20–1.39)	NR	NR	Higher tracer accumulation in patients with recent MI ($P = 0.02$), with hypercholesterolaemia ($P = 0.01$) and with established ischemic heart disease ($P = 0.04$)	CT plaque burden ($r = 0.37$, P=0.01), mean wall thickness ($r = 0.57$, $P < 0.001$), and plaque volume ($r = 0.56$, $P < 0.001$) recorded on CT	Tracer accumulation co-localized with areas of $\alpha_v\beta_3$ expression, angiogenic endothelial cells, and inflammatory macrophages (in four human carotid intimal samples)
Dietz et al. (21)	Common carotid arteries, ascending aorta, aortic arch, descending aorta, abdominal aorta, and iliac arteries	TBR 1.84 (1.62–2.04)	NR	NR	Higher tracer accumulation in patients with previous clinically documented atherosclerotic cardiovascular disease ($P = 0.001$). Positive correlation with prior cardiovascular or cerebrovascular event ($r = 0.33$, $P = 0.027$), BMI ($\rho = 0.38$, $P = 0.01$), and history of hypercholesterolemia ($r = 0.31$, $P = 0.04$).	CT plaque burden ($\rho = 0.31$, $P = 0.04$)	NR

NR, not reported.
r = Pearson correlation analysis.
ρ = Spearman correlation analysis.

TABLE 5 | Summary of PET findings for studies focused on stroke.

References	Explicit neurologic symptoms	RGD-based tracer accumulation				RGD-based tracer changes according to time after the event	Correlation between RGD uptake and stroke size	Other modalities used to determine the infarct zones	Uptake pattern	Histological correlates
		Days after the event	Positive number	SUV values	Negative number					
Choi et al. (22)	13/17 (per lesion analysis)	1–422 days	8/17 (per lesion analysis)	No SUV value reported, lesion to control ratios 3.9±4.09	9/17 (per lesion analysis)	No serial assessment. Higher tracer accumulation in the recent infarct group (<30 days after the event)	NR	Brain MRI/^{99m}Tc-HMPAO perfusion	Higher tracer accumulation in the three lesions with hyperperfusion as compared with the other lesions ($P = 0.033$)	NR
Sun et al. (16)	16/16 patients	4–13 years ($n = 16$)	8/16	SUV_{peak} 0.46 ± 0.29, SUV ratios 3.29 ± 1.09, with peak uptake 2 weeks after the event	8/16	Reduced intensity ($n = 1$) or disappearance ($n = 1$) on second PET/CT scans	In patients scanned 13th–26 days after the event ($r = 0.835$, $P = 0.003$)	Brain MRI/brain ^{18}F-FDG PET/CT	Punctate multifocal form	NR
		3 months ($n = 2$)	1/2	SUV_{peak} 0.16 ($n = 1$)	1/2			Brain ^{18}F-FDG PET/CT		

NR, not reported.

Main findings for studies focused on stroke

The stroke symptoms were described as hemiplegia, hemidysesthesia and/or hemianopsia in the 16 stroke patients included in the study from Sun et al. (16) and were not described in the 10 stroke patients included in the study from Choi et al. (22). The main outcome measures about the RGD-based tracer accumulation in cerebral infarct are listed in Table 5 and include correlation between RGD uptake and stroke size, characterization of RGD uptake pattern, and the temporal expression of RGD. The time interval between the event and RGD-based PET/CT varied from 1 day to 4 years, with most patients within 1 month after the cerebral attack. On a per-lesion analysis, 16 out of the 33 cerebral infarct zones (48%) displayed positive radiotracer uptake. 17 out of the 33 cerebral infarct zones (52%) were negative. Other modalities used to determine the infarct zones were ^{99m}Tc-HMPAO, brain MRI and ^{18}F-FDG PET/CT. Only one study studied the correlation between RGD uptake and stroke size, measured over the CT images by referring to the ^{18}F-FDG images (16). They found a positive correlation between RGD uptake and infarct size in a limited number of patients (n=10) scanned 13–26 days after the event (Table 5). However, the authors pointed out two patients scanned 4 days after the event with mildly elevated RGD uptake despite relatively large low-density stroke regions on CT (SUV_{peak} = 0.15 and 0.16, maximum diameters 69.8 and 101.3 mm, respectively). No other data about the correlation between RGD uptake and stroke size was reported. This same study described the uptake pattern as a punctate multifocal form, mainly along the surrounding blood vessels (16). These authors also assessed the temporal expression of the RGD uptake using serial assessments with repeated scans at 3 months post event, but with a very limited number of patients (n=2). They found a reduced intensity (n=1) or disappearance (n=1) on second PET/CT scans.

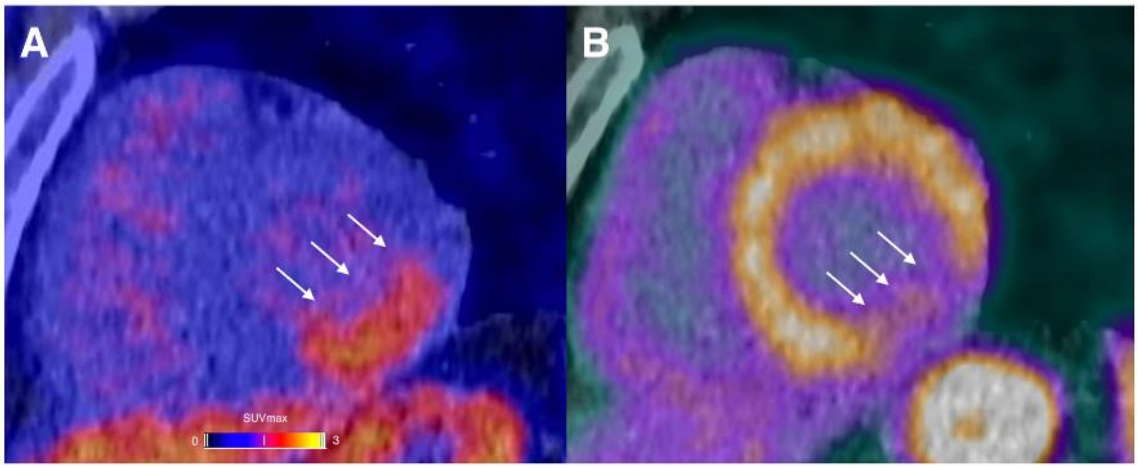

FIGURE 2 | A 44-year-old male presented with chest pain in the emergency room. The initial ECG displayed sinus-rhythm with ST elevation in inferior derivations. The laboratory results showed severely elevated cardiac troponin (up to 7,220 ng/l). Percutaneous coronary intervention with stenting of the completely occluded proximal left circumflex artery was performed without complications. A $\alpha_v\beta_3$-targeting PET agent (^{68}Ga-Nodaga-RGD) was used to assess integrin expression 9 days after the event. Focal tracer retention was localized in the basal and mid inferolateral segments (arrows; **A**). PET/CT examination using Rubidium-82 revealed a severely reduced myocardial blood flow in the same basal and mid inferolateral segments (arrows; **B**).

Discussion

Since the first successful clinical applications of an RGD PET radiopharmaceutical two decades ago, all the final eligible articles included in this review (n=7) were published in the last 9 years, reflecting a recent growing interest in RGD PET/CT imaging focused on cardiovascular diseases (16-22). These studies varied in size and methodology. Two main topics can be distinguished: the infarcted myocardium and atherosclerosis. Stroke is a third topic that can be distinguished, but slightly less studied. All studies had a relatively clearly stated, clinically relevant, and patient-related purpose. Longitudinal studies that tell more about the natural history of $\alpha_v\beta_3$ expression in cardiovascular diseases using PET imaging were in very short supply. Interventional studies or randomized controlled trials have not been conducted so far. Due to this diversity, our systematic review could not provide an answer to a particular scientific question; we were left to summarize the main information about RGD PET in cardiovascular diseases that the literature had provided until now and point to some major issues that remain unanswered.

Infarcted myocardium and $\alpha_v\beta_3$ integrin expression

Ventricular remodeling defines the changes that occur in structure, geometry, and function of the myocardium after MI. This biological process involves inflammation, angiogenesis, repair, and healing with specific biochemical and structural alterations in the infarcted myocardium, peri infarcted and remote regions. Several cell populations are involved, such as neutrophils, monocytes/macrophages, fibroblasts, T cells, stem cells, etc (23, 24). Understanding reparative mechanisms following MI is becoming increasingly important. In some circumstances,

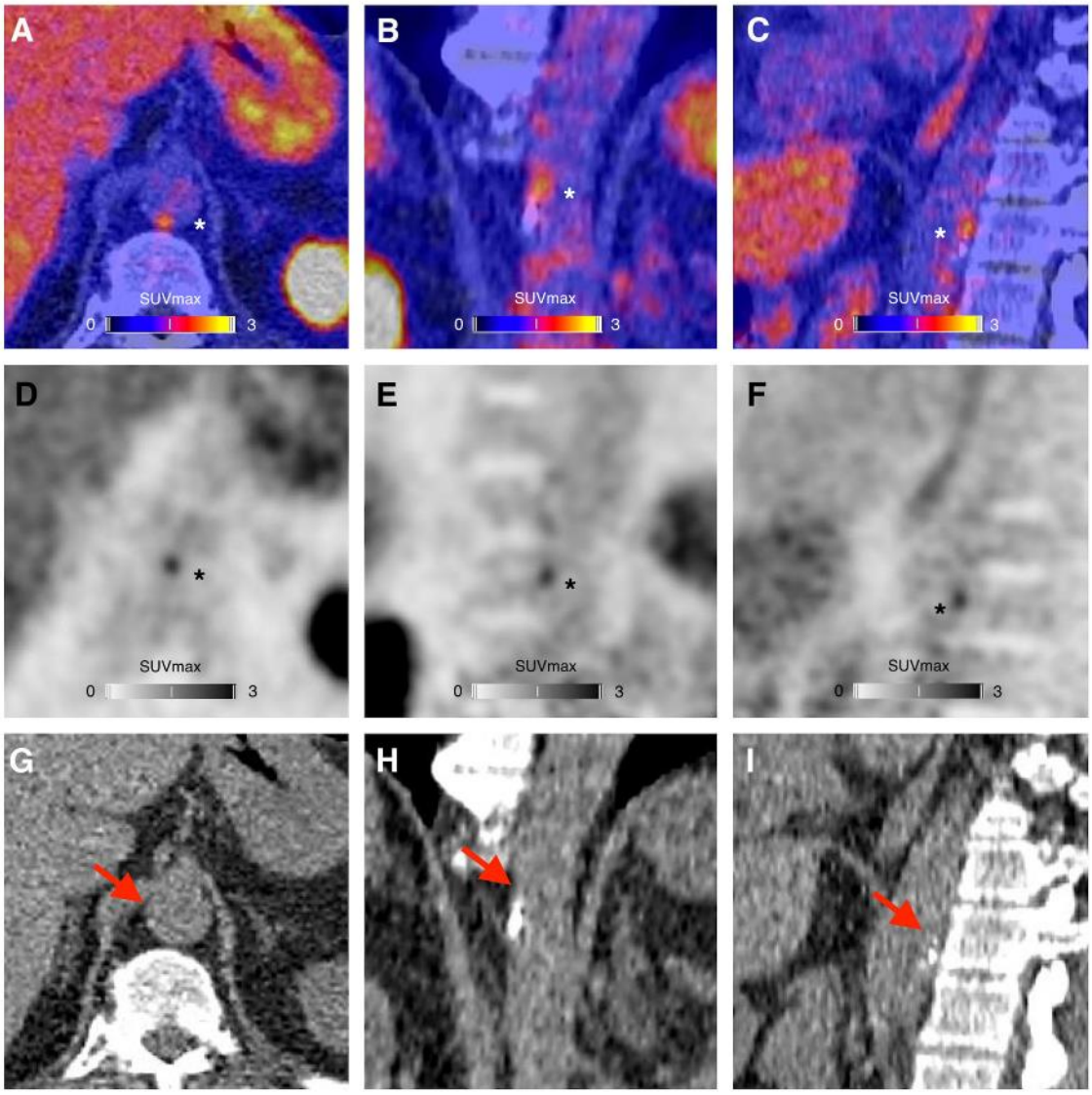

FIGURE 3 | PET/CT **(A–C)**, PET **(D–F)**, and CT **(G–I)** images showing a focus of ^{68}Ga-NODAGA-RGD arterial uptake (asterisks), in the periphery of a calcified atherosclerotic lesion (red arrows), in the wall of the abdominal aorta of a 63-year-old man who had a myocardial infarction with ST elevation 3 months before PET imaging. The risk factors of the patient were resumed to current tobacco use and family history of early coronary artery disease. At the time of the PET imaging the patient was treated with high intensity statin therapy, aspirin, ticagrelor, beta-blockers and an angiotensin-converting enzyme inhibitor, and was advised to adopt a healthy diet and to engage in regular physical activity.

maladaptive persistent processes may be detrimental. This may encourage remodeling and scarring to extend into the myocardium long after the initial causative injury, leading to progressive ventricular dilatation, ventricular dysfunction, and heart failure (25, 26).

The expression of $\alpha_v\beta_3$ integrin following MI, using PET imaging technique, could be of great interest. In contrast to a low level of expression by quiescent endothelial cells, $\alpha_v\beta_3$ integrin was found to be upregulated in state of angiogenesis within the myocardium after infarction in preclinical studies in rats (14, 27). $\alpha_v\beta_3$ integrin expression was also documented by both activated cardiac myofibroblasts and macrophages during margination and chemotaxis. Thus,

$\alpha_v\beta_3$ integrin expression could play a central role in the coordination of the repair processes following MI.

Prevalence and natural history of RGD PET uptake in the infarcted myocardium, and future potential directions

46 out of the 56 (90%) MI patients in PET studies focused on the infarcted myocardium presented RGD uptake in the infarcted area, demonstrating that $\alpha_v\beta_3$ integrin expression in the infarcted myocardium is well evident in RGD PET/CT scans.

In human studies of acute MI, RGD-based PET radiotracers accumulate at the site of infarction as early as 3 days and seem to be peaking at 1–3 weeks post-MI before being decreasing (16, 18). However, only one study assessed serial changes of myocardial RGD uptake after ischemic intervention (18). Moreover, the timepoint of the second ^{18}F-fluciclatide PET/CT after MI in this single study was particularly variable (76±19 days). Changes of myocardial RGD PET uptake in humans after coronary occlusion and reperfusion is still to be precisely determined. Serial changes of myocardial RGD PET uptake are studied in more detail in an ongoing prospective study (ClinicalTrial.gov NCT03809689).

Vessel damage with ischemic insult is expected to occur during the first days after MI (28, 29), which could lead to unspecific tracer diffusion in damaged leaky vessels. Here, the peak of tracer accumulation at 1–3 weeks post-MI is in favour of minimal effects of this unspecific tracer diffusion in damaged leaky vessels. Myocardial uptake post MI using RGD PET/CT may thus be predominantly due to integrin expression rather than unspecific leakage. However, no imaging was performed at day 1 in the different studies.

An interesting finding in both studies from Sun et al. (16) and Jenkins et al. (18) was the absence of increase in RGD uptake in chronically damaged myocardium, indicating minimal residual $\alpha_v\beta_3$ integrin expression in old ischemic injuries. Therefore, $\alpha_v\beta_3$ integrin expression seems rather to act as a marker of cardiac repair at sites of recent MI (16, 18).

Despite those promising results further prospective studies are nevertheless warranted to confirm a clinical value of RGD PET uptake as a prognostic marker for left ventricular remodeling. Moreover, some findings support increased $\alpha_v\beta_3$ expression also in non-viable tissue, which could be explain by a linking to the myofibroblasts (16, 30). Studies assessing the prognostic value of RGD PET uptake in the infarcted myocardium are still needed.

Atherosclerosis and $\alpha_v\beta_3$ integrin expression

The ability to accurately and non-invasively monitor inflammatory processes in atherosclerotic plaques would represent a major advance, and metabolic imaging using PET has the potential to fulfill this important unmet clinical need. Integrin $\alpha_v\beta_3$ has been widely studied in

atherosclerosis. In the development of atherosclerosis, expression of integrin $\alpha_v\beta_3$ has been found in endothelial cells as well as in CD68-positive macrophages, and both inflammation and angiogenesis processes are associated with plaque growth, plaque instability and clinical events (10-12). The necrotic core in the culprit plaque results from increasing inflammation (31). Pro-atherogenic stimuli lead to an infiltration of activated monocytes within the intima, which differentiate into pro-inflammatory macrophages (32). The apoptosis of the resident pro-inflammatory macrophages leads to the development of a lipid-rich or necrotic core (31). Matrix metalloproteinases secreted by macrophages weaken the fibrous cap, predisposing it to rupture. Angiogenesis is believed to occur in response to hypoxic conditions within the necrotic core. Neovessels, arising from the adventitial vasa vasorum, grow into the base of progressive atherosclerotic lesions and provide an alternative entry pathway for monocytes and immune cells. The plaque neovessels are fragile and leaky, giving rise to local extravasation of plasma proteins and erythrocytes (33). Plaque hemorrhage itself results in a pro-inflammatory response, plaque destabilization and clinical events (11, 34).

Attractive promising results of RGD-based PET agents in atherosclerosis

Overall, although the numbers are limited, the existing studies support the potential of RGD-based PET imaging of $\alpha_v\beta_3$ integrin expression in atherosclerosis. ^{18}F-fluciclatide PET/CT has proven itself as a potential valuable target for the imaging of unstable atherosclerosis (19). ^{68}Ga-NODAGA-RGD uptake in large vessels showed clinical correlation with atherosclerotic cardiovascular diseases (21). ^{18}F-Galacto-RGD PET/CT showed specific tracer accumulation in human atherosclerotic carotid plaques, with increased PET signals observed in stenotic compared with non-stenotic areas based on MR or CT angiography data, and with histological correlation with $\alpha_v\beta_3$ expression (17).

Intensity of RGD PET uptake in plaque imaging in humans

Background corrections were systematically used among different studies. Again, the median intensity of arterial tracer uptake as determined by TBR measurements were 1.31 (IQR 1.20–1.39) for the study from Jenkins et al. (19) and 1.84 (IQR 1.62–2.04) for the study from Dietz et al. (21). Interestingly, Dietz et al. used a SiPM PET system (Biograph Vision 600, Siemens Medical Solutions, Knoxville, USA) in 16 out of 44 (36%) of the patients included for the analysis, which could partly explain the highest TBR measurements. SiPM PET is a new PET technology with improved spatial and timing resolution and a relatively high sensitivity and count-rate capability as compared to PET scanners using conventional photomultiplier tubes (35).

The TBR measurements were slightly lower than those of other established tracers used for plaque imaging. In a study using ^{18}F-sodium fluoride for visualization of microcalcification in plaque in the major arteries, the mean TBR was 2.3 ± 0.7 (36). In another study using ^{68}Ga-Pentixafor for visualization of inflammatory cells, the mean TBR was 2.0 ± 0.5 (37).

The difference in intensity of TBR between non-calcified/mixed/calcified plaques on CT has not been studied so far. However, Dietz et al. found that only around 26% of ^{68}Ga-NODAGA-RGD highest uptake foci in their cohort were colocalized to calcification on CT (21). This result suggests that RGD accumulation could particularly occur mainly in the noncalcified vessel wall, which may indicate some association with pathophysiologic processes found in early atherosclerotic disease.

Future potential directions of $\alpha_v\beta_3$ integrin expression in plaque imaging

To date, RGD PET imaging in humans has emerged as a promising tool for the assessment of active atherosclerosis processes, but with a still very limited number of studies (n=3) (17, 19, 21). All studies were focused on subjects with established disease, and there is no work which has investigated whether RGD uptake could predict future events or whether it can provide additional prognostic information over current methods of risk stratification. Further works are also needed to establish whether RGD PET could monitor disease progression, guide therapeutic interventions, or assess novel anti-angiogenic therapies in cardiovascular diseases. It is also not well established whether having a recent MI would lead to a significant increase in aortic plaque microvessels, or indeed whether these changes are likely to occur within 1-3 weeks post MI. Because integrins $\alpha_v\beta_3$ are expressed in neovessels in plaques but also in CD68-positive macrophages, it is not possible to ascertain with PET only whether RGD is binding preferentially to one or the other of these processes. Aortic RGD uptake post MI in large vessels could be reporting predominantly on systemic inflammation rather than microvessels proliferation (38).

No study assessed the coronary arteries. The potential value of integrin tracers would be of great interest for future trials, as most PET tracers are not suitable due to too low signal for coronary artery disease assessment. Moreover, the capacity of the paradigm based on ischemia to prevent MI is increasingly being questioned, and the quantification of metabolic activity of atherosclerotic disease is of growing interest (39). PET imaging with integrin tracers could have the potential to add value to this purpose.

No PET study in humans assessed $\alpha_v\beta_3$ integrin expression in aortic aneurysm, which could be of clinical interest. Degraded aortic tissue is known to exhibit abnormal angiogenesis and is present in abundance at sites of aortic rupture (40). $\alpha_v\beta_3$ integrin expression stimulate

angiogenesis, typically in hypoxic environments (41). The predictive value of $\alpha_v\beta_3$ integrin expression imaging using PET in aortopathy to predict disease progression is unknown.

RGD PET uptake in stroke

PET studies focused on ischemic cerebral vascular disease are scarce (n=2) (16, 22). As in the normal myocardium, the PET RGD-peptide was absent in the normal brain, allowing a clear background to evaluate the post-stroke angiogenesis. However, the RGD PET uptake levels in stroke seem to be lower than those in MI (16). These could indicate difficulties of forming new capillaries from the pre-existing vessels after stroke (16). The existing data support that $\alpha_v\beta_3$ integrin expression in the cerebral infarct is prominent in the acute phase (< 30 days after the event) and decrease with time, but evidence is still lacking. Serial changes of cerebral RGD uptake were assessed for only two patients (16). However, both existing studies have consistent findings in chronically damaged brain, with absent or very weak uptake reported.

Some evidence supports a strong correlation between RGD uptake and stroke size but only in a limited number of patients scanned 13–26 days after the event (16). Like in MI, a non-perfect correlation between RGD uptake and standard measures of infarct severity like the infarct size could suggest that RGD uptake is not a surrogate of infarction but could relate more to the tissue-healing response to injury.

An interesting finding in the study from Sun et al. is a punctate multifocal RGD uptake along the surrounding blood vessels in stroke patients, contrasting with the patchy-form uptake found in MI patients (16). The authors explained that the myocardial remodeling could contribute to this different uptake pattern, but more data are needed to confirm these findings.

Radiolabeling of RGD-based PET agents

Most of the RGD-based radiotracers included in this systematic review were labelled with ^{18}F (4 out of the 7 studies: 57%). The remaining 2 out of the 7 studies (29%) used RGD-based radiotracers labelled with ^{68}Ga obtained from a $^{68}Ge/^{68}Ga$ generator. Imaging relatively thick structure like the left ventricle is not an issue using PET imaging but the use of ^{18}F labelled tracers for atherosclerotic PET imaging could have several physical and technical advantages as compared to ^{68}Ga labelled tracers. In fact, ^{68}Ga has higher positron energy and positron range which could lead to noisier images and worse spatial resolution, which could be amplified by a lower injected activity of ^{68}Ga compared with ^{18}F (at least using traditional photomultiplier tube PET/CT). However, the synthesis of ^{18}F-Galacto-RGD tracer used by Beer et al. could be complex and time consuming, making an automated production process, which is mandatory for routine clinical use, extremely difficult (17, 42-43). Moreover, ^{68}Ga labeled tracers have already been extensively used to image atherosclerotic plaques in large

vessels, and in vessels as small as the coronary arteries (44-46). The superiority of a labelling with ^{18}F or ^{68}Ga is not clear for RGD-based radiotracers for cardiovascular PET imaging.

Limitations

We should report several limitations in our systematic review, which could limit the scope of our results. Our eligibility criteria lead to a very small number of original articles eligible for inclusion in this systematic review, with limited histological assessment. This systematic review focused on PET, and studies focusing on SPECT were not included. Unlike SPECT imaging, PET imaging does not require an extrinsic collimator resulting in higher count sensitivity and spatial resolution. Moreover, accurate and well validated attenuation correction is available with PET. This provides routinely available quantitative assessments (47), which could be crucial. In fact, important potential clinical applications of molecular integrin imaging in cardiovascular diseases could provide quantitative endpoints for use in clinical trials.

There was significant heterogeneity across the studies in terms of technical aspects. Different radiotracers were used. The radiopharmaceutical injected activity and the mean time interval between radiotracer injection and image acquisition varied among the included studies.

For atherosclerosis imaging, it cannot be ruled out that tracer signals observed with RGD PET are at least partially attributable to noise, especially using ^{68}Ga labelling (48).

Finally, despite a high number of prospective studies with relatively clearly stated and patient-related purposes, according to the NIH quality assessment tool the quality of the seven selected studies is judged as moderate (see Supplementary Figure 1), mainly as they were single centre and with a limited number of patients. We have tried to minimize publication bias excluding case reports or small case series from this systematic review.

Conclusion

From this systematic review on the role of RGD-based PET agents in patients with cardiovascular diseases, we are led to conclude that data on PET imaging of integrin $\alpha_v\beta_3$ in patients with cardiovascular diseases are still very limited. PET imaging can provide insight on unique markers of disease activity, such as neoangiogenesis and inflammation, which are crucial to the pathogenesis of cardiovascular diseases. Promising applications using RGD-based PET agents are emerging, such as prediction of remodeling processes in the infarcted myocardium or detection of active atherosclerosis, with potentially significant clinical impact.

References

1. Dagenais GR, Leong DP, Rangarajan S, Lanas F, Lopez-Jaramillo P, Gupta R, et al. (2020). Variations in common diseases, hospital admissions, and deaths in middle-aged adults in 21 countries from five continents (PURE): a prospective cohort study. Lancet. 395, 785-94. doi: 10.1016/S0140-6736(19)32007-0
2. Pierschbacher MD, Ruoslahti E. (1984). Cell attachment activity of fibronectin can be duplicated by small synthetic fragments of the molecule. Nature. 309, 30–3. doi: 10.1038/309030a0
3. Aumailley M, Gurrath M, Müller G, Calvete J, Timpl R, Kessler H. (1991). Arg-gly-asp contrained within cyclic pentapeptides-strong and selective inhibitors of cell-adhesion to vitronectin and laminin fragment-P1. FEBS Lett. 291, 50–4. doi: 10.1016/0014-5793(91)81101-d
4. Brooks PC, Clark RAF, Cheresh DA. (1994). Requirement of vascular integrin αvβ3 for angiogenesis. Science. 264, 569–71. doi: 10.1126/science.7512751
5. Beer AJ, Haubner R, Göbel M, Luderschmidt S, Spilker ME, Wester HJ, et al. (2005). Biodistribution and pharmacokinetics of the αvβ3-selective tracer 18F-galacto-RGD in cancer patients. J Nucl Med. 46, 1333–41
6. Beer AJ, Haubner R, Sarbia M, Göbel M, Luderschmidt S, Grosu AL, et al. (2006). Positron emission tomography using 18F-Galacto-RGD identifies the level of integrin αvβ3 expression in man. Clin Cancer Res. 12, 3942–9. doi: 10.1158/1078-0432.CCR-06-0266
7. Chen H, Niu G, Wu H, Chen X. (2016). Clinical application of radiolabeled RGD peptides for PET imaging of integrin αvβ3. Theranostics. 6, 78–92. doi: 10.7150/thno.13242
8. Steiger K, Quigley NG, Groll T, Richter F, Zierke MA, Beer AJ, et al. (2021). There is a world beyond αvβ3-integrin: Multimeric ligands for imaging of the integrin subtypes αvβ6, αvβ8, αvβ3, and α5β1 by positron emission tomography. EJNMMI Res. 11, 106. doi: 10.1186/s13550-021-00842-2
9. Ebenhan T, Kleynhans J, Zeevaart JR, Jeong JM, Sathekge M. (2021). Non-oncological applications of RGD-based single-photon emission tomography and positron emission tomography agents. Eur J Nucl Med Mol Imaging. 48,1414-1433. doi: 10.1007/s00259-020-04975-9

10. Hoshiga M, Alpers CE, Smith LL, Giachelli CM, Schwartz SM. (1995). Alpha-v beta-3 integrin expression in normal and atherosclerotic artery. Circ Res. 77, 1129–35. doi: 10.1161/01.res.77.6.1129
11. Virmani R, Kolodgie FD, Burke AP, Finn AV, Gold HK, Tulenko TN, et al. (2005). Atherosclerotic plaque progression and vulnerability to rupture: angiogenesis as a source of intraplaque hemorrhage. Arterioscler Thromb Vasc Biol. 25, 2054–61. doi: 10.1161/01.ATV.0000178991.71605.18
12. Kolodgie FD, Gold HK, Burke AP, Fowler DR, Kruth HS, Weber DK, et al. (2003). Intraplaque hemorrhage and progression of coronary atheroma. N Engl J Med. 349, 2316-25. doi:10.1056/NEJMoa035655
13. Meoli DF, Sadeghi MM, Krassilnikova S, Bourk BN, Giardino FJ, Dione DP. (2004). Noninvasive imaging of myocardial angiogenesis following experimental myocardial infarction. J Clin Invest 113, 1684–91. doi: 10.1172/JCI20352
14. Higuchi T, Bengel FM, Seidl S, Watzlowik P, Kessler H, Hegenloh R, et al. (2008). Assessment of v 3 integrin expression after myocardial infarction by positron emission tomography. Cardiovasc Res. 78, 395–403. doi: 10.1093/cvr/cvn033
15. Page MJ, McKenzie JE, Bossuyt PM, Boutron I, Hoffmann TC, Mulrow CD, et al. (2021). The PRISMA 2020 statement: An updated guideline for reporting systematic reviews. Syst. Rev. 10, 1-11. doi : 10.1136/bmj.n71
16. Sun Y, Zeng Y, Zhu Y, Feng F, Xu W, Wu C, et al. (2014). Application of (68)Ga-PRGD2 PET/CT for αvβ3-integrin imaging of myocardial infarction and stroke. Theranostics. 25, 778-86. doi: 10.7150/thno.8809
17. Beer AJ, Pelisek J, Heider P, Saraste A, Reeps C, Metz S, et al. (2014). PET/CT imaging of integrin αvβ3 expression in human carotid atherosclerosis. JACC Cardiovasc Imaging. 7, 178-87. doi: 10.1016/j.jcmg.2013.12.003
18. Jenkins WS, Vesey AT, Stirrat C, Connell M, Lucatelli C, Neale A, et al. (2017). Cardiac αVβ3 integrin expression following acute myocardial infarction in humans. Heart. 103, 607-15. doi: 10.1136/heartjnl-2016-310115
19. Jenkins WS, Vesey AT, Vickers A, Neale A, Moles C, Connell M, et al. (2019). In vivo alpha-V beta-3 integrin expression in human aortic atherosclerosis. Heart. 105, 1868-1875. doi: 10.1136/heartjnl-2019-315103
20. Makowski MR, Rischpler C, Ebersberger U, Keithahn A, Kasel M, Hoffmann E, et al. (2021). Multiparametric PET and MRI of myocardial damage after myocardial

infarction: correlation of integrin αvβ3 expression and myocardial blood flow. Eur J Nucl Med Mol Imaging. 48, 1070-1080. doi: 10.1007/s00259-020-05034-z

21. Dietz M, Kamani CH, Deshayes E, Dunet V, Mitsakis P, Coukos G, et al. (2021). Imaging angiogenesis in atherosclerosis in large arteries with 68Ga-NODAGA-RGD PET/CT: relationship with clinical atherosclerotic cardiovascular disease. EJNMMI Res. 14, 11:71. doi: 10.1186/s13550-021-00815-5
22. Choi H, Phi JH, Paeng JC, Kim SK, Lee YS, Jeong JM, et al. (2013). Imaging of integrin α(V)β(3) expression using (68)Ga-RGD positron emission tomography in pediatric cerebral infarct. Mol Imaging. 12, 213-7.
23. Sutton MG, Sharpe N. (2000). Left ventricular remodeling after myocardial infarction. Pathophysiology and therapy. Circulation. 101, 2981–2988. doi: 10.1161/01.cir.101.25.2981
24. Weber KT. (1997). Extracellular matrix remodeling in heart failure: a role for de novo angiotensin II generation. Circulation. 96, 4065–4082. doi: 10.1161/01.CIR.96.11.4065
25. Swirski FK, Nahrendorf M. (2013). Leukocyte behavior in atherosclerosis, myocardial infarction, and heart failure. Science. 339, 161–166. doi: 10.1126/science.1230719
26. Jung K, Kim P, Leuschner F, Gorbatov R, Kim JK, Ueno T, et al. (2013). Endoscopic time-lapse imaging of immune cells in infarcted mouse hearts. Circ Res. 112, 891–899. doi: 10.1161/CIRCRESAHA.111.300484
27. Meoli DF, Sadeghi MM, Krassilnikova S, Bourke BN, Giordano FJ, Dione DP, et al. (2004). Noninvasive imaging of myocardial angiogenesis following experimental myocardial infarction. J Clin Invest 113, 1684–91. doi: 10.1172/JCI20352
28. Rochitte CE, Lima JA, Bluemke DA, Reeder SB, McVeigh ER, Furuta T, et al. (1998). Magnitude and time course of microvascular obstruction and tissue injury after acute myocardial infarction.Circulation. 98, 1006–1014. doi: 10.1161/01.cir.98.10.1006
29. Fernández-Jiménez R, Galán-Arriola C, Sánchez-González J, Agüero J, López-Martín GJ, Gomez-Talavera S, et al. (2017). Effect of Ischemia Duration and Protective Interventions on the Temporal Dynamics of Tissue Composition After Myocardial Infarction. Circ Res. 121, 439-450. doi: 10.1161/CIRCRESAHA.117.310901
30. van den Borne SW, Isobe S, Verjans JW, Petrov A, Lovhaug D, Li P, et al. (2008). Molecular imaging of interstitial alterations in remodeling myocardium after myocardial infarction. J Am Coll Cardiol. 52, 2017-28. doi: 10.1016/j.jacc.2008.07.067
31. Bentzon JF, Otsuka F, Virmani R, Falk E. (2014). Mechanisms of plaque formation and rupture. Circ Res. 114, 1852–66. doi: 10.1161/CIRCRESAHA.114. 302721

32. Clinton SK, Underwood R, Hayes L, Sherman ML, Kufe DW, Libby P, et al. (1992). Macrophage colony-stimulating factor gene expression in vascular cells and in experimental and human atherosclerosis. Am J Pathol. 140, 301–16
33. Sluimer JC, Kolodgie FD, Bijnens AP, Maxfield K, Pacheco E, Kutys B, et al. (2009). Thin-walled microvessels in human coronary atherosclerotic plaques show incomplete endothelial junctions relevance of compromised structural integrity for intraplaque microvascular leakage. J Am Coll Cardiol. 53, 1517-27. doi: 10.1016/j.jacc.2008.12.056
34. Moreno PR, Purushothaman KR, Fuster V, Echeverri D, Truszczynska H, Sharma SK, et al. (2004). Plaque neovascularization is increased in ruptured atherosclerotic lesions of human aorta: implications for plaque vulnerability. Circulation. 110:2032–8. doi: 10.1161/01.CIR.0000143233.87854.23
35. Koenders SS, van Dalen JA, Jager PL, Knollema S, Timmer JR, Mouden M, et al. (2022). Value of SiPM PET in myocardial perfusion imaging using Rubidium-82. J Nucl Cardiol. 29, 204-212. doi: 10.1007/s12350-020-02141-0
36. Derlin T, Tóth Z, Papp L, Wisotzki C, Apostolova I, Habermann CR, et al. (2011). Correlation of inflammation assessed by 18F-FDG PET, active mineral deposition assessed by 18F-fluoride PET, and vascular calcification in atherosclerotic plaque: a dual-tracer PET/CT study. J Nucl Med. 52, 1020–7. doi: 10.2967/jnumed.111.087452
37. Weiberg D, Thackeray JT, Daum G, Sohns JM, Kropf S, Wester HJ, et al. (2018). Clinical molecular imaging of chemokine receptor CXCR4 expression in atherosclerotic plaque using 68Ga-pentixafor PET: correlation with cardiovascular risk factors and calcified plaque burden. J Nucl Med. 59, 266–72. doi: 10.2967/jnumed.117.196485
38. Tarkin JM, Mason JC, Fayad ZA. (2019). Imaging at the inter-face of inflammation and angiogenesis by 18F-fluciclatide PET. Heart. 105, 1845-1847. doi: 10.1136/heartjnl-2019-315487
39. Dweck MR, Doris MK, Motwani M, Adamson PD, Slomka P, Dey D, et al. (2016). Imaging of coronary atherosclerosis - evolution towards new treatment strategies. Nat Rev Cardiol. 13, 533-48. doi:10.1038/nrcardio.2016.79
40. Choke E. (2006). Abdominal aortic aneurysm rupture is associated with increased medial neovascularization and overexpression of proangiogenic cytokines. Arterioscler Thromb Vasc Biol. 26, 2077–2082. doi: 10.1161/01.ATV.0000234944.22509.f9

41. Sadeghi MM, Krassilnikova S, Zhang J, Gharaei AA, Fassaei HR, Esmailzadeh L. (2004). Detection of injury-induced vascular remodeling by targeting activated alphavbeta3 integrin in vivo. Circulation. 110, 84–90. doi: 10.1161/01.CIR.0000133319.84326.70
42. Haubner R, Kuhnast B, Mang C, Weber WA, Kessler H, Wester HJ, et al. (2004). [18F]Galacto-RGD: synthesis, radiolabeling, metabolic stability, and radiation dose estimates. Bioconjug Chem. 15, 61–9. doi: 10.1021/bc034170n
43. Knetsch PA, Petrik M, Griessinger CM, Rangger C, Fani M, Kesenheimer C, et al. (2011). [68Ga]NODAGA-RGD for imaging αvβ3 integrin expression. Eur J Nucl Med Mol Imaging. 38, 1303-12. doi: 10.1007/s00259-011-1778-0
44. Tarkin JM, Joshi FR, Evans NR, Chowdhury MM, Figg NL, Shah AV, et al. (2017). Detection of atherosclerotic inflammation by (68)Ga-DOTATATE PET compared to [(18)F]FDG PET imaging. J Am Coll Cardiol. 69, 1774–91. doi: 10.1016/j.jacc.2017.01.060. 26
45. Li X, Samnick S, Lapa C, Israel I, Buck AK, Kreissl MC, et al. (2012). 68Ga-DOTATATE PET/CT for the detection of inflammation of large arteries: correlation with18F-FDG, calcium burden and risk factors. EJNMMI Res. 2, 52. doi: 10.1186/2191-219X-2-52
46. Weiberg D, Thackeray JT, Daum G, Sohns JM, Kropf S, Wester HJ, et al. (2018). Clinical Molecular Imaging of Chemokine Receptor CXCR4 Expression in Atherosclerotic Plaque Using 68Ga-Pentixafor PET: Correlation with Cardiovascular Risk Factors and Calcified Plaque Burden. J Nucl Med. 59, 266-72. doi: 10.2967/jnumed.117.196485
47. Zhang X, Xiong Z, Wu Y, Cai W, Tseng JR, Gambhir SS et al. (2006). Quantitative PET imaging of tumor integrin alphavbeta3 expression with 18F-FRGD2. J Nucl Med 47, 113–21
48. Derlin T, Thiele J, Weiberg D, Thackeray JT, Püschel K, Wester HJ, et al. (2016). Evaluation of 68Ga-glutamate carboxypeptidase II ligand positron emission tomography for clinical molecular imaging of atherosclerotic plaque neovascularization. Arterioscler Thromb Vasc Biol. 36, 2213–2219. doi: 10.1161/ATVBAHA.116.307701

PART II

Integrin $\alpha_v\beta_3$ expression after myocardial infarction

Chapter 3

Natural History of Myocardial $\alpha_v\beta_3$ Integrin Expression after Acute Myocardial Infarction: Correlation with Changes in Myocardial Blood Flow

J Nucl Med. (accepted with major revision)

Matthieu Dietz, Christel H. Kamani, Colin Bousige, Vincent Dunet, Judith Delage, Vladimir Rubimbura, Marie Nicod Lalonde, Niklaus Schaefer, Wail Nammas, Antti Saraste, Juhani Knuuti, Nathan Mewton, and John O. Prior

Abstract

Angiogenesis is an essential part of the cardiac repair process after myocardial infarction, but its spatio-temporal dynamics remain to be fully deciphered. ^{68}Ga-NODAGA-Arg-Gly-Asp (RGD) is a positron emission tomography (PET) tracer targeting $\alpha_v\beta_3$ integrin expression, which is a marker of angiogenesis.

Methods: In this prospective single-center trial, we aimed to monitor angiogenesis through myocardial integrin $\alpha_v\beta_3$ expression in 20 patients with ST elevated myocardial infarction (STEMI). In addition, the correlations between the expression levels of myocardial $\alpha_v\beta_3$ integrin and the subsequent changes in ^{82}Rb PET/computed tomography (CT) parameters, including rest and stress myocardial blood flow (MBF), myocardial flow reserve (MFR), and wall motion abnormalities were assessed. The patients underwent PET/CT imaging using ^{68}Ga-NODAGA-RGD PET/CT and rest and stress ^{82}Rb-PET/CT at 1 week, 1 month and 3 months after STEMI. To assess ^{68}Ga-NODAGA-RGD uptake, the summed rest ^{82}Rb and ^{68}Ga-NODAGA-RGD images were co-registered, and segmental standardized uptake values were calculated (RGD SUV).

Results: At 1 week after STEMI, 19 participants (95%) presented increased ^{68}Ga-NODAGA-RGD uptake in the infarcted myocardium. Seventeen participants completed the full imaging series. The values of the RGD SUV in the infarcted myocardium were stable 1 month after STEMI (1 week vs. 1 month, 1.47 [interquartile range, IQR: 1.37-1.64] vs. 1.47 [IQR: 1.30-1.66] g/mL, P=0.9), followed by a significant partial decrease at 3 months (1.32 [IQR: 1.12-1.71] g/mL, P=0.011 vs. 1 week, P=0.018 vs. 1 month). In segment-based analysis, positive correlations were found between RGD SUV at 1 week and the subsequent changes in stress MBF (Spearman rho: r=0.17, P=0.0033) and MFR (Spearman rho: r=0.31, P<0.0001) at 1 month. A negative correlation was found between RGD SUV at 1 week and the subsequent changes in wall motion abnormalities at 3 months (Spearman rho: r=–0.12, P=0.035).

Conclusion: The present study found that $\alpha_v\beta_3$ integrin expression is significantly increased in the infarcted myocardium 1 week after STEMI. This expression remains stable after 1 month and partially decreases after 3 months. Initial $\alpha_v\beta_3$ integrin expression at 1 week is significantly weakly correlated with subsequent improvements in stress MBF, MFR, and wall motion analysis.

Registration: URL: https://www.clinicaltrials.gov; Unique identifier: NCT03809689

Key Words: Integrin alphavbeta3; PET; myocardial infarction; angiogenesis; RGD.

INTRODUCTION

The initiation of cardiac repair after a myocardial infarction (MI) requires a complex series of processes. In the first few days following reperfusion, an inflammatory phase with intense inflammation and immune cell infiltration enables to clear the infarct from damaged cells. This phase is followed by a reparative and proliferative phase over the next several days, with a believed peak around day 7; it includes the resolution of inflammation, cardiac fibroblast proliferation, scar formation, and angiogenesis, which is an essential part of the repair process (*1*,*2*). However, the spatio-temporal dynamics of angiogenesis after a MI remain to be fully deciphered (*2*). To prevent heart failure after MI, an improved understanding of myocardial angiogenesis is essential for the future development of effective and targeted treatments.

The transmembrane glycoprotein $\alpha_v\beta_3$ integrin is involved in cell interaction with the extracellular matrix, migration, and proliferation. Integrin $\alpha_v\beta_3$ is expressed on activated endothelial cells where it plays a critical role in the angiogenic process within the myocardium after injury (*3*-*6*). Expression of integrin $\alpha_v\beta_3$ has also been reported in other various cell types, such as fibroblasts and activated macrophages (*7*-*10*). This diversity in expression may introduce some confounding effects. However, $\alpha_v\beta_3$ imaging holds promise for assessment of cardiac wound healing and repair after MI (*11*,*12*). In 2015, in a publication summarizing advanced techniques to evaluate angiogenesis, the American Heart Association cited the use of radiotracers to assess integrin expression (*13*). ^{68}Ga-NODAGA-Arg-Gly-Asp (RGD) is a positron emission tomography (PET) tracer having a high binding affinity for $\alpha_v\beta_3$ and favorable biokinetics (*14, 15*). A widely used PET perfusion tracer in clinical practice is ^{82}Rb, allowing for accurate measurement of rest and stress myocardial perfusion in absolute units, with a test-retest methodological precision around 20% (*16*).

We hypothesized that myocardial ^{68}Ga-NODAGA-RGD uptake is increased during the peak of the proliferative phase following acute ST-segment elevation myocardial infarction

(STEMI) and is reduced during later stages of infarct healing. The objective of the present study was to assess the expression levels of myocardial $\alpha_v\beta_3$ integrin at 1 week after STEMI and their potential evolution at 1 month and 3 months. In addition, the correlations between the expression levels of myocardial $\alpha_v\beta_3$ integrin and the subsequent changes in ^{82}Rb-PET/CT parameters, including rest and stress myocardial blood flow (MBF), myocardial flow reserve (MFR), and wall motion abnormalities were assessed.

MATERIALS AND METHODS

Study Design

This is a prospective single-center trial conducted in the Centre Hospitalier Universitaire Vaudois (Lausanne, Switzerland). All participants were included within the first 12 hours after symptom onset and underwent reperfusion (Supplemental materials). The study was approved by the ethics committee of the canton of Vaud (protocol CER-VD # 429/14) and registered on Clinical-Trials.gov (NCT03809689). All patients signed a written informed consent.

PET/CT Imaging

All participants had a ^{68}Ga-NODAGA-RGD PET/computed tomography (CT), and a rest and stress ^{82}Rb-PET/CT imaging at 1 week (4-10 days) after STEMI. Then, the participants underwent repeated ^{68}Ga-NODAGA-RGD PET/CT, and rest and stress ^{82}Rb-PET/CT imaging at 1 month and 3 months after STEMI (Figure 1). Participants underwent ^{82}Rb-PET/CT imaging as previously described (*17*). The complete imaging acquisition protocol is reported in the Supplemental materials. Briefly, 5 MBq/kg of ^{82}Rb (Ruby-Fill® generator and ^{82}Rb elution system, Jubilant DraxImage, Kirkland, Canada) was administered through an automated infusion system for 15-25 seconds, and 3-dimensional dynamic PET images were acquired for

6.1 minutes (12x8, 5x12, 1x30, 1x60, and 1x120 seconds). Stress acquisitions were then performed using the same protocol. Then, a median of 159 MBq of ^{68}Ga-NODAGA-RGD was injected as an intravenous bolus and was followed by a PET acquisition of 10 minutes after a median time of 60 minutes. Images were reconstructed using ordered subsets expectation maximization algorithms.

PET Image Analysis

Image analyses were performed using PMOD (PMOD Version 4.3, PMOD Technologies, Zürich, Switzerland).

^{82}Rb-PET/CT analysis

Perfusion was assessed quantitatively, measuring MBF in milliliters per minute per gram at rest and stress using a 1-tissue compartment model with a flow-dependent extraction correction (Supplemental materials). Perfusion was also assessed visually and semi-quantitatively. A segmental wall motion analysis was performed on rest-gated ^{82}Rb-PET images using a 5-point scoring scale and the summed rest score for wall motion was derived. Rest left ventricular (LV) end-diastolic and end-systolic volumes, as well as ejection fraction (EF), were computed.

^{68}Ga-NODAGA-RGD PET/CT analysis

^{68}Ga-NODAGA-RGD images were assessed visually and quantitatively. To assess the RGD uptake, the summed rest ^{82}Rb images and the ^{68}Ga-NODAGA-RGD images were co-registered (Supplemental Figure 1). Polar maps of ^{68}Ga-NODAGA-RGD uptake expressed as standardized uptake values (SUV; measured activity concentration [Bq/ml] x body weight [g]/injected dose at the time of image decay correction [Bq]) were generated, and mean

segmental SUVs were calculated (RGD SUV). The characterization of the infarcted myocardium and the remote myocardium is detailed in the Supplemental materials.

Statistical Analysis

No statistical methods were used to predetermine sample size. All statistical analyses were performed using the R software (version 4.2.2, R Project, Vienna, Austria). A *P* value <0.05 was considered statistically significant. Continuous variables were expressed as median [IQR] or as mean±standard error of the mean. The comparisons were performed using a Wilcoxon signed-ranks test. Categorical data were expressed as count and percentage. The Friedman test was used to compare continuous variables across multiple time points. When statistical significance was reached, *post-hoc* Dunn's multiple comparison tests were used for pairwise comparisons. The correlations between RGD SUV and the subsequent changes in rest MBF, stress MBF, MFR and wall motion analysis were assessed on all segments using the Spearman correlation analysis. The tests were selected due to the non-normal distribution of the data, as determined by the Shapiro-Wilk test.

RESULTS

Participants

A total of 20 participants were included in the study (20% female; age: 63 [IQR: 58-69] years; Supplemental Table 1). Among the participants, 19 (95%) had no previous history of cardiovascular disease before the onset of acute STEMI. Only one participant had a history of prior coronary revascularization, with percutaneous coronary intervention (PCI) and coronary artery bypass graft surgery.

PCI was performed on all the participants 3.8 [IQR: 2.3-6.3] hours after symptoms onset. Invasive angiography found single-vessel obstructive disease in 7 (35%) participants and multivessel obstructive coronary artery disease in 13 (65%). All participants underwent stenting using drug-eluting stents of the culprit lesion. One participant (5%) had unsuccessful reperfusion with a post-PCI thrombolysis in myocardial infarction flow grade 1.

The 20 participants underwent rest and stress ^{82}Rb-PET/CT and ^{68}Ga-NODAGA-RGD PET/CT imaging 9 [IQR: 7-10] days after STEMI. A total of 18 participants underwent a second ^{82}Rb-PET/CT and ^{68}Ga-NODAGA-RGD PET/CT imaging 32 [IQR: 30-37] days after STEMI, and 17 participants underwent a third ^{82}Rb-PET/CT and ^{68}Ga-NODAGA-RGD PET/CT imaging 89 [IQR: 83-96] days after STEMI and completed the full imaging series. In segment-based analysis, rest and stress MBF, MFR, wall motion analysis and RGD SUV were assessed for the full imaging series in 289 segments (17x17 participants).

Imaging findings 1 week after STEMI

Complete reperfusion, as indicated by an absence of significant perfusion defect (summed stress score <4), was observed in 6 participants (33%). The rest MBF was 0.50 [IQR: 0.42-0.58] mL/min/g across the entire myocardium, 0.58 [IQR: 0.48-0.60] mL/min/g in the remote myocardium, and 0.38 [IQR: 0.34-0.52] mL/min/g in the infarcted myocardium. Rest LVEF was less than 50% in 12 participants (60%). A total of 14 participants (70%) demonstrated segmental wall motion abnormalities (summed rest score for wall motion >0).

A total of 19 participants (95%) presented RGD-positive segments (n=66); those segments were always included in myocardial tissue perfused by the culprit coronary artery. Among those 66 positive segments, 55 were obtained from the 17 participants who completed the full imaging series and were selected to represent the infarcted myocardium. Among the 6

participants who experienced a complete reperfusion and had no significant ^{82}Rb PET perfusion defect (summed stress score <4), RGD-positive segments were detected in 5 (83%).

Temporal changes

The values of the RGD SUV in the infarcted myocardium were stable 1 month after STEMI (*P*=0.9 for *post-hoc* comparison 1 week vs. 1 month; Table 1), followed by a significant decrease at 3 months (*P*=0.011 for *post-hoc* comparison with 1 week, *P*=0.018 for *post-hoc* comparison with 1 month; Table 1 and Figures 2 and 3). There was no significant change observed for the RGD SUV in the remote myocardium throughout the follow-up (Friedman test *P*=0.59). At all timepoints the RGD SUV values of the infarcted myocardium and the remote myocardium were significantly different (all *P*<0.001).

In participants with significant ^{82}Rb-PET/CT perfusion defects, areas of positive RGD uptake matched the extent of perfusion defects, with some slight extensions in border zones. In the 2 participants with the most severe infarcts (rest MBF in the infarcted myocardium at 1 week of 0.30 mL/min/g and 0.26 mL/min/g), the RGD SUV values of the infarcted myocardium increased by at least 20% at 1 month, without change in clinical status, nor occurrence of events (Figure 4 and Supplemental Figure 2). In these 2 participants the RGD uptake started in the border zone and extended into the necrotic infarct core (Figure 4). The RGD uptake was relatively homogeneous in all the other participants with smaller infarcts.

In participant-based analysis, global ^{82}Rb-PET/CT parameters and hemodynamics during ^{82}Rb-PET/CT imaging did not significantly change between initial and follow-up imaging (Supplemental Tables 2 and 3). LVEF improved by at least 5% in 8 (12%) of the 17 participants who completed the full imaging series. In segment-based analysis, rest MBF improved by at least 20% in 163 segments (56%), stress MBF improved by at least 20% in 164

segments (57%), MFR improved by at least 20% in 151 segments (52%) and wall motion abnormalities improved (difference score for wall motion ≥1) in 61 segments (21%).

Correlations between RGD SUV and the subsequent changes in ^{82}Rb-PET parameters

In segment-based analysis, positive correlations were found between initial RGD SUV at 1 week and the subsequent changes at 3 months in stress MBF (Spearman rho: r=0.13, P=0.026) and MFR (Spearman rho: r=0.18, P=0.003). There was no correlation found between RGD SUV at 1 week and the subsequent changes in rest MBF at 3 months (Spearman rho: r=–0.08, P=0.19). A negative correlation was found between RGD SUV at 1 week and the subsequent changes in wall motion abnormalities at 3 months (Spearman rho: r=–0.12, P=0.035).

In further analysis, positive significant correlations were found between RGD SUV and the subsequent changes in stress MBF and MFR in the 1-week to 1-month period (Spearman rho: r=0.17, P=0.0033, and Spearman rho: r=0.31, P<0.0001, respectively, Figure 5). No correlation was found between RGD SUV at 1 month and the subsequent changes at 3 months in stress MBF (Spearman rho: r=0.05, P=0.44), nor in MFR (Spearman rho: r=–0.02, P=0.72). No correlation was found during these shorter periods between RGD SUV and the subsequent changes in wall motion abnormalities (1-week to 1-month period, Spearman rho: r=0.02, P=0.7; 1-month to 3-month period, Spearman rho: r=0.06, P=0.33).

DISCUSSION

The present study reported *in vivo*, in humans, an increased $\alpha_v\beta_3$ integrin expression in the infarcted myocardium 1 week after STEMI. The levels of $\alpha_v\beta_3$ integrin expression remained stable at 1 month after STEMI and partially decreased at 3 months, suggesting that angiogenesis remains active 3 months after the infarct. Moreover, there were significant weak correlations

between the segmental levels of $\alpha_v\beta_3$ integrin expression at 1 week and the subsequent improvements in stress MBF, MFR, and wall motion analysis.

The kinetics of angiogenesis after MI in humans remain poorly understood (*2*). The results reported herein on myocardial $\alpha_v\beta_3$ integrin expression *in vivo* in the human infarcted myocardium found a persistent activity at 1 month, followed by a partial decline at 3 months. The present results are consistent with the serial changes of vascular endothelial growth factor (VEGF) levels observed in several studies within the peripheral blood of patients with acute MI. These levels were reported to reach a peak at 6 weeks and subsequently decline to baseline levels at 5 months (*18*). Another study found a progressive increase of VEGF levels that started on the first day after acute MI, peaked at 2 weeks and then subsequently declined (*19*). Hence, it can be thought that this prolonged increase is necessary to preserve the remaining myocardium and limit hypoxic cellular destruction.

The prolonged $\alpha_v\beta_3$ integrin upregulation found herein agrees with previous studies using radiolabeled RGD peptides after MI (*4*,*11*,*20*,*21*). In a rat model, the uptake of the ^{18}F-Galacto-RGD tracer was detected only 3 days after MI and reached its highest levels between 1 and 3 weeks; the levels were still detectable after 6 months. Moreover, the evolution of ^{18}F-Galacto-RGD tracer uptake was well correlated with neovascularization as assessed by immunohistochemical CD31 staining (*4*). Similarly, the uptake pattern of ^{18}F-AlF-NOTA-PRGD2, in the infarcted area at various time points following MI, also started after only 3 days and reached its peak between 1 and 3 weeks; a subsequent partial decrease was reported 4 months after MI (*20*). In humans, Jenkins et al. (*11*) found that ^{18}F-labeled RGD uptake was increased within 2 weeks in the infarcted myocardium. It persisted but was reduced after approximately 10 weeks. There was no uptake found at sites of established old infarctions. It is of note that in the present study, an examination of established old infarction sites was not conducted since none of the participants had a MI history prior to acute STEMI. Nevertheless,

in our ongoing trial evaluating tumoral angiogenesis (NCT02666547), which includes some patients with a prior history of MI, we do not observe any visually positive uptake of ^{68}Ga-NODAGA-RGD in the myocardium.

The present study reported significant correlations between the segmental levels of $\alpha_v\beta_3$ integrin at 1 week and the subsequent improvements in clinically relevant physiological parameters, such as stress MBF, MFR, and wall motion analysis. Although the correlations found were weak, they were determined using Spearman's rank correlation coefficient, which is insensitive to outliers. Additionally, the alignment of PET findings could have been more accurate, since distinct radiotracers (with high energy positrons) and acquisitions were used. A stronger effect of these correlations can be assumed, which means that the correlations are likely relevant. Notably, a slightly stronger correlation was observed between $\alpha_v\beta_3$ integrin expression levels and improvements in MFR, which is considered a more robust independent prognostic factor compared with stress MBF (*22*). Furthermore, no correlation was found between $\alpha_v\beta_3$ integrin expression levels and subsequent changes in rest MBF, a parameter unrelated to clinical outcomes and unaffected by post-MI recovery (*23*,*24*). The significant but weak correlation between $\alpha_v\beta_3$ integrin expression levels at 1 week and functional outcomes aligns with previous challenges to translate microscopic levels of angiogenesis into functional improvements. For example, Wu *et al.* reported only trends towards lower perfusion defects and metabolism deficits in VEGF-treated animal models, without statistically significant changes (*25*). Nevertheless, as herein, several studies suggested that elevated $\alpha_v\beta_3$ integrin expression after ischemic myocardial injury is associated with subsequent improvement in regional LV function (*6*,*11*,*12*,*26*,*27*). Recently, using the same PET tracer with ^{68}Ga-NODAGA-RGD, Nammas *et al.* reported in humans that $\alpha_v\beta_3$ integrin expression levels 1 week after MI was linked to regional and global systolic dysfunction, as well as elevated LV filling pressure, and predicted improved global LV function 6 months after MI (*12*). Despite these insights, further studies are

warranted to better understand whether the angiogenic response is associated with functional recovery.

Variability was observed in the temporal pattern of ^{68}Ga-NODAGA-RGD uptake, with a notable increase found at 1 month in 2 participants. Interestingly, the 2 participants affected were those experiencing the most severe infarcts. Based on these findings, it remains uncertain whether this increase in ^{68}Ga-NODAGA-RGD uptake is related to intensified reendothelialization and angiogenesis and/or indicates a shift towards myofibroblast cell types, suggesting an intensified fibrotic response. This delayed phase of repair is characterized by a reduction in inflammation and angiogenesis, and a reorganization of the extracellular matrix through myofibroblast-driven type I and III collagen production (*1*). This more intense uptake during follow-up in infarcted areas where perfusion is most profoundly reduced, with a trend toward a delayed 1-month peak, may reflect the need for a more intense healing process in those tissues.

The present trial has several limitations. Inflammatory cells and fibroblasts can express integrins such as $\alpha_v\beta_3$ (*7-10*), which can lead to reduced specificity. This may explain the weak correlations found between the 1-week ^{68}Ga-NODAGA-RGD uptake and the subsequent improvements in flow, as well as the absence of correlation found from the 1-month onwards. The positron range is higher for ^{68}Ga than for ^{18}F, which may affect the image quality, especially in relatively small moving structures. Nevertheless, ^{68}Ga-NODAGA-RGD has the advantage to be synthesized straightforward at room temperature with high radiochemical yield and purity. It can be radiolabeled rapidly (<30 minutes) and in a fully automated good-manufacturing-practice compliant manner. Furthermore, the on-site availability of ^{68}Ge/^{68}Ga generators for centers without access to a cyclotron makes it a good alternative for ^{18}F-labeled compounds. Moreover, a higher uptake of multimeric RGD tracers as compared to monomeric tracers was reported (*28*). A multimodal imaging strategy, such as PET/MRI, could precisely delineate the

area at-risk and its border zone. The study would have been strengthened by an independent measure of regional function using echocardiography or MRI. Furthermore, the contribution of non-specific uptake to ^{68}Ga-NODAGA-RGD accumulation cannot be excluded. However, positive uptake was found in segments with preserved perfusion and in segments with very low perfusion, and as radiolabeled RGD-based peptides have shown a rapid clearance from the circulation (*4*,*14*), it seems unlikely that non-specific uptake related to changes in vascular permeability played a major role. Finally, the potential impact of standard medication regimens for coronary artery disease (e.g., statins, antihypertensives) on the uptake of ^{82}Rb or ^{68}Ga-NODAGA-RGD remains uncertain.

CONCLUSION

The present study found that $\alpha_v\beta_3$ integrin expression is significantly increased in the infarcted myocardium 1 week after STEMI. This expression remains stable after 1 month and partially decreases after 3 months. Initial $\alpha_v\beta_3$ integrin expression at 1 week is significantly weakly correlated with subsequent improvements in stress MBF, MFR, and wall motion analysis. An enhanced comprehension of the mechanistic aspects of infarct $\alpha_v\beta_3$ integrin expression could provide multiple therapeutic options.

REFERENCES

1. Prabhu SD, Frangogiannis NG. The Biological Basis for Cardiac Repair After Myocardial Infarction: From Inflammation to Fibrosis. *Circ Res*. 2016;119:91–112.

2. Wu X, Reboll MR, Korf-Klingebiel M, Wollert KC. Angiogenesis after acute myocardial infarction. *Cardiovasc Res*. 2021;117:1257–1273.

3. Meoli DF, Sadeghi MM, Krassilnikova S, et al. Noninvasive imaging of myocardial angiogenesis following experimental myocardial infarction. *J Clin Invest*. 2004;113:1684–1691.

4. Higuchi T, Bengel FM, Seidl S, et al. Assessment of alphavbeta3 integrin expression after myocardial infarction by positron emission tomography. *Cardiovasc Res*. 2008;78:395–403.

5. Brooks PC, Clark RA, Cheresh DA. Requirement of vascular integrin alpha v beta 3 for angiogenesis. *Science*. 1994;264:569–571.

6. Sherif HM, Saraste A, Nekolla SG, et al. Molecular imaging of early αvβ3 integrin expression predicts long-term left-ventricle remodeling after myocardial infarction in rats. *J Nucl Med*. 2012;53:318–323.

7. Antonov AS, Kolodgie FD, Munn DH, Gerrity RG. Regulation of Macrophage Foam Cell Formation by αVβ3 Integrin. *Am J Pathol*. 2004;165:247–258.

8. van den Borne SWM, Isobe S, Verjans JW, et al. Molecular imaging of interstitial alterations in remodeling myocardium after myocardial infarction. *J Am Coll Cardiol*. 2008;52:2017–2028.

9. Asano Y, Ihn H, Yamane K, Jinnin M, Mimura Y, Tamaki K. Increased expression of integrin alpha(v)beta3 contributes to the establishment of autocrine TGF-beta signaling in scleroderma fibroblasts. *J Immunol*. 2005;175:7708–7718.

10. de Haas HJ, Arbustini E, Fuster V, Kramer CM, Narula J. Molecular imaging of the cardiac extracellular matrix. *Circ Res*. 2014;114:903–915.

11. Jenkins WSA, Vesey AT, Stirrat C, et al. Cardiac $\alpha_V\beta_3$ integrin expression following acute myocardial infarction in humans. *Heart*. 2017;103:607–615.

12. Nammas W, Paunonen C, Teuho J, et al. Imaging of Myocardial αvβ3 Integrin Expression for Evaluation of Myocardial Injury After Acute Myocardial Infarction. *J Nucl Med*. 2024;65:132-138.

13. Simons M, Alitalo K, Annex BH, et al. American Heart Association Council on Basic Cardiovascular Sciences and Council on Cardiovascular Surgery and Anesthesia. State-of-the-Art Methods for Evaluation of Angiogenesis and Tissue Vascularization: A Scientific Statement From the American Heart Association. *Circ Res*. 2015;116:e99-132.

14. Knetsch PA, Petrik M, Griessinger CM, et al. [68Ga]NODAGA-RGD for imaging αvβ3 integrin expression. *Eur J Nucl Med Mol Imaging*. 2011;38:1303–1312.

15. Pohle K, Notni J, Bussemer J, Kessler H, Schwaiger M, Beer AJ. 68Ga-NODAGA-RGD is a suitable substitute for (18)F-Galacto-RGD and can be produced with high specific activity in a cGMP/GRP compliant automated process. Nucl Med Biol. 2012;39:777-84.

16. Kitkungvan D, Johnson NP, Roby AE, Patel MB, Kirkeeide R, Gould KL. Routine Clinical Quantitative Rest Stress Myocardial Perfusion for Managing Coronary Artery Disease: Clinical Relevance of Test-Retest Variability. JACC Cardiovasc Imaging. 2017;10:565-577.

17. Dietz M, Kamani CH, Allenbach G, et al. Comparison of the prognostic value of impaired stress myocardial blood flow, myocardial flow reserve, and myocardial flow capacity on low-dose Rubidium-82 SiPM PET/CT. *J Nucl Cardiol*. 2023;30:1385–1395.

18. Lee KW, Lip GYH, Blann AD. Plasma Angiopoietin-1, Angiopoietin-2, Angiopoietin Receptor Tie-2, and Vascular Endothelial Growth Factor Levels in Acute Coronary Syndromes. *Circulation*. 2004;110:2355–2360.

19. Hojo Y, Ikeda U, Zhu Y, et al. Expression of vascular endothelial growth factor in patients with acute myocardial infarction. *J Am Coll Cardiol*. 2000;35:968–973.

20. Gao H, Lang L, Guo N, et al. PET imaging of angiogenesis after myocardial infarction/reperfusion using a one-step labeled integrin-targeted tracer 18F-AlF-NOTA-PRGD2. *Eur J Nucl Med Mol Imaging*. 2012;39:683–692.

21. Makowski MR, Rischpler C, Ebersberger U, et al. Multiparametric PET and MRI of myocardial damage after myocardial infarction: correlation of integrin αvβ3 expression and myocardial blood flow. *Eur J Nucl Med Mol Imaging*. 2021;48:1070–1080.

22. Juárez-Orozco LE, Tio RA, Alexanderson E, et al. Quantitative myocardial perfusion evaluation with positron emission tomography and the risk of cardiovascular events in patients with coronary artery disease: a systematic review of prognostic studies. *Eur Heart J Cardiovasc Imaging*. 2018;19:1179–1187.

23. Johnson NP, Gould KL, De Bruyne B. Autoregulation of Coronary Blood Supply in Response to Demand: JACC Review Topic of the Week. *J Am Coll Cardiol*. 2021;77:2335–2345.

24. Cuculi F, De Maria GL, Meier P, et al. Impact of Microvascular Obstruction on the Assessment of Coronary Flow Reserve, Index of Microcirculatory Resistance, and Fractional Flow Reserve After ST-Segment Elevation Myocardial Infarction. *J Am Coll Cardiol*. 2014;64:1894–1904.

25. Wu JC, Chen IY, Wang Y, et al. Molecular imaging of the kinetics of vascular endothelial growth factor gene expression in ischemic myocardium. *Circulation*. 2004;110:685–691.

26. Bentsen S, Jensen JK, Christensen E, et al. [68Ga]Ga-NODAGA-E[(cRGDyK)]2 angiogenesis PET following myocardial infarction in an experimental rat model predicts cardiac functional parameters and development of heart failure. *J Nucl Cardiol.* 2023;30:2073-2084.

27. Follin B, Hoeeg C, Hunter I, et al. [68Ga]Ga-NODAGA-E[(cRGDyK)]2 and [64Cu]Cu-DOTATATE PET Predict Improvement in Ischemic Cardiomyopathy. *Diagnostics (Basel)*. 2023;13:268.

28. Notni J, Pohle K, Wester HJ. Be spoilt for choice with radiolabelled RGD peptides: preclinical evaluation of (6)(8)Ga-TRAP(RGD)(3). *Nucl Med Biol.* 2013;40:33-41.

TABLE 1. Temporal changes in the infarcted and the remote myocardium.

	1 week	1 month	3 months
Infarcted myocardium			
RGD SUV (g/mL)	1.47 [1.37-1.64]	1.47 [1.30-1.66]	**1.32 [1.12-1.71]***
Rest myocardial blood flow (mL/min/g)	0.38 [0.34-0.52]	0.44 [0.31-0.58]	0.44 [0.37-0.52]
Stress myocardial blood flow (mL/min/g)	1.16 [0.71-1.61]	1.49 [0.77-1.96]	**1.51 [0.92-2.18]†**
Myocardial flow reserve (1)	3.04 [1.96-3.90]	2.94 [2.42-3.62]	3.50 [2.32-4.65]
Remote myocardium			
RGD SUV (g/mL)	1.05 [0.92-1.11]	1.01 [0.99-1.11]	1.05 [0.94-1.15]
Rest myocardial blood flow (mL/min/g)	0.58 [0.48-0.60]	0.57 [0.46-0.75]	0.50 [0.49-0.69]
Stress myocardial blood flow (mL/min/g)	1.88 [1.30-2.19]	1.99 [1.24-2.16]	1.92 [1.22-2.39]
Myocardial flow reserve (1)	3.35 [2.67-4.16]	3.19 [2.28-3.51]	2.98 [2.27-4.75]

Variables are expressed as median [IQR]. **P*=0.011 vs. 1 week and *P*=0.018 vs. 1 month.
†*P*=0.035 vs. 1 week.

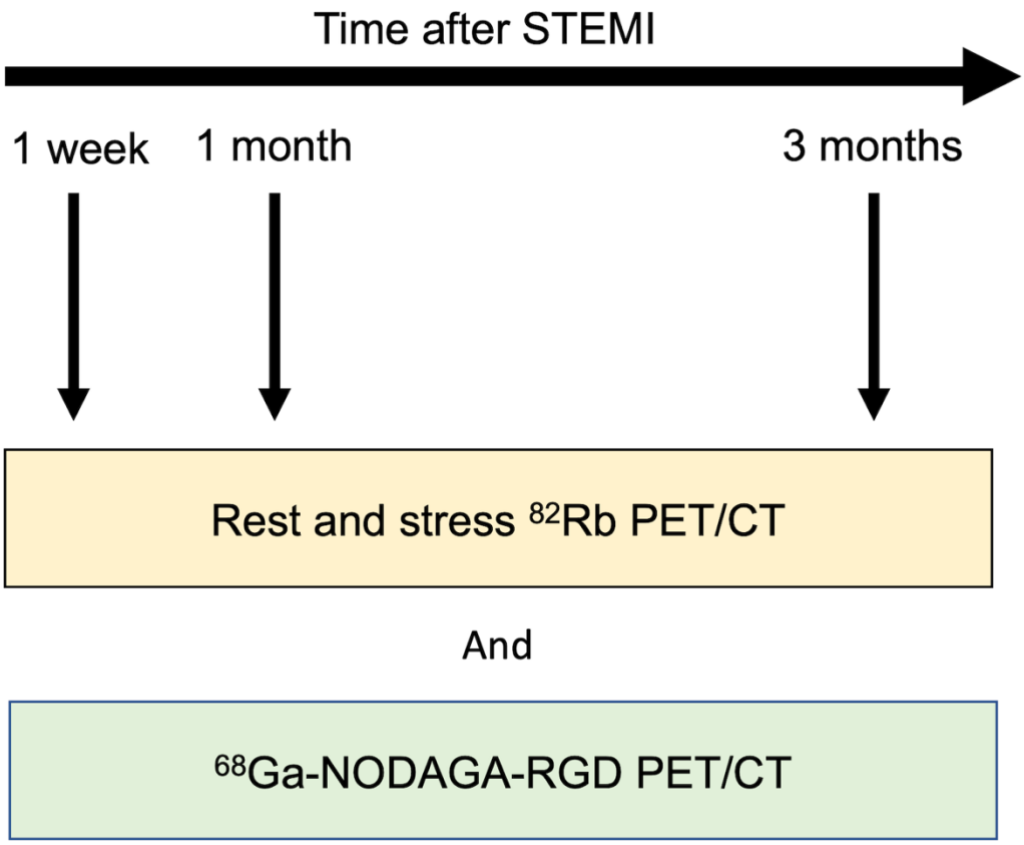

FIGURE 1. Experimental timeline.

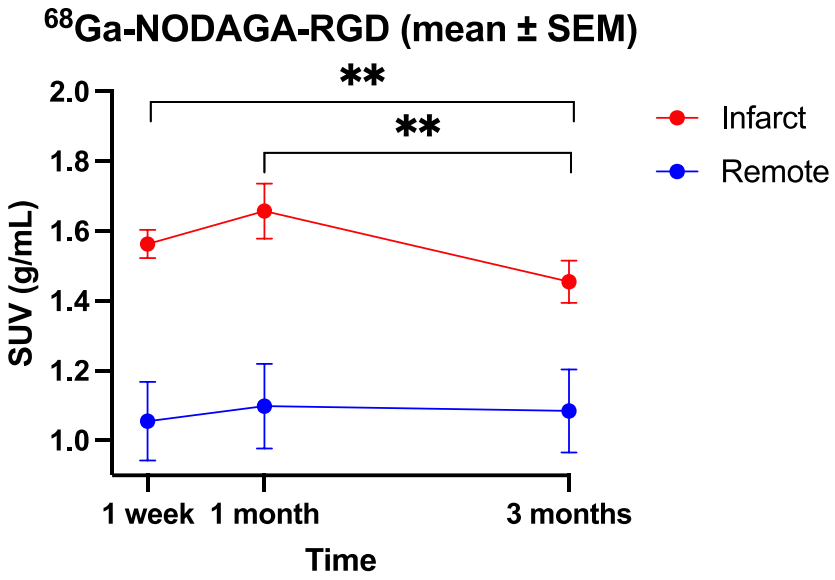

FIGURE 2. $\alpha_v\beta_3$ integrin expression in the infarcted myocardium remained stable 1 month after STEMI, followed by a significant partial decrease at 3 months. SEM, standard error of the mean. ***P*≤0.01.

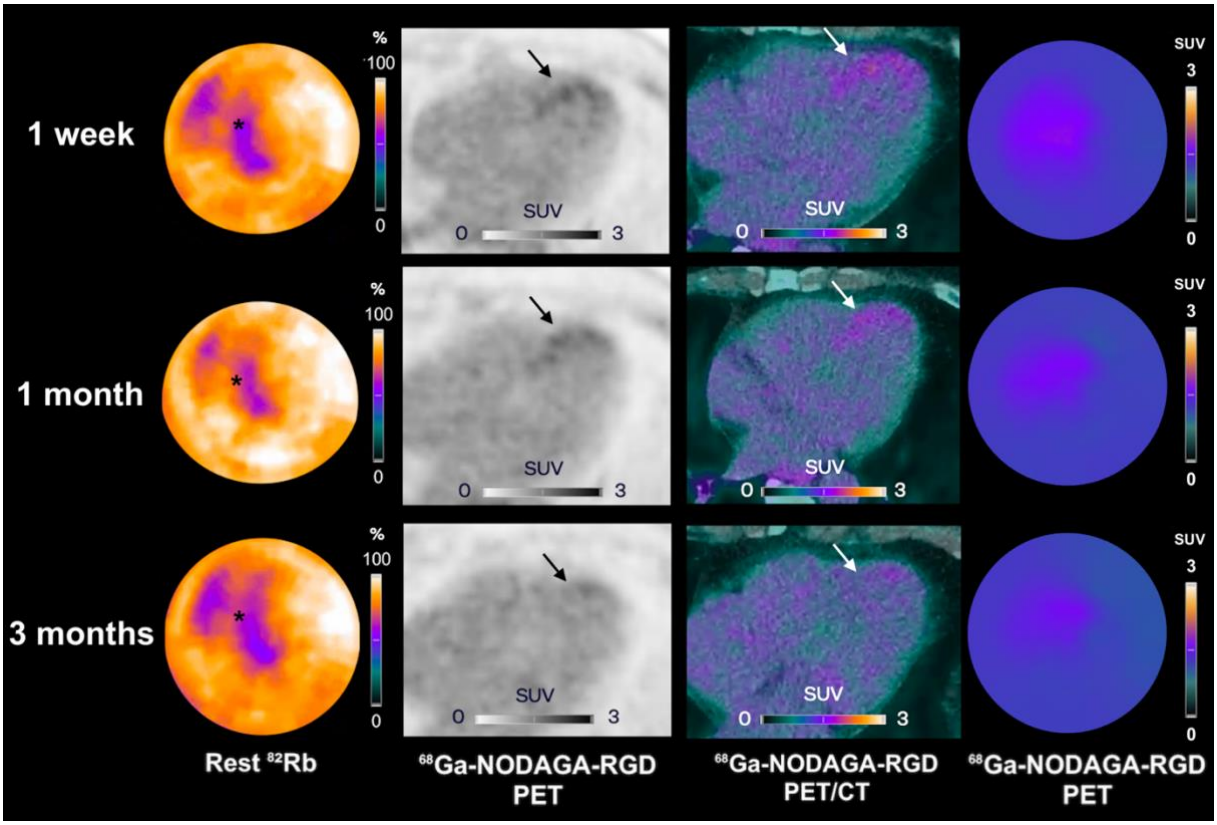

FIGURE 3. Participant example with a decrease in $\alpha_v\beta_3$ integrin expression levels (arrows) in the infarcted myocardium (asterisks) after 1 week to follow-up at 3 months. Rest ^{82}Rb, ^{68}Ga-NODAGA-RGD PET and ^{68}Ga-NODAGA-RGD PET/CT images at 1 week (first row), 1 month (second row) and 3 months (third row) after STEMI.

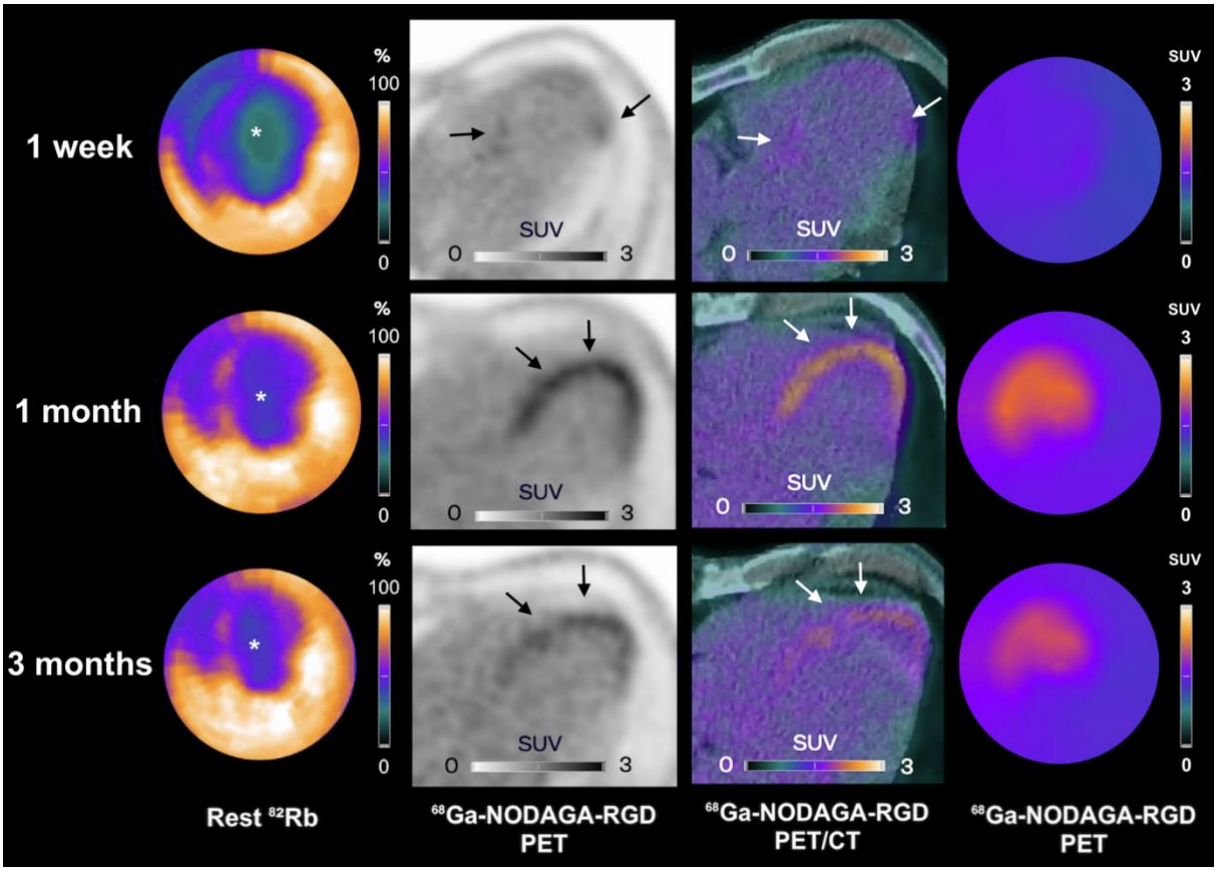

FIGURE 4. Participant example with an increase in $\alpha_v\beta_3$ integrin expression levels (arrows) throughout follow-up within the infarcted myocardium (asterisks). Rest ^{82}Rb, ^{68}Ga-NODAGA-RGD PET and ^{68}Ga-NODAGA-RGD PET/CT images at 1 week (first row), 1 month (second row) and 3 months (third row) after STEMI. The ^{68}Ga-NODAGA-RGD uptake started in the border zone at 1 month and subsequently extended into the necrotic infarct core at both 1 and 3 months.

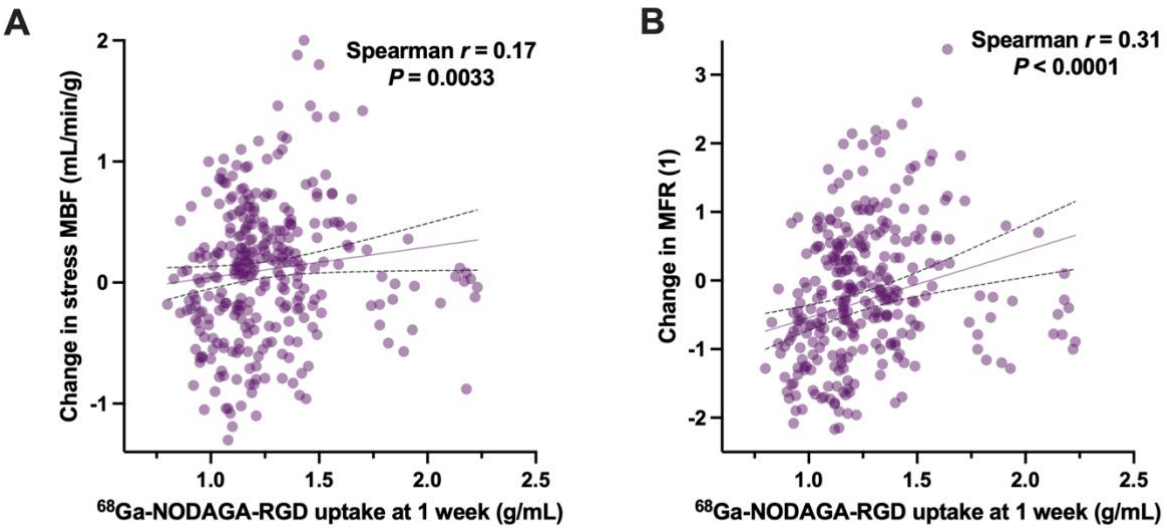

FIGURE 5. Correlations of ^{68}Ga-NODAGA-RGD uptake at 1 week after STEMI with subsequent changes in stress MBF (A) and MFR (B) at 1 month. Data points represent mean segmental values.

Chapter 4

Imaging of myocardial $\alpha_v\beta_3$ integrin expression for evaluation of myocardial injury after acute myocardial infarction

J Nucl Med. 2024 doi:10.2967/jnumed.123.266148

Wail Nammas, Christian Paunonen, Jarmo Teuho, Reetta Siekkinen, Pauliina Luoto, Meeri Käkelä, Ari Hietanen, Tapio Viljanen, **Matthieu Dietz**, John O. Prior, Xiang-Guo Lia,e, Anne Roivainen, Juhani Knuuti, Antti Saraste

Abstract

[^{68}Ga]Ga-NODAGA-RGD is a positron emission tomography (PET) tracer targeting $\alpha_v\beta_3$ integrin, which is upregulated during angiogenesis soon after acute myocardial infarction (AMI). We prospectively evaluated determinants of myocardial uptake of [^{68}Ga]Ga-NODAGA-RGD, and its associations with left ventricular (LV) function in patients after AMI.

Methods: Myocardial blood flow (MBF) and [^{68}Ga]Ga-NODAGA-RGD uptake (60 minutes after injection) were evaluated by PET in 31 patients 7.7±3.8 days after primary percutaneous coronary intervention for ST-elevation AMI. Transthoracic echocardiography of LV function was performed on the day of PET and at 6-month follow-up.

Results: PET images showed increased uptake of [^{68}Ga]Ga-NODAGA-RGD in the ischemic area at risk, predominantly in injured myocardial segments. The standardized uptake value in the segment with the highest uptake (SUV_{max}) in the ischemic area at risk was higher than the mean SUV of the remote myocardium (0.73±0.16 vs. 0.51±0.11, $p<0.001$). Multivariable predictors of [^{68}Ga]Ga-NODAGA-RGD uptake in the area at risk included high peak NT-proBNP ($p<0.001$), low LV ejection fraction, low global longitudinal strain (GLS, $p=0.01$), and low longitudinal strain in the area at risk ($p=0.01$). [^{68}Ga]Ga-NODAGA-RGD uptake corrected for MBF and perfusable tissue fraction in the area at risk predicted improvement in GLS at follow-up ($p=0.002$), independent of peak troponin, NT-proBNP, and LV ejection fraction.

Conclusion: [^{68}Ga]Ga-NODAGA-RGD uptake shows increased $\alpha_v\beta_3$ integrin expression in the ischemic area at risk early after AMI that is associated with regional and global systolic dysfunction, as well as increased LV filling pressure. Increased [^{68}Ga]Ga-NODAGA-RGD uptake predicts improvement of global LV function 6 months after AMI.

Introduction

Acute myocardial infarction (AMI) initiates several maladaptive changes in cardiac myocytes and the extracellular matrix, which can contribute to left ventricular (LV) dysfunction, adverse remodeling, and eventual failure *(1)*. The repair process aimed at restoration of the capillary network, elimination of necrotic tissue, and deposition of new extracellular matrix is essential for healing of AMI, and can counteract the development of chronic LV dysfunction *(1)*. In parallel with inflammation and fibrosis, angiogenesis (sprouting of pre-existing capillaries) plays an important role in myocardial repair after AMI *(2)*.

Integrin $\alpha_v\beta_3$ is a glycoprotein transmembrane receptor the expression of which is upregulated in proliferating endothelial cells, and can serve as a biomarker of angiogenesis *(3)*. After AMI, $\alpha_v\beta_3$ integrin expression increases in vascular structures during the early repair process *(4)*. Studies in experimental models and humans demonstrated the feasibility of using radiolabeled tracers containing the Arg-Gly-Asp (RGD) motif for the non-invasive detection of $\alpha_v\beta_3$ integrin expression after AMI *(5-13)*. However, clinical utility of $\alpha_v\beta_3$ integrin as a biomarker after AMI remains uncertain.

We therefore sought to study the determinants of $\alpha_v\beta_3$ integrin expression, and its association with LV function following AMI. We prospectively evaluated myocardial uptake of [^{68}Ga]Ga-NODAGA-RGD *(10,14)*, a positron emission tomography (PET) radiotracer targeting $\alpha_v\beta_3$ integrin, within 2 weeks of reperfusion in patients with AMI. Function of the LV was evaluated by echocardiography at the time of PET scan and 6 months later.

Methods

Study Cohort and design

We prospectively recruited patients who underwent primary percutaneous coronary intervention because of ST-elevation AMI and who had an LV ejection fraction (LVEF) <50% during the index hospitalization in Turku University Hospital from December 2018 to January 2021. Exclusion criteria are listed in the supplemental data. Each patient signed an informed consent form. The study conforms to the Declaration of Helsinki, and the institutional review boards of the Hospital District of Southwest Finland, Finnish Medicines Agency, and Turku University Hospital approved the study. The study was registered in clinicaltrials.gov with identifier NCT04871217.

To evaluate myocardial αvβ3 integrin expression, patients underwent [^{15}O]O-water PET followed by [^{68}Ga]Ga-NODAGA-RGD PET within 3 to 14 days after AMI. To evaluate LV function, transthoracic echocardiography was performed at baseline on the day of PET imaging and at 6-month follow-up. Peak cardiac troponin T and N-terminal pro-b-type natriuretic peptide (NT-proBNP) levels were recorded during hospitalization and at the time of PET imaging. Data on cardiovascular risk factors, medications, and cardiovascular events were collected from electronic medical reports. The myocardial area at risk (AAR) and the remote area were defined based on the culprit coronary arterial segment, determined from the invasive coronary angiography and electrocardiography.

PET imaging

Synthesis of [^{68}Ga]Ga-NODAGA-RGD is described in supplemental data. For each patient, resting [^{15}O]O-water and [^{68}Ga]Ga-NODAGA-RGD PET scans were performed using a single dedicated PET/computed tomography (CT) scanner (Discovery MI, GE Healthcare, Milwaukee, WI, USA) on the same day, as previously described *(15)* (supplemental data). In brief, [^{15}O]O-water (Radiowater Generator, Hidex Oy, Turku, Finland) was injected as an intravenous bolus (target injected radioactivity 500 MBq) over 15 seconds, and a dynamic PET was acquired over 4 min and 40 sec, starting 25 seconds after injection, with the patient at rest. Then, an average of 179 ± 15 MBq of [^{68}Ga]Ga-NODAGA-RGD was injected as an intravenous bolus followed by a list-mode PET acquisition over 15 minutes after a 60-minute uptake period.

PET image analysis and interpretation

Images were analyzed using Carimas 2.9 software (Turku PET Centre, Turku, Finland) *(10,16)* (supplemental data). In brief, polar maps of [^{68}Ga]Ga-NODAGA-RGD uptake (standardized

uptake value, SUV) in the LV myocardium were generated based on myocardial contours and sampling points matching with co-registered [^{15}O]O-water images. The maximum [^{68}Ga]Ga-NODAGA-RGD uptake (SUV_{max}) was defined as the highest segmental uptake. An indexed SUV_{max} corrected for the mean MBF (MBF_{mean}) and perfusable tissue fraction in the area at risk was also calculated to account for reduced amount of viable tissue in the infarct zone *(16)*.

Echocardiography

Transthoracic echocardiography was performed using Vivid E9 or E95 (GE Vingmed Ultrasound, Horten, Norway) devices equipped with MS5 and 4Vc-D 4D matrix cardiac probes. All images were digitally stored for offline analysis (EchoPAC PC version 203; GE Vingmed, Horten, Norway) of LV global and segmental function (supplemental data). The LV volumes and LVEF were measured using the biplane Simpson's method. Myocardial global longitudinal strain (GLS) and segmental longitudinal strain (LS) were analyzed using the speckle-tracking method and reported as absolute values. Segments with baseline LS <13.5% were defined as injured *(17)*.

Statistical analysis

Continuous data are reported as mean and standard deviation, and are compared using Student's *t* test when normally distributed, and with the Mann-Whitney test otherwise. Categorical data are reported as count (percentage), and are compared with Chi-square or Fisher's exact tests, as appropriate. Univariable and multivariable linear regression models were constructed to identify predictors of [^{68}Ga]Ga-NODAGA-RGD uptake at baseline and predictors of improvement in LV function from baseline to follow-up. Statistically significant variables in the univariable analysis were added to multivariable models as covariates. Intra- and interobserver reproducibility of [^{68}Ga]Ga-NODAGA-RGD SUV_{max} measures were assessed in seven randomly selected patients by calculating the coefficient of variation. Statistical significance was set at $p<0.05$. Statistical analyses were performed using SPSS v. 25.0 (IBM Corporation, New York, USA).

Results

We enrolled 31 patients with the first ST-elevation AMI. Table 1 summarizes baseline characteristics of patients. All patients underwent primary percutaneous coronary intervention at 4.9 ± 6.1 hours from symptom onset. The AAR was in the left anterior descending, the right

and the left circumflex coronary artery territories in 48.4%, 29.0% and 22.6% of patients, respectively.

Patients underwent [^{15}O]O-water and [^{68}Ga]Ga-NODAGA-RGD PET scans at 7.7 ± 3.8 days (median 8 days, interquartile range 7 days) after the index AMI. The clinical characteristics were similar between patients who underwent PET <7 days (n=14) and ≥7 days (n=17) after AMI.

One patient was lost to follow-up. Consequently, 30 patients underwent both baseline and follow-up echocardiography 210 ± 38 days after AMI. There were no deaths or heart failure hospitalizations during follow-up, but one patient had non-ST-elevation AMI caused by a coronary lesion other than the index lesion.

Left ventricular function

Table 2 summarizes the echocardiograph data. All patients initially had LVEF <50%, whereas at baseline evaluation on the day of PET scanning, LVEF was <50% in five patients and GLS was <16% in 17. In the AAR, myocardial injury (segmental LS <13.5%) was present in 26 (84%) patients. The average number of injured segments per patient was 3.1 ± 2.2.

At follow-up, LS in the AAR showed significant improvement from baseline (p=0.03). LVEF improved by ≥5% in 12 (40%) patients and worsened by ≥5% in six (20%). In turn, GLS improved by ≥3% in nine (30%) patients and worsened by ≥3% in four (13%). Only four patients had an LV end-diastolic volume increase of ≥20%.

[^{68}Ga]Ga-NODAGA-RGD uptake after AMI

Uptake of [^{68}Ga]Ga-NODAGA-RGD was visible in the AAR in PET images from all patients (FIGURE 1 and supplemental Figure 1). The segment with the highest [^{68}Ga]Ga-NODAGA-RGD uptake (SUV_{max}) was within or immediately adjacent to the AAR in all patients. Segments in the AAR (n=168) showed higher [^{68}Ga]Ga-NODAGA-RGD SUV than segments in the remote area (0.66 ± 0.18 vs. 0.55 ± 0.14, p<0.001, FIGURE 2).

The [^{68}Ga]Ga-NODAGA-RGD SUV_{max} co-localized with the segment with the most severe contractile abnormality or the immediately adjacent segment in 22 patients. In remaining patients, SUV_{max} was either in the border of a large injured area (n=4) or there was no contractile abnormality in the AAR (n=5). Within the AAR, the average [^{68}Ga]Ga-NODAGA-RGD SUV was higher in segments with myocardial injury (n=97) than in other segments (0.71 ± 0.19 vs. 0.61 ± 0.14, p<0.001, FIGURE 2), and inversely correlated with LS (p<0.001, FIGURE 3A).

MBF was lower in the AAR than remote myocardium (0.73 ± 0.23 vs. 0.83 ± 0.23 mL/g/minute, p <0.001). There was no correlation between segmental SUV and MBF in the AAR (p=0.1), but SUV_{max} correlated with MBF in the non-injured myocardial segments within or immediately adjacent to AAR (r=0.49, p=0.017, supplemental Figure 2).

In patient-based analysis, SUV_{max} and indexed SUV_{max} were higher in the AAR than the remote area (Table 3). SUV_{max} in the AAR was higher than blood pool SUV (0.73 ± 0.16 vs. 0.64 ± 0.15, p<0.001), but lower than liver SUV (0.73 ± 0.16 vs. 1.04 ± 0.16, p<0.001). SUV_{max} was similar between patients who underwent PET <7 and ≥7 days after AMI (p>0.05).

Measurement of SUV_{max} was reproducible, with an intraobserver coefficient of variation of 1.4% and interobserver coefficient of variation of 10.9%.

Predictors of [^{68}Ga]Ga-NODAGA-RGD uptake after AMI

Univariable predictors of [^{68}Ga]Ga-NODAGA-RGD SUV_{max} and indexed SUV_{max} in the AAR at baseline included peak troponin T, peak NT-proBNP, GLS, and regional LS in the AAR (Table 4). Neither age or peak CRP level predicted SUV_{max} or indexed SUV_{max} (p>0.05 both) and they were similar in patients with TIMI flow grade 2 and 3 after revascularization (P=0.6). In multivariable models, the only independent predictor of SUV_{max} in the AAR was peak NT-proBNP (FIGURE 3B, Table 4), whereas peak troponin T, LVEF, and GLS predicted indexed SUV_{max} (Table 4).

[^{68}Ga]Ga-NODAGA-RGD uptake and LV function at follow-up

In univariable analysis, indexed [^{68}Ga]Ga-NODAGA-RGD SUV_{max} in the AAR, peak troponin T, peak NT-proBNP, and baseline LVEF predicted improvement of GLS adjusted for baseline (Table 5). Neither time from symptom onset to revascularization nor the post-revascularization TIMI flow grade predicted improvement of GLS. In multivariable analysis, indexed SUV_{max} in the AAR was the only independent predictor of improvement of GLS at follow-up (p=0.002; FIGURE 4).

Although associated with global LV function improvement, indexed SUV_{max} was not associated with improvement of regional LS in the AAR in 26 patients with myocardial injury at baseline (p=0.7). Furthermore, segmental [^{68}Ga]Ga-NODAGA-RGD SUV did not correlate with change in LS in injured segments in the AAR (p=0.2).

Discussion

We found that uptake of [^{68}Ga]Ga-NODAGA-RGD increased in the myocardium distal to the culprit lesion of the infarct-related artery (AAR) in patients with recent ST-elevation AMI. Uptake of [^{68}Ga]Ga-NODAGA-RGD was associated with myocardial injury, regional and global LV systolic dysfunction as well as increased LV filling pressure. Furthermore, the intensity of [^{68}Ga]Ga-NODAGA-RGD uptake was associated with improvement in global LV function at 6-month follow-up. These results indicate that [^{68}Ga]Ga-NODAGA-RGD PET provides information about the severity of acute ischemic myocardial injury and the potential for recovery of LV function.

Preclinical and clinical studies demonstrated the feasibility of non-invasive nuclear imaging of $\alpha_v\beta_3$ integrin expression using radiolabeled tracers containing the RGD-motif after recent AMI *(5-13)*. Early after AMI, $\alpha_v\beta_3$ integrin is expressed by vascular endothelial cells *(4)*, and uptake of RGD-based tracers correlates with neovascularization *(5-13)*. However, $\alpha_v\beta_3$ integrin has also been implicated in mediating the macrophage response to inflammatory signals *(18)* and myofibroblast differentiation through the activation of latent transforming growth factor-β1 *(19)* that may be also targeted by RGD-based tracers at later stages after myocardial infarction *(20)*. Thus, $\alpha_v\beta_3$ integrin expression may provide information about the activation of the repair process after ischemic myocardial injury, but its utility as an imaging biomarker after human AMI remains uncertain.

Uptake of [^{68}Ga]Ga-NODAGA-RGD after myocardial infarction

^{68}Ga-RGD tracers were previously demonstrated to accumulate in areas of injured myocardium in experimental models of ischemic myocardial injury, and to correlate with $\alpha_v\beta_3$ integrin expression *(8,10)*. In this study, we found consistently increased uptake of [^{68}Ga]Ga-NODAGA-RGD in the ischemic AAR <14 days after AMI, which is in line with previous studies showing accumulation of RGD-based tracers as early as 3 days after ischemic myocardial injury, then peaking at 1–3 weeks *(6)*. Uptake of [^{68}Ga]Ga-NODAGA-RGD was sometimes also observed adjacent to the area at risk, which is consistent with previous evidence showing uptake of RGD-based tracers extending into the peri-infarct zone *(12,21)*. In contrast to AMI, accumulation of RGD-based tracers was not found in patients with chronic coronary total occlusion *(12)* or old MI *(11,12,21)*.

We found that the highest segmental uptake of [^{68}Ga]Ga-NODAGA-RGD (SUV_{max}) was 1.43-fold higher than the mean SUV in the remote myocardium. This is similar to the target-to-background ratios (1.34-2.33) reported in previous studies using RGD-based tracers *(11,12,13)*.

Using a rat model of AMI, we previously showed that measurement of SUV using static images showed comparable results to kinetic modelling of the distribution volume of [^{68}Ga]Ga-DOTA-RGD uptake, thereby simplifying *in vivo* analysis *(9)*. We also measured [^{68}Ga]Ga-NODAGA-RGD uptake corrected for both MBF and perfusable tissue fraction (indexed SUV_{max}) in order to account for reduced MBF and reduced distribution volume due to loss of viable tissue as previously shown *(22)*. Developments in scanner technology and motion correction algorithms could further facilitate quantification of the [^{68}Ga]Ga-NODAGA-RGD signal.

Determinants of [^{68}Ga]Ga-NODAGA-RGD uptake

Uptake of [^{68}Ga]Ga-NODAGA-RGD co-localized with injured myocardial areas based on reduced systolic LS on echocardiography and correlated with the degree of LS reduction after AMI. In a previous study, LS reduction was associated with the transmurality of myocardial injury according to late gadolinium enhancement on cardiac magnetic resonance (CMR) *(17)*. Thus, our findings are consistent with experimental *(10)* as well as clinical studies that found co-localization of RGD-based tracer uptake with resting myocardial perfusion defects *(11,13,21)*, hypokinesia, *(12)* and late gadolinium enhancement *(12,21)*. Of note, in line with previous studies using other RGD-based tracers *(12,21)*, [^{68}Ga]Ga-NODAGA-RGD uptake was also present in the peri-infarct border zones and in five patients without wall motion abnormality at the time of the PET scan, indicating that it is a sensitive marker of recent ischemic myocardial injury.

Myocardial infarct size determined by peak troponin was not an independent predictor of the indexed [^{68}Ga]Ga-NODAGA-RGD SUV_{max}, indicating that $\alpha_v\beta_3$ integrin expression is also dependent on factors other than the extent of myocardial injury. Our finding is consistent with no association between ^{18}F-Fluciclatide uptake and infarct size quantified by CMR early after AMI in a previous study *(12)*. However, other studies reported correlations between uptake of other RGD-based tracers and infarct size at later time-points after AMI (31 ± 14 days and 8 weeks) *(13,21)*. Furthermore, an inverse relationship between ^{18}F-Galacto-RGD uptake and resting MBF was reported *(13)*. In our study, [^{68}Ga]Ga-NODAGA-RGD uptake did not correlate with MBF, which may be explained by [^{15}O]O-water PET measuring MBF in the viable myocardium and only mildly reduced MBF in the AAR at the time of PET.

A novel finding in the present study is that in addition to LV dysfunction in the AAR, reduced LVEF, impaired GLS, and high NT-proBNP were independent predictors of the [^{68}Ga]Ga-NODAGA-RGD uptake. These findings are consistent with the key roles of hemodynamic stress and pressure overload in modifying the responses of different cell types towards

maintenance of cardiac function following injury *(1)*. Taken together, our results are consistent with the increased expression of $\alpha_v\beta_3$ integrin after ischemic myocardial injury, and with the intensity of [^{68}Ga]Ga-NODAGA-RGD uptake reflecting both regional and global LV dysfunction, as well as increased LV filling pressure. Since global LV remodeling and dysfunction are robust risk factors for heart failure and mortality after AMI *(1,23)*, our findings indicate that [^{68}Ga]Ga-NODAGA-RGD uptake is a potentially relevant prognostic biomarker.

Uptake of [^{68}Ga]Ga-NODAGA-RGD and ventricular function after AMI

Despite improvements in acute management, AMI remains one of the most important causes of chronic heart failure *(1)*. Early identification of at-risk patients could provide the opportunity for targeted therapies to attenuate adverse LV remodeling and systolic dysfunction *(1)*. We hypothesized that $\alpha_v\beta_3$ integrin expression is a marker of myocardial repair and could be used to predict improvement in LV function after AMI.

A novel finding of our study is that increased indexed [^{68}Ga]Ga-NODAGA-RGD SUV_{max} was associated with improvement in global LV function at follow-up, independent of peak troponin T, elevated NT-proBNP, and impaired LVEF. Our finding is in line with preclinical and clinical data suggesting that increased $\alpha_v\beta_3$ integrin expression after AMI predicts subsequent improvement of regional LV function *(12)* and the absence of adverse remodeling *(7,21)*. However, in our study, [^{68}Ga]Ga-NODAGA-RGD was not directly associated with the functional outcome of the myocardium in the AAR. This may be explained by this functional outcome being mainly dependent on the extent of irreversible myocardial injury, whereas the repair processes affects viable surrounding myocardium, impacting adverse LV remodeling and global LV function *(1)*.

Limitations of the study

We studied patients within 3–14 days after AMI on the basis of experimental studies indicating that $\alpha_v\beta_3$ integrin expression peaks at 1–3 weeks after index AMI *(6)*. In favor of relatively stable uptake, we did not find significant difference in the [^{68}Ga]Ga-NODAGA-RGD uptake between patients scanned before or after 7 days after the index AMI. Our ability to detect associations between the uptake of [^{68}Ga]Ga-NODAGA-RGD and changes in post-MI LV structure and function may have been limited by the modest degree of changes and limited number of patients with significant LV remodeling despite relatively long time from symptom onset to revascularization. Although CMR provides more precise quantification of cardiac

structure and function than echocardiography, echocardiograms were performed and analyzed by experienced investigators according to a pre-defined protocol. Endothelial progenitor cells, proposed to contribute to neoangiogenesis, were not measured, and their predictive value vs. [^{68}Ga]Ga-NODAGA-RGD PET imaging for cardiac functional recovery will need to be explored in future studies. Although formal power calculation was not feasible, the sample size of 30 patients would be sufficient to detect difference in tracer uptake between those with and without significant remodeling based on a previous experimental study *(7)*.

Conclusion

In patients with AMI, [^{68}Ga]Ga-NODAGA-RGD uptake was increased in the ischemic AAR, correlating with the extent of myocardial injury, global and regional LV dysfunction, and LV filling pressure. Furthermore, [^{68}Ga]Ga-NODAGA-RGD uptake predicted global LV function improvement at mid-term follow-up. These results suggest that targeted imaging of $\alpha_v\beta_3$ integrin is a potential approach to evaluate myocardial injury responses after AMI.

References

1. Frantz S, Hundertmark MJ, Schulz-Menger J, Bengel FM, Bauersachs J. Left ventricular remodelling post-myocardial infarction: pathophysiology, imaging, and novel therapies. *Eur Heart J*. 2022;43:2549–2561.
2. Wu X, Reboll MR, Korf-Klingebiel M, Wollert KC. Angiogenesis after acute myocardial infarction. *Cardiovasc Res*. 2021;117:1257–1273.
3. Simons M, Alitalo K, Annex BH, et al. State-of-the-Art Methods for Evaluation of Angiogenesis and Tissue Vascularization: A Scientific Statement From the American Heart Association. *Circ Res*. 2015;116:e99–132.
4. Sun M, Opavsky MA, Stewart DJ, et al. Temporal response and localization of integrins beta1 and beta3 in the heart after myocardial infarction: regulation by cytokines. *Circulation.* 2003;107:1046–1052.
5. Meoli DF, Sadeghi MM, Krassilnikova S, et al. Noninvasive imaging of myocardial angiogenesis following experimental myocardial infarction. *J Clin Invest.* 2004;113:1684–1691.
6. Higuchi T, Bengel FM, Seidl S, et al. Assessment of αvβ3 integrin expression after myocardial infarction by positron emission tomography. *Cardiovasc Res*. 2008;78:395–403.
7. Sherif HM, Saraste A, Nekolla SG, et al. Molecular imaging of early αvβ3 integrin expression predicts long-term left-ventricle remodeling after myocardial infarction in rats. *J Nucl Med*. 2012;53:318–323.
8. Laitinen I, Notni J, Pohle K, et al. Comparison of cyclic RGD peptides for αvβ3 integrin detection in a rat model of myocardial infarction. *EJNMMI Res*. 2013;3:38.
9. Kiugel M, Dijkgraaf I, Kytö V, et al. Dimeric [(68)Ga]DOTA-RGD peptide targeting αvβ 3 integrin reveals extracellular matrix alterations after myocardial infarction. *Mol Imaging Biol*. 2014;16:793–801.
10. Grönman M, Tarkia M, Kiviniemi T, et al. Imaging of alphavbeta3 integrin expression in experimental myocardial ischemia with [(68)Ga]NODAGA-RGD positron emission tomography. *J Transl Med*. 2017;15:144.
11. Sun Y, Zeng Y, Zhu Y, et al. Application of (68)Ga-PRGD2 PET/CT for αvβ3-integrin imaging of myocardial infarction and stroke. *Theranostics*. 2014;4:778–786.
12. Jenkins WS, Vesey AT, Stirrat C, et al. Cardiac αVβ3 integrin expression following

acute myocardial infarction in humans. *Heart*. 2017;103:607–615.

13. Makowski MR, Rischpler C, Ebersberger U, et al. Multiparametric PET and MRI of myocardial damage after myocardial infarction: correlation of integrin αvβ3 expression and myocardial blood flow. *Eur J Nucl Med Mol Imaging*. 2021;48:1070–1080.
14. Gnesin S, Mitsakis P, Cicone F, et al. First in-human radiation dosimetry of 68Ga-NODAGA-RGDyK. *EJNMMI Res*. 2017;7:43.
15. Lehtonen E, Teuho J, Koskinen J, et al. A Respiratory Motion Estimation Method Based on Inertial Measurement Units for Gated Positron Emission Tomography. *Sensors*. 2021;21:3983.
16. Grönman M, Tarkia M, Stark C, et al. Assessment of myocardial viability with [15O]water PET: A validation study in experimental myocardial infarction. *J Nucl Cardiol*. 2021;28:1271–1280.
17. Rost C, Rost MC, Breithardt OA, et al. Relation of functional echocardiographic parameters to infarct scar transmurality by magnetic resonance imaging. *J Am Soc Echocardiogr*. 2014;27:767–774.
18. Antonov AS, Antonova GN, Munn DH, et al. αVβ3 integrin regulates macrophage inflammatory responses via PI3 kinase/Akt-dependent NF-κB activation. *J Cell Physiol*. 2011;226:469–476.
19. Sarrazy V, Koehler A, Chow ML, et al. Integrins αvβ5 and αvβ3 promote latent TGF-β1 activation by human cardiac fibroblast contraction. *Cardiovasc Res*. 2014;102:407–417.
20. van den Borne SW, Isobe S, Verjans JW, et al. Molecular imaging of interstitial alterations in remodeling myocardium after myocardial infarction. *J Am Coll Cardiol*. 2008;52:2017–2028.
21. Verjans J, Wolters S, Laufer W, et al. Early molecular imaging of interstitial changes in patients after myocardial infarction: comparison with delayed contrast-enhanced magnetic resonance imaging. *J Nucl Cardiol*. 2010;17:1065–1072.
22. MacAskill MG, Stadulyte A, Williams L, et al. Quantification of Macrophage-Driven Inflammation During Myocardial Infarction with 18F-LW223, a Novel TSPO Radiotracer with Binding Independent of the rs6971 Human Polymorphism. *J Nucl Med*. 2021;62:536–544.
23. Konstam MA, Kramer DG, Patel AR, Maron MS, Udelson JE. Left ventricular remodeling in heart failure: current concepts in clinical significance and assessment. *J*

Am Coll Cardiol Img. 2011;4:98–108.

Figures and legends

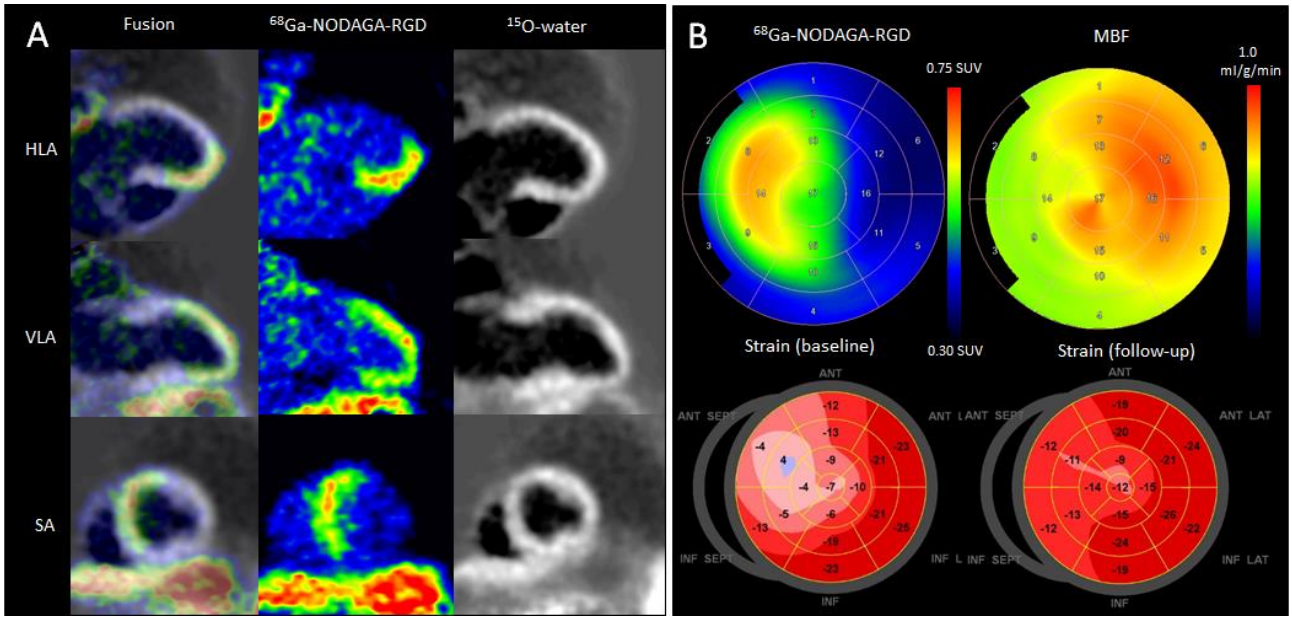

Figure 1. Uptake of 68Ga-NODAGA-RGD 7 days after acute occlusion of the proximal left anterior descending coronary artery. Panel A shows myocardial contours in [^{15}O]O-water images, 68Ga-NODAGA-RGD uptake images, and corresponding fusion images. Panel B shows polar maps of 68Ga-NODAGA-RGD uptake, resting myocardial blood flow (MBF), and longitudinal strain at the time of PET and 6 months later. Note the reduced longitudinal strain in the anteroseptal region at baseline and partial functional recovery at 6 months. HLA=horizontal long axis, SA=short axis, SUV=standardized uptake value, VLA=vertical long axis.

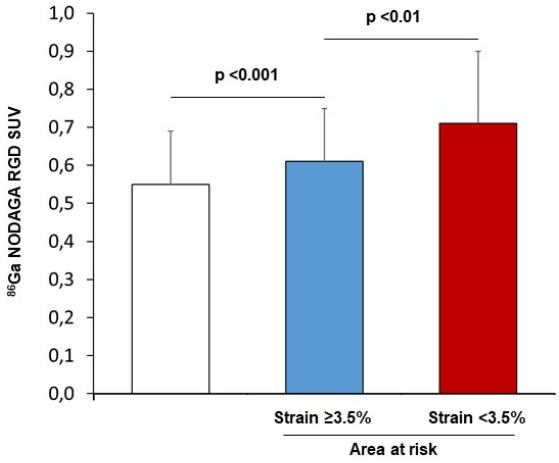

Figure 2. At baseline, segmental uptake of [^{68}Ga]Ga-NODAGA-RGD was higher in the area at risk than in remote myocardium, and was highest in segments with myocardial injury (longitudinal strain <13.5%).

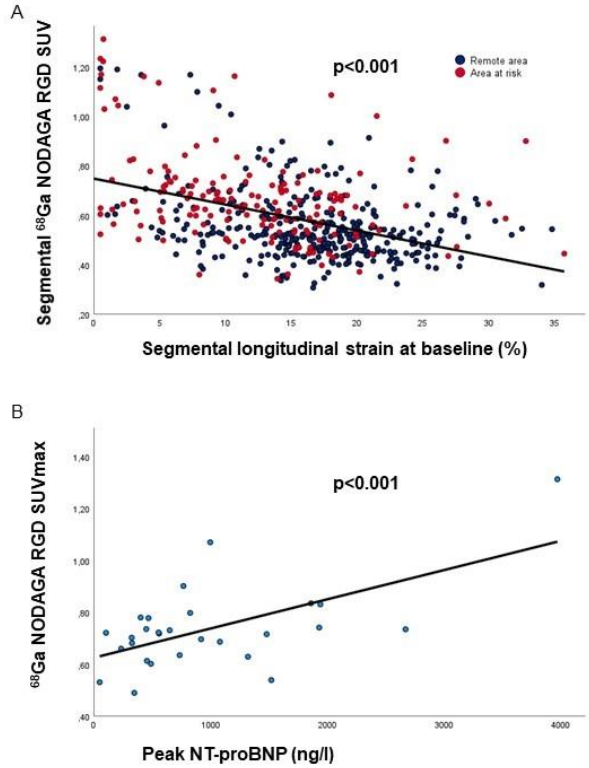

Figure 3. (A) Segmental uptake of [^{68}Ga]Ga-NODAGA-RGD inversely correlated with segmental longitudinal strain (r=−0.0355, p<0.001). (B) Increased NT-pro-BNP level predicted [^{68}Ga]Ga-NODAGA-RGD uptake (SUV_{max}) in the area at risk (p<0.001). SUV=standardized uptake value

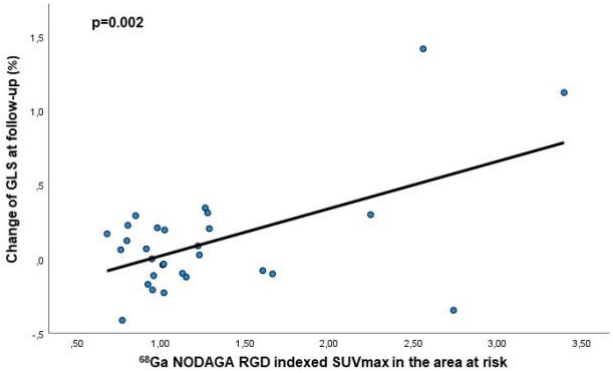

Figure 4. At follow-up, [^{68}Ga]Ga-NODAGA-RGD uptake (SUV_{max}) in the area at risk predicted segmental improvement of longitudinal strain. SUV=standardized uptake value

TABLE 1. Patient characteristics

Cohort (N=31)	
Age (years)	64.2±9.2
Male sex	28 (90.3)
Body mass index (kg/m^2)	25.4±4.8
Current smoking	11 (35.5)
Diabetes mellitus	3 (9.7)
Hypertension	13 (41.9)
Hypercholesterolemia	17 (54.8)
Family history of CAD	9 (31)
Time from symptoms to PCI (hours)	4.9±6.1
Culprit coronary artery territory	
Left anterior descending artery	15 (48.4)
Circumflex artery	7 (22.6)
Right coronary artery	9 (29)
Post-PCI TIMI flow	
Grade 2	10 (32.3)
Grade 3	21 (67.7)
Peak troponin T (ng/L)	3884.3±4391.7
Peak NT-proBNP (ng/L)	979.4±871.5
Total cholesterol (mmol/L)	4.2±1.1
LDL cholesterol (mmol/L)	2.9±0.9
Duration of hospital stay (days)	3.7±1.8
Loop diuretics	10 (32.3)
Inotropic medication	7 (22.6)

Medication at discharge	
Aspirin	30 (96.8)
Statin	30 (96.8)[a]
ACEI/ARB	29 (93.5)
Beta blocker	25 (80.6)

Data are shown as mean ± standard deviation or number (percentage).

[a]high-intensity statin in 27 (87.1%).

ACEI=angiotensin converting enzyme inhibitors, ARB= angiotensin receptor blockers, CAD=coronary artery disease, LDL=low-density lipoprotein, PCI=percutaneous coronary intervention

TABLE 2. Echocardiography data

	Baseline (N=31)	Follow-up (N=30)	p-value
LV end-diastolic volume (mL)	94.7±27.7	93.6±30.1	0.7
LV end-systolic volume (mL)	42.7±17.1	40.8±19.1	0.4
LV EF (%)	55.8±6.9	57.5±7.3	0.2
GLS (%)	14.9±4.6	15.4±3.9	0.3
LS in the area at risk (%)	12.5±6.0	13.8±5.2	0.03
Mitral E/A ratio	0.96±0.35	1.01±0.36	0.4
E/e′ ratio	8.9±2.7	7.7±1.8	0.01

Data are shown as mean ± standard deviation.

LV=left ventricular, EF=ejection fraction, GLS=global longitudinal strain

TABLE 3. [^{68}Ga]Ga-NODAGA-RGD and [^{15}O]O-water positron emission tomography data

	Area at risk	Remote area	p value
[^{68}Ga]Ga-NODAGA-RGD SUV_{max}	0.727±0.16	0.529±0.14	<0.001
[^{68}Ga]Ga-NODAGA-RGD SUV_{mean}	0.652±0.15	0.511±0.11	<0.001
MBF_{mean}	0.732±0.23	0.827±0.23	<0.001
Indexed [^{68}Ga]Ga-NODAGA-RGD SUV_{max}	1.263±0.64	0.789±0.24	<0.001

Data are shown as mean ± standard deviation. SUV=standardized uptake value, MBF=resting myocardial blood flow

TABLE 4. Predictors of [^{68}Ga]Ga-NODAGA-RGD uptake in the area at risk after acute myocardial infarction

	Univariable analysis			Multivariable analysis		
	B coefficient (95% CI)	R coefficient	p value	B coefficient (95% CI)	R coefficient	p value
SUV_{max}						
Age	0.001 (95%CI −0.005–0.008)	0.077	p=0.6			
Peak troponin T	0.002 (95%CI 0.001–0.003)	0.603	p<0.001			
Peak NT-proBNP	0.001 (95%CI 0.001–0.002)	0.605	p<0.001	0.001 (95%CI 0.001–0.002)	0.605	p<0.001
Baseline LV EF	−0.008 (95%CI −0.016–0.000)	−0.348	p=0.055			
Baseline GLS	0.016 (95%CI 0.004–0.028)	0.447	p=0.01			
Area at risk LS	0.010 (95%CI 0.001–0.020)	0.394	p=0.02			
Indexed SUV_{max}						
Age	−0.002 (95%CI −0.030–0.026)	−0.033	p=0.8			
Peak troponin T	0.011 (95%CI 0.008–0.015)	0.765	p<0.001	0.008 (95%CI 0.005–0.012)	0.542	p<0.001
Peak NT-proBNP	0.004 (95%CI 0.002–0.007)	0.561	p=0.002			
Baseline LV EF	−0.067 (95%CI −0.093–0.041)	−0.701	p<0.001	−0.045 (95%CI −0.067–0.023)	−0.476	p<0.001
Baseline GLS	0.106 (95%CI 0.069–0.143)	0.741	p<0.001	0.061 (95%CI 0.014–0.109)	0.422	p=0.01
Area at risk LS	0.071 (95%CI 0.040–0.101)	0.668	p<0.001	0.035 (95%CI −0.002–0.071)	0.315	p=0.059

Covariates in the multivariable model were peak troponin T, peak NT-proBNP, and either LV EF, GLS, or area at risk longitudinal strain. Peak troponin T is for a 100-unit increment and peak NT-proBNP is for a 10-unit increment.

CI=confidence interval, SUV=standardized uptake value, LV=left ventricular, EF=ejection fraction, GLS=global longitudinal strain,

TABLE 5. Predictors of left ventricular function improvement at follow-up

	B coefficient (95% CI)	R coefficient	p value
Improvement in LV EF[a]			
Age	0.004 (95%CI −0.001–0.009)	0.272	p=0.1
Peak troponin T	0.000 (95%CI −0.001–0.001)	−0.071	p=0.7
Peak NT-proBNP	0.000 (95%CI −0.001–0.000)	−0.228	p=0.2
SUV_{max} in the area at risk	0.004 (95%CI −0.309–0.316)	0.005	p=0.9
Indexed SUV_{max} in the area at risk	0.047 (95%CI −0.031–0.125)	0.233	p=0.2
Baseline GLS	0.007 (95%CI −0.003–0.018)	0.260	p=0.1
Improvement in GLS[a]			
Age	0.010 (95%CI −0.006–0.025)	0.232	p=0.2
Peak troponin T	0.004 (95%CI 0.002–0.007)	0.519	p=0.003
Peak NT-proBNP	0.002 (95%CI 0.000–0.004)	0.435	p=0.02
SUV_{max} in the area at risk	0.666 (95%CI −0.190–1.523)	0.288	p=0.1
Indexed SUV_{max} in the area at risk	0.319 (95%CI 0.128–0.510)	0.550	p=0.002
Baseline LV EF	−0.023 (95%CI −0.042−0.004)	−0.423	p=0.02

[a]Adjusted for baseline. Peak troponin T is for a 100-unit increment and peak NT-proBNP is for a 10-unit increment.

CI=confidence interval, LV=left ventricular, EF=ejection fraction, SUV=standardized uptake value, GLS=global longitudinal strain

PART III

$\alpha_v\beta_3$ integrin expression of atherosclerotic disease

Chapter 5

Imaging Angiogenesis in Atherosclerosis in Large Arteries with 68Ga-NODAGA-RGD PET/CT: Relationship with Clinical Atherosclerotic Cardiovascular Disease

EJNMMI Res. 2021;11(1):71.

Matthieu Dietz, Christel H. Kamani, Emmanuel Deshayes, Vincent Dunet, Periklis Mitsakis, George Coukos, Marie Nicod Lalonde, Niklaus Schaefer, John O. Prior

Abstract

Background

Integrin alpha-V-beta-3 (αvβ3) pathway is involved in intraplaque angiogenesis and inflammation and represents a promising target for molecular imaging in cardiovascular diseases such as atherosclerosis. The aim of this study was to assess the clinical correlates of arterial wall accumulation of ^{68}Ga-NODAGA-RGD, a specific $\alpha_v\beta_3$ integrin ligand for PET.

Materials and methods

The data of 44 patients who underwent ^{68}Ga-NODAGA-RGD PET/CT scans were retrospectively analyzed. Tracer accumulation in the vessel wall of major arteries was analyzed semi-quantitatively by blood-pool-corrected target-to-background ratios. Tracer uptake was compared with clinically documented atherosclerotic cardiovascular disease, cardiovascular risk factors and calcified plaque burden. Data were compared using the Mann-Whitney U test, Pearson correlation and Spearman correlation.

Results

^{68}Ga-NODAGA-RGD arterial uptake was significantly higher in patients with previous clinically documented atherosclerotic cardiovascular disease (mean TBR 2.44 [2.03-2.55] vs. 1.81 [1.56-1.96], p = 0.001) and showed a significant correlation with prior cardiovascular or cerebrovascular event (r = 0.33, p = 0.027), BMI (ρ = 0.38, p = 0.01), plaque burden (ρ = 0.31, p = 0.04), and hypercholesterolemia (r = 0.31, p = 0.04).

Conclusions

^{68}Ga-NODAGA-RGD holds promise as a non-invasive marker of disease activity in atherosclerosis, providing information about intraplaque angiogenesis.

Introduction

Cardiovascular atherosclerotic disease is the leading cause of death worldwide (1). Atherosclerosis is a systemic condition consisting of the accumulation of fatty and/or fibrous material in the subendothelial space (intima) of medium and large-sized arteries. This process results in the formation of progressive inflammatory plaques that represent the hallmark lesion (2). The development of atherosclerosis is an intricate process of cellular alterations over a prolonged period. In atherosclerotic lesions, the combination of macrophage infiltration and apoptotic death together with hypoxia-induced necrosis is thought to promote neovascularization (3). Angiogenesis within the vessel wall is comprised of a network of capillaries that arise from the adventitial vasa vasorum and extend into the intimal layer. These capillaries are thought to be important regulators of plaque growth and as a key factor in lesion instability. Increased density of capillaries is associated with intraplaque hemorrhage and plaque rupture (3, 4).

Combined positron emission tomography and computed tomography (PET/CT) is a non-invasive hybrid imaging technique that could potentially be used to measure inflammatory activity within the vasculature, the most numerous publications being with ^{18}F-FDG (5). However, a more straightforward marker of atherosclerosis, with less physiologic uptake, no interaction with blood glucose and no requirement for a fasting period before imaging could be of interest. Integrins αvβ3 are transmembrane glycoproteins that are involved in the migration of activated endothelial cells during the formation of new vessels. Integrins αvβ3 are expressed in endothelial cells, medial and some intimal smooth muscle cells. Expression of αvβ3 integrin was also found in CD68-positive macrophages in the shoulder of advanced plaques and in the perimeter of the necrotic core of atherosclerotic lesions (6). Integrin αvβ3 contains a distinctive RGD-amino acid sequence (arginine-glycine-aspartate) in the cell-ligand interaction site. Hence, a few RGD-based PET agents have been tested for imaging integrin in atherosclerosis, mainly in preclinical models (7-11), and in two recent clinical evaluations (12, 13).

^{68}Ga-NODAGA-RGD is an emerging RGD-based PET radiotracer with strong affinity for the αvβ3 integrin (14, 15). We hypothesized that ^{68}Ga-NODAGA-RGD may act as an imaging marker of inflammation and angiogenesis in atherosclerosis. The purpose of this study was to examine the relationship between arterial wall ^{68}Ga-NODAGA-RGD uptake in large arteries and the incidence of atherosclerotic cardiovascular diseases.

Methods

Patients

The population of this retrospective study consisted of consecutive patients who had been referred to our institution for a ^{68}Ga-NODAGA-RGD PET/CT within clinical study protocols. Included in this analysis were trials assessing tumoral angiogenesis (NCT02666547, NCT03475134), cardiac lesions angiogenesis (NCT03809689), and inflammatory atheromatous plaques in the carotid arteries (NCT01608516) (15). Patients were included if they underwent a ^{68}Ga-NODAGA-RGD PET/CT from vertex to mid-thigh. Patients could not be included if they did explicitly refuse the retrospective use of their data for research. All procedures performed in this study were in accordance with the ethical standards of the institutional and/or national research committee and with the 1964 Helsinki declaration and its last amendments or comparable ethical standards. The Ethics Committee Vaud (CER-VD) approved this retrospective study protocol (CER-VD #2018_01513) and waived the need for patient informed consent for the study analysis.

Clinical data

Clinical data were collected retrospectively from the medical records of the patients. History of atherosclerotic cardiovascular disease (ASCVD) was collected, according to the strict same definitions as listed by Mach et al. (16), including previous acute coronary syndrome (myocardial infarction or unstable angina), stable angina, coronary revascularization (percutaneous coronary intervention, coronary artery bypass graft surgery, and other arterial revascularization procedures), stroke and transient ischemic attack, and peripheral arterial disease. Subjects with any type of clinically documented ASCVD were classified into the ASCVD group. Subjects with no clinically documented ASCVD were classified into the control group. Cardiovascular risk factors including age, sex, body mass index (BMI), arterial hypertension, hypercholesterolemia, smoking (current or former), and diabetes mellitus were also collected for every subject. Potential last previous systemic anticancer therapies and time intervals between last systemic anticancer therapies and PET scans were also collected. Because of the potential influence

of statins on expression of vascular endothelial growth factor on monocytes, treatments with statins were also recorded (17).

Image acquisitions

^{68}Ga-NODAGA-RGD PET/CT were performed at our hospital. Pregnancy was excluded in women of childbearing age before each PET/CT. ^{68}Ga-NODAGA-RGD PET/CT images were acquired 63 [59-71] minutes after intravenous administration of 190 [175-210] MBq of ^{68}Ga-NODAGA-RGD in an antecubital vein followed by 10 mL of 0.9% NaCl solution.

Images were acquired on a Discovery 690 TOF (GE Healthcare, Waukesha, WI, USA), or a Biograph Vision 600 (Siemens Medical Solutions, Knoxville, USA) PET/CT. Acquisitions were performed with 3 min per bed position (Discovery), or a continuous flow mode (Biograph Vision). PET data were reconstructed using OSEM (Discovery: 3 iterations, 16 subsets; Biograph Vision: 4 iterations, 5 subsets). Head to mid-thigh unenhanced CT was acquired for attenuation correction (Discovery: 120 kV, 40 mA, 0.8 s/rotation, pitch 0.9; Biograph Vision: 100 kV, 40 mA, 0.5 s/rotation, pitch 0.8).

Image analysis

Transaxial PET, CT, and fused ^{68}Ga-NODAGA-RGD PET/CT images were analyzed both visually and semi-quantitatively on a dedicated workstation (Syngo.Via, VB30 Siemens Healthcare), blinded to the patient's clinical information.

^{68}Ga-NODAGA-RGD uptake

Maximal standardized uptake values (SUVmax) for ^{68}Ga-NODAGA-RGD were measured in the following arterial segments: both common carotid arteries, ascending aorta, aortic arch, descending aorta, abdominal aorta, and both iliac arteries, using a previously validated method (18). Briefly, on axial coregistered PET/CT slices, simple circular regions of interest (ROIs) were placed to cover arterial walls and lumen. For those vessels of greater diameter, 1-cm diameter ROIs were placed along the arterial walls and were slid along the arterial segments to locate the highest SUVmax within the tubular arterial segment, avoiding areas of ^{68}Ga-NODAGA-RGD spillover. For blood pool SUV measurements, three different 1-cm diameter ROIs were placed in both the mid-lumen of

the inferior and superior vena cava, and the SUVmean of the 6 measurements was collected (blood pool activity = average of the 6 SUVmean measurements). SUVmax were then corrected for blood pool activity to provide tissue-to-background ratios (TBR = SUVmax / blood pool activity) measurements, as a measure of arterial tracer uptake (18). The average TBR (mean TBR) was calculated for each patient, considering all assessed segments. TBRaorta was the average of ascending aorta, aortic arch, descending aorta, and abdominal aorta TBR measurements. TBRcarotid was the average of both common carotid arteries TBR measurements. TBRiliac was the average of both iliac arteries TBR measurements.

Plaque burden

The CT scans were examined for the presence of calcified plaque (high-density mural areas with attenuation > 130 Hounsfield units) in the walls of the same arterial segments investigated by PET (19). The amount of calcification was semi-quantitatively ranked according to a previously validated scale (18):

- 0: absent calcified plaque,
- 1: small, calcified plaque covering less than 10% of the vessel circumference,
- 2: calcified plaque involving 10%-25% of the vessel circumference,
- 3: calcified plaque involving 25%-50% of the circumference,
- 4: calcified plaque involving more than 50% of the vessel circumference.

The calcified plaque scores were then summed for the 8 areas (18).

Direct visual comparisons of ^{68}Ga-NODAGA-RGD foci on PET/CT images to calcification sites on CT images

To understand if ^{68}Ga-NODAGA-RGD foci are located or not in calcified plaques on CT images, visual comparisons of highest ^{68}Ga-NODAGA-RGD foci to calcification sites on CT were evaluated within the fifty tubular arterial segments with the highest TBR measurements.

Statistics

We assessed the distribution of data with the Shapiro-Wilk test. Continuous parametric variables were expressed as mean ± SD and compared using Student's t-tests. Nonparametric data were presented as median [interquartile range] and compared using the Mann-Whitney U test. Categorical variables were collected as numbers (n) and percentages (%) and compared using the chi-square test or Fisher exact test. Pearson correlation analysis (r) or Spearman correlation analysis (ρ) were used to correlate mean TBR with prior cardiovascular and cerebrovascular event, age, sex, BMI, arterial hypertension, hypercholesterolemia, smoking, and diabetes mellitus. A p value less than or equal to 0.05 was considered statistically significant. The statistical analysis was performed using R version 4.0.3 (R Foundation for Statistical Computing, Vienna, Austria).

Results

Patients

In total, fifty-six patients underwent a ^{68}Ga-NODAGA-RGD PET/CT at our institution and forty-four patients could be included retrospectively. A flowchart of the study design is shown in Figure 1. Clinical characteristics of the patients are reported in Table 1. Thirty-nine of forty-four patients (89%) were referred within oncologic studies and five of forty-four patients (11%) were referred before carotid endarterectomy.

Eight of the forty-four patients (18%) had previous myocardial infarction, coronary revascularization, stroke or transient ischemic attack, and/or peripheral arterial disease and were thus classified into the ASCVD group. The thirty-six remaining patients (82%) were classified into the control group. All the five patients referred for carotid endarterectomy were included in the ASCVD group. In this group, the three remaining patients were referred for esophagus, lung, and head and neck tumors. The median age was higher in the ASCVD than in the control group, and the ASCVD group included a higher proportion of men as compared to the control group (respectively 64 years [61-72] vs. 59 years [50-65], p = 0.059, and 7 men of 8 patients; 87%, vs. 17 men of 36 patients; 46%, p = 0.054). The ASCVD group included a higher prevalence of hypertension (5 of 8 patients; 62%) as well of hypercholesterolemia (6 of 8 patients; 75%), as compared to

the control group (respectively 8 of 36 patients; 23%, $p = 0.037$, and 6 of 36 patients; 17%, $p = 0.003$). BMI, smoking and diabetes mellitus did not significantly differ between the two groups.

All the 39 oncology patients were referred for baseline PET/CT before receiving additional treatments (chemotherapy, anti-angiogenic therapy, or surgery). Among them 14 patients had previous systemic anticancer therapies, with a median time interval of 113 [22-189] days between last systemic anticancer therapies and PET scans. The last previous systemic anticancer therapy for each of these 14 patients and time intervals between last systemic anticancer therapies and PET scans are shown in Table 2. None of these last previous systemic anticancer therapies included antiangiogenic drugs. Six patients had systemic anticancer therapy within 4 weeks before imaging.

When the mean TBR values were compared, there was no difference between patients who had previous systemic anticancer therapies and patients who had not previous systemic anticancer therapies (1.84 [1.57-1.89] vs. 1.89 [1.62-2.24] respectively, $p = 0.33$).

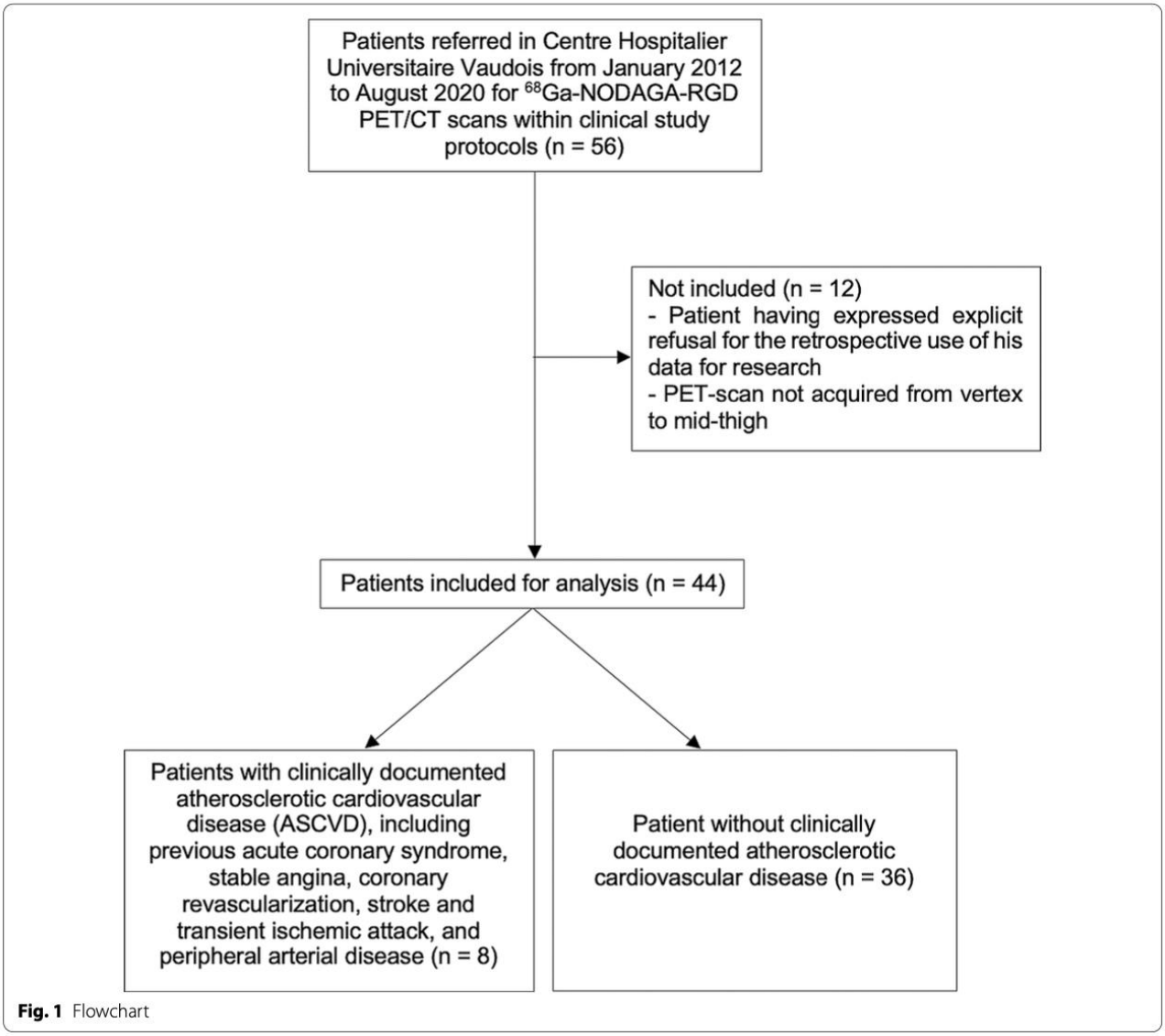

Fig. 1 Flowchart

Arterial Wall ^{68}Ga-NODAGA-RGD uptake and plaque burden

In the entire group of 44 patients, a total of 352 arterial segments were evaluated and statistically analyzed. The PET/CT was acquired on the Discovery PET/CT in 28 patients and on the Biograph Vision PET/CT in the remaining 16 patients. When blood pool activities were compared, no significant difference was found between Discovery PET/CT and Biograph Vision PET/CT acquisitions (1.03 [0.87-1.18] g/mL vs. 1.11 [0.91-1.23] g/mL respectively, $p = 0.25$). Furthermore, when the mean TBR values were compared, there was no difference between patients who had Discovery PET and patients who had Biograph Vision PET (1.77 [1.56-2.10] vs. 1.89 [1.81-2.03] respectively, $p = 0.37$).

The highest TBRs were documented in the descending and abdominal aorta (1.97 [1.72-2.33] and 2.09 [1.69-2.57], respectively) whereas the lowest TBRs were seen in the

ascending aorta and common carotid arteries (1.67 [1.39-2.05] and 1.57 [1.31-1.78], respectively). Among the fifty tubular arterial segments with the highest TBR measurements, 13 (26%) highest ^{68}Ga-

Table 1 Patient characteristics

Characteristics	Data
Patients (n)	44
Sex (n)	
Men	24 (55%)
Women	20 (45%)
Age (y)	60 [53–66]
Body mass index (kg/m^2)	28 ± 4
Previous clinically documented ASCVD*	
Coronary revascularization†	6 (14%)
Myocardial infarction	5 (11%)
Stroke and transient ischemic attack	2 (5%)
Peripheral arterial disease	2 (5%)
Statin therapy (n)	8 (18%)
Acetylsalicylic acid treatment	10 (23%)
Systemic inflammatory disease	
Rheumatoid arthritis	1 (2%)
Ulcerous-hemorrhagic recto-colitis	1 (2%)
Cardiovascular risk factors (n)	
Arterial hypertension	13 (30%)
Hypercholesterolemia	12 (27%)
Smoking (current or former)	19 (43%)
Diabetes mellitus	4 (9%)
Type of disease (n)	
Head and neck tumors	10 (23%)
Melanoma	10 (23%)
Esophagus carcinoma	6 (14%)
Carotid endarterectomy	5 (11%)
Lung carcinoma	2 (5%)
B-cell lymphoma	2 (5%)
Ovarian cancer	2 (5%)
Pancreatic cancer	2 (5%)
Stomach cancer	2 (5%)
Leiomyosarcoma	1 (2%)
Breast cancer	1 (2%)
Glioma	1 (2%)

*ASCVD: atherosclerotic cardiovascular disease

† Percutaneous coronary intervention or coronary artery bypass graft surgery

NODAGA-RGD foci did correspond to CT calcification, and 37 (74%) foci did not correspond to CT calcification. Examples of foci of ^{68}Ga-NODAGA-RGD arterial uptake are shown in Figure 2. Calcified plaque scores were the highest in the abdominal aorta (2 [0-4]).

Table 2 Description of the last previous systemic anticancer therapy and the time interval between the last systemic anticancer therapy and the PET scan for each of the 14 concerned patients

Patient	Last previous systemic anticancer therapy	
	Type of therapy	Days before PET scan
1	Trastuzumab, cisplatine pertuzumab	127
2	Cyclophosphamide, oxaliplatine, adriamycin	288
3	Carbotaxol	100
4	Nab-paclitaxel	9
5	Cobimetinib, vemurafenib	28
6	Dabrafenib, trametinib	16
7	Cisplatin, vindesine	20
8	Nivolumab, ipilimumab	208
9	Nivolumab	131
10	Spartalizumab	321
11	Pembrolizumab	130
12	Nivolumab, ipilimumab	46
13	Encorafenib binimetinib	1
14	Pembrolizumab	378

Clinical baseline characteristics and plaque burden correlation

Prior cardiovascular or cerebrovascular event significantly correlated with ^{68}Ga-NODAGA-RGD mean TBR (r = 0.33, p = 0.027). ^{68}Ga-NODAGA-RGD mean TBR also showed a significant correlation with BMI (ρ = 0.38, p = 0.01), plaque burden (ρ = 0.31, p = 0.04; Figure 3), and hypercholesterolemia (r = 0.31, p = 0.04). There was no significant correlation between ^{68}Ga-NODAGA-RGD mean TBR and smoking, age, diabetes mellitus and arterial hypertension. Interestingly, ^{68}Ga-NODAGA-RGD mean TBR showed nevertheless a tendency for a higher uptake in diabetic patients (2.21 [1.83-2.68] in diabetic patients vs. 1.84 [1.54-2.02] in non-diabetic patients, p = 0.14; Figure 4).

Quantitative assessment across groups

Quantitative assessment is reported in Table 3. With blood-pool activities being comparable between both groups (0.98 [0.89-1.06] g/mL in the ASCVD group vs. 1.07 [0.89-1.27] g/mL in the control group, $p = 0.39$), mean TBR (Figure 3) and TBRaorta of ^{68}Ga-NODAGA-RGD were significantly higher in the ASCVD group as compared to the control group (respectively 2.44

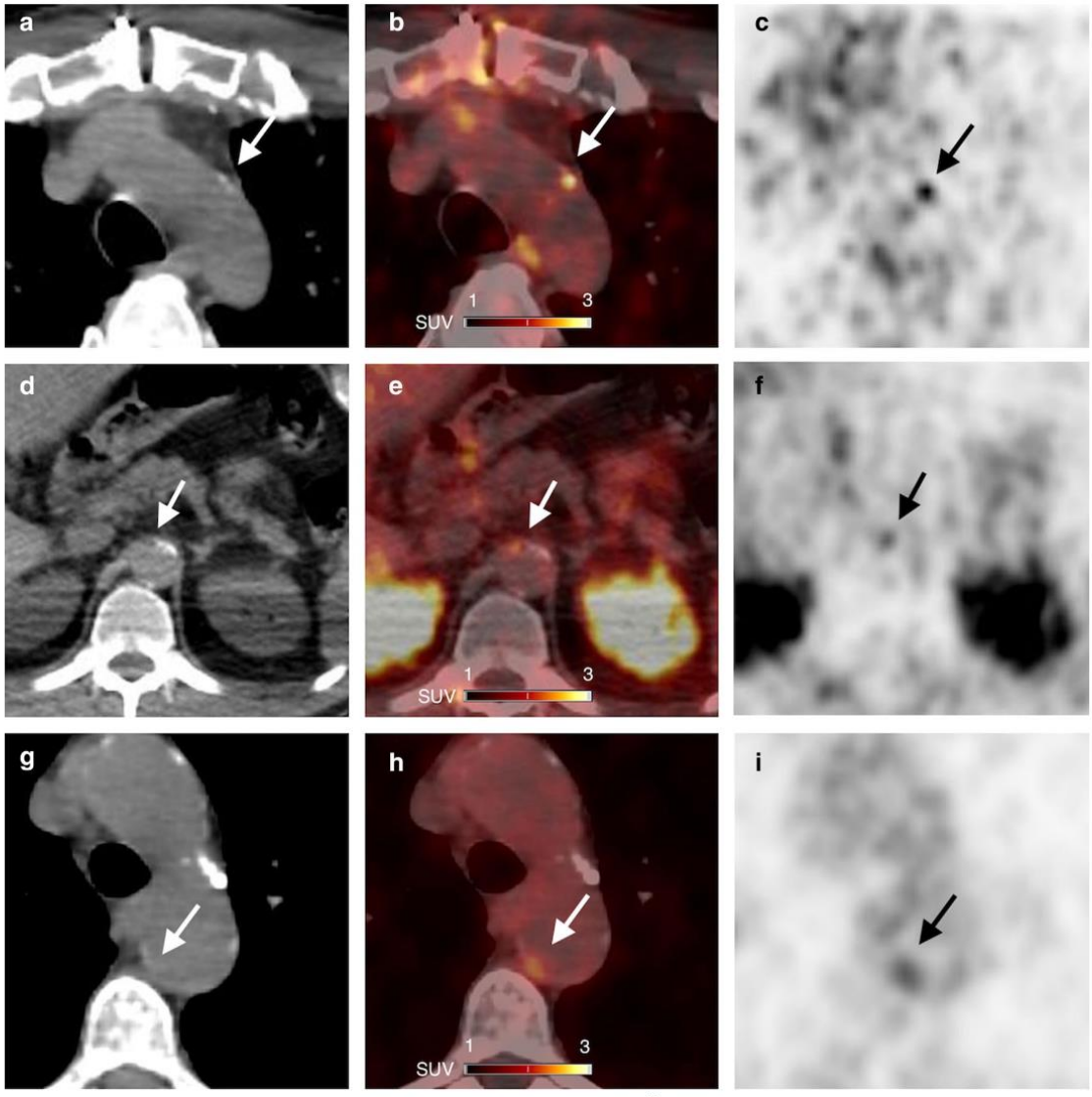

Fig. 2 CT (**A**, **D**, **G**), PET/CT (**B**, **E**, **H**) and PET images (**C**, **F**, **I**) in axial views show foci of ^{68}Ga-NODAGA-RGD arterial uptake in partly calcified atherosclerotic lesions (arrows): (**A**, **B**, **C**) in wall of arch aorta in a 62-year-old man who had a myocardial infarction 5 months before PET imaging; (**D**, **E**, **F**) in wall of abdominal aorta in a 54-year-old man who had a transient ischemic attack one week before PET imaging; (**G**, **H**, **I**) in wall of arch aorta in a 74-year-old woman who had a myocardial infarction 33 months before PET imaging

[2.03-2.55] vs. 1.81 [1.56-1.96], $p = 0.001$; and 2.51 [2.31-2.81] vs. 1.86 [1.62-2.04], $p = 0.001$). TBRcarotid and TBRiliac showed a tendency for a higher uptake in the ASCVD

group (respectively 1.69 [1.66-2.26] vs. 1.49 [1.27-1.77], $p = 0.08$; and 2.43 [1.68-2.93] vs. 1.92 [1.55-2.14], $p = 0.098$).

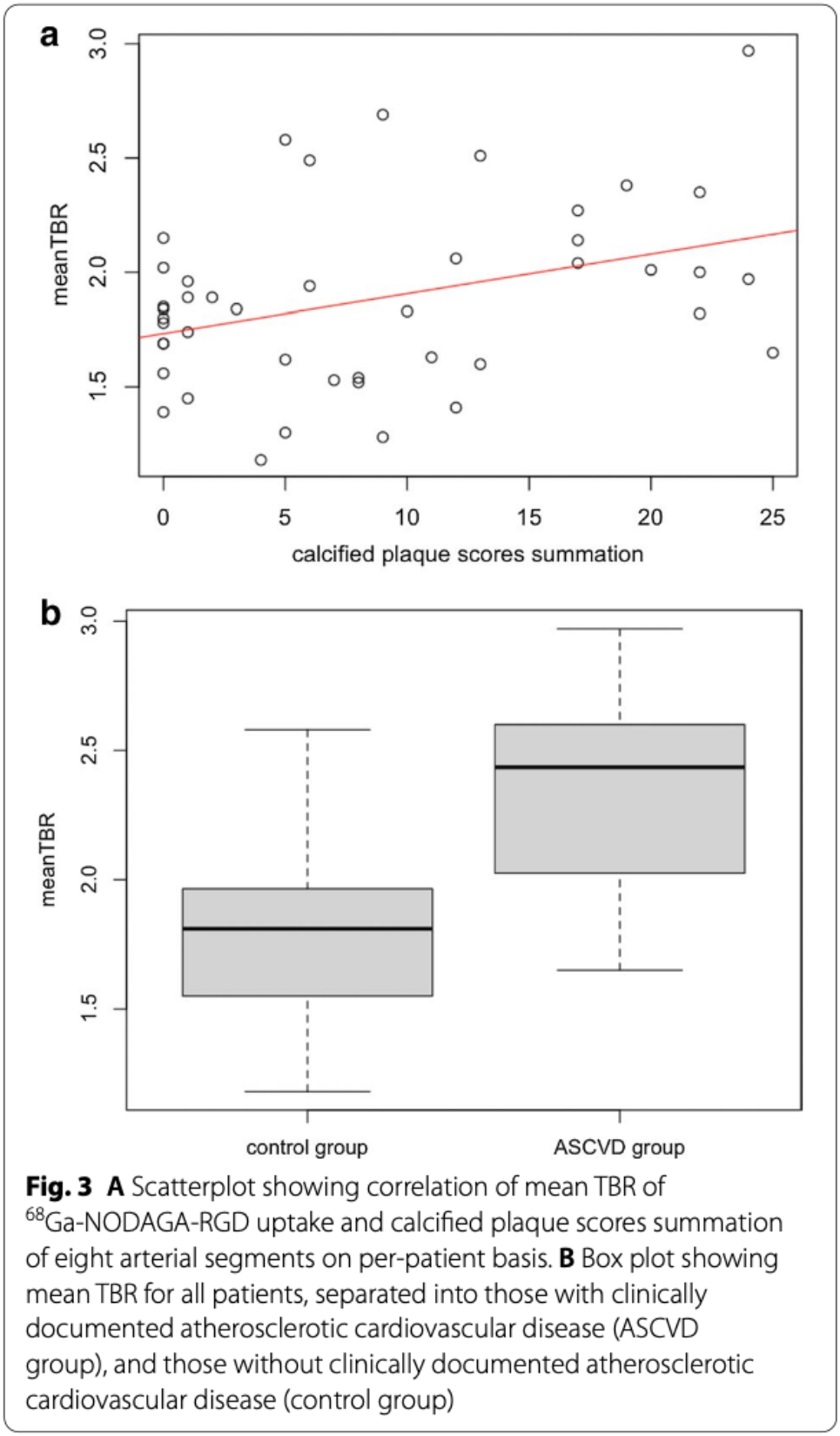

Fig. 3 **A** Scatterplot showing correlation of mean TBR of ^{68}Ga-NODAGA-RGD uptake and calcified plaque scores summation of eight arterial segments on per-patient basis. **B** Box plot showing mean TBR for all patients, separated into those with clinically documented atherosclerotic cardiovascular disease (ASCVD group), and those without clinically documented atherosclerotic cardiovascular disease (control group)

Discussion

Our main results are that ^{68}Ga-NODAGA-RGD arterial wall uptake was higher in patients with previous clinically documented ASCVD and correlated with prior cardiovascular or cerebrovascular event and with progressive atherosclerotic plaque burden. Our study would suggest that ^{68}Ga-NODAGA-RGD holds promise as a non-invasive marker of disease activity in atherosclerosis, providing information on key features of high-risk atheroma: inflammation and angiogenesis.

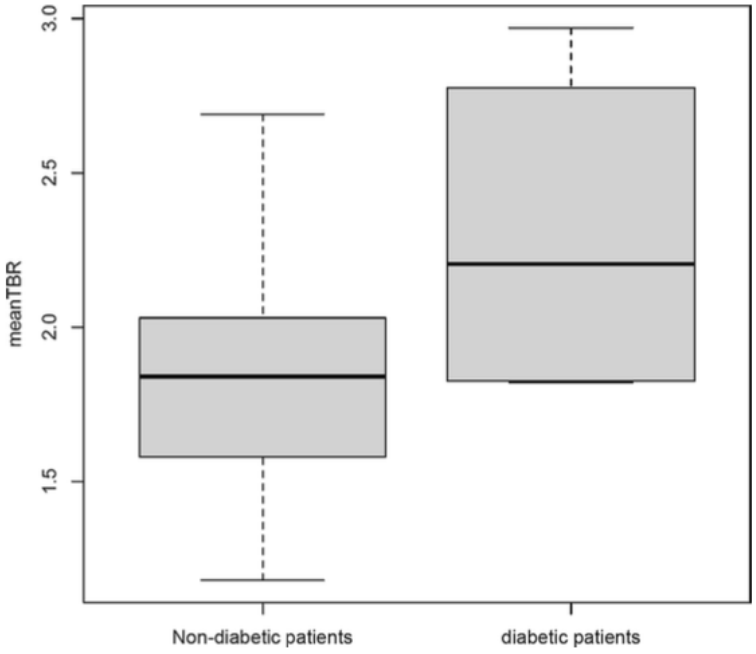

Fig. 4 Box plot showing mean TBR for all patients, separated into non-diabetic patients and diabetic patients

Table 3 Quantitative assessment per group

Characteristic Patients (*n*)	ASCVD[§] group 8	Control group 36	*p* Between groups
Mean TBR	2.44 [2.03–2.55]	1.81 [1.56–1.96]	0.001
TBR_{aorta}	2.51 [2.31–2.81]	1.86 [1.62–2.04]	0.001
$TBR_{carotid}$	1.69 [1.66–2.26]	1.49 [1.27–1.77]	0.08
TBR_{iliac}	2.43 [1.68–2.93]	1.92 [1.55–2.14]	0.098
Blood pool activity (g/mL)	0.98 [0.89–1.06]	1.07 [0.89–1.27]	0.39

[§] *ASCVD* atherosclerotic cardiovascular disease

Both inflammation and angiogenesis processes are associated with atheroma progression, plaque rupture and clinical events. The necrotic core in culprit plaques forms as result of increasing inflammation (20). In response to pro-atherogenic stimuli, activated monocytes infiltrated within the intima and differentiate into pro-inflammatory macrophages (21). While progressing, atherosclerotic plaques will develop a lipid-rich or necrotic core, resulting from the apoptosis of the resident pro-inflammatory macrophages (20). Pro-inflammatory macrophage activities within the atherosclerotic plaque lead to the weakening of the protective fibrous cap, mediated by the matrix metalloproteinases, that degrade the extracellular matrix components, predisposing it to rupture (22). Angiogenesis is believed to occur in response to hypoxic conditions within the necrotic core. Indeed, increasing wall thickness during atherosclerosis lead to a reduction of the intravascular oxygen amount, a situation further exacerbated by the increased oxygen consumption of high metabolic activated inflammatory cells within the atherosclerotic plaque (23). Vascular endothelial growth factor further modulates the activation state of the adventitial vasa vasorum endothelial cells to a highly migratory and proliferative state, resulting in neovessels formation towards the base of the plaque (24). Neovessels, arising from the adventitial vasa vasorum, grow into the base of progressive atherosclerotic lesions and provide an alternative entry pathway for monocytes and immune cells. The plaque neovessels are fragile and leaky, giving rise to local extravasation of plasma proteins and erythrocytes (25). Plaque hemorrhage itself results in a pro-inflammatory response, plaque destabilization and clinical events (3-4).

The use of the PET technique to visualize inflammation in vivo in atherosclerosis in large arteries has been performed with success using tracers such as ^{18}F-FDG, DOTA-derived somatostatin analogs, or ^{68}Ga-Pentixafor (18, 26-28). A non-invasive imaging technique that can inform about the activity of two adverse pathological processes, namely inflammation and angiogenesis, might therefore be even more accurate in identifying patients with active high-risk atheroma and potentially predicting risk of rupture. Hence, over the past decade, pre-clinical studies using RGD-based tracers have shown interesting results. In vivo imaging with a small animal PET/CT demonstrated ^{18}F-galacto-RGD PET signal corresponding to the advanced calcified plaques of the aortic arch region of hypercholesterolemic mice (11). Another study on atherosclerotic mice showed accumulation of ^{68}Ga-DOTA-RGD into aortic plaques (9). The role of a single photon emission computed tomography ^{99m}Tc-RGD-based probe in detection of inflammation in

mouse models of carotid arteries remodeling has been demonstrated (8). More recently, Su et al. demonstrated a ^{18}F-labeled RGD preferentially binds to aortic plaque in an ApoE knock out mouse model of atherosclerosis, and Golestani et al. demonstrated a good correlation between ^{18}F-RGD-K5 uptake and intraplaque neovessels density in carotid endarterectomy specimens (7, 10).

The discussion about the assessment of the atherosclerotic inflammatory activity as a marker of plaque vulnerability relies among others on data showing that non-obstructive coronary artery disease is responsible for most acute coronary syndromes (29, 30). Moreover, some data from catheterization laboratories have shown a high proportion of significant stenosis (>70% reduction of the coronary lumen) of culprit lesions in patients presenting with ST-segment elevation myocardial infarction (31). In the same line, it has been demonstrated that acute coronary event resulting from obstructive coronary plaque with prior inducible ischemia have better outcome in comparison to acute coronary event from non-obstructive coronary plaque without prior inducible ischemia (32). The protective adaptative changes resulting from the myocardial preconditioning could explain these different outcomes depending on the severity of the artery lumen stenosis and the presence of inducible ischemia prior acute coronary event (33). Nevertheless, these observations further confirm that other criteria above the solely angiographic evaluation of the coronary plaque stenosis should be considered. For this purpose, ^{68}Ga-NODAGA-RGD PET/CT may aid our pathophysiological understanding of this important condition and help to identify patients at increased risk of adverse cardiovascular events.

Even if some previous literature reported on the role of RGD-based tracers in the imaging of atherosclerosis in humans, it needs to be further established. Thus far, only two recent studies have evaluated the imaging of atherosclerotic lesions with RGD-based PET agents in humans. Beer et al. documented the expression of αvβ3 integrin in macrophage infiltrates of plaque specimens obtained from a small sample of patients with high-grade carotid artery stenosis (12). Jenkins et al. have demonstrated that in vivo expression of αvβ3 integrin with ^{18}F-fluciclatide PET/CT in human aortic atheroma is associated with plaque burden and is increased in patients with recent myocardial infarction (13). Our results are consistent with the promising results of these existing findings.

Regarding the colocalization of arterial uptake foci and calcification sites, the findings of this study add novel observations about RGD uptake in atherosclerotic lesions. In the

present study, around 26% of ^{68}Ga-NODAGA-RGD highest uptake foci were colocalized to calcification. Our study suggests that ^{68}Ga-NODAGA-RGD accumulation particularly occurs mainly in the noncalcified vessel wall, which may indicate some association with pathophysiologic processes found in early atherosclerotic disease, whereas calcification is seen in more advanced lesions (20, 24).

When analyzing the intensity of ^{68}Ga-NODAGA-RGD uptake in arterial segments, the measured TBRs were comparable with those for other established tracers used for plaque imaging. In the present study, the median intensity of tracer uptake as determined by TBR was 1.84 [1.62-2.04]. In a study using ^{18}F-sodium fluoride for visualization of microcalcification in plaque, mean TBR was 2.3 ± 0.7 (34). In another study using ^{68}Ga-Pentixafor, mean TBR was 2.0 ± 0.5 (27). In a study on vascular FDG uptake, mean TBR in the abdominal aorta was 1.57 ± 0.35 (18).

Holding promise as a marker of disease activity, targeting the integrin αvβ3 pathway could also represent an attractive therapeutic strategy in atherosclerosis. Humanised monoclonal antibodies against integrin αvβ3 (etaracizumab) have been developed (35). And researchers develop attractive therapeutic strategies conjugating RGD to delivery systems (e.g., nanoparticles) to selectively deliver the chemotherapeutic agents to cells expressing integrin αvβ3 (36).

Limitations

Because integrins αvβ3 are expressed in neovessels in plaques but also in CD68-positive macrophages, we are unable to ascertain whether ^{68}Ga-NODAGA-RGD was binding preferentially to one or the other of these processes. However, non-selectivity between inflammation and angiogenesis is not necessarily a disadvantage. Both inflammation and angiogenesis are hallmark of unstable atheroma and to combine both processes could be of additional value. There was no histopathological correlation in our study to examine the relation between αvβ3 integrin expression by ^{68}Ga-NODAGA-RGD uptake and plaque composition. One other limiting factor is the relatively lower spatial resolution of PET systems compared with other imaging techniques. Further developments in hybrid imaging promise to enhance the scope of molecular imaging. Although the use of ^{68}Ga is widespread with ease of use and good availability of this radioisotope through a ^{68}Ge/^{68}Ga generator, the lower positron energy of ^{18}F compared to ^{68}Ga could potentially improve spatial resolution and reduce blurring effects. Given the difficulty in identifying the exact

borders of the coronary arteries on the non-contrast-enhanced and non-gated CT image scans, we did not evaluate the coronary arteries. The 2 different PET camera systems have resulted in different imaging quality, but no significative difference was found between mean TBR values of patients who had a Discovery PET and of patients who had a Biograph Vision PET. The impact of previous anticancer therapies on vascular inflammation cannot be excluded (although none of the last previous systemic anticancer therapies included antiangiogenic drugs, and only 6 patients (7%) had systemic anticancer therapy within 4 weeks before imaging). Furthermore, given the relatively limited number of patients studied using univariate analyses, with a heterogeneous sample, we cannot exclude confounding of our results by other confounding factors.

Conclusion

In conclusion, among consecutive patients who had been referred to our institution for a ^{68}Ga-NODAGA-RGD PET/CT, ^{68}Ga-NODAGA-RGD arterial uptake correlated with prior cardiovascular or cerebrovascular event and plaque burden and was increased in patients with previous clinically documented ASCVD. Although further study is required, our data suggest that RGD-based tracers hold promise as a non-invasive marker of disease activity in atherosclerosis, providing information on inflammation and angiogenesis, with clinical significance.

References

1. Dagenais GR, Leong DP, Rangarajan S, Lanas F, Lopez-Jaramillo P, Gupta R, et al. Variations in common diseases, hospital admissions, and deaths in middle-aged adults in 21 countries from five continents (PURE): a prospective cohort study. Lancet. 2020;395:785-94. https://doi.org/10.1016/S0140-6736(19)32007-0.
2. Libby P, Buring JE, Badimon L, Hansson GK, Deanfield J, Bittencourt MS, et al. Atherosclerosis. Nat Rev Dis Primers. 2019;5:56. https://doi: 10.1038/s41572-019-0106-z.
3. Virmani R, Kolodgie FD, Burke AP, Finn AV, Gold HK, Tulenko TN, et al. Atherosclerotic plaque progression and vulnerability to rupture: angiogenesis as a source of intraplaque hemorrhage. Arterioscler Thromb Vasc Biol. 2005;25:2054-61. https://doi.org/10.1161/01.ATV.0000178991.71605.18.
4. Moreno PR, Purushothaman KR, Fuster V, Echeverri D, Truszczynska H, Sharma SK, et al. Plaque neovascularization is increased in ruptured atherosclerotic lesions of human aorta: implications for plaque vulnerability. Circulation. 2004;110:2032-8. https://doi.org/10.1161/01.CIR.0000143233.87854.23.
5. Dweck MR, Aikawa E, Newby DE, Tarkin JM, Rudd JH, Narula J, et al. Noninvasive Molecular Imaging of Disease Activity in Atherosclerosis. Circ Res. 2016;119:330-40. https://doi.org/10.1161/CIRCRESAHA.116.307971.
6. Hoshiga M, Alpers CE, Smith LL, Giachelli CM, Schwartz SM. Alpha-v beta-3 integrin expression in normal and atherosclerotic artery. Circ Res. 1995 ;77:1129-35. https://doi.org/doi: 10.1161/01.res.77.6.1129.
7. Golestani R, Mirfeizi L, Zeebregts CJ, Westra J, de Haas HJ, Glaudemans AW. Feasibility of [18F]-RGD for ex vivo imaging of atherosclerosis in detection of αvβ3 integrin expression. J Nucl Cardiol. 2015;22:1179-86. https://doi.org/10.1007/s12350-014-0061-8.
8. Razavian M, Marfatia R, Mongue-Din H, Tavakoli S, Sinusas AJ, Zhang J, et al. Integrin-targeted imaging of inflammation in vascular remodeling. Arterioscler Thromb Vasc Biol. 2011;31:2820-6. https://doi.org/10.1161/ATVBAHA.111.231654.
9. Haukkala J, Laitinen I, Luoto P, Iveson P, Wilson I, Karlsen H, et al. 68Ga-DOTA-RGD peptide: biodistribution and binding into atherosclerotic plaques in mice. Eur J Nucl Med Mol Imaging. 2009;36:2058-67. https://doi.org/10.1007/s00259-009-1220-z.

10. Su H, Gorodny N, Gomez LF, Gangadharmath UB, Mu F, Chen G, et al. Atherosclerotic plaque uptake of a novel integrin tracer ^{18}F-Flotegatide in a mouse model of atherosclerosis. J Nucl Cardiol. 2014;2:553-62. https://doi.org/10.1007/s12350-014-9879-3.
11. Laitinen I, Saraste A, Weidl E, Poethko T, Weber AW, Nekolla SG, et al. Evaluation of alphavbeta3 integrin-targeted positron emission tomography tracer 18F-galacto-RGD for imaging of vascular inflammation in atherosclerotic mice. Circ Cardiovasc Imaging. 2009;2:331-8. https://doi.org/10.1161/CIRCIMAGING.108.846865.
12. Beer AJ, Pelisek J, Heider P, Saraste A, Reeps C, Metz S, et al. PET/CT imaging of integrin αvβ3 expression in human carotid atherosclerosis. JACC Cardiovasc Imaging. 2014;7:178-87. https://doi.org/10.1016/j.jcmg.2013.12.003.
13. Jenkins WS, Vesey AT, Stirrat C, Connell M, Lucatelli C, Neale A, et al. Cardiac $\alpha_v\beta_3$ integrin expression following acute myocardial infarction in humans. Heart. 2017;103:607-15. https://doi.org/10.1136/heartjnl-2016-310115.
14. Knetsch PA, Petrik M, Griessinger CM, Rangger C, Fani M, Kesenheimer C, et al. [68Ga]NODAGA-RGD for imaging αvβ3 integrin expression. Eur J Nucl Med Mol Imaging 2011;38:1303-12. https://doi.org/10.1007/s00259-011-1778-0.
15. Durante S, Dunet V, Gorostidi F, Mitsakis P, Schaefer N, Delage J, et al. Head and neck tumors angiogenesis imaging with ^{68}Ga-NODAGA-RGD in comparison to ^{18}F-FDG PET/CT: a pilot study. EJNMMI Res. 2020;10:47. https://doi.org/10.1186/s13550-020-00638-w.
16. Mach F, Baigent C, Catapano AL, Koskinas KC, Casula M, Badimon L, et al. ESC Scientific Document Group. 2019 ESC/EAS Guidelines for the management of dyslipidaemias: lipid modification to reduce cardiovascular risk. Eur Heart J. 2020;41:111-88.
17. Jaipersad AS, Shantsila E, Blann A, Lip GY. The effect of statin therapy withdrawal on monocyte subsets. Eur J Clin Invest. 2013;43:1307-13. https://doi.org/10.1111/eci.12183.
18. Rominger A, Saam T, Wolpers S, Cyran CC, Schmidt M, Foerster S, et al. 18F-FDG PET/CT identifies patients at risk for future vascular events in an otherwise asymptomatic cohort with neoplastic disease. J Nucl Med. 2009;50:1611-20. https://doi.org/10.2967/jnumed.109.065151.
19. de Weert TT, Ouhlous M, Meijering E, Zondervan PE, Hendriks JM, van Sambeek MR, et al. In vivo characterization and quantification of atherosclerotic carotid plaque

components with multidetector computed tomography and histopathological correlation. Arterioscler Thromb Vasc Biol. 2006;26:2366-72. https://doi.org/10.1161/01.ATV.0000240518.90124.57.

20. Bentzon JF, Otsuka F, Virmani R, Falk E. Mechanisms of plaque formation and rupture. Circ Res. 2014;114:1852-66. https://doi.org/10.1161/CIRCRESAHA.114.302721.
21. Clinton SK, Underwood R, Hayes L, Sherman ML, Kufe DW, Libby P, et al. Macrophage colony-stimulating factor gene expression in vascular cells and in experimental and human atherosclerosis. Am J Pathol. 1992;140:301–16
22. Galis ZS, Sukhova GK, Lark MW, Libby P. Increased expression of matrix metalloproteinases and matrix degrading activity in vulnerable regions of human atherosclerotic plaques. J Clin Invest. 1994;94:2493–2503. https://doi.org/10.1172/JCI117619.
23. Parathath S, Mick SL, Feig JE, Joaquin V, Grauer L, Habiel DM, et al. Hypoxia is present in murine atherosclerotic plaques and has multiple adverse effects on macrophage lipid metabolism. Circ Res 2011;109:1141–52. https://doi.org/10.1161/CIRCRESAHA.111.246363
24. Celletti FL, Waugh JM, Amabile PG, Brendolan A, Hilfiker PR, Dake MD . Vascular endothelial growth factor enhances atherosclerotic plaque progression. Nat Med 2001;7:425–29. https://doi.org/10.1038/86490.
25. Sluimer JC, Kolodgie FD, Bijnens AP, Maxfield K, Pacheco E, Kutys B, et al. Thin-walled microvessels in human coronary atherosclerotic plaques show incomplete endothelial junctions relevance of compromised structural integrity for intraplaque microvascular leakage. J Am Coll Cardiol. 2009;53:1517-27. https://doi.org/10.1016/j.jacc.2008.12.056.
26. Li X, Samnick S, Lapa C, Israel I, Buck AK, Kreissl MC, et al. 68Ga-DOTATATE PET/CT for the detection of inflammation of large arteries: correlation with18F-FDG, calcium burden and risk factors. EJNMMI Res. 2012;2:52. https://doi.org/10.1186/2191-219X-2-52.
27. Weiberg D, Thackeray JT, Daum G, Sohns JM, Kropf S, Wester HJ, et al. Clinical Molecular Imaging of Chemokine Receptor CXCR4 Expression in Atherosclerotic Plaque Using ^{68}Ga-Pentixafor PET: Correlation with Cardiovascular Risk Factors and Calcified Plaque Burden. J Nucl Med. 2018;59:266-72. https://doi.org/10.2967/jnumed.117.196485.

28. Malmberg C, Ripa RS, Johnbeck CB, Knigge U, Langer SW, Mortensen J, et al. 64Cu-DOTATATE for Noninvasive Assessment of Atherosclerosis in Large Arteries and Its Correlation with Risk Factors: Head-to-Head Comparison with 68Ga-DOTATOC in 60 Patients. J Nucl Med. 2015;56:1895-900. https://doi.org/10.2967/jnumed.115.161216.
29. Hoffmann U, Ferencik M, Udelson JE, Picard MH, Truong QA, Patel MR, et al. Prognostic Value of Noninvasive Cardiovascular Testing in Patients with Stable Chest Pain: Insights from the PROMISE Trial (Prospective Multicenter Imaging Study for Evaluation of Chest Pain). Circulation 2017;135:2320–32. https://doi.org/10.1161/CIRCULATIONAHA.116.024360.
30. Chang HJ, Lin FY, Lee SE, Andreini D, Bax J, Cademartiri F, et al. Coronary Atherosclerotic Precursors of Acute Coronary Syndromes. J Am Coll Cardiol 2018;71:2511–22. https://doi.org/10.1016/j.jacc.2018.02.079.
31. Manoharan G, Ntalianis A, Muller O, Hamilos M, Sarno G, Melikian N, et al. Severity of Coronary Arterial Stenoses Responsible for Acute Coronary Syndromes. Am J Cardiol 2009;103:1183–88. https://doi.org/10.1016/j.amjcard.2008.
32. Farb A, Burke AP, Tang AL, Liang TY, Mannan P, Smialek J, et al. Coronary plaque erosion without rupture into a lipid core: A frequent cause of coronary thrombosis in sudden coronary death. Circulation 1996;93:1354–63. https://doi.org/10.1161/01.cir.93.7.1354
33. Murry CE, Jennings RB, Reimer KA. Preconditioning with ischemia: A delay of lethal cell injury in ischemic myocardium. Circulation 1986;74:1124–36. https://doi.org/10.1161/01.cir.74.5.1124.
34. Derlin T, Tóth Z, Papp L, Wisotzki C, Apostolova I, Habermann CR, et al. Correlation of inflammation assessed by 18F-FDG PET, active mineral deposition assessed by 18F-fluoride PET, and vascular calcification in atherosclerotic plaque: a dual-tracer PET/CT study. J Nucl Med 2011;52:1020-7. https://doi.org/10.2967/jnumed.111.087452.
35. Hersey P, Sosman J, O'Day S, Richards J, Bedikian A, Gonzalez R, et al. Etaracizumab Melanoma Study Group. A randomized phase 2 study of etaracizumab, a monoclonal antibody against integrin alpha(v)beta(3), + or - dacarbazine in patients with stage IV metastatic melanoma. Cancer 2010 Mar 15;116:1526-34. https://doi.org/10.1002/cncr.24821.
36. Chen F, Ehlerding EB, Cai W. Theranostic nanoparticles. J Nucl Med 2014;55:1919-22. https://doi.org/10.2967/jnumed.114.146019.

Chapter 6

Cardiac Theranostics: A Possible Role of ^{177}Lu-DOTATATE Therapy in Coronary Atherosclerotic Plaque Inflammation

Med Nucl. 2022. 46(4), 201-203.

Dietz M, Boughdad S, Kamani CH, Prior JO, Schaefer N.

The theranostic approach represents a successful paradigm in oncology, in which the same molecule is used for diagnosis and subsequent therapy by changing only the associated isotope. Somatostatin receptor subtype-2 (SST_2) targeted peptide receptor radionuclide therapy (PRRT) with Lutetium-177 DOTA-0-Tyr3-Octreotate (^{177}Lu-DOTATATE) has shown considerable good results for the treatment of neuroendocrine tumors (NET) (1). PRRT allows for the delivery of radionuclides directly to cells which express high levels of SST_2, and SST_2 targeting positron emission tomography (PET) studies play an important role for NET staging and patient selection before PRRT. Activated macrophages are involved in the pathophysiology of atherosclerosis, and the SST_2 is also overexpressed on the surface of activated macrophages (2). It was recently demonstrated that ^{68}Ga-DOTATATE, an SST_2-PET ligand, could identify proinflammatory macrophages within coronary atherosclerotic plaques (3). We hypothesized that ^{177}Lu-DOTATATE therapy might reduce coronary artery inflammation, as quantified on SST_2-PET studies.

The study group consisted of 19 consecutive patients referred to our institution for PRRT with ^{177}Lu-DOTATATE, with baseline and follow-up SST_2-PET/CT scans available (n=38). The Ethics Committee Vaud (CER-VD) approved this retrospective study protocol (CER-VD 2018-01513).

The mean patients' age was 63±12 years [range 44–84], and 12/19 (63%) of the patients were women. Five patients had hypertension, four had dyslipidemia, four were former or current smokers, two had renal impairment, two had diabetes mellitus, one had peripheral arterial disease, and none had history of known coronary artery disease. One patient was taking statins. Eight patients were undergoing octreotide or lanreotide therapy. A single patient had systemic anticancer therapy within 6 weeks before imaging (sunitinib six days before the baseline SST_2-PET/CT scan).

All patients received 4 cycles of ^{177}Lu-DOTATATE with a mean cumulative activity of 26±5 GBq [range 16-30]. Standard images were acquired with 77±17 min [range 53-104] after intravenous injection of 143±34 MBq [range 77-202] ^{68}Ga-DOTATATE (n=21) or ^{68}Ga-DOTATOC (n=17). PET/CT scans were examined using the previously validated maximum target-to-background (TBR_{max}) quantification, blinded to the patient's clinical information (4). Three-dimensional spherical regions of interest were drawn around focal SST_2-PET ligand uptakes in the proximal and midportions of the three main coronary arteries on fused PET/CT slices to quantify the maximum standard uptake value (SUV_{max}). TBR_{max} values were calculated by dividing the coronary SUV_{max} by the blood pool activity measured in the center

of the right atrium (SUV_{max} of spherical volumes of interest at the level of the right coronary artery ostium: volume 3 cm^3). T-test and Fisher exact test were used.

SST_2-PET ligands exhibited low background myocardial binding, rendered all scans interpretable. At baseline, 5 focal coronary uptakes were distinguishable in 4 patients (21%), coinciding with CT macrocalcification in 2 sites. The presence of focal coronary uptakes on SST_2-PET/CT scans at baseline was associated with a higher Framingham risk score (11±7% vs. 23±10%; p = 0.015). When the presence of focal coronary uptakes at baseline was compared, there was no difference between patients who were under octreotide or lanreotide therapy (2 of 8 patients; 25%) and patients who were not under octreotide or lanreotide therapy (2 of 11 patients; 18%, p > 0.9). On follow-up SST_2-PET scans 116±47 days [range 83-263] after last cycles of therapy, we observed a significant reduction on a lesion-based analysis (TBR_{max}, 1.69±0.34 [range 1.29–2.03] vs. 0.82±0.18 [range 0.54–1.00], p = 0.023, Fig. 1). Importantly, no new focal high uptake was found.

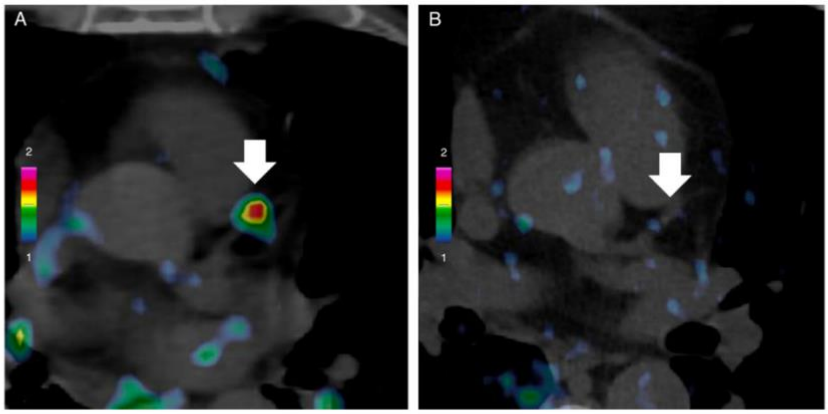

Fig. 1. (A) Initially focal SST_2-PET ligand uptake (TBR_{max} 2.0) in the left main coronary artery (white arrow). (B) It declined after 4 cycles of ^{177}Lu-DOTATATE (TBR_{max} 0.78) (white arrow).
(A) Captation focale du ligand SST_2 (TBR_{max} 2,0) au niveau de l'artère coronaire interventriculaire antérieure sur la TEP initiale (flèche blanche). (B) Cette captation diminua en intensité après 4 cycles de thérapie par ^{177}Lu-DOTATATE (TBR_{max} 0,78) (flèche blanche).

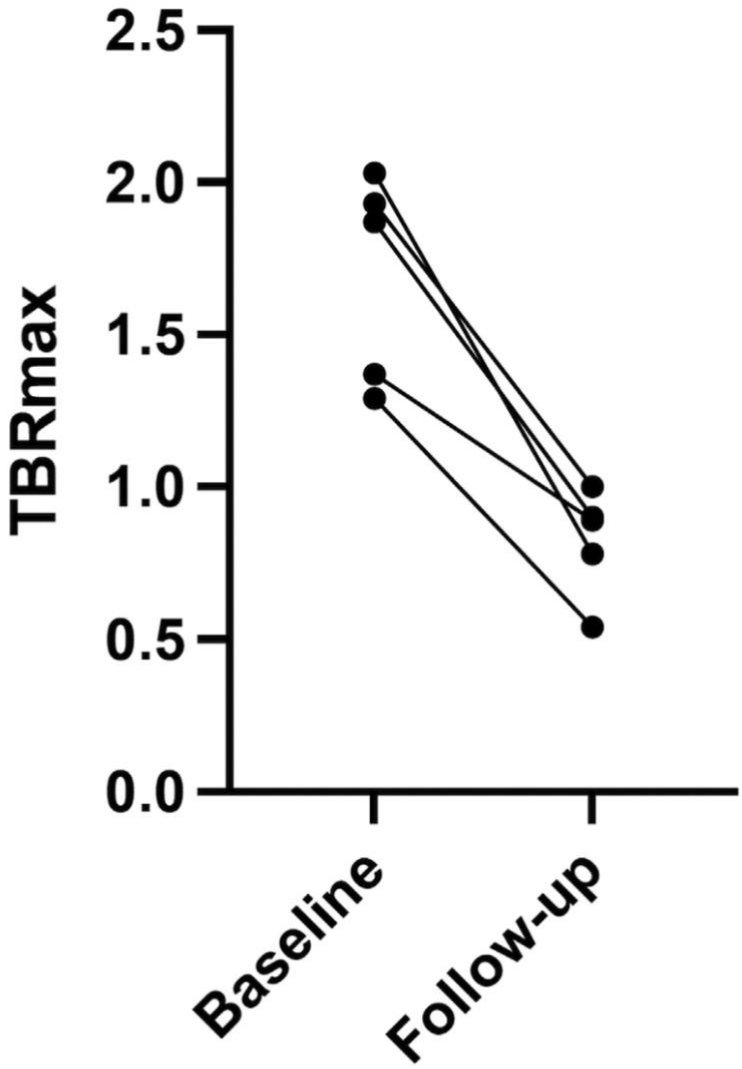

Fig. 2. Per-lesion temporal changes after PRRT in SST_2-PET ligand coronary uptake.
Changements après radiothérapie interne vectorisée de l'intensité des captations focales visualisées au niveau des artères coronaires sur les TEP aux ligands des récepteurs SST2.

This retrospective study was neither placebo-controlled or randomized, and this analysis was limited by the inclusion of only a small number of patients, with concomitant oncologic disease. Given that no ECG-gated coronary CT angiogram was performed, the present study did not allow an estimation of plaque morphology or characteristics. One of the responding patients was already taking long-term statin therapy.

Our observations are consistent with Shatka et al. who previously showed a PRRT-related reduction of DOTATATE uptake in large vessels (5) and with this report we aim to expand this paradigm for coronary arteries. Our dataset indicates that ^{177}Lu-DOTATATE therapy has the potential to reduce persistent coronary atherosclerotic plaque inflammation. This could be of importance, since such treatments at very low activities could be directly administered locally

Table 1
SST2-PET/CT scans per patient analysis.
Analyse des TEP/TDM aux ligands des récepteurs SST2 selon chaque patient.

Patient	Woman	Age	BMI	Framingham risk score	Octreotide or lanreotide therapy	Presence of focal coronary uptakes at baseline	Localization	Coinciding CT macrocalcification	Baseline TBR_{max}	Follow-up TBR_{max}
1	1	72	17	10.8	0	0				
2	0	48	22	6.8	1	0				
3	0	59	28	28.4	1	0				
4	0	76	25	30.0	0	1	RCA	1	1.29	0.54
5	1	55	44	8.4	0	0				
6	1	53	22	4.8	0	0				
7	0	69	21	29.2	1	1	LCx	1	1.87	0.9
8	1	75	22	14.1	1	0				
9	1	84	21	25.1	1	1	LM	0	1.37	0.89
10	1	44	34	4.2	0	0				
11	1	70	20	18.0	1	0				
12	1	50	32	2.7	1	0				
13	1	74	16	12.4	1	0				
14	1	71	21	11.5	0	0				
15	1	63	52	13.1	0	0				
16	0	69	20	19.6	0	0				
17	1	55	34	7.6	0	1	LAD/LCx	0/0	2.03/1.93	0.78/1.0
18	0	47	19	9.7	0	0				
19	0	55	21	9.9	0	0				

TBR_{max}: target-to-background; RCA: right coronary artery; LM: left main coronary artery; LCx: left circumflex coronary artery; LAD: left anterior descending artery.

in the coronary arteries reducing further the risk of systemic relevant radiation burden. Our hypothesis-generating analysis would require confirmation in a prospective trial.

References

1. Strosberg J, El-Haddad G, Wolin E, Hendifar A, Yao J, Chasen B, Mittra E, Kunz PL, Kulke MH, Jacene H, et al. Phase 3 trial of (177)Lu-Dotatate for midgut neuroendocrine tumors. *N Engl J Med*. 2017;376:125-135. doi: 10.1056/NEJMoa1607427.

2. Dalm VA, van Hagen PM, van Koetsveld PM, Achilefu S, Houtsmuller AB, Pols DH, van der Lely AJ, Lamberts SW, Hofland LJ. Expression of somatostatin, cortistatin, and somatostatin receptors in human monocytes, macrophages, and dendritic cells. *Am J Physiol Endocrinol Metab*. 2003;285:E344–53. doi: 10.1152/ajpendo.00048.2003.

3. Tarkin JM, Joshi FR, Evans NR, Chowdhury MM, Figg NL, Shah AV, Starks LT, Martin-Garrido A, Manavaki R, Yu E, et al. Detection of atherosclerotic inflammation by (68)Ga-DOTATATE PET compared to [(18)F]FDG PET imaging. *J Am Coll Cardiol*. 2017;69:1774–91. doi: 10.1016/j.jacc.2017.01.060.

4. Joshi NV, Vesey AT, Williams MC, Shah AS, Calvert PA, Craighead FH, Yeoh SE, Wallace W, Salter D, Fletcher AM, et al. 18F-fluoride positron emission tomography for identification of ruptured and high-risk coronary atherosclerotic plaques: a prospective clinical trial. *Lancet*. 2014;383:705–13. doi: 10.1016/S0140-6736(13)61754-7.

5. Schatka I, Wollenweber T, Haense C, Brunz F, Gratz KF, Bengel FM. Peptide receptor-targeted radionuclide therapy alters inflammation in atherosclerotic plaques. *J Am Coll Cardiol.* 2013;62:2344-5. doi: 10.1016/j.jacc.2013.08.1624.

PART IV

Investigating PET/CT scan for Myocardial Perfusion Imaging

Chapter 7

Comparison of the prognostic value of impaired stress myocardial blood flow, myocardial flow reserve, and myocardial flow capacity on low-dose Rubidium-82 SiPM PET/CT

J Nucl Cardiol. 2022 doi:10.1007/s12350-022-03155-6

Matthieu Dietz, Christel H. Kamani, Gilles Allenbach, Vladimir Rubimbura, Stephane Fournier, Vincent Dunet, Giorgio Treglia, Marie Nicod Lalonde, Niklaus Schaefer, Eric Eeckhout, Olivier Muller, and John O. Prior, PhD

Abstract

Background

The most reliable quantitative variable on Rubidium-82 (^{82}Rb) cardiac PET/CT for predicting major adverse cardiovascular events (MACE) has not been characterized with low-dose silicon photomultipliers (SiPM) technology, which allows halving injected activity and radiation dose delivering less than 1.0 mSv in a 70-kg individual.

Methods and Results

We prospectively enrolled 234 consecutive participants with suspected myocardial ischemia. Participants underwent ^{82}Rb cardiac SiPM PET/CT (5 MBq/kg) and were followed-up for MACE over 652 days (interquartile range: 559–751 days). For each participant, global stress myocardial blood flow (stress MBF), global myocardial flow reserve (MFR), and regional severely reduced myocardial flow capacity (MFC_{severe}) were measured. The Youden index was used to select optimal thresholds.

In multivariate analysis after adjustments for clinical risk factors, reduced global stress MBF <1.94ml/min/g, reduced global MFR <1.98, and regional MFC_{severe} >3.2% of left ventricle emerged all as independent predictors of MACE (HR 4.5, 3.1, and 3.67, respectively, p<0.001). However, only reduced global stress MBF remained an independent prognostic factor for MACE after adjusting for clinical risk factors and the combined use of global stress MBF, global MFR, and regional MFC_{severe} impairments (HR 2.81, p=0.027).

Conclusion

Using the latest SiPM PET technology with low-dose ^{82}Rb halving the standard activity to deliver <1 mSv for a 70-kg patient, impaired global stress MBF, global MFR, and regional MFC were powerful predictors of cardiovascular events, outperforming traditional cardiovascular risk factors. However, only reduced global stress MBF independently predicted MACE, being superior to global MFR and regional MFC impairments.

Introduction

Myocardial perfusion imaging is a powerful non-invasive functional tool for risk stratification, recommended by clinical practice guidelines (1-5). Compared with relative perfusion images, absolute quantification of myocardial blood flow (MBF) by positron emission tomography (PET) could improve risk stratification (6). Global and regional perfusion provide information on different aspects of myocardial perfusion. Impairment in global perfusion may be caused by either multivessel epicardial disease or microcirculatory dysfunction. Regional absolute perfusion measurements may enable the additive detection of small regional defects caused by epicardial coronary artery disease (CAD), which could not be detected with average global perfusion measurements (6).

The myocardial flow capacity (MFC) concept is a precise regional approach integrating both MFR and stress MBF through the pathophysiologic severity of CAD to depict regional quantitative flow metrics on a per pixel basis (6, 7). MFC may overcome some of the limitations of using stress MBF or MFR alone and represents a promising tool to improve clinical decision-making (7-9). However, despite a robust conceptual validation and recently promising clinical data especially after revascularization, further validations of the prognostic potential of MFC in comparison to stress MBF and MFR are still needed (8-10).

Silicon photomultipliers with digital readout (SiPM) PET represents a major advancement in PET technology. This new system including smaller crystals exhibits a much higher sensitivity and outperforms previous PET scanners using conventional photomultiplier tubes according to essential PET parameters such as spatial and timing resolution or noise-equivalent count-rate (11). Moreover, this novel technology allows for the reduction of the standard dose, with an improved image quality (12). Although research about the diagnostic accuracy of this dedicated SiPM PET system has been performed in a preliminary comparative study with a small sample size (13), no previous study has evaluated the prognostic value of PET myocardial perfusion imaging with SiPM.

The aim of this study was to prospectively compare on a low-dose SiPM PET camera, halving the activity and radiation dose of Rubidium-82 (^{82}Rb), the prognostic value for cardiovascular events of stress MBF, MFR, and MFC.

Methods

Study Population

We prospectively enrolled participants with clinical suspicion of myocardial ischemia (at the discretion of the referring clinician) to undergo 82Rb cardiac SiPM PET/Computed

Tomography (CT) between June 2018 and June 2019 at the Lausanne University Hospital. Participants' cardiovascular risk factors and medication use were ascertained at time of PET imaging. A history of CAD ("known CAD") was defined as evidence of myocardial infarction (MI), previous percutaneous coronary intervention (PCI) or coronary artery bypass graft (CABG), or angiographically significant coronary stenosis (>50% of the left main coronary artery or >70% stenosis in any epicardial coronary artery). All procedures performed in this study were in accordance with the 1964 Helsinki declaration and its last amendments or comparable ethical standards. The Local Ethics Committee approved this study protocol (#PB_2017-00634), and all participants gave written informed consent prior to inclusion.

Imaging protocol with SiPM ^{82}Rb PET/CT

For each participant, a rest and adenosine or regadenoson stress SiPM PET/CT scan was performed, using a single dedicated camera (Biograph Vision 600, Siemens Medical Solutions, Knoxville, USA). Participants were instructed to fast for 6 h and avoid caffeine-containing food or beverages 24 h prior to the test. At rest, a 15–25 s intravenous (i.v.) infusion of low-dose (5 MBq/kg) ^{82}Rb (Ruby-Fill® generator and ^{82}Rb elution system [v3], Jubilant DraxImage, Kirkland, QC, Canada) was administered with an automatic infusion system and three-dimensional (3D) dynamic PET images were acquired starting at the beginning of the infusion over 6 min 19 s (12 × 8, 5 × 12, 1 × 30, 1 × 60, and 1 × 120 s). A second acquisition was then started following the same protocol with similar activity 2 min after the beginning of an adenosine infusion (140 mg/kg/min over 6 min) or following a regadenoson administration (400 µg over 10 s). A low-dose CT (100 keV, 16 mAs) transmission scan was used for attenuation correction. Images were reconstructed by ordered subsets expectation maximization algorithms (4 iterations, 5 subsets, 4.0 mm Full Width at Half Maximum (FWHM) gaussian post-filter, 220 × 220-pixel matrix size). Blood pressure, heart rate, and a 12-lead ECG were recorded throughout the procedure. The radiation dose for a 70 kg participant was estimated to be 2 × 0.39 mSv for rest and stress ^{82}Rb, and 1 × 0.17 mSv for the low-dose attenuation correction CT plus CT scout, resulting in a total dose of 0.95 mSv.

Usual quantitative myocardial perfusion analysis

Perfusion was assessed quantitatively measuring MBF in milliliter per minute per gram at rest and stress, using the highly automated FlowQuant v2.7 software (Ottawa, Ontario, Canada), with a 1-tissue compartment model with a flow-dependent extraction correction (14). MFR was calculated as followed: MFR = stress MBF/rest MBF. Rate-pressure product adjusted rest MBF

and MFR were determined to account for high resting heart rate or systolic blood pressure by multiplying rest MBF by 8500 mmHg/min and dividing by rate-pressure product (resting heart rate multiplied by resting systolic blood pressure). To reduce the potential spillover in image-derived blood activity curves, a dual spill-over correction was systematically applied (15). Global partial-volume recovery correction and motion correction were also systematically applied (16).

Myocardial flow capacity

MFC, developed by Johnson and Gould using ^{82}Rb PET imaging, is a metric that integrates per pixel combination of resting MBF, stress MBF and MFR into pathophysiologic severity categories by an integrated color map (7-9). MFC pixels (n=513 on the polar map) having both MFR ≤ 1.5 and stress MBF ≤ 1.1 mL/min/g were defined as severely reduced MFC (MFC_{severe}) and were quantified as percent of left ventricle (LV). Because regional MFC_{severe} was the MFC category previously associated with the higher risk among all MFC category, only regional MFC_{severe} was included for MFC in this prognostic study (8, 9).

Clinical follow-up

The endpoint of the study was major adverse cardiovascular event (MACE), defined as cardiac death, MI, delayed revascularization (> 6 months post-PET/CT), hospitalization for congestive heart failure or de novo stable angina. Early revascularizations observed within the first 6 months post-PET/CT were considered to have been triggered by the myocardial perfusion study and were excluded. Death from cardiac cause was defined as death from MI, congestive heart failure, valvular heart disease, sudden death, death without a witness or of unknown cause, and cardiac interventional/surgical procedure related. Hospitalization for de novo stable angina was defined as angina or chest pain of cardiac origin and requiring further investigations and hospitalization. Outcome information was obtained from medical records available in the hospital information system. If unsuccessful, participant follow-up was obtained by a phone call to cardiologists or general practitioners and/or participants. In participants with multiple MACE, only the first one was considered for survival analysis. Outcome data were collected from January to February 2021.

Statistics

We assessed the distribution of data with the Shapiro-Wilk test. Continuous normally distributed variables were presented as mean ± SD and compared using Student's t-tests.

Continuous non-normally distributed variables were presented as median [interquartile range] and compared using the Mann-Whitney U test. The chi-square test or Fisher exact test was used for analysis of categorical variables.

The Youden index was used to select optimal thresholds based on receiver operating characteristic curves for stress MFR, MFR, and MFC_{severe} measurements. Kaplan-Meier curves were used to elucidate the survival distributions regarding MACE. Differences in the outcomes of participants were assessed using the log-rank test. A Cox proportional hazard regression with adjustment for potential confounders was performed to determine the predictors of worse outcome. To prevent overfitting of the multivariate Cox proportional hazards models, only cardiovascular risk factors with p values < 0.05 in univariate Cox proportional regression models were considered in the multivariate models.

Collinearity between global stress MBF, global MFR and regional MFC_{severe} was assessed by calculating the variance inflation factors in the final model (lower than five for each variable) (17).

The statistical analysis was performed using R version 4.1.1 (R Foundation for Statistical Computing, Vienna, Austria). All p values used were two-sided, with $p < 0.05$ considered statistically significant.

Results

Participant's characteristics

The flowchart of the study is shown in Figure 1. From June 2018 to June 2019, low-dose ^{82}Rb SiPM PET/CT was performed in 279 participants. Two studies were excluded because of technical issues (delayed imaging after infusion start). Follow-up was successful in 274 of 277 remaining participants (99%). 40 participants were censored due to early revascularization (5 CABG surgery and 35 PCI, < 6 months after PET/CT). Baseline characteristics of the remaining study population of 234 participants are given in Table 1. Participants had a high prevalence of known CAD (54%), with a high burden of cardiovascular risk factors (hypertension: 73%; current or former tobacco use: 45%; dyslipidemia: 68%; diabetes: 36%). Preventive therapies were highly prescribed in the overall population: 58% with aspirin, 62% with beta-blockers, 58% with angiotensin-converting enzyme inhibitors/angiotensin receptor blockers, and 66% with lipid-lowering agents.

Clinical outcomes

Over the 652 days [IQR: 559 to 751 days] of follow-up, a total of 47 participants experienced a MACE event (13 nonfatal MI, 5 cardiac deaths (1 participant had MI and then cardiac death), 10 cases of delayed revascularization, 19 hospitalizations for congestive heart failure or de novo stable angina).

Comparative analysis

Participants with MACE had significantly worse global stress MBF, global MFR, and regional MFC_{severe} when compared with participants without (Table 2). In contrast, global rest MBF were similar among both groups. There was a significantly higher prevalence of known CAD or history of MI in participants with MACE as compared to participants without MACE (Table 1).

Optimal prognostic thresholds

Using the Youden index, we calculated the maximum potential effectiveness of global stress MBF, global MFR, and regional MFC_{severe} cutoffs for MACE prediction. For global absolute myocardial perfusion measurements, a threshold of 1.94 mL/min/g for global stress MBF achieved a specificity and sensitivity of 59% and 83%, a threshold of 1.98 for global MFR achieved a specificity and sensitivity of 73% and 64%, and a threshold of 3.2% of LV for regional MFC_{severe} achieved a specificity and sensitivity of 74% and 64%. Based on these calculated optimal thresholds, global MFR as well as regional MFC_{severe} were impaired in 78 (33%) participants, whereas global stress MBF was impaired in 113 (48%) participants (Table 2).

Univariate and multivariate analysis

The Kaplan-Meier survival curves indicated that participants with impaired global stress MBF, global MFR, or regional MFC_{severe} had significantly higher rates of MACE (all $p < 0.0001$) as compared with those with normal perfusion (Figure 2). On univariate Cox proportional regression, global stress MBF, global MFR, and regional MFC_{severe} emerged all as significant predictors of MACE (Table 3). Male sex, as well as known history of CAD and history of MI were also found to be significantly predictive of MACE (Table 3).

In multivariate analysis with 3 separate models including each time clinical risk factors and separately global stress MBF, global MFR, and regional MFC_{severe}, each one of these PET variables emerged as powerful independent predictors of MACE (Table 4). In contrast, clinical variables such as male sex, known CAD, and history of MI did not (Table 4).

Moreover, for the most comprehensive model including clinical parameters and all global MFR, global stress MBF and regional MFC_{severe}, only global stress MBF emerged as an independent prognostic factor for MACE (Hazard Ratio (HR) 2.81, $p = 0.027$), while global MFR and regional MFC_{severe} did not (Table 4).

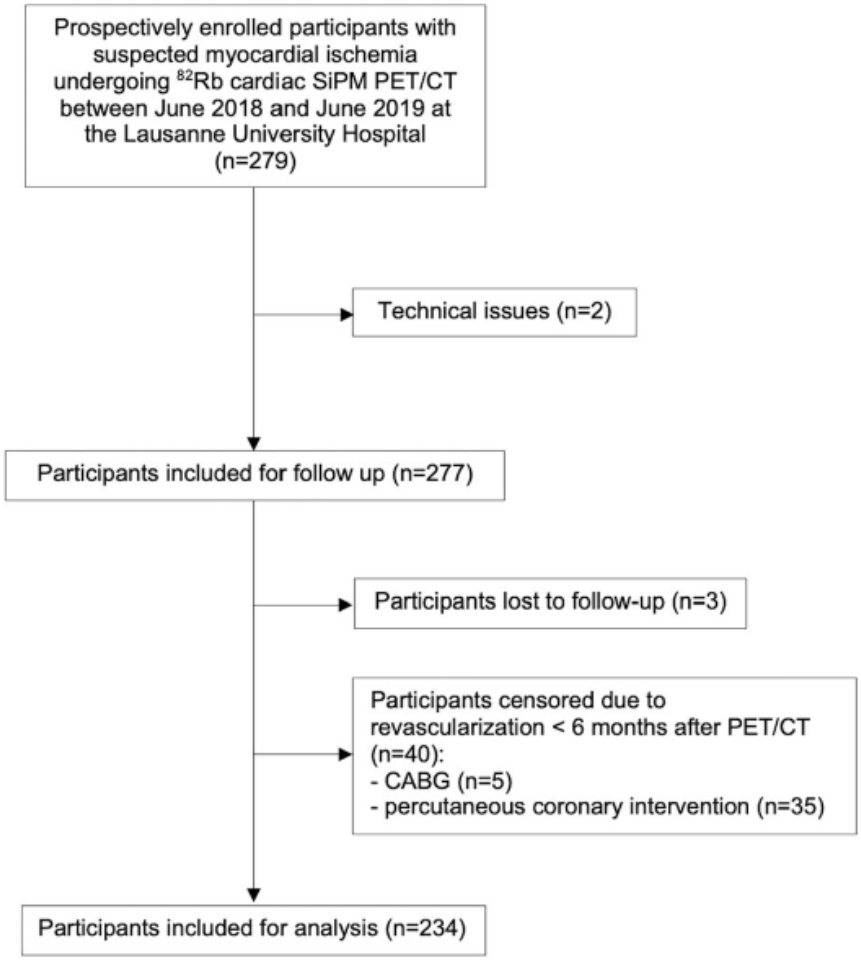

Figure 1. Study flowchart. CABG - coronary artery bypass graft; CT - computed tomography; PET - positron emission tomography; ^{82}Rb - rubidium-82; SiPM - silicon photomultipliers with digital readout.

Discussion

Our results support that impaired global stress MBF, global MFR, and regional MFC_{severe}, as assessed by using low-dose ^{82}Rb with the latest PET SiPM technology, allowing halving of the standard injected activity and radiation dose, are powerful predictors of cardiovascular events, outperforming traditional cardiovascular risk factors such as the presence of known CAD or

history of MI. In a comprehensive analysis, we found that only reduced global stress MBF independently predicted MACE.

PET myocardial perfusion imaging is well established for the diagnostic and prognostic evaluation of patients with suspected CAD. Novel PET cameras using SiPM detectors offer a considerable advantage in radiation dose compared with the conventional PET cameras. For a

Table 1. Baseline clinical characteristics

	Overall population (n = 234)	MACE (n = 47)	No MACE (n = 187)	p-value
Age, years, median [IQR]	72 [61-78]	73 [68-79]	71 [60-77.5]	0.105
Male sex, n (%)	153 (65%)	36 (77%)	117 (63%)	0.081
Body mass index, kg/m^2, median [IQR]	31 [28-36]	32 [28.5-35.5]	31 [28-36]	0.78
Cardiovascular risk factors, n (%)				
Hypertension	171 (73%)	38 (81%)	133 (71%)	0.18
Current or former smoker	106 (45%)	26 (55%)	80 (43%)	0.12
Dyslipidemia	159 (68%)	34 (72%)	125 (67%)	0.47
Diabetes	85 (36%)	20 (43%)	65 (35%)	0.32
Insulin-requiring diabetes	35 (15%)	10 (21%)	25 (13%)	0.14
Known CAD	126 (54%)	34 (72%)	92 (49%)	**0.004**
History of MI	100 (43%)	28 (60%)	72 (39%)	**0.01**
Medications, n (%)				
Aspirin	135 (58%)	28 (60%)	107 (57%)	0.35
Beta-blockers	144 (62%)	33 (70%)	111 (59%)	0.15
ACE inhibitors/ARB	135 (58%)	32 (68%)	103 (55%)	0.15
Diuretics	82 (35%)	27 (57%)	55 (29%)	**0.0002**
Nitroglycerine therapy (short-acting or long-acting nitrates)	24 (10%)	6 (13%)	18 (10%)	0.61
Lipid-lowering agent	154 (66%)	32 (68%)	122 (65%)	0.71

ACE, angiotensin-converting enzyme; *ARB*, angiotensin receptor blocker; *CAD*, coronary artery disease; *MI*, myocardial infarction

70-kg patient, the effective radiation dose could be reduced from >4-mSv with the conventional PET cameras to <1-mSv (18). However, no previous clinical study has evaluated the prognostic value of PET myocardial perfusion imaging with SiPM.

The independent prognostic value of reduced global stress MBF, being superior to global MFR and regional MFC_{severe} impairments, was unexpected and is discrepant as compared to previous studies. Regarding the prediction of cardiovascular deaths, Gupta et al. investigated the importance of global stress MBF and MFR (10). In this study, in multivariate analysis, the authors reported that the cardiovascular mortality was independently driven by global MFR, irrespective of whether the global stress MBF was impaired or preserved. Similar findings had been reported in the retrospective study by Fukushima et al. (19) with a similar sample size as compared to the current study (n = 224 vs. n = 234 in the current study). However, compared with Fukushima et al. (19) study, the current study has a longer follow-up (median, 652 vs. 426

days), and population as well as medication use depicted some difference (male sex, 65% vs. 40%; prior history of MI, 43% vs. 11%; beta-blockers, 62% vs. 18%). Taqueti et al. demonstrated that the prognostic value of MFR for the occurrence of MACE was independent of the extent and severity of coronary lesions as evaluated on coronary angiography, but stress MBF was not included in multivariate analysis (20). In an observational study by Patel et al., a threshold of 1.8 for global MFR has been identified to yield a benefit of coronary revascularization over medical treatment, independently of means of revascularization or the extent of myocardial ischemia on semi-quantitative analysis, but, again, stress MBF was not studied (21).

Similar to the current cohort, other studies reported that global stress MBF was independently predictive for events, whereas global MFR was not. Global stress MBF was shown to be superior to global MFR for the prediction of MACE in a ^{82}Rb PET/CT study by Farhad et al. (18), and for the prediction of a composite of death and MI in a recent [^{15}O]H_2O PET/CT study by Bom et al. (22). Since MFR is inherently dependent on resting flow, which is known to be highly sensitive to hemodynamic conditions, impairment of MFR may be less specific for the occurrence of events. However, importantly, both the study by Bom et al. and the current cohort used adjusted MFR for the resting rate-pressure-product, accounting at least partially for changes in resting flow caused by differences in hemodynamic conditions. The present finding of a superiority of global stress MBF vs. global MFR impairments is consistent with the lack of association between resting MBF and clinical prognosis (23).

Studies evaluating the prognostic value of MFC in comparison to stress MBF and MFR are scarce. Gould et al. showed in two recent observational studies with large cohorts over long-term follow-up that the extent of severe regional impairment of MFC, expressed as percent of LV as in the current cohort, provides optimal risk stratification and is associated with a survival benefit gain after revascularization (8, 9). This risk stratification after revascularization was better assessed by severe regional MFC alteration rather than global MBF alteration (9). Recent studies using modified MFC with average MFR and stress MBF per coronary territory have shown an association with cardiovascular death and MACE (24, 25).

Considering other regional quantitative measures, our results are consistent with Bom et al. who found in a [^{15}O]H_2O PET/CT study that both global and regional stress MBF have prognostic value in predicting cardiac events, while the combination of global and regional stress MBF did not improve the prognostic performance compared to either alone (22). Harjulahti et al. found similar results using also [^{15}O]H_2O PET/CT (4). In contrast, Von Felten et al. recently demonstrated using ^{13}N-ammonia, an independent prognostic value of regional MFR < 2, being

superior to global stress MBF and MFR (26). In the current study, the first using the latest SiPM technology, whose characteristics might offer potential benefits for precise analysis, we found that severe regional per pixel MFC impairment is a powerful predictor of cardiovascular events, independent from traditional cardiovascular risk factors, but not from global perfusion parameters. Although the current study has inherent limitations which could limit the scope of the results, these data support a close relationship between global and regional perfusion (22).

Limitations

This study must be interpreted in the context of its single-center design, with an average sample size despite a high completeness of follow-up, which still limits extensive subgroup analysis. The follow-up period was middle range, with a low incidence of hard cardiac events such as cardiac death. The present thresholds for the MFC_{severe} category (pixel having both MFR $\leq$ 1.5 and stress MBF $\leq$ 1.1 mL/min/g) were slightly different as compared to the thresholds used by Johnson and Gould (pixel having both MFR $\leq$ 1.27 and stress MBF $\leq$ 0.83 mL/min/g). However, significant contributions of these slight differences to the present results seem unlikely. Furthermore, currently available SiPM cameras differ significantly in design, and it cannot be excluded that different SiPM cameras have different prognostic ability. The current study emphasized on myocardial blood flow measurements, and LV ejection fraction, LV volumes, regional wall motion, coronary artery calcium score and semi-quantitative evaluation of relative perfusion defects were not assessed in this study based on myocardial blood flow quantification, despite representing important information that could be part of routine PET/CT imaging. Finally, the current prognostic study did not assess diagnostic accuracy, which could be a strength of the quantification of regional perfusion with MFC.

New Knowledge Gained

This study shows the prognostic value of impaired stress MBF, MFR and MFC for cardiovascular event using low-dose ^{82}Rb SiPM PET/CT technology with halved injected activity delivering <1.0-mSv radiation dose for a 70-kg patient.

Table 2. Myocardial perfusion imaging results

	Overall population (n = 234)	MACE (n = 47)	No MACE (n = 187)	p-value
PET pharmacological stress agent, n (%)				
Adenosine	204 (87%)	40 (85%)	164 (88%)	0.56
Hemodynamics during PET/CT, median [IQR]				
Rest-HR, bpm	70 [61-78]	71 [61-81.5]	69 [61-75.5]	0.12
Stress-HR, bpm	83 [74-95]	82 [75-99]	85 [74-94.5]	0.72
Rest-SBP, mmHg	136 ± 23	134 ± 24	136 ± 22	0.6
Stress-SBP, mmHg	120 [104-137]	118 [101-131]	120 [107.5-138]	0.07
Rest-DBP, mmHg	71 ± 12	69 ± 11	71 ± 12.5	0.3
Stress-DBP, mmHg	61 [54-70]	60 [52-63.5]	62 [55-71]	0.11
Rest-RPP > 8500 mmHg/min, n (%)	153 (65%)	29 (62%)	124 (66%)	0.60
^{82}Rb quantitative imaging,				
Global rest MBF, mL/min/g, median [IQR]	0.82 [0.65-1.06]	0.72 [0.51-0.925]	0.75 [0.59-0.97]	0.34
Global stress MBF, mL/min/g, median [IQR]	1.96 [1.32-2.71]	1.5 [1.08-1.87]	2.16 [1.54-2.88]	**< 0.0001**
Global stress MBF < 1.94 mL/min/g, n (%)	113 (48%)	37 (79%)	76 (41%)	**< 0.0001**
Global MFR, median [IQR]	2.39 [1.72-3.0]	1.75 [1.395-2.47]	2.49 [1.93-3.1]	**< 0.0001**
Global MFR < 1.98, n (%)	78 (33%)	29 (62%)	49 (26%)	**< 0.0001**
MFC_{severe}, % of LV, median [IQR]	0 [0-9.5]	9.3 [0-30.7]	0 [0-3.7]	**< 0.0001**
MFC_{severe} > 3.2% of LV, n (%)	78 (33%)	30 (64%)	48 (26%)	**< 0.0001**

DBP, diastolic blood pressure; *HR*, heart rate, *LV*, left ventricle; *MBF*, myocardial blood flow; *MFC*, myocardial flow capacity; *MFR*, myocardial flow reserve; *RPP*, rate-pressure product (HR × SBP); *SBP*, systolic blood pressure

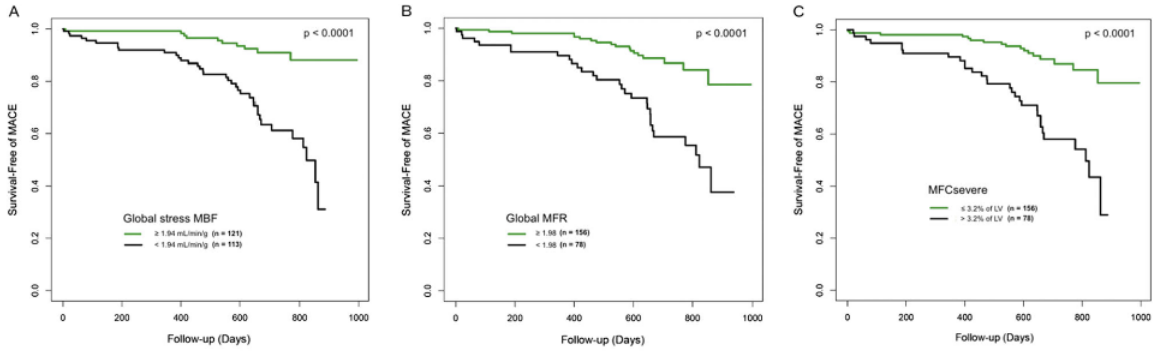

Figure 2. MACE-free survival curves (n = 234) according to global stress MBF (**A**), global MFR (**B**), and MFCsevere (**C**), based on optimal thresholds using the Youden Index. MACE - major adverse cardiovascular event; MBF - myocardial blood flow; MFC - myocardial flow capacity; MFR - myocardial flow reserve.

Table 3. Prediction of major adverse cardiovascular events (MACE) during follow-up. Univariate Cox proportional regression models

	MACE	
	Hazard ratio (95% CI)	**p-value**
Global stress MBF < 1.94 mL/min/g	5.19 (2.6-10.5)	**< 0.001**
Global MFR < 1.98	3.68 (2.0-6.6)	**< 0.001**
MFC_{severe} > 3.2% of LV	4.19 (2.3-7.6)	**< 0.001**
Age	1.02 (1.0-1.0)	0.15
Male sex	2.08 (1.1-4.1)	**0.034**
BMI	0.99 (0.9-1.0)	0.68
Hypertension	1.77 (0.9-3.7)	0.13
Current or former smoker	1.64 (0.9-2.9)	0.093
Dyslipidemia	1.41 (0.7-2.7)	0.3
Diabetes	1.52 (0.9-2.7)	0.17
Known CAD	2.41 (1.3-4.6)	**0.005**
History of MI	2.19 (1.2-3.9)	**0.008**

BMI - body mass index; other abbreviations as in Tables 1 and 2

Table 4. Independent predictors of MACE in different Cox regression models

Multivariate model	**Hazard ratio (95% CI)**	**p-value**
Model 1: Clinical variables and global stress MBF		
Global stress MBF < 1.94 mL/min/g	4.5 (2.1-9.7)	**< 0.001**
Male sex	1.03 (0.5-2.2)	0.94
Known CAD	1.42 (0.5-3.7)	0.47
History of MI	1.03 (0.4-2.5)	0.94
Model 2: Clinical variables and global MFR		
Global MFR < 1.98	3.1 (1.7-5.8)	**< 0.001**
Male sex	1.33 (0.7-2.8)	0.47
Known CAD	1.76 (0.7-4.5)	0.24
History of MI	0.96 (0.4-2.3)	0.93
Model 3: Clinical variables and MFC_{severe}		
MFC_{severe} > 3.2% of LV	3.67 (1.9-7.1)	**< 0.001**
Male sex	1.48 (0.7-3.0)	0.29
Known CAD	1.58 (0.6-4.1)	0.35
History of MI	0.81 (0.3-2.0)	0.64
Model 4: Clinical variables, global MFR, global stress MBF, and MFC_{severe}		
Global stress MBF < 1.94 mL/min/g	2.81 (1.1-7)	**0.027**
Global MFR < 1.98	1.54 (0.7-3.7)	0.33
MFC_{severe} > 3.2% of LV	1.56 (0.6-4.1)	0.37
Male sex	1.05 (0.5-2.3)	0.9
Known CAD	1.59 (0.6-4.2)	0.35
History of MI	0.82 (0.3-2)	0.67

Abbreviations as in Tables 1 and 2

Conclusion

In conclusion, this study using the latest SiPM PET technology with low-dose ^{82}Rb, halving the standard activity, demonstrates that impaired global stress MBF, global MFR, and regional MFC are powerful predictors of cardiovascular events, outperforming traditional cardiovascular risk factors. However, we found that only reduced global stress MBF independently predicted MACE, being superior to global MFR and regional MFC impairments.

References

1. Knuuti J, Wijns W, Saraste A, Capodanno D, Barbato E, Funck-Brentano C et al. 2019 ESC Guidelines for the diagnosis and management of chronic coronary syndromes. Eur Heart J 2020;41:407-77.
2. Juarez-Orozco LE, Tio RA, Alexanderson E, Dweck M, Vliegenthart R, El Moumni M et al. Quantitative myocardial perfusion evaluation with positron emission tomography and the risk of cardiovascular events in patients with coronary artery disease: a systematic review of prognostic studies. Eur Heart J Cardiovasc Imaging 2018;19:1179-87.
3. Zampella E, Acampa W, Assante R, Gaudieri V, Nappi C, Mannarino T et al. Combined evaluation of regional coronary artery calcium and myocardial perfusion by (82)Rb PET/CT in predicting lesion-related outcome. Eur J Nucl Med Mol Imaging 2020;47:1698-704.
4. Harjulahti E, Maaniitty T, Nammas W, Stenstrom I, Biancari F, Bax JJ et al. Global and segmental absolute stress myocardial blood flow in prediction of cardiac events: [(15)O] water positron emission tomography study. Eur J Nucl Med Mol Imaging 2021;48:1434-44.
5. Weber BN, Stevens E, Perez-Chada LM, Brown JM, Divakaran S, Bay C et al. Impaired Coronary Vasodilator Reserve and Adverse Prognosis in Patients With Systemic Inflammatory Disorders. JACC Cardiovasc Imaging 2021;14:2212-20.
6. Gould KL, Johnson NP, Bateman TM, Beanlands RS, Bengel FM, Bober R et al. Anatomic versus physiologic assessment of coronary artery disease. Role of coronary flow reserve, fractional flow reserve, and positron emission tomography imaging in revascularization decision-making. J Am Coll Cardiol 2013;62:1639-53.
7. Johnson NP, Gould KL. Integrating noninvasive absolute flow, coronary flow reserve, and ischemic thresholds into a comprehensive map of physiological severity. JACC Cardiovasc Imaging 2012;5:430-40.
8. Gould KL, Johnson NP, Roby AE, Nguyen T, Kirkeeide R, Haynie M et al. Regional, Artery-Specific Thresholds of Quantitative Myocardial Perfusion by PET Associated with Reduced Myocardial Infarction and Death After Revascularization in Stable Coronary Artery Disease. J Nucl Med 2019;60:410-7.
9. Gould KL, Kitkungvan D, Johnson NP, Nguyen T, Kirkeeide R, Bui L et al. Mortality Prediction by Quantitative PET Perfusion Expressed as Coronary Flow Capacity With and Without Revascularization. JACC Cardiovasc Imaging 2021;14:1020-34.

10. Gupta A, Taqueti VR, van de Hoef TP, Bajaj NS, Bravo PE, Murthy VL et al. Integrated Noninvasive Physiological Assessment of Coronary Circulatory Function and Impact on Cardiovascular Mortality in Patients With Stable Coronary Artery Disease. Circulation 2017;136:2325-36.
11. van Sluis J, de Jong J, Schaar J, Noordzij W, van Snick P, Dierckx R et al. Performance Characteristics of the Digital Biograph Vision PET/CT System. J Nucl Med 2019;60:1031-6.
12. Wagatsuma K, Miwa K, Sakata M, Oda K, Ono H, Kameyama M et al. Comparison between new-generation SiPM-based and conventional PMT-based TOF-PET/CT. Phys Med 2017;42:203-10.
13. Koenders SS, van Dalen JA, Jager PL, Knollema S, Timmer JR, Mouden M et al. Value of SiPM PET in myocardial perfusion imaging using Rubidium-82. J Nucl Cardiol 2022;29:204-12.
14. Dekemp RA, Declerck J, Klein R, Pan XB, Nakazato R, Tonge C et al. Multisoftware reproducibility study of stress and rest myocardial blood flow assessed with 3D dynamic PET/CT and a 1-tissue-compartment model of 82Rb kinetics. J Nucl Med 2013;54:571-7.
15. Efseaff M, Klein R, Ziadi MC, Beanlands RS, deKemp RA. Short-term repeatability of resting myocardial blood flow measurements using rubidium-82 PET imaging. J Nucl Cardiol 2012;19:997-1006.
16. Hunter CR, Klein R, Beanlands RS, deKemp RA. Patient motion effects on the quantification of regional myocardial blood flow with dynamic PET imaging. Med Phys 2016;43:1829.
17. Sheather SJ. A Modern Approach to Regression with R. New York: Springer; 2009.
18. Farhad H, Dunet V, Bachelard K, Allenbach G, Kaufmann PA, Prior JO. Added prognostic value of myocardial blood flow quantitation in rubidium-82 positron emission tomography imaging. Eur Heart J Cardiovasc Imaging 2013;14:1203-10.
19. Fukushima K, Javadi MS, Higuchi T, Lautamaki R, Merrill J, Nekolla SG et al. Prediction of short-term cardiovascular events using quantification of global myocardial flow reserve in patients referred for clinical 82Rb PET perfusion imaging. J Nucl Med 2011;52:726-32.
20. Taqueti VR, Hachamovitch R, Murthy VL, Naya M, Foster CR, Hainer J et al. Global coronary flow reserve is associated with adverse cardiovascular events independently of

luminal angiographic severity and modifies the effect of early revascularization. Circulation 2015;131:19-27.

21. Patel KK, Spertus JA, Chan PS, Sperry BW, Al Badarin F, Kennedy KF et al. Myocardial blood flow reserve assessed by positron emission tomography myocardial perfusion imaging identifies patients with a survival benefit from early revascularization. Eur Heart J 2020;41:759-68.
22. Bom MJ, van Diemen PA, Driessen RS, Everaars H, Schumacher SP, Wijmenga JT et al. Prognostic value of [15O]H2O positron emission tomography-derived global and regional myocardial perfusion. Eur Heart J Cardiovasc Imaging 2020;21:777-86.
23. Johnson NP, Gould KL, De Bruyne B. Autoregulation of Coronary Blood Supply in Response to Demand: JACC Review Topic of the Week. J Am Coll Cardiol 2021;77:2335-45.
24. Miura S, Naya M, Kumamaru H, Ando A, Miyazaki C, Yamashita T. Prognostic value of modified coronary flow capacity by (13)N-ammonia myocardial perfusion positron emission tomography in patients without obstructive coronary arteries. J Cardiol 2022;79:247-56.
25. de Winter RW, Jukema RA, van Diemen PA, Schumacher SP, Driessen RS, Stuijfzand WJ et al. The impact of coronary revascularization on vessel-specific coronary flow capacity and long-term outcomes: a serial [15O]H2O positron emission tomography perfusion imaging study. Eur Heart J Cardiovasc Imaging 2022;23:743-52.
26. von Felten E, Benz DC, Benetos G, Baehler J, Patriki D, Rampidis GP et al. Prognostic value of regional myocardial flow reserve derived from (13)N-ammonia positron emission tomography in patients with suspected coronary artery disease. Eur J Nucl Med Mol Imaging 2021;49:311-20.

Chapter 8

The Interrelation between cardiac and brain small vessel disease: A pilot quantitative PET and MRI study

Eur J Hybrid Imaging. 2023 doi:10.1186/s41824-023-00180-7

Bianca Mazini, **Matthieu Dietz**, Bénédicte Maréchal, Ricardo Corredor-Jerez, John O. Prior, Vincent Dunet

Abstract

Aims

Small-vessel disease (SVD) plays a crucial role in cardiac and brain ischemia, but little is known about potential interrelation between both. We aimed at assessing the interrelation between cardiac and brain SVD by using quantitative ^{82}Rb cardiac PET/CT and brain MRI.

Methods and results

We retrospectively evaluated 370 patients, of whom 38 had pure cardiac SVD and 176 had normal myocardial perfusion. All underwent both a cardiac ^{82}Rb PET/CT and a brain 1.5T or 3T MRI. Left-ventricle myocardial blood flow (LV-MBF) and flow reserve (LV-MFR) were recorded from ^{82}Rb PET/CT, while Fazekas score, white-matter lesion (WMab) volume, deep grey-matter lesion (GMab) volume, and brain morphometry using the MorphoBox prototype software were derived from MRI. Groups were compared with Kruskal-Wallis test, and the potential interrelation between heart and brain SVD markers was assessed using Pearson's correlation coefficient. Patients with cardiac SVD had lower stress LV-MBF and MFR ($P<0.001$) than healthy controls but similar Fazekas scores and WMab volumes ($p>0.45$). In patients with cardiac SVD only, increased rest LV-MBF was associated with left-putamen Z-score reduction (rho=–0.62, P=0.033), right-thalamus (rho=0.64, P=0.026) and right-pallidum (rho=0.60, P=0.039) GMab volume increase. Decreased stress LV-MBF was associated with left-caudate Z-score reduction (rho=0.69, P=0.014), while decreased LV-MFR was associated with left- (rho=0.75, P=0.005) and right- (rho=0.59, P=0.045) putamen Z-score reduction, as well as increased right-thalamus GMab volume (rho=–0.72, P=0.009).

Conclusion

Significant interrelations between cardiac and cerebral SVD markers were found, especially regarding deep grey-matter alterations, which supports the hypothesis of SVD as a systemic disease.

Introduction

Ischemic heart disease, stroke, and dementia are the most frequent causes of mortality and disability worldwide, especially among the elderly population (1, 2).

The epidemiology and pathophysiology of large-vessel atherosclerosis are well defined in the scientific literature. Thus, effective preventive and therapeutic measures can be implemented. On the other hand, although the pathophysiology and impact of microvascular pathologies on the general population as well as their link with cardiovascular risk factors are clear, there is little data in the literature on the correlation of microvascular disease between different organs, particularly between the heart and the brain (3, 4). Heart and brain small-vessel disease likely represent variations of the same systemic, pathologic process (3).

Heart small-vessel disease (SVD), which can manifest clinically as angina, myocardial infarction and heart failure, can be quantitatively analyzed with cardiac ^{82}Rb PET/CT. Indeed, this imaging technique is currently considered the gold standard for the quantification of myocardial blood flow (MBF) and myocardial flow reserve (MFR) (5), which represent markers of cardiac vascular damage; in particular, an abnormal value of myocardial flow reserve is part of the diagnostic criteria for cardiac microvascular pathology (6).

Brain SVD, which is a substrate of stroke, dementia, cerebral atrophy, and gait disorders, can be evaluated using cerebral magnetic resonance imaging (MRI) (7). MRI can detect markers such as leucopathy, small subcortical infarcts, lacunae of presumed vascular origin, cerebral atrophy, microbleeds, and prominent perivascular spaces (8, 9). Moreover, with new automatic segmentation software, it is possible to perform not only qualitative but also quantitative analyses of such lesions (10).

The purpose of this study was to look for a potential link between heart and brain with the help of imaging techniques, particularly by analyzing cardiac perfusion with cardiac ^{82}Rb PET/CT and radiological signs of cerebral SVD with brain MRI automated morphometry.

Methods

Study design

The flowchart of this retrospective single center study is presented in **Figure 1**. From June 2011 to June 2019, 2569 patients underwent a cardiac ^{82}Rb PET/CT to explore ischemic heart disease

in the Department of Nuclear Medicine and Molecular Imaging at Lausanne University Hospital. Of this cohort, inclusion criteria were: (1) patients older than 18 years; and (2) who underwent a brain MRI. We excluded patients with large cerebral sequelae (history of brain metastasis or tumor, neurosurgery, severe traumatic brain injury [TBI]), bad image quality due to motion artifacts, or proved non-vascular leukoencephalopathy. From patients' medical records, we collected the following clinical variables: sex, age, cardiovascular risk factors (diabetes, hypertension, smoking, dyslipidemia, sleep apnea syndrome), coronary artery disease (CAD), history of myocardial infarct or stroke, history of peripheral arterial disease, current medications. All participants provided fully informed written consent for using their data for research purposes. The study was approved by the ethics committee (#CERVD 152/08, #BASEC PB_2017-00634).

Cardiac PET/CT analysis

Cardiac ^{82}Rb PET/CT acquisitions were performed on a Discovery 690 TOF scanner (GE Healthcare, Waukesha, WI, USA). Patients were asked to fast for at least 6 hours and refrain from any caffeine intake for at least 24 hours before examination. Cardiac PET/CT acquisition was performed at rest and at stress after intravenous infusion of adenosine, as previously described (11). Cardiac PET analysis was performed by 2 experimented nuclear medicine physicians (JOP and MD, with >20 and 6 years' experience, respectively).

Cardiac perfusion was assessed and analyzed in a semi-quantitative and in a quantitative manner. Summed rest, summed stress and summed difference scores (SRS, SSS, and SDS, respectively) were computed applying the 17-segment model of the American Heart Association (12, 13). An SSS ≥4 was considered abnormal (Ziadi et al JACC 2011).

For the quantitative part, left ventricle (LV) rest myocardial blood flow (MBF), stress MBF, and myocardial flow reserve (MFR) were obtained by processing data with the fully automated FlowQuant software (Ottawa Heart Institute, Ottawa, Canada) (14, 15). Quantitative analysis was assessed globally and for all 3 vascular territories derived from standard segmentation: left anterior descending (LAD), left circumflex (LCx), and right coronary artery (RCA). A global LV MFR <2 was considered abnormal, as previously documented (16).

Three groups were generated based on ^{82}Rb PET/CT: I, abnormal SSS ≥4, suggesting hemodynamically obstructive coronary artery disease (CAD) lesions or myocardial infarction (17, Ruddy et al. Journal of nuclear cardiology 2022), II, normal SSS <4 and normal LV MFR >2 (normal cardiac ^{82}Rb PET/CT), III, normal SSS <4 and LV MFR <2. For this last group, an invasive coronary angiography was available to distinguish between flow-limiting epicardial

lesions (presence of obstructive CAD) or SVD (absence of obstructive CAD) (14, 15). Obstructive CAD by invasive coronary angiography was defined as >50% diameter reduction or fractional flow reserve <0.80 (14, 15).

Cerebral MRI analysis

Brain MRIs were acquired on 1.5 or 3T scanners (all Siemens Healthcare, Erlangen, Germany). Included patients had all at least an axial T2 spin echo (T2SE) and a 3D T1 magnetization-prepared rapid gradient-echo (MPRAGE) with acquisition parameters that follow the Alzheimer's Disease Neuroimaging Initiative guidelines (18).

Images were first qualitatively analyzed by an experimented neuroradiologist (VD with 13-years' experience in neuroimaging) in order to find brain sequelae due to non-lacunar stroke or to other pathologies (brain metastasis or tumor, neurosurgery, severe TBI). In the remaining patients, leucopathy was assessed on the T2SE images and divided into 4 categories by using the Fazekas score (19).

Quantitative evaluation of brain volume was performed by two experimented neuroimaging research engineers. Brain regions were segmented from the 3D T1-MPRAGE sequences using the MorphoBox prototype software (10) providing absolute and relative volumes (in mL and % of the total intracranial volume [TIV], respectively) of: total gray and white matter, central nuclei, hippocampus, brainstem, lobar gray and white matter, intracranial cerebrospinal fluid, ventricular system. The Z-score of each structure was provided by comparing these volumes to a group of healthy patients of the comparable age and sex based on the ADNI cohort (20). The software also estimates the volume of abnormal white matter (WMab) and the lesion load in the deep grey nuclei (GMab) (21).

Statistical analysis

Statistical analyses were performed with Stata 16.0 software (StataCorp, College Station, TX, USA). Continuous variables are presented as median with interquartile range (IQR) or mean with standard deviation (SD) when normally distributed. Categorical variables are reported as number or percentage. ^{82}Rb PET/CT perfusion parameters and MRI morphometry were compared between patients with normal myocardial perfusion (SSS <4 and LV MFR >2) and patients with cardiac SVD using the Kruskal-Wallis test. Potential interrelation between heart and brain SVD markers was assessed using Pearson's correlation coefficient in these two groups only. A P value<0.05 was considered statistically significant. The significance level was not corrected for multiple comparisons.

Results

Population characteristics

Of 2569 patients, we enrolled 370 patients who had both cardiac ^{82}Rb PET/CT and brain MRI (**Figure 1**). The population clinical characteristics that we recorded are available in **Table 1**.

Cardiac ^{82}Rb PET/CT data

Of 370 patients, 176 showed a normal cardiac ^{82}Rb PET/CT, 86 showed abnormal SSS ≥4, and 108 showed normal SSS and abnormal LV MFR <2. Among them, 70 were classified with obstructive CAD and 38 with cardiac SVD based on invasive coronary angiographic data.

All quantitative results are displayed in **Table 2**. Compared with patients with normal myocardial perfusion, patients with cardiac SVD had lower stress LV-MBF and MFR in all three coronary territories and globally ($p<0.0019$)

MR data

Of 370 patients, 70 had non-lacunar stroke sequelae or sequelae from other disease on brain MRI and were excluded from the MRI quantitative analysis. Of the 300 remaining patients, 114 were excluded due to CAD. One hundred and twenty-three could not be segmented because the 3D T1-MPRAGE that did not follow ADNI guidelines. The 3D T1-MPRAGE was segmented in 63 subjects with normal myocardial perfusion or cardiac SVD (**Figure 1**).

Compared to patients with normal myocardial perfusion, patients with SVD had similar Fazekas score (P=0.45) but lower z-score for right and left frontal WM volumes (P=0.024 and P=0.021) and higher z-score for left and third ventricles (P=0.042 and P=0.016). There was also a trend for higher GMab volume and higher right ventricle z-score in SVD patients compared to patients with normal myocardial perfusion. The z-score for all segmented structures for patients with normal myocardial perfusion and SVD are reported in **Table 3**.

PET/CT and MRI interrelation

Regarding the qualitative analysis, no correlation was found; indeed, there was no association between Fazekas score and LV-MBF at rest (rho=0.03, P=0.72), at stress (rho=0.06, P=0.44) and LV-MFR (rho=0.03, P=0.71).

Taking into account all patients with normal cardiac perfusion and patients with SVD (N=63), rest LV-MBF was negatively correlated with z-score of total brain (rho=–0.29, P=0.028), right occipital GM (rho=–0.31, P=0.018) and left (rho=–0.35, P=0.007) and right (rho=–0.33, P=0.012) temporal WM volumes; LV-MFR was positively correlated with z-score of total brain (rho=0.35, P=0.007), total GM (rho=0.27, P=0.037), left (rho=0.34, P=0.008) and right (rho=0.31, P=0.016) parietal GM volumes, left (rho=0.31, P=0.016) pallidum z-score and negatively correlated with z-score of total CSF (rho=–0.37, P=0.005). There was no significant correlation between cardiac perfusion parameters and WMab or GMab volumes (P>0.18).

When considering only microvascular patients (N=12), we found that rest LV-MBF was negatively correlated with left putamen z-score (rho=-0.62, P=0.033), stress LV-MBF was positively correlated with left caudate z-score (rho=0.69, P=0.014), and LV-MFR was positively correlated with left (rho=0.75, P=0.005) and right (rho=0.59, P=0.045) putamen z-score. Also, in SVD patients, we found a positive correlation between rest LV-MBF and right-thalamus (rho=0.64, P=0.026) and right-pallidum (rho=0.60, P=0.039) GMab volume. Moreover, we found a negative correlation between LV-MFR and right-thalamus GMab volume (rho=–0.72, P=0.009). On the other hand, no correlation was found between an abnormal cardiac perfusion and WMab volumes (P>0.47).

Discussion

This study focused on the potential association between cardiac and cerebral microvascular pathologies. The main results can be summarized as followed: 1) patients with SVD have lower LV stress MBF and MFR; 2) SVD have lower frontal WM z-score, higher ventricular z-scores and tend to have higher GMab volume; 3) In SVD patients, LV MBF and MFR correlate with deep grey matter z-scores and GMab volumes.

While cardiac pathology due to epicardial coronary artery disease is well known, ischemic heart disease resulting from SVD is still poorly understood. Several cardiovascular imaging techniques have been proposed to assess microvascular dysfunction (22), including cardiac PET/CT. Some studies reported that MFR<2 has a significant prognostic value in symptomatic women with non-obstructive CAD (23) as well as in patients without perfusion defect (24). Considering patients with no obstructive epicardial CAD, SVD patients represented 38/214 patients (17.8%), which is quite lower than previous reports. Indeed, Rauf et al. (24) recently reported in a large population that 27.9% of the patients (N=2175) with no significant perfusion

defect on ^{82}Rb cardiac PET had a MFR<2, while other authors even reported higher SVD prevalence up to 54% in patients without perfusion defect (25). While the authors did not report angiography results, they considered that low calcium score were likely indicative to low risk of triple vessel CAD. Based on coronary angiography results, we found that 38 of 108 patients (35.2%) with MFR<2 had SVD, while 70 of 108 patients (64.8 %) in fact had obstructive CAD. Compared to patients with normal myocardial perfusion imaging, SVD patients had similar LV rest MBF and impaired LV stress MBF, which is also concordant with the most recent literature (24, 26). Considering that an abnormal value of MFR is part of the diagnostic criteria of microvascular angina according to the COVADIS steering group (6), and that the abnormal absolute values of stress MBF and MFR that we found are concordant to the literature (27), this indicates that our SVD patients' population is representative of patients in other studies. Still, it remained unknown whether patients with cardiac SVD may have significant brain changes.

We found that patients with cardiac SVD, had a higher degree of frontal white matter atrophy, ventricular dilatation and a higher volume of deep gray matter lacunae compared with patients with normal cardiac perfusion imaging. These parameters are considered as common markers of cerebral SVD (8, 9, 28-30). While cerebral SVD may present with remarkable heterogeneous clinical symptoms and various patterns on imaging (31) , automatic segmentation and quantification brain lesions has been used to estimate the global burden of SVD (32). Hence, it was demonstrated that brain lesions quantification is a strong predictor of early and long-term cognitive decline and functional disability in the general population or in patients with synchronous neurodegenerative diseases (33, 34). Nonetheless, to the best of our literature search, we found no study evaluating the brain morphometry of patients with proven cardiac SVD in details. Mejia-Renteria et al.(4) recently reported no significant difference in total GM and WM volumes but higher white-matter hyperintensity volume in patients with coronary small-vessel disease compared to patients with normal coronary flow reserve, Our results confirm that these patients have both cardiac and cerebral signs of SVD. While cerebral SVD is now considered as a global organ disease (31, 35) our findings even suggest this might be a multiple organ disease.

Heart and brain indeed display similarities in vascular anatomy, as they comprise three compartments: on one hand large arteries on the surface of the organ, on the other hand resistant arterioles and smaller vessels penetrating within the depth of the organ (36). Nevertheless, whether brain changes could be interrelated with myocardial perfusion findings has been rarely

evaluated. In a recent systematic review article by Berry et al. (3), the authors only identified 9 research articles that provided results on SVD in both the brain and the heart, thus highlighting the gap in the knowledge in this disorder. In a clinico-pathological study of 175 cases, Andin et al. (37), found that patients with pathological evidence of cerebral SVD had more cardiac pathologies than patients with other vascular dementia groups. Similarly, Weidman et al. (38) reported that 72 of 95 patients with syndrome X and normal coronary angiogram had pathologic brain ^{99m}Tc-HMPAO perfusion single photon emitting tomography. Also, one study evaluating patients with cerebral autosomal dominant arteriopathy with subcortical infarcts and leukopathy (CADASIL), a NOTCH3 mutation related SVD, reported that similar small vessel alterations can be found on myocardial specimens than in the brain (39). More recently, Argiro et al. (40) demonstrated that patients with CADASIL had lower stress MBF and MFR using cardiac $^{13}NH_3$ PET compared to healthy controls. Perfusion parameters were not correlated with qualitative or semi-quantitative markers of SVD. Also Meiira-Renteira et al. (4) did not find any significant relation between coronary flow reserve and white-matter hyperintensity volume (beta=-0.20, P=0.47). In accordance, we did not find any significant interrelation between Fazekas score and MBF or MFR using ^{82}Rb PET. However, these authors did not explore detailed brain morphometry, while we found that rest MBF, stress MBF and MFR were significantly correlated with striatal z-score and abnormal gray matter volume in SVD patients. As lacunae of presumed vascular origin (GMab in our study) and brain atrophy (Z score in our study) are listed between signs of SVD on conventional MRI in the literature (8), the interrelations between increased GMab volume and reduced basal ganglia Z score with impaired myocardial blood flow, supports the hypothesis that microvascular dysfunction is a systemic disease (41).

Despite encouraging results, we have to address some limitations in this study. First, despite the large population screened for SVD only a small number of patients had both a cardiac PET/CT and a MRI that included a T1-MPRAGE sequence allowing to process brain morphometry. However, patients were well characterized, as every cases with MFR<2 were categorized by coronary angiography to identify balanced obstructive CAD, which was not systematically addressed in previous studies. This also reflects the overall lower incidence of pure SVD than previously reported (17.8% vs 27.9-54%)(24, 25). Despite cardiac stress-induced regional perfusion deficits are generally caused by hemodynamically obstructive CAD lesions (17), some cases with solely coronary microvascular dysfunction might be missed and were hereby excluded. Moreover, our selective approach did not allow an inclusion of potential patients with cardiac SVD and regional perfusion defect (SSS ≥4). Second, while MRI were

performed on different scanners, brain morphometry demonstrated high reproducibility (43), which limits potential bias. Also, we did not have 3D fluid attenuated inversion recovery sequence to estimate the white-matter hyperintensity volume and potential relation with MFR, despite negative results from other authors (4). Finally, the respective and cumulative effects of different cardiovascular risks factors on heart and brain SVD interrelation could not be assessed. This should be evaluated in large preferably prospective studies, as patients with SVD often have several congenital and acquired risk factors that contribute to microvascular dysfunction by different pathophysiological mechanisms (44).

Conclusion

In this retrospective study, significant interrelations between cardiac and cerebral small vessel disease quantitative parameters, especially regarding deep grey matter alterations, derived from PET/CT and brain morphometry were found. This overall supports the hypothesis of an association between cardiac and brain SVD as a systemic disorder. Further larger prospective studies are now needed to understand the pathophysiological mechanisms and respective or cumulative effects of congenital and acquired risk factors.

References

1. Global, regional, and national disability-adjusted life-years (DALYs) for 333 diseases and injuries and healthy life expectancy (HALE) for 195 countries and territories, 1990-2016: a systematic analysis for the Global Burden of Disease Study 2016. Lancet. 2017;390(10100):1260-344.
2. Benjamin EJ, Virani SS, Callaway CW, Chamberlain AM, Chang AR, Cheng S, et al. Heart Disease and Stroke Statistics-2018 Update: A Report From the American Heart Association. Circulation. 2018;137(12):e67-e492.
3. Berry C, Sidik N, Pereira AC, Ford TJ, Touyz RM, Kaski JC, et al. Small-Vessel Disease in the Heart and Brain: Current Knowledge, Unmet Therapeutic Need, and Future Directions. J Am Heart Assoc. 2019;8(3):e011104.
4. Mejia-Renteria H, Travieso A, Matias-Guiu JA, Yus M, Espejo-Paeres C, Finocchiaro F, et al. Coronary microvascular dysfunction is associated with impaired cognitive function: the Cerebral-Coronary Connection study (C3 study). Eur Heart J. 2023;44(2):113-25.
5. Pelletier-Galarneau M, Dilsizian V. Microvascular Angina Diagnosed by Absolute PET Myocardial Blood Flow Quantification. Curr Cardiol Rep. 2020;22(2):9.
6. Ong P, Camici PG, Beltrame JF, Crea F, Shimokawa H, Sechtem U, et al. International standardization of diagnostic criteria for microvascular angina. Int J Cardiol. 2018;250:16-20.
7. De Guio F, Duering M, Fazekas F, De Leeuw FE, Greenberg SM, Pantoni L, et al. Brain atrophy in cerebral small vessel diseases: Extent, consequences, technical limitations and perspectives: The HARNESS initiative. J Cereb Blood Flow Metab. 2020;40(2):231-45.
8. Wardlaw JM, Smith EE, Biessels GJ, Cordonnier C, Fazekas F, Frayne R, et al. Neuroimaging standards for research into small vessel disease and its contribution to ageing and neurodegeneration. Lancet Neurol. 2013;12(8):822-38.
9. Wardlaw JM, Smith C, Dichgans M. Small vessel disease: mechanisms and clinical implications. Lancet Neurol. 2019;18(7):684-96.
10. Schmitter D, Roche A, Maréchal B, Ribes D, Abdulkadir A, Bach-Cuadra M, et al. An evaluation of volume-based morphometry for prediction of mild cognitive impairment and Alzheimer's disease. Neuroimage Clin. 2015;7:7-17.
11. Farhad H, Dunet V, Bachelard K, Allenbach G, Kaufmann PA, Prior JO. Added prognostic value of myocardial blood flow quantitation in rubidium-82 positron emission tomography imaging. Eur Heart J Cardiovasc Imaging. 2013;14(12):1203-10.

12. Dilsizian V, Bacharach SL, Beanlands RS, Bergmann SR, Delbeke D, Dorbala S, et al. ASNC imaging guidelines/SNMMI procedure standard for positron emission tomography (PET) nuclear cardiology procedures. J Nucl Cardiol. 2016;23(5):1187-226.
13. Cerqueira MD, Weissman NJ, Dilsizian V, Jacobs AK, Kaul S, Laskey WK, et al. Standardized myocardial segmentation and nomenclature for tomographic imaging of the heart. A statement for healthcare professionals from the Cardiac Imaging Committee of the Council on Clinical Cardiology of the American Heart Association. Circulation. 2002;105(4):539-42.
14. Dunet V, Klein R, Allenbach G, Renaud J, deKemp RA, Prior JO. Myocardial blood flow quantification by Rb-82 cardiac PET/CT: A detailed reproducibility study between two semi-automatic analysis programs. J Nucl Cardiol. 2016;23(3):499-510.
15. Klein R, Renaud JM, Ziadi MC, Thorn SL, Adler A, Beanlands RS, et al. Intra- and inter-operator repeatability of myocardial blood flow and myocardial flow reserve measurements using rubidium-82 pet and a highly automated analysis program. J Nucl Cardiol. 2010;17(4):600-16.
16. Herzog BA, Husmann L, Valenta I, Gaemperli O, Siegrist PT, Tay FM, et al. Long-term prognostic value of 13N-ammonia myocardial perfusion positron emission tomography added value of coronary flow reserve. J Am Coll Cardiol. 2009;54(2):150-6.
17. Schindler TH, Schelbert HR, Quercioli A, Dilsizian V. Cardiac PET imaging for the detection and monitoring of coronary artery disease and microvascular health. JACC Cardiovasc Imaging. 2010;3(6):623-40.
18. Jack CR, Jr., Bernstein MA, Fox NC, Thompson P, Alexander G, Harvey D, et al. The Alzheimer's Disease Neuroimaging Initiative (ADNI): MRI methods. J Magn Reson Imaging. 2008;27(4):685-91.
19. Fazekas F, Chawluk JB, Alavi A, Hurtig HI, Zimmerman RA. MR signal abnormalities at 1.5 T in Alzheimer's dementia and normal aging. AJR Am J Roentgenol. 1987;149(2):351-6.
20. Wyman BT, Harvey DJ, Crawford K, Bernstein MA, Carmichael O, Cole PE, et al. Standardization of analysis sets for reporting results from ADNI MRI data. Alzheimers Dement. 2013;9(3):332-7.
21. Fang E, Ann CN, Maréchal B, Lim JX, Tan SYZ, Li H, et al. Differentiating Parkinson's disease motor subtypes using automated volume-based morphometry incorporating white matter and deep gray nuclear lesion load. J Magn Reson Imaging. 2020;51(3):748-56.
22. Mathew RC, Bourque JM, Salerno M, Kramer CM. Cardiovascular Imaging Techniques to Assess Microvascular Dysfunction. JACC Cardiovasc Imaging. 2020;13(7):1577-90.

23. Gulati M, Cooper-DeHoff RM, McClure C, Johnson BD, Shaw LJ, Handberg EM, et al. Adverse cardiovascular outcomes in women with nonobstructive coronary artery disease: a report from the Women's Ischemia Syndrome Evaluation Study and the St James Women Take Heart Project. Arch Intern Med. 2009;169(9):843-50.
24. Rauf M, Hansen KW, Galatius S, Wiinberg N, Brinth LS, Hojstrup S, et al. Prognostic implications of myocardial perfusion imaging by 82-rubidium positron emission tomography in male and female patients with angina and no perfusion defects. Eur Heart J Cardiovasc Imaging. 2022.
25. Murthy VL, Naya M, Taqueti VR, Foster CR, Gaber M, Hainer J, et al. Effects of sex on coronary microvascular dysfunction and cardiac outcomes. Circulation. 2014;129(24):2518-27.
26. Miura S, Naya M, Kumamaru H, Ando A, Miyazaki C, Yamashita T. Prognostic value of modified coronary flow capacity by (13)N-ammonia myocardial perfusion positron emission tomography in patients without obstructive coronary arteries. J Cardiol. 2022;79(2):247-56.
27. Bateman TM, Heller GV, Beanlands R, Calnon DA, Case J, deKemp R, et al. Practical Guide for Interpreting and Reporting Cardiac PET Measurements of Myocardial Blood Flow: An Information Statement from the American Society of Nuclear Cardiology, and the Society of Nuclear Medicine and Molecular Imaging. J Nucl Med. 2021;62(11):1599-615.
28. Cannistraro RJ, Badi M, Eidelman BH, Dickson DW, Middlebrooks EH, Meschia JF. CNS small vessel disease: A clinical review. Neurology. 2019;92(24):1146-56.
29. Li Q, Yang Y, Reis C, Tao T, Li W, Li X, et al. Cerebral Small Vessel Disease. Cell Transplant. 2018;27(12):1711-22.
30. Litak J, Mazurek M, Kulesza B, Szmygin P, Litak J, Kamieniak P, et al. Cerebral Small Vessel Disease. Int J Mol Sci. 2020;21(24).
31. Ter Telgte A, van Leijsen EMC, Wiegertjes K, Klijn CJM, Tuladhar AM, de Leeuw FE. Cerebral small vessel disease: from a focal to a global perspective. Nat Rev Neurol. 2018;14(7):387-98.
32. Jokinen H, Koikkalainen J, Laakso HM, Melkas S, Nieminen T, Brander A, et al. Global Burden of Small Vessel Disease-Related Brain Changes on MRI Predicts Cognitive and Functional Decline. Stroke. 2020;51(1):170-8.
33. Dunet V, Fartaria MJ, Deverdun J, Le Bars E, Maury F, Castelnovo G, et al. Episodic memory decline in Parkinson' s disease: relation with white matter hyperintense lesions and influence of quantification method. Brain Imaging Behav. 2019;13(3):810-8.

34. Maillard P, Carmichael O, Fletcher E, Reed B, Mungas D, DeCarli C. Coevolution of white matter hyperintensities and cognition in the elderly. Neurology. 2012;79(5):442-8.
35. Shi Y, Wardlaw JM. Update on cerebral small vessel disease: a dynamic whole-brain disease. Stroke Vasc Neurol. 2016;1(3):83-92.
36. Moroni F, Ammirati E, Hainsworth AH, Camici PG. Association of White Matter Hyperintensities and Cardiovascular Disease: The Importance of Microcirculatory Disease. Circ Cardiovasc Imaging. 2020;13(8):e010460.
37. Andin U, Gustafson L, Passant U, Brun A. A clinico-pathological study of heart and brain lesions in vascular dementia. Dement Geriatr Cogn Disord. 2005;19(4):222-8.
38. Weidmann B, Jansen WC, Bock A, Assheuer J, Tauchert MO. Technetium-99m-HMPAO brain SPECT in patients with syndrome X. Am J Cardiol. 1997;79(7):959-61.
39. Lesnik Oberstein SA, Jukema JW, Van Duinen SG, Macfarlane PW, van Houwelingen HC, Breuning MH, et al. Myocardial infarction in cerebral autosomal dominant arteriopathy with subcortical infarcts and leukoencephalopathy (CADASIL). Medicine (Baltimore). 2003;82(4):251-6.
40. Argiro A, Sciagra R, Marchi A, Beltrami M, Spinelli E, Salvadori E, et al. Coronary microvascular function is impaired in patients with cerebral autosomal dominant arteriopathy with subcortical infarcts and leukoencephalopathy. Eur J Neurol. 2021;28(11):3809-13.
41. Feuer DS, Handberg EM, Mehrad B, Wei J, Bairey Merz CN, Pepine CJ, et al. Microvascular Dysfunction as a Systemic Disease: A Review of the Evidence. Am J Med. 2022;135(9):1059-68.
42. Schindler TH, Dilsizian V. Coronary Microvascular Dysfunction: Clinical Considerations and Noninvasive Diagnosis. JACC Cardiovasc Imaging. 2020;13(1 Pt 1):140-55.
43. Yan S, Qian T, Marechal B, Kober T, Zhang X, Zhu J, et al. Test-retest variability of brain morphometry analysis: an investigation of sequence and coil effects. Ann Transl Med. 2020;8(1):12.
44. Ostergaard L, Engedal TS, Moreton F, Hansen MB, Wardlaw JM, Dalkara T, et al. Cerebral small vessel disease: Capillary pathways to stroke and cognitive decline. J Cereb Blood Flow Metab. 2016;36(2):302-25.

TABLES

Table 1: Main population characteristics

Characteristics	**N=370**
Age (years)	66 [60-73]
Sex female / male	115 / 255
Weight (kg)	79.5 [68-90]
Body mass index (kg/m^2)	27.2 [23.8-31.2]
Cardiovascular risk factors	
Smoking	94 / 370
Hypertension	274 / 370
Diabetes	145 / 370
Dyslipidemia	233 / 370
Other comorbidities	
Obstructive sleep apnea syndrome	67 / 370
Lower extremity arterial disease	62 / 370
Treatments	
Platelet antiaggregants	250 / 370
Beta-blockers	210 /370
ACE inhibitors	208 / 370
Diuretic	156 / 370
Nitroglycerin	44 /370
Lipids lowering agents	228 /370

ACE angiotensin-converting enzyme

Table 2: ^{82}Rb PET/CT quantitative data

Variables	**Normal N=176**	**Small-vessel disease N=38**	**P-value**
Rest MBF LAD	0.9 ± 0.4	0.9 ± 0.3	0.48
Stress MBF LAD	2.5 ± 0.9	1.5 ± 0.4	**0.0001**
MFR LAD	3.0 ± 1.1	1.7 ± 0.5	**0.0001**
Rest MBF LCX	1.0 ± 0.4	1.0 ± 0.3	0.67
Stress MBF LCX	2.6 ± 0.9	1.6 ± 0.5	**0.0001**
MFR LCX	2.8 ± 1.0	1.6 ± 0.4	**0.0001**
Rest MBF RCA	1.0 ± 0.4	1.0 ± 0.3	0.74
Stress MBF RCA	2.7 ± 1.0	1.6 ± 0.5	**0.0001**
MFR RCA	3.0 ± 1.2	1.7 ± 0.6	**0.0001**
Rest MBF LV	1.0 ± 0.4	1.0 ± 0.3	0.60
Stress MBF LV	2.6 ± 0.9	1.5 ± 0.4	**0.0001**
MFR LV	2.9 ± 1.0	1.7 ± 0.5*	**0.0001**

LAD: left anterior artery, LCX: left circumflex, RCA: right coronary artery, LV: left ventricle, MBF: myocardial blood flow, MFR: myocardial flow reserve

Table 3: MRI morphometry quantitative data

Parameters	**Normal perfusion N=51**	**Small-vessel disease N=12**	**P-value**
Brain	-0.82 ± 1.75	-1.13 ± 1.34	0.29
Total GM	-0.70 ± 1.99	-0.75 ± 1.09	0.44
Cortical GM	-0.67 ± 1.82	-0.67 ± 1.12	0.62
Right frontal GM	-0.84 ± 1.58	-0.83 ± 1.07	0.93
Left frontal GM	-0.73 ± 1.51	-0.75 ± 0.89	0.71
Right temporal GM	-0.43 ± 1.65	-0.26 ± 1.09	0.85
Left temporal GM	-0.73± 1.73	-0.74 ± 1.69	1.0
Right parietal GM	-0.40 ± 1.74	-0.50 ± 1.19	0.72
Left parietal GM	-0.32 ± 1.45	-0.56 ± 1.10	0.37
Right occipital GM	0.04 ± 1.23	0.24 ± 0.69	0.88
Left occipital GM	0.13 ± 1.18	-0.02 ± 0.57	0.39
Right hippocampus	0.35 ± 1.09	0.63 ± 1.41	0.53
Left hippocampus	-0.08 ± 1.21	0.59 ± 1.44	0.14
Right caudate nucleus	0.38 ± 1.35	0.45 ± 1.19	0.85
Left caudate nucleus	0.15 ± 1.23	0.42 ± 1.16	0.39
Right putamen	-0.27 ± 1.38	-0.31 ±1.42	0.87
Left putamen	-0.36 ± 1.34	-0.47 ± 1.10	0.76
Right pallidum	0.03 ± 1.26	0.05 ± 1.28	0.91
Left pallidum	-0.18 ± 1.30	-0.49 ± 0.71	0.44
Right thalamus	0.18 ± 1.20	0.15 ± 1.45	0.85
Left thalamus	0.02 ± 1.19	0.15 ± 1.46	0.90
Total GMab (mL)	0.28 ± 0.10	0.33 ± 0.12	0.09
Total WM	-0.40 ±1.47	-0.72 ± 1.09	0.32
Right frontal WM	-0.82 ± 1.14	-1.76 ± 1.29	**0.024**
Left frontal WM	-0.63 ± 1.11	-1.59 ± 1.30	**0.021**
Right temporal WM	-0.33 ± 1.53	-0.68 ± 1.42	0.56
Left temporal WM	-0.44 ± 1.35	-0.73 ± 1.63	0.68
Right parietal WM	-0.43 ± 1.16	-0.89 ± 1.00	0.15

Left parietal WM	-0.36 ± 1.05	-0.71 ± 1.24	0.42
Right occipital WM	0.09 ± 1.44	-0.01 ± 1.00	0.49
Left occipital WM	0.14 ± 1.27	0.18 ± 0.74	0.93
Total WMab (mL)	3.54 ± 6.61	4.75 ± 11.9	0.58
Mesencephalon	-0.19 ± 1.27	-0.43 ± 1.11	0.60
Pons	-0.13 ± 0.95	-0.23 ± 0.91	0.94
Medulla oblongata	0.16 ± 1.06	0.17 ± 0.95	0.84
Corpus callosum	-0.15 ± 0.96	-0.52 ± 1.04	0.22
CSF	0.72 ± 1.29	1.11 ± 1.19	0.34
Right ventricle	0.53 ± 1.12	1.05 ± 1.26	0.09
Left ventricle	0.41 ± 1.16	1.25 ± 1.33	**0.042**
Third ventricle	0.61 ± 1.14	1.37 ± 0.74	**0.016**
Fourth ventricle	0.15 ± 0.98	0.30 ± 1.43	0.97

Mean Z-score values and standard deviations are reported in this Table, unless otherwise specified. CSF cerebrospinal fluid, GM grey matter, GMab abnormal grey matter, WM white matter, WMab abnormal white matter.

FIGURES

Graphical abstract.

Of 370 participants, who underwent both ^{82}Rb cardiac PET/CT and brain MRI, 51 patients with normal myocardial perfusion imaging (MPI) and 12 patients with cardiac small-vessel disease (SVD) were used for evaluating potential interrelation between heart and brain SVD. Significant interrelations between cardiac and cerebral SVD markers were found, especially regarding deep grey-matter alterations, which supports the hypothesis of SVD as a systemic disease.

GMab abnormal grey matter, LV left ventricle, MBF myocardial blood flow, MFR myocardial flow reserve, MPI myocardial perfusion imaging, SVD small-vessel disease.

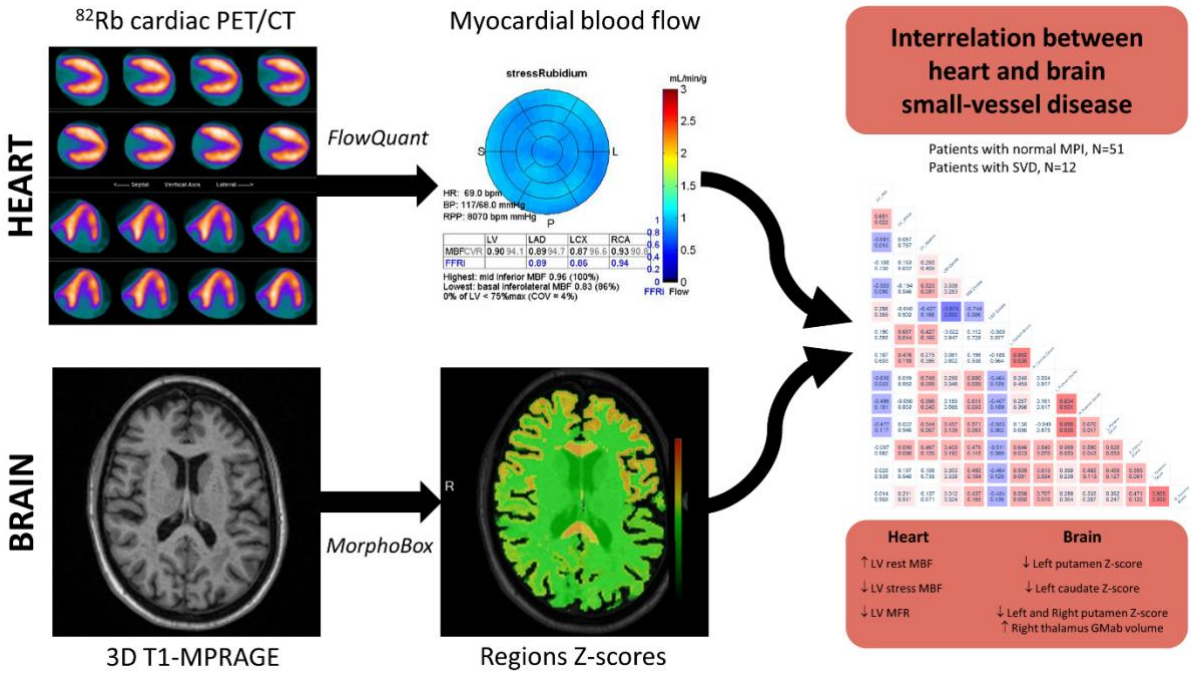

Figure 1: Study's flowchart.

cMRI, conventional MRI, CAD coronary artery disease, morphoMRI with 3D T1-MPRAGE morphometry, SVD small vessel disease

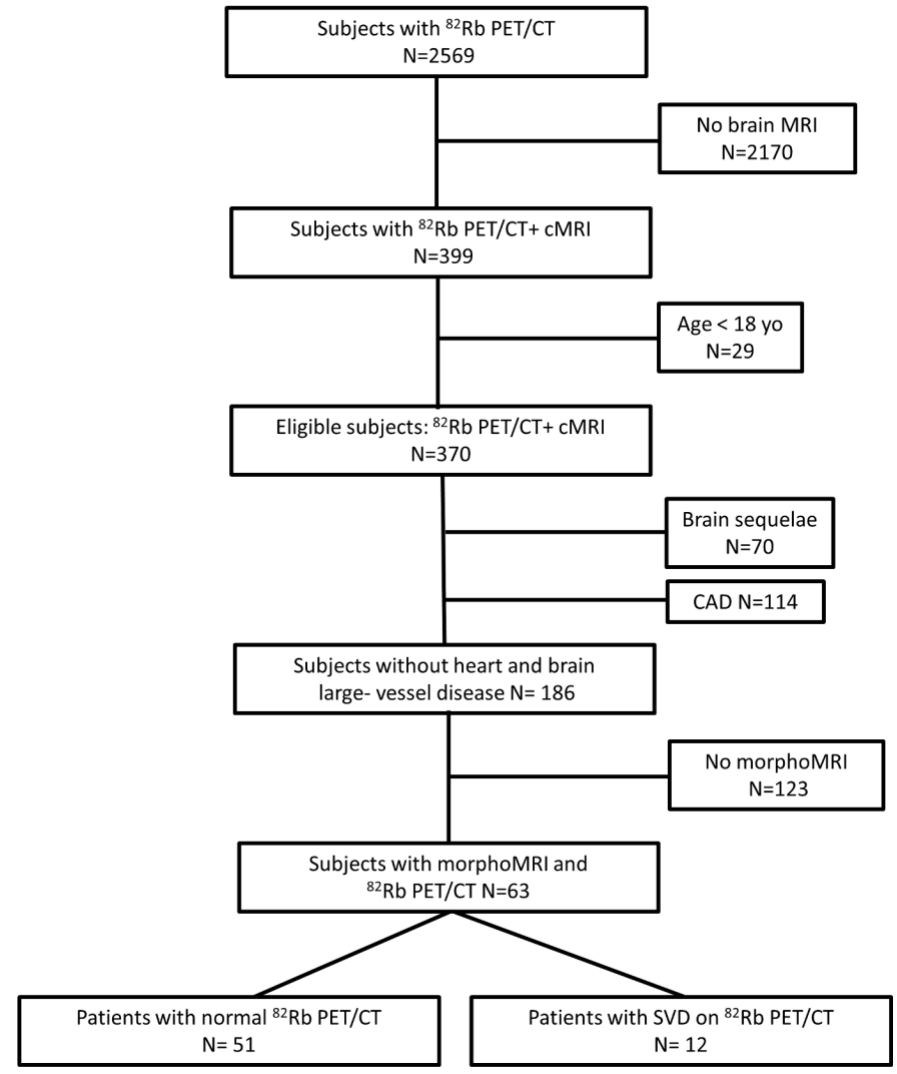

Chapter 9

Human biodistribution and radiation dosimetry of [^{82}Rb] at rest and during peak adenosine stress in a paediatric population

Radiology. (submitted)

Christel H. Kamani, Silvano Gnesin, Stefano Di Bernardo, **Matthieu Dietz**, Gilles Allenbach, Melda Dolan, Marie Nicod-Lalonde, Niklaus Schaefer, Nicole Sekarski, John O. Prior

Abstract

Introduction:

There is no recommendation on the use of [^{82}Rb] PET/CT in the paediatric population, mainly due on lack of [^{82}Rb] dosimetry data in this population. We aimed to estimate paediatric dosimetry based on adult biokinetic data and prospectively acquired paediatric biokinetic data.

Materials and methods:

Organ absorbed doses (OAD) and effective doses (E) were estimated using ICRP-103 based OLINDA/EXM 2.1 software. We extrapolated paediatric OAD and E from existing adult biokinetic data ($OAD_{p,Ab}$ and $E_{p,Ab}$ respectively). Thus, [^{82}Rb] EANM paediatric dosage card (PDC) cluster and the recommended administered activity were determined. Ten paediatric participants (M:F 7:3; mean age 8.8±6.6) underwent dynamic rest and stress 3D-SiPM [^{82}Rb] PET/CT scans in this prospective study. Using PMOD software, source organs volumes were delineated to obtain source organ time activity curves and participant specific organ masses based on PET/CT data. Thus, subject specific OAD (OAD_p and E_p respectively) were derived from original paediatric data.

Results:

[^{82}Rb] was assigned to the EANM PDC B-Cluster. Estimated ranges for $E_{p,Ab}$ resp. E_p were 2.19E-02 −1.15E-03 resp. 9.62E-03 −1.04E-03 mSv/MBq. $E_{p,Ab}$ after a single [^{82}Rb] infusion was between 0.5-0.7 mSv, similar to E_p from for 3D PMT (0.4-0.8 mSv), while E_p was reduced by 0.2-0.4 mSv for 3D SiPM PET/CT. In the paediatric model, the most irradiated organs were the kidneys and the heart wall in infant and newborn group, followed by heart wall in the other age groups, hence, the small intestine, pancreas, lungs, adrenals, and rest of the gastrointestinal tract. [^{82}Rb] PET/CT was safe and well-tolerated by all participants.

Conclusion:

We firstly provide original dosimetry data for the use of [^{82}Rb] PET/CT in the paediatric population, showing reasonably low radiation exposure, and confirming safety and tolerability of [^{82}Rb] PET/CT in this population. Based on our estimations, we provided recommendations for the insertion of [^{82}Rb] in the EANM PDC.

Introduction

In the paediatric population, a thorough non-invasive assessment of myocardial perfusion in certain cardiac conditions such as congenital heart disease, Kawasaki disease or cardiac post-transplant follow-up can be necessary. In this population, the choice of the adequate myocardial perfusion imaging (MPI) tool can be restricted by the length of the acquisition, physiological and dosimetry concerns (1, 2). In regard to limitations, [^{82}Rb] PET/CT could appear as a reasonable alternative to other non-invasive MPI tools such as perfusion SPECT/CT, since it allows for accurate absolute quantitative assessment of myocardial perfusion in a reasonable acquisition time, with reduced radiation exposure due to the [^{82}Rb] short half-life of 75 seconds (sec) (3, 4). Nowadays, while [^{82}Rb] PET/CT is widely recommended in the adult population (5), no recommendation for the administered activity in the paediatric population is available (6, 7), mainly due to the lack of paediatric dosimetry studies. Therefore, the literature on the use of [^{82}Rb] PET/CT in the paediatric population remains scarce (1-3).

The use of adult biokinetic data to derive paediatric radiation dosimetry is a well-established process in nuclear medicine, thus avoiding unnecessary clinical trials in children (8). However, this process relies on the accuracy of adult biokinetic data and on the reliability of translation methods to paediatric subjects. The in-adult biodistribution of [^{82}Rb] has been reported in different studies based on human cohorts and phantoms models (9-16) with up to a four-fold difference in the estimation of the effective dose coefficient (E_{coeff}). Due to their higher risk for adverse events resulting from exposure to radioactive tracers (8), it is strongly recommended to have evidence-based rules striving for the prescription of the minimum [^{82}Rb] activity, providing adequate diagnostic image quality in an acceptable acquisition time in the paediatric population. This study aimed to estimate the organ biokinetic, absorbed doses and effective doses based on prospectively acquired data from a paediatric population as well as extrapolated paediatric biodistribution from previously published adult biokinetic data (12). In addition to dosimetry estimates, we also provided administered-activity recommendation derived from adult biokinetic data (12) in accordance with the European Association of Nuclear medicine (EANM) paediatric dosage card (PDC) methodology (6, 7).

Methods

Participants

Ten paediatric participants referred to our tertiary center with cardiac condition requiring non-invasive MPI were prospectively included in this study. For female participant in childbearing

age, pregnancy was ruled out using a urinary pregnancy test. We included the participants in three groups based on their age with at least 3 participants in each group:

- from 12 to less than 18 years (n=4)
- from 2 to less than 12 years (n=3)
- from 1 month to less than 2 years (n=3)

We enrolled participants in three consecutive steps, first the 12-18 age group, followed by decreasing age groups. A written informed consent was obtained from all participants or his / her legal representative. The protocol was approved by the local ethic committee (CER-VD 2018-02359).

^{82}Sr/^{82}Rb generator

The commercially available ^{82}Sr/^{82}Rb generator from Jubilant DraxImage Inc. (RUBY-FILL® Rubidium [^{82}Rb] Generator) and a dedicated Rubidium Elution System (RbES) (17) were used to provides sterile, nonpyrogenic doses of [^{82}Rb] chloride ([^{82}Rb]Cl), ranging from 37-829 MBq (1 to 22 mCi). Daily quality controls as well as calibration tests were performed before the injection of the first scheduled participant. No significant strontium breakthrough activity was detected during the quality control tests.

Paediatric participant imaging protocol

Participants were asked to fast at least 6 hours prior PET/CT and to abstain from any xanthine derivates (e.g., caffeine or aminophylline) for at least 24 h prior the adenosine stress test. All participants underwent a dynamic rest and adenosine stress silicon photomultiplier (SiPM) PET/CT scan in 3-dimension (3D) acquisition mode, 25-cm axial field-of-view (Biograph Vision 600, Siemens Medical Solutions, Knoxville, USA). The PET acquisition was followed by a low-dose thoraco-(abdominal) CT scan for attenuation correction using automated tube voltage (Care kV, Siemens with quality reference of 100 kV) and automated current modulation (Care DOSE4D, Siemens with a quality reference of 20 mAs). A first dynamic PET/CT acquisition covering the thorax (including heart, thyroid, lung, liver, spleen, stomach, and red bone marrow) and possibly the abdominal region was performed after intravenous (i.v.) administration of 55 - 829 MBq of [^{82}Rb]Cl over 30 sec. In participants where the abdominal organs could not be completely acquired in the initial rest acquisition, a second dynamic PET/CT acquisition centered on the abdomen was performed at rest after a second i.v. administration of 285 - 827 MBq of [^{82}Rb]Cl over 30 sec. The rest phase was followed by a continuous infusion of adenosine at 140 µg/kg/min over 6 min, with concomitant i.v.

administration of 56 - 817 MBq of [^{82}Rb]Cl over 30 sec, from the second minute after starting the adenosine infusion. Further details on the acquisitions protocol can be found in the supplementary material.

Radiation dosimetry formalism

OLINDA/EXM 2.1 software (18) was used to estimate the mean absorbed organ dose $D(r_T)$ to a target organ T from a source organ S, according to the MIRD formalism (19):

$$D(r_T) = \Sigma_S \tilde{A}(r_S) \cdot S(r_T \leftarrow r_S)$$

where $\tilde{A}(r_S)$ is the time-integrated activity coefficient (TIAC) also called ''residence time'' in the considered source organ, S; and $S(r_T \leftarrow r_S)$, also called dose factor, is the specific absorbed dose in a target organ generated by a single decay occurred in a source organ (19). Σ_S indicated that the total absorbed dose to a target organ, from here on called organ absorbed dose (OAD), is obtained by summing the absorbed dose contributions from all relevant source organs in which the radiotracer distributed. In absence of strontium breakthrough on the daily quality controls of the ^{82}Sr/^{82}Rb generator, the contribution of strontium decay chain to the absorbed dose was negligeable.

The effective dose (E) is a radiological protection quantity expressed by the equation:

$$E = \Sigma\, H(r_T) = \Sigma\, D(r_T) \cdot W_T$$

That allows for the estimation of the population-based stochastic risk from internal radiation exposure (20). It is obtained from the sum of all equivalent doses (H) delivered to individual organs. For a specific target tissue, H is obtained by multiplication of $D(r_T)$ for the organ-specific radiation weighting factor (W_T), here form the ICRP-103, which accounts for the specific radiosensitivity to stochastic effects of the considered target organ.

Extrapolation of paediatric OAD and E from adult biokinetic (Ab) data

We extrapolated [^{82}Rb] paediatric $OAD_{P,Ab}$ and $E_{P,Ab}$ from previously published biokinetic data obtained in a cohort of 10 healthy adult volunteers aged between 18 and 50 years old (12). At this purpose, adult TIACs were used in input to OLINDA/EXM 2.1 software program (18), adopting the available paediatric phantom models (15-y, 10-y, 5, 1-y, and newborn). The $E_{P,Ab}$ values were obtained for the gender averaged subjects according to the ICRP 103 formalism (20).

Determination of the baseline administered activity in paediatric participants

The administered radiotracer activity (A_{admin}, in units of MBq) for paediatric participants in our cohort was determined based on the EANM paediatric dosage card (6) using the formula:

$$A_{admin}\,(MBq) = A_B\,(MBq) \cdot CM$$

Where A_B is the radiotracer specific baseline activity in MBq; and CM is the adjusted cluster- and weight-dependent factor.

The paediatric A_B corresponds to the baseline activity to be administered to participants with a body weight of 3kg (6, 7, 21). As previously reported (22, 23), A_B is the 7% of the reference 70-Kg adult baseline activity (700 MBq for PMT and 350 MBq for SiPM PET devices respectively). Moreover, limitation of the infusion system of the $^{82}Sr/^{82}Rb$ generator, which cannot inject less than 37 MBq, should be taken into consideration.

CM depends on the participant body weight, and it is defined for clusters of radiopharmaceuticals. The EANM PDC considers three clusters. We used the methodology proposed by Jacobs et al (21)to determine the pertinent cluster for [^{82}Rb]Cl. More details on the [^{82}Rb]Cl cluster determination can be found in the supplementary material.

OAD and E from paediatrics biokinetic data

To derive in-pediatric organ absorbed dose (OAD_P) and effective doses (E_P), PMOD (PMOD Technologies, Zurich, Switzerland v.4.105) was used to delineate the source organs in the co-registered PET/CT images of the 10 included paediatric participants, with CT data as reference for morphologic organ segmentation. For each participant, for both the rest and stress conditions, we obtained organ specific normalized TACs (nTACs), organ specific time-integrated activity coefficient (TIACs in MBq·h/MBq), mean OAD_P (in mGy/MBq), the $W_{T.ICRP-103}$ specific E_P (in mSv/MBq) and subject E_P (in mSv) were obtained. Further details on the dosimetry can be found in the supplementary methods.

Dosimetry comparison: extrapolation form adult biokinetic vs. paediatric biokinetic data

For the cases 3D PMT and SiPM PET/CT cardiac examinations, we compared E_p and $E_{P,Ab}$ after a single infusion of [^{82}Rb]Cl. Regarding the effective dose for SiPM PET/CT in the newborn group, due to the technical limitation of the infuser, the minimal injected activity was

37 MBq in our study. For the calculation of the effective doses, we used the reference body weight for different age groups as proposed by the ICRP 89 (24).

Safety and tolerability

Safety and tolerability data were assessed in all participants. Safety and tolerability endpoints, including assessment of vital signs, clinical symptoms, electrocardiograms at different timepoints, and advert events in a time interval of 7 days after [^{82}Rb]Cl administration were reviewed throughout the study. We performed a safety evaluation after completion of each age group before moving on to the next younger age group.

Results

Participant characteristics

Ten paediatric participants (7 male and 3 female) aged between 1 month and 16 years (8.8 ± 6.6) were included in the study. All participants underwent one rest and one stress dynamic [^{82}Rb]Cl PET/CT. Five participants underwent a second dynamic rest acquisition centered on abdomen. Table 1 gives a summary of the participant characteristics.

Paediatric dose extrapolated from adult biokinetic data

Extrapolated target $OAD_{P,Ab}$ (mGy/MBq) and specific $E_{P,Ab}$ (mSv/MBq) are reported in table 2.

Dosimetry from paediatric biokinetic data

In Figure 1, we show a representative example of the contouring of the source organs for the estimation of TACs.

Figure 2 shows nTACs for both rest and stress conditions in selected source organs while for the same organs, Figure 3 displays the %IA/g obtained in rest condition as a function of the considered age group.

In Table 3, we reported $OAD_{P,mean}$ and $E_{P,mean}$ as average (rest and stress conditions) subject OAD_P for target organs and E_P obtained from our paediatric participant cohort (OLINDA/EXM 2.1 and ICRP 103 formalism), stratified for group of ages.

Comparison of paediatric Effective dose obtained from in-adult extrapolated and paediatric biokinetic data

Figure 4 illustrates a comparison between $E_{P,Ab}$ resp. $E_{P,mean}$ (in mSv), after a single [^{82}Rb]Cl infusion, obtained from in-adult biokinetic data (data from 3D-PMT PET/CT) resp. from the paediatric population (data from 3D-PMT and SiPM PET/CT) analyzed in the present study.

Figure 5 illustrates the difference in the mean effective dose coefficient between the in-adult biokinetic data and from the paediatric population analyzed in the present study, as presented in Tables 2 and 3.

In supplemental Table 1 and 2, we reported the source organ TIACs, the OAD_P and E_P for the 10 paediatric participants obtained in both rest and stress conditions. In supplement Figure 1, we show an illustration on the calculation of the "*a*-value" and r^2 value.

Calculation of "*a* value" for the [^{82}Rb] EANM PDC cluster classification

We calculated an "*a* value" of -0.89 (R^2 =0.99) and -0.92 (R^2 =0.99) for [^{82}Rb]Cl, from adult biokinetic extrapolations to paediatrics and paediatric participant data respectively.

Figure 6 illustrates the [^{82}Rb]Cl "a value" in relation to the "a factor" range of the different radiopharmaceuticals. Based on these calculations, [^{82}Rb]Cl can be classified in the B cluster of the EANM PDC.

Recommendation for the [^{82}Rb]Cl baseline administered activity for paediatrics

We calculated an A_B of 49 resp. 24.5 MBq for PMT resp. SiPM [^{82}Rb] PET/CT examination respectively. However, due to the limitation of the infusion system of the ^{82}Sr/^{82}Rb generator, which cannot inject less than 37 MBq, this latter activity value was given as the baseline and minimum recommended [^{82}Rb]Cl activity. Thus, following recommendation can be made for the paediatric dosage card:

Safety and tolerability of [^{82}Rb]Cl administered intravenously

No safety issue related to the administration of [^{82}Rb]Cl were noted during the whole study. Furthermore, no significant safety issue or adverse events in relation to [^{82}Rb]Cl administration or not related to [^{82}Rb]Cl administration were reported.

Discussion

Our study provides the first dosimetry estimates of the cardiac [^{82}Rb] PET/CT in a paediatric population, based on extrapolated estimation from in-adult biokinetic data (12) as well as prospective paediatric biokinetic data. E_P obtained from our paediatric population as well as from the extrapolation from in-adult biokinetic data, were estimated between 1E-3 and 11E-3 mSv/MBq, depending on the age group. This information supports the approach of adjusting the administered activity of [^{82}Rb]Cl as a function of the body weight of the paediatric patient as applied in the EANM PDC approach.

Available [^{82}Rb] biokinetic data obtained in previous studies used different methodological approaches, namely the in-vivo in-adult human or animal and the Monte Carlo absorbed dose extrapolation from Monte Carlo computation of in-silico adult subjects. Based on the model used, a significant variation in the estimation of [^{82}Rb] E up to four-fold was observed (9-16), with values ranging between 3.4E-3 mSv/MBq (ICRP 53 model (25)), 1.7E-3mSv/MBq (Leggett et al. model al (26)) and 0.79E-3 mSv/MBq (Stabin model (9)). In 2010, Senthamizhchelvan et al. published adult biokinetic data on 10 healthy volunteers at rest, using a multi-bed, multi-injection PET/CT acquisition protocol allowing the inclusion of many relevant source organs (12). Using the OLINDA/EXM 1.0 and both the $W_{T.ICRP-60}$ (15) and $W_{T.ICRP-103}$ (20), the authors calculated an [^{82}Rb] E of 1.1 resp. 1.26E-3 mSv/MBq, respectively. These results were confirmed under stress conditions in a successive human dosimetry study (13). Finally, Hunter et al. investigated the [^{82}Rb] biodistribution in 30 participants with known or suspected CAD (11), using a multibed, multi-injection protocol. The authors estimated an $W_{T.ICRP-103}$ E by 0.8E-3 mSv/MBq, a value close to the estimated value of the Stabin model (9).

We based our paediatric dosimetry extrapolation on adult biokinetic data from Senthamizhchelvan et al (12). This choice was motivated by the similarity of the PET acquisition methodology. Secondly, the results are a reasonable compromise between the Leggett et al model (26) and the ICRP 53 model (25). Finally, the estimated E in (12) is the most conservative among the available estimates based on human data. $E_{P,Ab}$ was between 1.12E-3 and 11E-3 mSv/MBq, corresponding to an estimated subject $E_{P,Ab}$ after a single infusion of [^{82}Rb] between 0.5 mSv and 0.7 mSv for 3D PMT acquisitions. The most irradiated organs in all age groups were kidneys, followed by heart wall, adrenal, spleen, lung, pancreas, thyroid, and the gastrointestinal tract.

Our prospective paediatric study, conducted in accordance with the EANM PDC (6, 7) methodology, enabled a specific assessment of the [^{82}Rb] cluster, baseline and minimum

activity required to adapt the PDC approach for the specific examination. [^{82}Rb] assignment to the B-Cluster was expected, since [^{82}Rb] is neither a tracer for renal studies (Cluster A) nor an iodine-labelled tracer for thyroid study (Cluster C). The choice of 700 MBq as adult reference activity for the determination of the baseline activity was guided by its proximity to the mean administered activity used in the Ruby-Fill™ efficacy study to support [^{82}Rb] adult marketing application (27) as well as to the lower limit of adult activity recommended in the MPI guidelines (22). We do not recommend a minimum activity of [^{82}Rb] beyond the baseline activity based on the controversy in the determination of a minimum activity for 18 fluorine ([^{18}F]) tracers in the paediatric population (6, 7, 28, 29), and due to the absence of significant clinical experiences supporting this rationale, as stated by the authors of the first EANM PDC (30).

In our original and prospective paediatric biokinetic analysis, using the same methodology as Senthamizhchelvan et al. (12), and following the above-mentioned recommendations, we estimated E_P between 1E-3 and 10E-3 mSv/MBq, corresponding to an estimated subject E_P after a single infusion of [^{82}Rb] between 0.5 mSv and 0.8 mSv for 3D PMT acquisitions, for the 15yo and the new-born subject respectively. We observed no significant variation of E between stress and rest study, as reported in the adult population (13). Organ TAC from both rest and stress conditions (Figure 2) showed the same behaviors and very similar values at method time. Kidneys and the heart wall in infant and newborn group received the higher absorbed dose, followed by heart wall (in the other age groups), small intestine, pancreas, spleen, lungs, adrenals, and the rest of gastrointestinal tract. The analysis of the %IA/g values (Figure 3) as a function of the time after administration and stratified by age group (12-18, 3-12 and 0-3 yo respectively) clearly showed that higher values are obtained in the younger patient population characterized by organs of reduced volumes. This fact translated in higher OAD_P and E_P values as the subject age decreases (Table 3). When compared to the extrapolated paediatric dosimetry estimations from in-adult data, the prospective paediatric dosimetry estimations showed no significant difference in the age-specific and subject effective dose for 3D PMT acquisitions (Figures 4 and 5). Thus, our prospective acquired paediatric biokinetic data confirmed the estimation obtained from the paediatric extrapolation from in-adult biokinetic data.

Using 3D-SiPM instead of 3D-PMT PET/CT allows for halving the adult reference activity (23). This results in an important reduction of the subject E_P after a single infusion of [^{82}Rb] between 0.2 mSv and 0.4 mSv for 3D-SiPM PET/CT (Figure 3). Even when considering the minimum injected activity of 37 MBq due to the infusion system, the estimated newborn E_P in

the 3D-SiPM group remains lower in comparison to the one in the 3D-PMT group (Figure 3). Thus, a rest and stress [^{82}Rb] PET/CT study is feasible in the paediatric population with less than 1 mSv irradiation when using 3D-SiPM PET/CT system, in opposition to the estimation between 11 mSv and 40 mSv in a previous study using older PET/CT technology (1). This places [^{82}Rb] in the same lower dose range as alternative PET perfusion tracers such as ammonia (31). Moreover, besides advantages such as the better resolution, the shorter procedure time and the possibility for absolute quantification of MBF supporting the preference for PET/CT over SPECT/CT, especially in the paediatric population (31), [^{82}Rb] PET/CT helps to guide the clinical management of these patients, avoiding the need for invasive coronarography in some patients. Finally, no significant adverse events related to the use of [^{82}Rb]Cl were reported in our study, which was in line with previous reports (1-3).

Even if the population is prospectively included, our study is limited by the small number of participants. However, previous relevant studies on adult dosimetry (12, 13) also included the same number of patients. In our study, for a better representation of the different age classes, participants were divided into different age groups and inclusion was made according to these classifications. Using this strategy helped to guarantee a minimum of representability of each paediatric age group.

Conclusion

Our study is the first providing comprehensive and detailed dosimetry for [^{82}Rb] in the paediatric population. Our data suggest a reasonably low paediatric radiation exposure for a full stress and rest study, with less than 1 mSv irradiation when using 3D-SiPM PET/CT system. The procedure is safe and well tolerated in this population. Based on these results, we proposed a recommendation for an additional line in the EANM PDC for [^{82}Rb] 3D-PMT and 3D-SiPM PET/CT.

Table 1: Characteristics of the studied paediatric participant population

Participant	Age	Sex	Height (cm)	Weight (kg)	BMI (kg/m^2)	Reference Phantom (year)	[^{82}Rb]Cl administered activity (MBq)			Sedation	Diagnosis	Surgery
							Rest - Thorax	Rest- Abdomen	Stress- Thorax			
1	15	M	170	80	28	15	829	827	817	No	Congenital dilated cardiomyopathy	Cardiac transplantation
2	16	M	173	74	25	15	763	765	762	No	Anomalous insertion of the LCA	Reimplantation of the LCA
3	15	M	176	56	18	15	598	594	576	No	Transposition of the great arteries	Arterial switch surgery
4	14	F	151	46	20	15	489	492	492	No	Transposition of the great arteries	Arterial switch surgery
5	8	M	135	33	18	10	377	NA	379	No	Non-familial hypertrophic cardiomyopathy	Cardiac transplantation
6	7	F	121	21	14	5	257	NA	260	No	Acute cardiac decompensation with cardiac arrest	Cardiac transplantation
7	8	M	121	24	16	10	283	285	288	No	Kawasaki disease	NA
8	< 1	F	60	5.8	16	NB	87	NA	87	Drug sedation	Anomalous insertion of the LCA	Reimplantation of the LCA
9	1	M	78	9.8	16	1	134	NA	135	Breastfeeding before the PET/CT	Pulmonary atresia with intact interventricular septum	Ligation of the ductus arteriosus and right Blalock-Taussig shunt
10	< 1	M	56	4	13	NB	55	NA	56	Breastfeeding before the PET/CT	Transposition of the great arteries	Arterial switch surgery

BMI : Body mass index ; LCA : left coronary artery ; MBq : Megabecquerel; NA: not applicable

Table 2: $OAD_{P,Ab}$ and (Olinda/EXM v.2.1, ICRP-103) $E_{P,Ab}$ estimates from in-adult biokinetic data

		Adult	15 yo	10 yo	5 yo	1 yo	Newborn
TARGET $OAD_{P,Ab}$ (mGy/MBq)	Adrenals	2.51E-03	3.39E-03	4.83E-03	7.17E-03	1.05E-02	1.34E-02
	Brain	1.48E-04	1.48E-04	1.69E-04	2.11E-04	3.07E-04	7.05E-04
	Breasts	1.50E-04	2.20E-04	0.00E+00	0.00E+00	0.00E+00	0.00E+00
	Esophagus	4.42E-04	5.36E-04	8.94E-04	1.68E-03	3.28E-03	1.00E-02
	Eyes	3.02E-04	3.55E-04	5.96E-04	1.11E-03	2.13E-03	5.77E-03
	Gallbladder Wall	9.13E-04	1.09E-03	1.77E-03	2.99E-03	5.74E-03	1.58E-02
	Left colon	9.50E-04	1.16E-03	1.95E-03	2.96E-03	4.55E-03	1.04E-02
	Small Intestine	1.39E-03	1.58E-03	2.65E-03	3.96E-03	5.88E-03	1.23E-02
	Stomach Wall	1.12E-03	1.34E-03	2.23E-03	3.40E-03	5.23E-03	1.20E-02
	Right colon	7.57E-04	9.30E-04	1.55E-03	2.40E-03	3.81E-03	8.80E-03
	Rectum	7.12E-04	8.72E-04	1.50E-03	2.38E-03	3.87E-03	8.92E-03
	Heart Wall	2.50E-03	3.12E-03	5.93E-03	8.05E-03	1.06E-02	3.31E-02
	Kidneys	*5.35E-03*	*6.32E-03*	*8.46E-03*	*1.35E-02*	*2.06E-02*	*5.27E-02*
	Liver	1.11E-03	1.33E-03	2.03E-03	2.98E-03	5.09E-03	1.23E-02
	Lungs	2.13E-03	2.70E-03	4.24E-03	6.81E-03	1.26E-02	2.73E-02
	Ovaries	3.15E-04	4.47E-04	7.12E-04	1.11E-03	2.22E-03	7.06E-03
	Pancreas	1.75E-03	2.12E-03	3.54E-03	5.86E-03	9.79E-03	2.83E-02
	Prostate	3.20E-04	4.00E-04	6.72E-04	1.17E-03	2.74E-03	6.12E-03
	Salivary Glands	3.18E-04	3.84E-04	4.01E-04	1.16E-03	2.20E-03	6.13E-03
	Red Marrow	3.26E-04	3.68E-04	5.92E-04	1.03E-03	2.28E-03	6.20E-03
	Osteogenic Cells	2.51E-04	3.17E-04	4.75E-04	7.09E-04	1.41E-03	3.51E-03
	Spleen	2.15E-03	2.33E-03	3.67E-03	5.83E-03	9.88E-03	2.68E-02
	Testes	1.80E-04	3.24E-04	1.80E-03	2.30E-03	3.14E-03	5.37E-03
	Thymus	5.23E-04	6.15E-04	9.87E-04	1.82E-03	3.67E-03	1.12E-02
	Thyroid	1.51E-03	2.18E-03	3.13E-03	6.44E-03	9.86E-03	1.39E-02
	Urinary Bladder Wall	4.24E-04	5.00E-04	8.14E-04	1.56E-03	2.86E-03	8.01E-03
	Uterus	9.22E-04	2.14E-03	1.26E-02	1.62E-02	2.85E-02	1.39E-02
	Total Body	4.64E-04	5.43E-04	9.04E-04	1.50E-03	2.82E-03	7.74E-03
	$E_{P,Ab}$ (mSv/MBq)	8.97E-04	1.12E-03	1.80E-03	2.89E-03	4.91E-03	1.11E-02

Orange italic represents highest absorbed dose

Table 3: $OAD_{P,mean}$, specific/subject $E_{P,mean}$ (Olinda/EXM v.2.1, ICRP-103) from paediatric biokinetic data.

	Ref. phantom (yo)	15	10	5	1	NB
	Nb. of participants	4	2	1	1	2
	Nb. of [^{82}Rb] studies	8	4	2	2	4
TARGET OAD (mGy/MBq)	Adrenals	1.71E-03	2.42E-03	4.14E-03	7.27E-03	1.14E-02
	Brain	2.76E-04	5.11E-04	7.56E-04	1.72E-03	3.75E-03
	Breasts	9.25E-05	0.00E+00	0.00E+00	0.00E+00	0.00E+00
	Esophagus	4.81E-04	8.06E-04	1.34E-03	3.81E-03	9.85E-03
	Eyes	2.76E-04	5.12E-04	7.43E-04	2.18E-03	4.33E-03
	Gallbladder Wall	5.40E-04	9.08E-04	1.20E-03	3.36E-03	6.29E-03
	Left colon	2.05E-03	4.98E-03	6.35E-03	5.25E-03	1.55E-02
	Small Intestine	3.23E-03	9.42E-03	1.13E-02	9.16E-03	2.27E-02
	Stomach Wall	1.11E-03	2.76E-03	5.77E-03	7.84E-03	1.49E-02
	Right colon	1.49E-03	3.47E-03	4.54E-03	3.93E-03	1.16E-02
	Rectum	1.37E-03	3.26E-03	4.17E-03	4.25E-03	1.10E-02
	Heart Wall	4.23E-03	6.95E-03	1.11E-02	*2.36E-02*	*3.92E-02*
	Kidneys	*7.84E-03*	*1.00E-02*	*1.34E-02*	*2.20E-02*	*2.75E-02*
	Liver	1.43E-03	2.79E-03	3.54E-03	5.72E-03	1.10E-02
	Lungs	2.10E-03	4.01E-03	4.80E-03	1.37E-02	1.70E-02
	Ovaries	1.08E-04	0.00E+00	9.36E-04	0.00E+00	1.42E-03
	Pancreas	3.04E-03	5.35E-03	6.57E-03	1.00E-02	1.94E-02
	Prostate	2.39E-04	6.48E-04	0.00E+00	2.45E-03	2.97E-03
	Salivary Glands	2.99E-04	5.41E-04	8.02E-03	2.19E-03	2.84E-02
	Red Marrow	6.54E-04	1.25E-03	1.03E-03	3.45E-03	7.09E-03
	Osteogenic Cells	5.11E-04	7.93E-04	7.40E-04	2.22E-03	5.42E-03
	Spleen	2.61E-03	3.28E-03	5.15E-03	8.48E-03	1.45E-02
	Testes	2.01E-04	5.20E-04	1.53E-03	2.43E-03	7.82E-03
	Thymus	5.39E-04	8.32E-04	0.00E+00	3.95E-03	4.30E-03
	Thyroid	5.57E-04	3.62E-03	4.84E-03	4.49E-03	9.75E-03
	Urinary Bladder Wall	3.65E-04	5.97E-04	8.41E-04	2.44E-03	5.21E-03
	Uterus	1.15E-04	0.00E+00	1.01E-03	0.00E+00	1.55E-03
	Total Body	4.96E-04	9.61E-04	1.37E-03	2.89E-03	5.83E-03
	Specific $E_{P,mean}$ (mSv/MBq)	1.04E-03	2.16E-03	3.08E-03	5.17E-03	9.62E-03
	Subject $E_{p,mean}$ (mSv)	6.68E-01	6.85E-01	7.96E-01	6.87E-01	6.82E-01

Values are obtained as mean of rest and stress values grouped according to participant age. *Orange italic* represents highest absorbed dose

Table 4: Recommendation for an additional line in the EANM PDC on the use of [^{82}Rb] PET/CT

Radiopharmaceutical (PET/CT system)	Class	Baseline activity * (MBq)	Minimum recommended activity (MBq)
[^{82}Rb] (3D, SiPM detectors) Recommended in children	B	24.5	37
[^{82}Rb] (3D, PMT detectors)	B	49.0	49

*for calculation purpose only

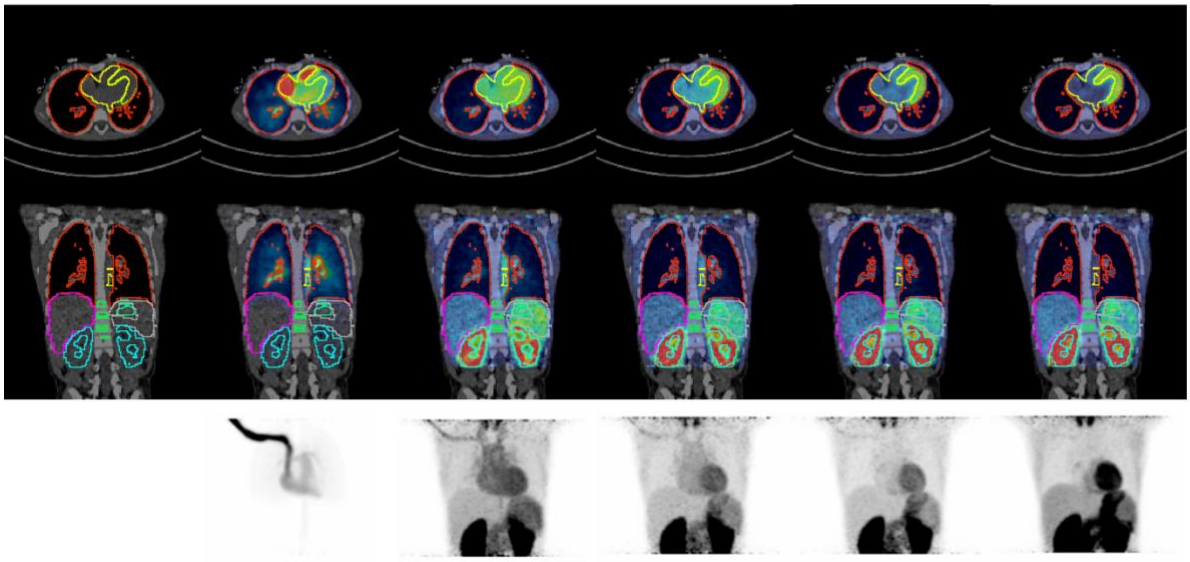

Figure 1: PET/CT axial, coronal and MPI of Participant #6 for the frames (from the left to the right) 4, 28, 60, 92, 138, 306 sec after the start of the administration. PET image intensity is decay-corrected at the start of the administration.

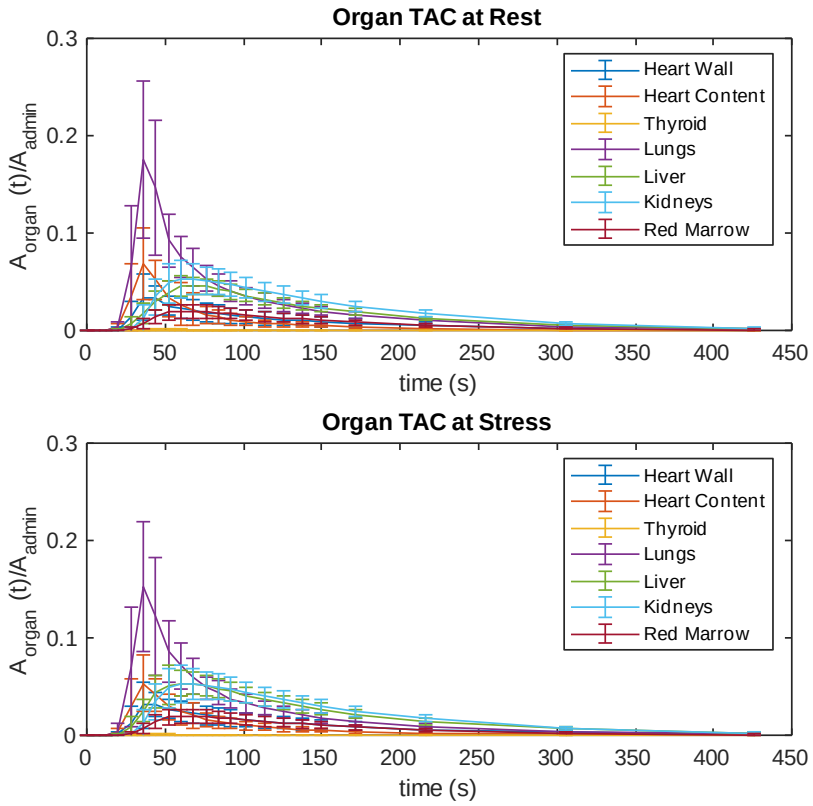

Figure 2: [^{82}Rb]Cl organ time-activity curves of selected source organs at rest and stress.

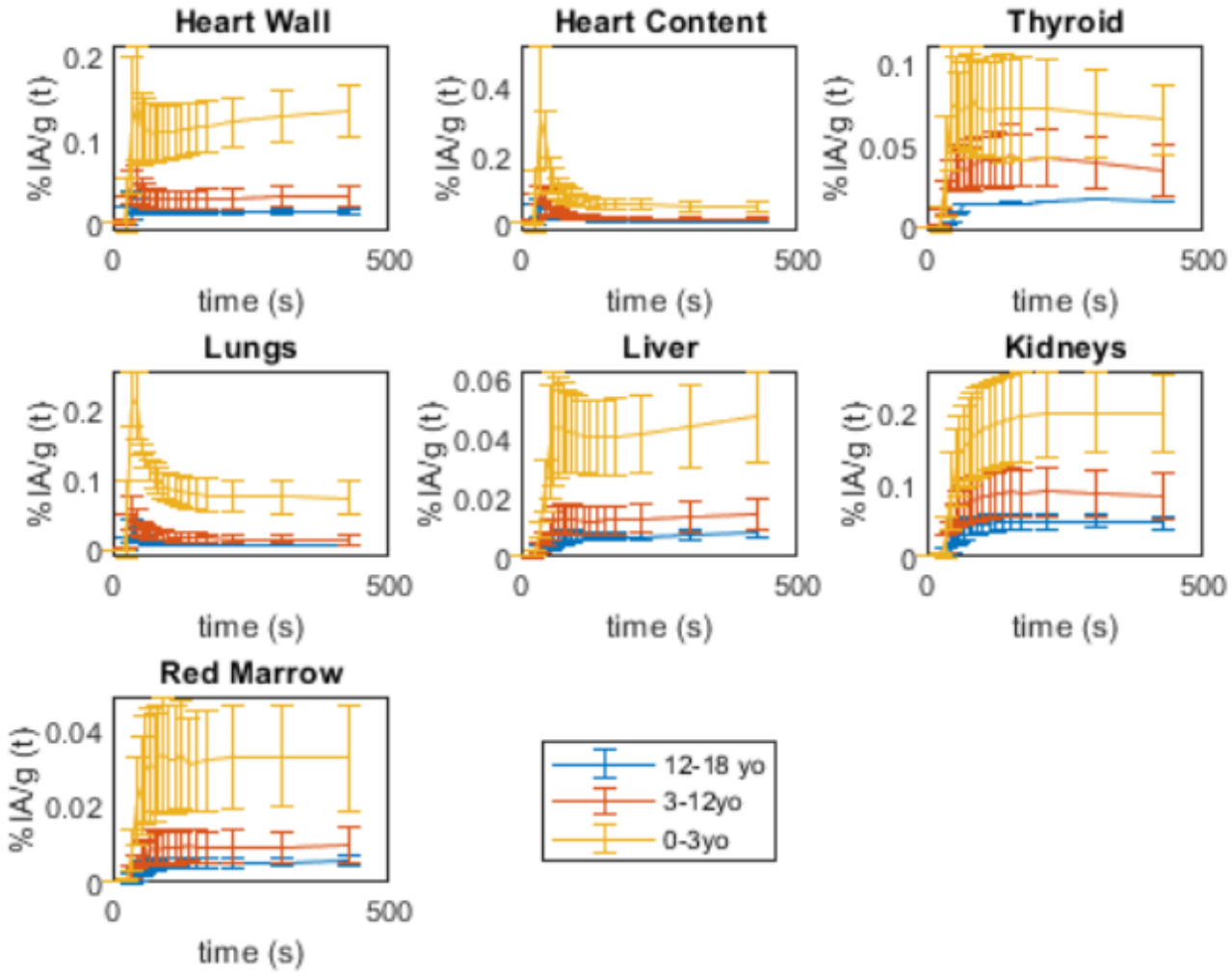

Figure 3: [^{82}Rb]Cl %IA/g of selected source organs at rest. The values are displayed as a function of the specific group of age. %IA/g are corrected for physical decay at the time of the start of the administration.

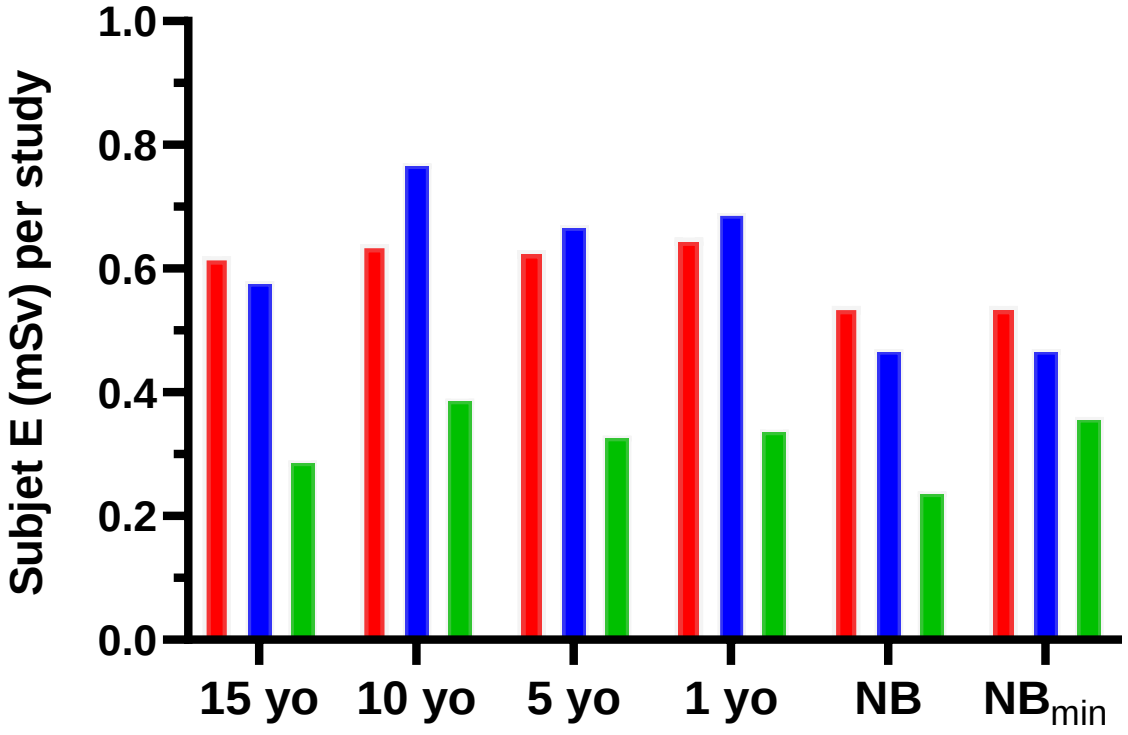

Figure 4: Comparison of the effective dose per single [^{82}Rb]Cl study as estimated from in-adult biokinetic data (12) (in red) and from the considered paediatric biokinetic data. For this latter, a further differentiation was made between 3D-PMT (in blue) and 3D-SiPM PET/CT (in green). NB_{min} represents the estimation of the effective dose in the newborn group, taking into consideration the minimal injected activity of 37 MBq of the infuser for the 3D-SiPM model.

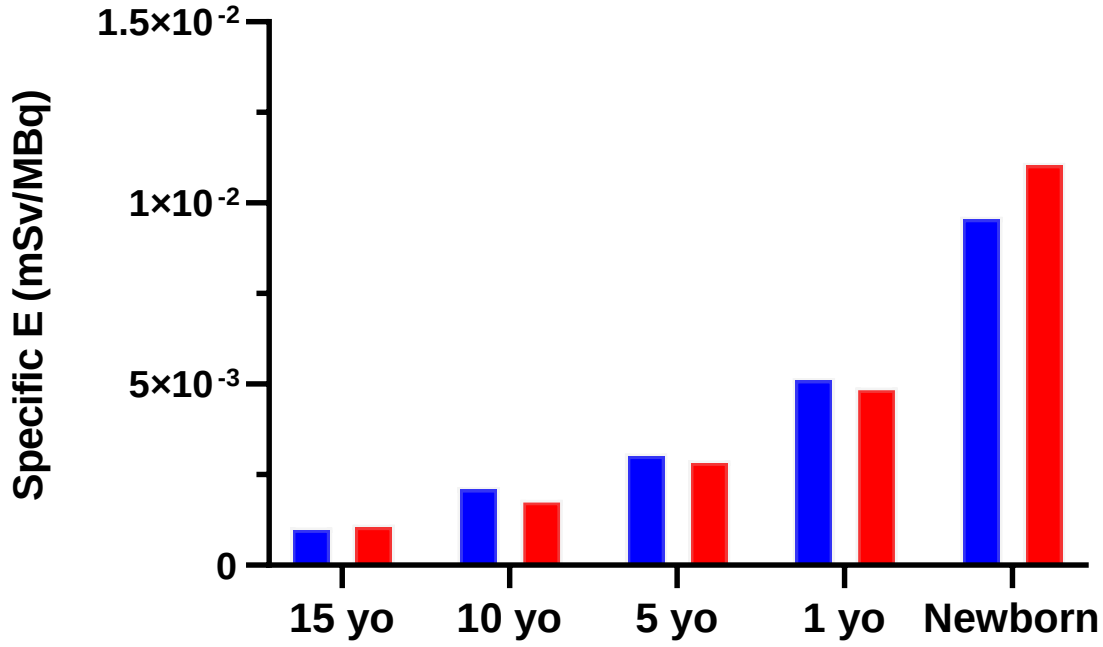

Figure 5: Illustration of the difference in the mean effective dose coefficient as estimated by the in-adult extrapolated paediatric biokinetic data (12) (in red) and those from our paediatric population (in blue).

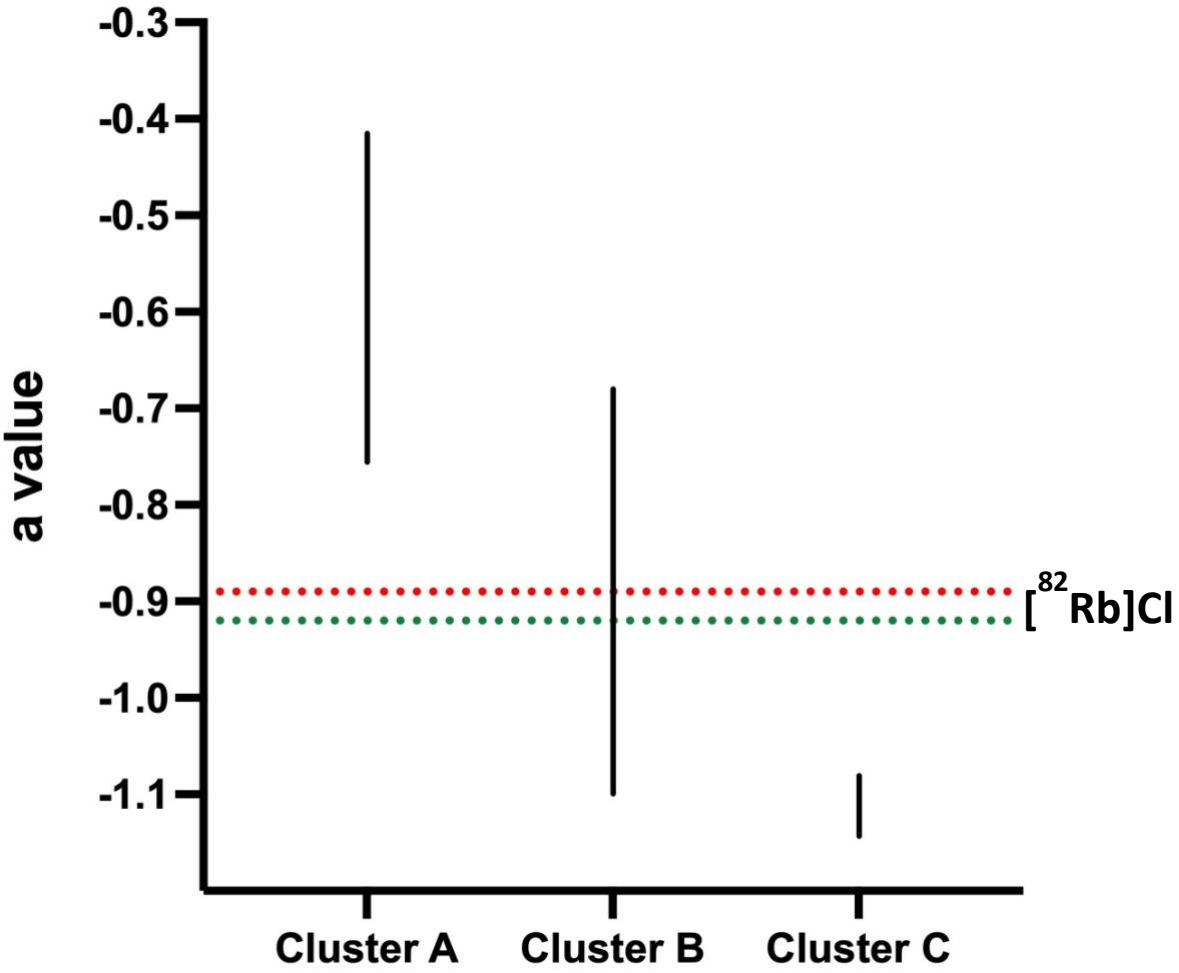

Figure 6: Representation of the [^{82}Rb]Cl "*a* value" in relation to the "*a* value" ranges of the different radiopharmaceuticals. Continue black lines represent the "a value" ranges of the cluster groups of the EANM paediatric dosage card. Discontinued lines represent the corresponding [^{82}Rb]Cl a value calculated from $E_{P,Ab}$ (red line) and E_P (green line).

References

1. Chhatriwalla AK, Prieto LR, Brunken RC, Cerqueira MD, Younoszai A, Jaber WA. Preliminary data on the diagnostic accuracy of rubidium-82 cardiac PET perfusion imaging for the evaluation of ischemia in a pediatric population. Pediatr Cardiol 2008;29(4):732-738. doi: 10.1007/s00246-008-9232-1

2. Hernandez-Pampaloni M, Allada V, Fishbein MC, Schelbert HR. Myocardial perfusion and viability by positron emission tomography in infants and children with coronary abnormalities: correlation with echocardiography, coronary angiography, and histopathology. J Am Coll Cardiol 2003;41(4):618-626. doi: 10.1016/s0735-1097(02)02867-x

3. Venet M, Friedberg MK, Mertens L, Baranger J, Jalal Z, Tlili G, Villemain O. Nuclear Imaging in Pediatric Cardiology: Principles and Applications. Front Pediatr 2022;10:909994. doi: 10.3389/fped.2022.909994

4. Prior JO, Allenbach G, Valenta I, Kosinski M, Burger C, Verdun FR, Bischof Delaloye A, Kaufmann PA. Quantification of myocardial blood flow with 82Rb positron emission tomography: clinical validation with 15O-water. Eur J Nucl Med Mol Imaging 2012;39(6):1037-1047. doi: 10.1007/s00259-012-2082-3

5. Knuuti J, Wijns W, Saraste A, Capodanno D, Barbato E, Funck-Brentano C, Prescott E, Storey RF, Deaton C, Cuisset T, Agewall S, Dickstein K, Edvardsen T, Escaned J, Gersh BJ, Svitil P, Gilard M, Hasdai D, Hatala R, Mahfoud F, Masip J, Muneretto C, Valgimigli M, Achenbach S, Bax JJ, Group ESCSD. 2019 ESC Guidelines for the diagnosis and management of chronic coronary syndromes. Eur Heart J 2020;41(3):407-477. doi: 10.1093/eurheartj/ehz425

6. Lassmann M, Biassoni L, Monsieurs M, Franzius C, Jacobs F, Dosimetry E, Paediatrics C. The new EANM paediatric dosage card. Eur J Nucl Med Mol Imaging 2007;34(5):796-798. doi: 10.1007/s00259-007-0370-0

7. Lassmann M, Biassoni L, Monsieurs M, Franzius C, Jacobs F, Dosimetry E, Paediatrics C. The new EANM paediatric dosage card. Eur J Nucl Med Mol Imaging 2008;35(9):1748. doi: 10.1007/s00259-007-0572-5

8. Treves ST, Falone AE, Fahey FH. Pediatric nuclear medicine and radiation dose. Semin Nucl Med 2014;44(3):202-209. doi: 10.1053/j.semnuclmed.2014.03.009

9. Stabin MG. Radiopharmaceuticals for nuclear cardiology: radiation dosimetry, uncertainties, and risk. J Nucl Med 2008;49(9):1555-1563. doi: 10.2967/jnumed.108.052241
10. Einstein AJ, Moser KW, Thompson RC, Cerqueira MD, Henzlova MJ. Radiation dose to patients from cardiac diagnostic imaging. Circulation 2007;116(11):1290-1305. doi: 10.1161/CIRCULATIONAHA.107.688101
11. Hunter CR, Hill J, Ziadi MC, Beanlands RS, deKemp RA. Biodistribution and radiation dosimetry of (82)Rb at rest and during peak pharmacological stress in patients referred for myocardial perfusion imaging. Eur J Nucl Med Mol Imaging 2015;42(7):1032-1042. doi: 10.1007/s00259-015-3028-3
12. Senthamizhchelvan S, Bravo PE, Esaias C, Lodge MA, Merrill J, Hobbs RF, Sgouros G, Bengel FM. Human biodistribution and radiation dosimetry of 82Rb. J Nucl Med 2010;51(10):1592-1599. doi: 10.2967/jnumed.110.077669
13. Senthamizhchelvan S, Bravo PE, Lodge MA, Merrill J, Bengel FM, Sgouros G. Radiation dosimetry of 82Rb in humans under pharmacologic stress. J Nucl Med 2011;52(3):485-491. doi: 10.2967/jnumed.110.083477
14. Kearfott KJ. Radiation absorbed dose estimates for positron emission tomography (PET): K-38, Rb-81, Rb-82, and Cs-130. J Nucl Med 1982;23(12):1128-1132.
15. 1990 Recommendations of the International Commission on Radiological Protection. Ann ICRP 1991;21(1-3):1-201.
16. Ryan J, Harper P, Stark V, Peterson E, Lathrop K. Radiation absorbed dose estimate for rubidium-82 determined from in-vivo measurements in human subjects. Oak Ridge Associated Universities 1985(Fourth International Radiopharmaceutical Dosimetry Symposium):346-358.
17. Klein R, Adler A, Beanlands RS, Dekemp RA. Precision-controlled elution of a 82Sr/82Rb generator for cardiac perfusion imaging with positron emission tomography. Phys Med Biol 2007;52(3):659-673. doi: 10.1088/0031-9155/52/3/009
18. Stabin MG. OLINDA/EXM 2-The Next-generation Personal Computer Software for Internal Dose Assessment in Nuclear Medicine. Health Phys 2023. doi: 10.1097/HP.0000000000001682
19. Bolch WE, Eckerman KF, Sgouros G, Thomas SR. MIRD pamphlet No. 21: a generalized schema for radiopharmaceutical dosimetry--standardization of nomenclature. J Nucl Med 2009;50(3):477-484. doi: 10.2967/jnumed.108.056036
20. The 2007 Recommendations of the International Commission on Radiological Protection. ICRP publication 103. Ann ICRP 2007;37(2-4):1-332. doi: 10.1016/j.icrp.2007.10.003

21. Jacobs F, Thierens H, Piepsz A, Bacher K, Van de Wiele C, Ham H, Dierckx RA, European Association of Nuclear M. Optimised tracer-dependent dosage cards to obtain weight-independent effective doses. Eur J Nucl Med Mol Imaging 2005;32(5):581-588. doi: 10.1007/s00259-004-1708-5
22. Dilsizian V, Bacharach SL, Beanlands RS, Bergmann SR, Delbeke D, Dorbala S, Gropler RJ, Knuuti J, Schelbert HR, Travin MI. ASNC imaging guidelines/SNMMI procedure standard for positron emission tomography (PET) nuclear cardiology procedures. J Nucl Cardiol 2016;23(5):1187-1226. doi: 10.1007/s12350-016-0522-3
23. Alahdab F, Al Rifai M, Ahmed AI, Al-Mallah MH. Advances in Digital PET Technology and Its Potential Impact on Myocardial Perfusion and Blood Flow Quantification. Curr Cardiol Rep 2023. doi: 10.1007/s11886-023-01850-5
24. Basic anatomical and physiological data for use in radiological protection: reference values. A report of age- and gender-related differences in the anatomical and physiological characteristics of reference individuals. ICRP Publication 89. Ann ICRP 2002;32(3-4):5-265.
25. Radiation dose to patients from radiopharmaceuticals. A report of a Task Group of Committee 2 of the International Commission on Radiological Protection. Ann ICRP 1987;18(1-4):1-377.
26. Leggett RW, Williams LR. A proposed blood circulation model for Reference Man. Health Phys 1995;69(2):187-201. doi: 10.1097/00004032-199508000-00003
27. Klein R, Ocneanu A, Renaud JM, Ziadi MC, Beanlands RSB, deKemp RA. Consistent tracer administration profile improves test-retest repeatability of myocardial blood flow quantification with (82)Rb dynamic PET imaging. J Nucl Cardiol 2018;25(3):929-941. doi: 10.1007/s12350-016-0698-6
28. Holm S, Borgwardt L, Loft A, Graff J, Law I, Hojgaard L. Paediatric doses--a critical appraisal of the EANM paediatric dosage card. Eur J Nucl Med Mol Imaging 2007;34(11):1713-1718. doi: 10.1007/s00259-007-0508-0
29. Warbey VS, Schleyer PJ, Barrington SF, O'Doherty M J. The new EANM paediatric dosage card--does it conform to ALARA for PET/CT? Eur J Nucl Med Mol Imaging 2007;34(11):1881-1882. doi: 10.1007/s00259-007-0565-4
30. Piepsz A, Hahn K, Roca I, Ciofetta G, Toth G, Gordon I, Kolinska J, Gwidlet J. A radiopharmaceuticals schedule for imaging in paediatrics. Paediatric Task Group European Association Nuclear Medicine. Eur J Nucl Med 1990;17(3-4):127-129. doi: 10.1007/BF00811439

31. Milanesi O, Stellin G, Zucchetta P. Nuclear Medicine in Pediatric Cardiology. Semin Nucl Med 2017;47(2):158-169. doi: 10.1053/j.semnuclmed.2016.10.008

Chapter 10

Predicting MACE from [^{82}Rb] PET: Can AI outperform more traditional quantitative assessment of the myocardial perfusion ?

Sci Rep. (accepted with major revision)

Sacha Bors, Daniel Abler, **Matthieu Dietz**, Vincent Andrearczyk, Julien Fageot, Marie Nicod-Lalonde, Niklaus Schaefer, Robert DeKemp, Christel H. Kamani, John O. Prior, and Adrien Depeursinge

Abstract

Assessing the individual risk of Major Adverse Cardiac Events (MACE) is of major importance as cardiovascular diseases remain the leading cause of death worldwide. Quantitative Myocardial Perfusion Imaging (MPI) based on [82Rb] PET using scores based on the global myocardial average of the stress uptake or on the Myocardial Flow Capacity (MFC) constitutes the gold standard for prognosis assessment. We propose a systematic investigation of the value of Artificial Intelligence (AI) to leverage [82Rb] Silicon PhotoMultiplier (SiPM) PET MPI for MACE prediction. We establish a general pipeline for AI model validation to assess and compare the performance of global, segmental, radiomics and Convolutional Neural Network (CNN) models leveraging various MPI signals including stress Myocardial Blood Flow (MBF), Myocardial Flow Reserve (MFR) or MFC radius based on a dataset of 234 patients. Results showed that all regional AI models significantly outperformed the traditional global model ($p < 0.001$), where the best AUC of 73.9 (CI: 72.5-75.3) was obtained with a CNN model. A radiomics model based on intensity features only revealed that the global average was the least important feature when compared to other aggregations of the MPI signal over the myocardium. We conclude that AI models can allow better personalized prognosis assessment for MACE.

Introduction

Major Adverse Cardiac Events (MACE) commonly designates stroke, myocardial infarction, or cardiac death. As of 2023, those events are most common outcomes of cardiovascular diseases and remain among the leading causes of death across the world[1]. Personalized patient prognosis and the prediction of MACE is therefore a challenge of real interest. Well established risk factors, such as physical inactivity, unhealthy diet, tobacco, and alcohol use are to take into account[2], as well as family history and genetics when considering clinical predictors[3], while most accurate MACE predictors are based on related medical history[4]. All those clinical features are not accurate enough when employed for patient personalized prediction, since a large proportion of the population with cardiovascular diseases does not manifest any of those classical risk factors.

Myocardial Perfusion Imaging (MPI) using Single-Photon Emission Computed Tomography (SPECT) is the most frequently performed nuclear cardiology procedure. It provides a sensitive tool for the detection, the localization, and the risk stratification of ischemic heart disease, as well as the assessment of left ventricular function, and the myocardial viability. Furthermore, MPI based on Magnetic Resonance Imaging (MRI) is used for its anatomic detail, tissue contrast, spatial and temporal resolution, as well as the lack of ionizing radiation[5]. As an alternative, quantitative MPI can be obtained using [^{82}Rb] Positron Emission Tomography (PET) and is nowadays a functional and non-invasive method for assessing the risk of MACE, or to investigate physiological consequences on the organ after a cardiac event[6–10]. It is already known to surpass the clinical interpretation of SPECT for MACE prediction[11] and was proven cost effective[12]. This procedure quantifies the Myocardial Blood Flow (MBF)
and the Myocardial Flow Reserve (MFR) in the left ventricle. The MFR constitutes the ratio of MBF during maximal coronary vasodilatation to resting MBF and is therefore impacted by both rest and stress flow. Thus, it represents the relative reserve of the coronary circulation. Both MBF and MFR are then mapped onto a Polar Map (PM) for visualization. PM visualization yields a controlled positioning and parcellation of all subregions of the left ventricle across patients and acquisitions, based on the 17-segment model of the American Heart Association (AHA)[13].

Various alterations of the MBF have reported associations with an increased risk of MACE. Physiological expectations of global MBF impairment are related to multi-vessel epicardial disease or microcirculatory dysfunction. Global stress MBF (i.e., average of the full PM) is known to be predictive for MACE[14]. More isolated MBF alterations could be related to small

defects caused by epicardial coronary artery disease15. To this end, Gould et al. introduced the Myocardial Flow Capacity (MFC) combining stress MBF and MFR in a two-dimensional representation[15] for categorizing MACE risk.

Nevertheless, the wealth and complexity of the information contained in PMs can be difficult to fully leverage with the naked eye (e.g., micro lesions or subtle patterns) and is subject to inter- and intra- observer variability with semiquantitative visual assessment alone[16]. More informative imaging is needed to provide better individualized risk estimates, with epidemiological effectiveness but also cost efficiency. Artificial Intelligence (AI) has the potential to fully exploit the information provided by PET MPI and dramatically enhance the utility of this powerful modality. Machine Learning (ML) already surpassed the clinical interpretation of SPECT MPI for MACE prediction in[17]. The incorporation of AI techniques to standardize and automate processing of PET MPI could further improve risk prediction[18], [19] to noninvasively support clinical decision for using coronary revascularization[20], as well as an accurate and systematic assessment of tissue perfusion hemodynamics in a one-stop-shop.

In the specific context of MPI assessed via nuclear medicine and molecular imaging, the very first studies originated in the 90s. A large body of literature focused on SPECT thanks to its large usage and availability[21]. In 1995, Hamilton et al. used a three-layered Fully Connected Neural Network (FCNN) fed by vectorized 24 territorial values of PMs from [^{201}TI] SPECT to classify normal and abnormal regions with an AUC (Area Under the receiver operating characteristic Curve) of 0.9622. In 2020, Slomka et al. established the REgistry of Fast Myocardial Perfusion Imaging with NExt generation SPECT (REFINE SPECT)[23], an outstanding data resource with MACE as the primary endpoint. It includes > 20,000 patients from nine centers with [^{99m}Tc] SPECT along with extensive additional relevant parameters concerning patient data, ECG, and interventional information. Using the REFINE SPECT database, the prognostic performance of the semi-quantitative assessment of SPECT PMs (via stress Total Perfusion Deficit, TPD[24]) was found to be superior to visual assessment for predicting MACE[25]. Betancur et al. used LogitBoost26, a ML approach based on clinical and semi-quantitative imaging variables from [^{99m}Tc] SPECT (e.g., TPD) to predict MACE (3-year risk), which outperformed visual and semi-quantitative assessments[27].

Deep Learning (DL) is a subcategory of ML that can directly use images as input. It can deduce and extract optimal image features for the task at hand, obviating the need to handcraft specific features like in radiomics ML models for instance. [^{99m}Tc] SPECT-based DL using a Convolutional Neural Network (CNN) was found to be marginally more predictive of obstructive coronary artery disease (CAD) when compared to semi-quantitative assessment via

stress TPD[28]. Diagnosing obstructive CAD using a CNN based on multiple channel input including stress MBF, wall motion, and wall thickening maps from [^{99m}Tc] SPECT and was evaluated on the REFINE SPECT[29]. Apostolopoulos et al. used CNNs with [^{99m}Tc] SPECT PMs to classify 216 patients with either flow-limiting- or no- CAD, which reach performance on par with physicians[30,31]. Spier et al. compared various DL approaches to classify between normal and abnormal [^{99m}Tc] SPECT stress and rest PMs32. They compare FCNNs, CNNs on flattened PMs and Graph CNNs (GCNNs). A large performance gain (≈ 10%) is observed with GCNNs when compared to CNNs, suggesting that it is crucial to adequately manage PM geometry.

First studies on the relevance of AI in PET MPI were recently published33. Juarez-Orozco et al. used LogitBoost ML with 4 demographic, 8 clinical, and 9 functional variables from [13N] ammonia PET to predict myocardial ischemia and MACE[34]. Wang et al.[35] compared the performance of a Support Vector Machine (SVM) ML model based on 6 MPI variables derived from both [^{13}N] ammonia and [^{18}F] FDG PET to predict vascular stenosis in patients with suspected obstructive CAD and achieved an AUC of 0.68. A multi-task ML based on [^{13}N] ammonia PET was developed by Yeung et al. to identify impaired MFR as well as cardiovascular risk factors[36]. Kwiecinski et al. used ML based on [^{18}F] sodium fluoride PET and quantitative plaque analysis on CT angiography to predict the risk of myocardial infarction[37].

To date, the potential of AI methods to leverage the wealth of [^{82}Rb] PET has been little explored. Wang et al. used a FCNN to increase MPI quality[38] and DL was used to improve motion correction in[39]. However, to the best of our knowledge, no AI method was proposed yet for predicting diagnosis or prognosis from [^{82}Rb] PET.

This study aims to provide a systematic exploration of the prognostic value of [^{82}Rb] PET-based MPI analysis using AI for MACE prediction. To this end, we systematically evaluate and compare standard AI approaches from simple Logistic Regression (LR) based on handcrafted features (e.g., global or regional intensity or radiomics with and without texture features) to CNNs, as well as their combined performance with clinical data. We address the following research questions when considering MACE prediction. (i) can regional AI models based on the AHA 17-segments or the full MBF signal outperform the global MBF average? (ii) can spatial pattern analysis (i.e. radiomics texture or CNN) improve intensity aggregation (i.e. radiomics first order statistics)? (iii) can we combine MPI and clinical data to improve MACE prediction?

The paper is structured as follows. Section 1 contains an overview and detailed descriptions of the dataset, the validation pipeline to compare and evaluate all AI models and all model-specific information. The predictive performance for MACE is presented, compared, and analyzed in Sections 2 and 3, respectively.

Methods

This section systematically details the different steps followed across the study, starting with the descriptions of study population, images acquisition protocols and data format. We then presenting the general pipeline used to construct and evaluate the LR and CNN models considered for the classification task of predicting which patients will encounter a MACE based on [^{82}Rb] PET.

Studied population

Participants with suspected myocardial ischemia were enrolled to undergo [^{82}Rb] cardiac Silicon PhotoMultiplier (SiPM) PET/CT at the Lausanne University Hospital between June 2018 and June 2019. All their cardiovascular risk factors and medication use were determined at time of PET imaging. The Local Ethics Committee approved this study protocol (#PB_2017 − 00634), and all participants gave written informed consent prior to inclusion. The dataset used for this study consists of MBF measurements at rest and under stress for 234 patients, along with a set of 19 clinical features for each patient (see Appendix A). Among this cohort, there were 187 patients with no observed MACE in the follow-up days and 47 patients labeled as having a MACE, the median number of days between PET imaging and first MACE or last news being 632.

Imaging protocol

All subjects underwent a rest and adenosine or regadenoson stress SiPM PET/CT scan using a single scanner (Biograph Vision 600, Siemens Medical Solutions, Knoxville, USA). They fasted for 6 hours and avoided caffeine 24 hours before the test. At rest, a 15–25 seconds (s) i.v. infusion of 5 MBq/Kg of 82Rb was injected with an automatic infusion system (Ruby-Fill® generator and [82Rb] elution system [v3], Jubilant DraxImage, Kirkland, QC, Canada). 3D dynamic PET images were acquired starting with the infusion over 6 min. 19 s (12 × 8, 5 × 12, 1 × 30, 1 × 60, and 1 × 120 s). The stress acquisition followed the same protocol with similar activity 2 min. into an adenosine infusion (140 mg/kg/min. over 6 min.) or following a

regadenoson administration (400 μg over 10 s). An accompanying low-dose CT (100 keV, 16 mAs) transmission scan was acquired for attenuation correction. An ordered subsets expectation maximization algorithm was used for image reconstruction (4 iterations, 5 subsets, 4.0 mm FWHM gaussian post-filter, 220 × 220 pixel matrix size). Blood pressure, heart rate, and a 12-channel ElectroCardioGram (ECG) were collected during the image acquisitions.

Quantitative myocardial perfusion assessment and data format

Perfusion was quantitatively assessed via MBF in ml/g/min. at rest and stress, using the FlowQuant v2.7 software (Ottawa, Ontario, Canada) based on a 1-tissue compartment model and flow-dependent extraction correction[40]. Rate-pressure product adjusted rest MBF and MFR were established to account for elevated resting heart rate or systolic blood pressure by multiplying rest MBF by 8500 mmHg/min. and dividing by rate-pressure product (resting heart rate multiplied by resting systolic blood pressure). A dual spill-over correction[41] as well as global partial-volume recovery correction and motion correction[42] were systematically applied to reduce the potential spillover in image-derived blood activity curves. The semi-automated segmentation of the myocardium was performed using FlowQuant.

The MBF measurements are provided in the form of a polar-pixelized PM stored in 24 × 36 matrices of nonnegative float numbers. The last 8 rows of those matrices were cut off to match with the set of values commonly used to produce the standard PMs representing the perfusion of the left ventricle (see the mapping between the MBF matrix and the MBF PMs according to the 17-segment model in Fig. 1). A measurement matrix is denoted by $S = (S[m,n])1 \leq m \leq 16, 1 \leq n \leq 36 \in R16 \times 36$. Each value S[m,n] represents the perfusion signal at a given polar pixel, where m characterizes the radius to the pole and n the angular position of the polar pixel. Note that the matrix has a periodic structure in the sense that the columns 1 and 36 are spatial neighbors in the PM. MBF values were acquired under stress and at rest, leading to two measurement matrices Sstress MBF and Srest MBF. Three candidates MPI signals were considered for MACE prediction based on Dietz et al.[14]:

MBF values measured under stress Sstress MBF,

- MFR values, obtained by taking the ratio between MBF values under stress and at rest for every element of the MBF matrix; that is SMFR[n,m] = (Sstress MBF[n,m]) / (Srest MBF[n,m]) and
- MFC radius signal[15] defined as $SMFC[n,m] = \sqrt{(Sstress\ MBF[n,m]^2 + SMFR[n,m]^2)}$.

In what follow, we denote by S the measurement matrix, which is one of the three MPI signals introduced above. We also denote by $y \in \mathrm{R}^n$ the feature vector, where n is the number of considered features for the corresponding model. The various feature vectors y considered are systematically detailed in the models' descriptions below. We represent the outcome no MACE versus MACE by the output variable $z \in \{0, 1\}$, so that we learn the parameters of the different LR on the (y, z) relations. All computational operations were performed with Python v3.9.13, and mainly using scikit-learn v1.0.2 and TensorFlow v2.9.1 libraries.

General pipeline for AI model validation

The considered AI models divide in three categories. LR based on global or segmental analysis, LR using radiomics features (with or without texture features), as well as CNNs trained from scratch. Moreover, for each type of LR model we also built a late fusion with a LR exclusively based on the non-image related 19 clinical features. For all image analysis approaches, we chose to not to use those PMs as input but to stick with the tabular format S[m,n]. This allowed to avoid any kind of data transformation such as spatial resampling or intensity binning, as well as empty corners around the PM. This tabular representation was also used with CNNs in Spier et al.[32].

To systematically compare the different models and assess performance variability, we followed the same procedure for each model family. We repeated 100 random stratified splits of the data into a training and a test set, with a 75%-25% proportion (i.e., 175 training cases, including 35 positive and 140 negative ones). Within each split, the minority class was oversampled in the training set by duplicating twice every positive case, increasing the training size up to 245 cases (counting 105 positive and 140 negative cases). This was done to address the imbalance of our data, whose positive outcomes only represent a fifth of the total sample. For each tested model, the splits and the shuffling of the training set were the same. The LRs and the CNN models were then trained (see the details below), and their performances measured and stored for each split. The intensity and texture features were first standardized based on training samples in the case of the LRs. The AUC of the considered model was computed for each split, and the Youden index was used to determine the optimal cutoff value providing the optimal trade-off between sensitivity and specificity. We finally report the test average performances measured across the 100 splits. Confidence Intervals (CI) of the average were built from 1000 bootstraps to compare all approaches. An overview of the general validation pipeline is depicted in Fig. 2.

Segment-based models

The first two models that we evaluated were based on two distinct parcellations of the considered PMs, hence of the 16 × 36 MBF matrices S (see Fig. 1). The 1-segment model of the PM corresponds to a global average over the matrix, leading to the single-valued measure yglobal = 1/36x36 $\sum 1 \leq m \leq 36,\ 1 \leq n \leq 16$ S[m, n]. We then learn a straightforward LR model taking the global 16×36 average value of the matrix as unique feature. The 1-segment model was already reported to be predictive for MACE by Dietz et al.[14] and will serve as our baseline. The second model is based on the standard 17-segment AHA model[13] and corresponds to regional averages, yielding a vector ysegment ∈ R17 of 17 features over each delimited regions as in Fig. 1. The 17-segment model corresponds to a systematic and quantitative assessment of the traditional PM visualization. A multivariate LR model was build based on the input $y_{segment}$. For both 1- and 17- segment models LRs were trained using the ElasticNet penalty combining L1 and L2 regularization[43], which was optimized by cross-validated grid-search over a range of L1_ratio. The range of values was chosen to promote L1 penalty and thus the sparsity of the model. The optimized score was AUC, allowing to determine the best estimator over this set of parameters.

Radiomics models

To proceed to the radiomics features extraction, three sets of images were produced, using respectively stress MBF, MFR and MFC radius. The SimpleITK Python module was used to create images from the MBF matrices, which are then saved as image files. A straightforward global mask was use for feature extraction, which was achieved using PyRadiomics v3.0.1. Regional masks (e.g., 17 segments) were not considered to limit the number of radiomics features and risk of overfit.

For the first radiomics model (referred to as "radiomics full"), the full set of standard radiomics features was included (excluding shape features). We used first order statistics (18 features) as well as second order (i.e. texture) including Gray Level Cooccurence Matrix (GLCM, 24 features), Gray Level Run Length Matrix (GLRLM, 16 features), Gray Level Size Zone Matrix (GLSZM, 16 features), Neighbouring Gray Tone Difference Matrix (NGTDM, 5 features), and Gray Level Dependence Matrix (GLDM, 14 features), for a total of 93 features yielding a vector yfull radiomics ∈ R93.

The second radiomics model (referred to as "radiomics intensity") was only based on the 18 intensity features (i.e. first order statistics) and all texture features were left out, yielding a vector yintensity ∈ R18, where yintensity = yifull radiomics for i = 1,...,18. We set the binWidth

as the max range of the values across the whole data divided by 16, and the interpolator was sitkBSpline. The two abovementioned radiomics models were used to investigate the specific value of spatial pattern analysis via texture features when compared to simpler intensity measurements.

Late fusion with clinical features

For all four LR-based models previously described, we also implemented a late fusion with a LR using the 19 clinical features, i.e. yclinical ∈ R19. It was implemented the same way as the other LR and trained on the exact same splits (see Fig. 2). The decision function was simply based on an unweighted average of the prediction score (probabilities) of the considered image model and the clinical model. The LR model was on yclinical has also been evaluated on its own.

Convolutional Neural Networks

We explored the ability of CNN learn and capture more complex spatial patterns (see Fig. 3) when compared to all LR-based models. To this end, we compare two shallow architectures with increasing depths (CNN1 and CNN2). Deeper and pre-trained CNNs (i.e. Resnet50) were preliminary evalutated which did not provided improved results. We focused on the shallow architectures for the sake of simplicity.

For all CNN models, an extra step consisting of data augmentation was included in the general pipeline, which was carried out after each train-test split. Since the acquisition of the images is very controlled, we only introduced minor transformations on the PMs simulating the effect of annotation uncertainty. In order to do so, the size of the training set was quadrupled using two types of transformations on the measurement matrices S, corresponding to small variations in the segmentation of the left ventricle. The first transformation was to apply simple shifts of the columns of the matrix (on the right and on the left), corresponding to rotations of the PM of ±10 degrees (in both directions). Formally, we define the new matrix with the shift on the right by S′ with S′ = Sij−1 for j = 2,...,36 and S′ = Si36. Similarly, we define the new matrix with the shift on the left by ij i1 S″ with S″ = Sij+1 for j = 1,...,35 and S″ = Si1. For the second transformation, the last 3 rows of the matrix (corresponding ij i36

to the outer part of the PM) were erased, and the remaining 13 rows were stretched back to 16 rows using linear interpolation. This simulates variations in the adjustment of the segmentation of the left ventricle on the PET-scan.

For the simplest CNN, referred to as "CNN 1", we input the matrices and use a convolution layer with 64 filters of size 5 × 5, before the Global Average Pooling (GAP) layer. The architecture ended with a FC layer with 256 hidden neurons and 2 output neurons. The Rectified Linear Unit (ReLU) activation function was used for the convolutions and FC layers. A softmax activation function was used for the output layer (see CNN 1 in Fig. 3). For training the CNNs, we used a L1-L2 regularizer, an Adam optimizer, and a categorical cross-entropy as the loss function. We set up a 50 epochs training and used early stopping to avoid overfitting.

A slightly deeper architecture was considered as used by Spier et al. to analyze SPECT-based MPI in[32] (see "CNN 2" in Fig. 3). Similarly to the CNN 1 model, the MBF matrices were used as input followed by two successive convolution layers. The first one included 64 filters of size 5 × 5, and the second one had 128 filters of size 3 × 3. Each of them used a ReLU activation function and was followed by a (2 × 2)-max-pooling layer. A flattening layer was used before the FC layer including 256 hidden neurons and 2 output neurons. ReLU and softmax activation functions were used similarly to the previous model.

Results

Table 1 summarizes all the results computed for all tested models when using stress MBF, MFR and MFC radius. Fig. 4 compares Kaplan-Meier curves and log-rank tests based on the risk scores of the clinical, global and CNN2 models. The low versus high risk groups are based on the median of the scores for each model. Fig. 5, reports the set of features selected by ElasticNet for the radiomics intensity model across all 100 split repetitions (see Fig. 2).

Discussion

In this study, we investigated the value of AI for analyzing [^{82}Rb] PET-based MPI in order to predict MACE. To this end, we systematically implemented and compared standard AI approaches with a global validation pipeline. In particular, we used LRs based either on MBF segmental or radiomics (with and without texture) features, as well as shallow neural networks with convolution. We also considered a late fusion with a LR model uniquely based on clinical features. The three input MPI signals including stress MBF, MFR and MFC radius were also compared for all models. The training and the evaluation of all these approaches was carried out with a systematic validation pipeline allowing fair and reproducible comparisons between the approaches. The respective performance of models and MPI signals were evaluated based on AUC, sensitivity and specificity estimated across 100 random train/test splits of the original data.

We interpret the comprehensive performance comparisons presented in Table 1 as follows. First, the use of stress MBF or MFR seems to perform equivalently on most of the models, whereas for the MFC radius the performance is consistently better. When focusing on the models based on MFC radius, we observe a significant improvement in average performance when using the regional information across the 17 segments versus using the global average alone (average AUCs of 73.4 and 70.5, respectively, $p < 0.001$). Next, we note that the models including clinical features do not yield higher AUCs than models that purely rely on image information. Thus, there is no real added value to include the clinical information for this approach, and purely image-based models perform best. Finally, we observe that the models including texture information such as CNNs and radiomics full do not systematically outperform models based on simpler intensity features (i.e., segment-based and radiomics intensity models). For instance, the performance of the 17-segment regional model (average AUC of 73.4) was found not to be significantly inferior ($p = 0.33$) to the one of the CNN2 model (average AUC of 73.9). It indicates that the texture information (i.e., subtle spatial patterns that are mostly invisible to the naked eye) contained in the MBF matrices does not predict MACE better than intensity information alone. This suggests that the spatial characteristics of MBF patterns are not relevant for MACE prediction. It is worth noting that the texture features were aggregated over the entire MBF matrix, and (3- or 17-) segmental aggregation was not investigated to keep smaller number of features per patient. When analyzing intensity features that are retained in the radiomics intensity model in Fig. 5, it is remarkable that "original_firstorder_Mean", being strictly equivalent to the global model, is the feature that is the least often selected. This suggest that the spatial aggregation of the MBF signal requires more sophisticated stategies than a global average. Skewness, kurtosis and the minimum of the MBF distribution constituted the best group of intensity features. The Kaplan-Meier analyses reported in Fig. 4 demonstrates that AI models allows better separability of low versus high risk groups when compared to the global average or clinical models.

We conclude that AI can be valuable to better leverage the complexity and the quantitative nature of [^{82}Rb] PET-based MPI when compared to a global average of the PMs, where both the radiomics intensity and CNN 2 models achieved the best observed average AUCs of 73.8 and 73.9 respectively. However, models that are able to leverage subtle spatial patterns did not improved the quality of MACE prediction.

We recognize several limitations of the current work. This study is based on a single center with relatively limited sample size. It would be of interest to apply this pipeline to a larger database collected across multiple centers. While this first study focused on traditional AI

methods (i.e. radiomics with LR and simple NNs), more advanced AI methods will be investigated in future work. In particular, the tabular representation (i.e. MFB matrix) used as input to the models suffers from spatial distortion. It is worth noting that using PMs as input would also involve spatial distortions in the apex region. Nevertheless, future work will consider graph-based CNNs as this approach showed to better leverage the spatially distorted content of PMs for MPI abnormality classification in SPECT-based MPI[32]. Another limitation of this study lies in the imbalance of the data, even though we reduce its impact by addressing the lack of positive cases with the oversampling of the minority class.

References

1. Vaduganathan, M., Mensah, G. A., Turco, J. V., Fuster, V. & Roth, G. A. The global burden of cardiovascular diseases and risk. J. Am. Coll. Cardiol. 80, 2361–2371, DOI: https://doi.org/10.1016/j.jacc.2022.11.005 (2022).
2. Naghavi, M. et al. From vulnerable plaque to vulnerable patient: a call for new definitions and risk assessment strategies: Part i. Circulation 108(14), 1664–1672, DOI: https://doi.org/10.1161/01.CIR.0000087480.94275.97 (2003).
3. Mozaffarian, D. et al. Heart disease and stroke statistics—2015 update. Circulation 131(4), e29–e39, DOI: https: //doi.org/10.1161/CIR.0000000000000152 (2015).
4. Cupples, L. A., Gagnon, D. R., Wong, N. D., Ostfeld, A. M. & Kannel, W. B. Preexisting cardiovascular conditions and long-term prognosis after initial myocardial infarction: The framingham study. Am. Hear. J. 125(3), 863–872, DOI: https://doi.org/10.1016/0002-8703(93)90182-9 (1993).
5. Wu, K. C. Myocardial perfusion imaging by magnetic resonance imaging. Curr. Cardiol. Reports 5, 63–68, DOI: https://doi.org/10.1007/s11886-003-0039-7 (2003).
6. Harjulahti, E. et al. Global and segmental absolute stress myocardial blood flow in prediction of cardiac events: [15o] water positron emission tomography study. Eur. J. Nucl. Medicine Mol. Imaging 48(5), 1434–1444, DOI: https://doi.org/ 10.1007/s00259-020-05093-2 (2021).
7. Juárez-Orozco, L. E. et al. Quantitative myocardial perfusion evaluation with positron emission tomography and the risk of cardiovascular events in patients with coronary artery disease: a systematic review of prognostic studies. Eur. Hear. J. - Cardiovasc. Imaging 19(10), 1179–1187, DOI: https://doi.org/10.1093/ehjci/jex331 (2018).
8. Neumann, F. J. et al. 2019 esc guidelines for the diagnosis and management of chronic coronary syndromes: The task force for the diagnosis and management of chronic coronary syndromes of the european society of cardiology (esc). Eur. Hear. J. 41(3), 407–477, DOI: https://doi.org/10.1093/eurheartj/ehz425 (2020).
9. N.Weber, B. et al. Impaired coronary vasodilator reserve and adverse prognosis in patients with systemic inflammatory disorders. JACC: Cardiovasc. Imaging 14(11), 2212–2220, DOI: https://doi.org/10.1016/j.jcmg.2020.12.031 (2021).
10. Zampella, E. et al. Combined evaluation of regional coronary artery calcium and myocardial perfusion by 82rb pet/ct in predicting lesion-related outcome. Eur. J. Nucl.

Medicine Mol. Imaging 47(7), 1698–1704, DOI: https://doi.org/10.1007/ s00259-019-04534-x (2020).

11. Hu, L. H. et al. Prognostically safe stress-only single-photon emission computed tomography myocardial perfusion imaging guided by machine learning: report from refine spect. Eur. Hear. J. - Cardiovasc. Imaging 22(6), 705–714, DOI: https://doi.org/10.1093/ehjci/jeaa134 (2021).
12. Mimouni, M. et al. Cost-effectiveness of 82-Rubidium PET myocardial perfusion imaging for the diagnosis of myocardial ischemia depending on the prevalence of coronary artery disease. EJNMMI Res. 13, 1–9 (2023).
13. Cerqueira, M. D. et al. Standardized Myocardial Segmentation and Nomenclature for Tomographic Imaging of the Heart. Circulation 105, 539–542, DOI: 10.1161/HC0402.102975 (2002).
14. Dietz, M. et al. Comparison of the prognostic value of impaired stress myocardial blood flow, myocardial flow reserve, and myocardial flow capacity on low-dose rubidium-82 sipm pet/ct. J. Nucl. Cardiol. DOI: https://doi.org/10.1007/ s12350-022-03155-6 (2022).
15. Gould, K. L. et al. Anatomic versus physiologic assessment of coronary artery disease: Role of coronary flow reserve, fractional flow reserve, and positron emission tomography imaging in revascularization decision-making. J. Am. Coll. Cardiol. 62(18), 1639–1653, DOI: https://doi.org/10.1016/j.jacc.2013.07.076 (2013).
16. Xu, Y. et al. Automatic and visual reproducibility of perfusion and function measures for myocardial perfusion SPECT. J. Nucl. Cardiol. 17, 1050, DOI: 10.1007/S12350-010-9297-0 (2010).
17. Hu, L. H. et al. Prognostically safe stress-only single-photon emission computed tomography myocardial perfusion imaging guided by machine learning: report from REFINE SPECT. Eur. Hear. J. - Cardiovasc. Imaging 22, 705–714, DOI: 10.1093/EHJCI/JEAA134 (2021).
18. Slomka, P. Future of nuclear cardiology is bright: Promise of cardiac PET/CT and artificial intelligence. J. Nucl. Cardiol. 2022 1–3, DOI: 10.1007/S12350-022-02942-5 (2022).
19. Slomka, P. J. et al. Quantitative Clinical Nuclear Cardiology, Part 2: Evolving/Emerging Applications. J. Nucl. Medicine 62, 168–176, DOI: 10.2967/JNUMED.120.242537 (2020).

20. Neumann, F. J. et al. 2019 ESC Guidelines for the diagnosis and management of chronic coronary syndromesThe Task Force for the diagnosis and management of chronic coronary syndromes of the European Society of Cardiology (ESC). Eur. Hear. J. 41, 407–477, DOI: 10.1093/EURHEARTJ/EHZ425 (2020).
21. Garcia, E. V. & Piccinelli, M. Preparing for the Artificial Intelligence Revolution in Nuclear Cardiology. Nucl. Medicine Mol. Imaging 57, 51–60, DOI: 10.1007/S13139-021-00733-3/FIGURES/6 (2022).
22. Hamilton, D., Riley, P. J., Miola, U. J. & Amro, A. A. A feed forward neural network for classification of bull's-eye myocardial perfusion images. Eur. J. Nucl. Medicine 1995 22:2 22, 108–115, DOI: 10.1007/BF00838939 (1995).
23. Slomka, P. J. et al. Rationale and design of the REgistry of Fast Myocardial Perfusion Imaging with NExt generation SPECT (REFINE SPECT). J. Nucl. Cardiol. 27, 1010–1021, DOI: 10.1007/S12350-018-1326-4/TABLES/7 (2020).
24. Nakazato, R. et al. Quantitative Upright–Supine High-Speed SPECT Myocardial Perfusion Imaging for Detection of Coronary Artery Disease: Correlation with Invasive Coronary Angiography. J. Nucl. Medicine 51, 1724–1731, DOI: 10.2967/JNUMED.110.078782 (2010).
25. Otaki, Y. et al. 5-Year Prognostic Value of Quantitative Versus Visual MPI in Subtle Perfusion Defects: Results From REFINE SPECT. JACC: Cardiovasc. Imaging 13, 774–785, DOI: 10.1016/J.JCMG.2019.02.028 (2020).
26. Friedman, J., Hastie, T. & Tibshirani, R. Additive logistic regression: a statistical view of boosting (With discussion and a rejoinder by the authors). The Annals Stat. 28, 337–407, DOI: 10.1214/AOS/1016218223 (2000).
27. Betancur, J. et al. Prognostic Value of Combined Clinical and Myocardial Perfusion Imaging Data Using Machine Learning. JACC: Cardiovasc. Imaging 11, 1000–1009, DOI: 10.1016/J.JCMG.2017.07.024 (2018).
28. Betancur, J. et al. Deep Learning for Prediction of Obstructive Disease From Fast Myocardial Perfusion SPECT: A Multicenter Study. JACC: Cardiovasc. Imaging 11, 1654–1663, DOI: 10.1016/J.JCMG.2018.01.020 (2018).
29. Otaki, Y. et al. Clinical Deployment of Explainable Artificial Intelligence of SPECT for Diagnosis of Coronary Artery Disease. JACC: Cardiovasc. Imaging DOI: 10.1016/J.JCMG.2021.04.030 (2021).
30. Apostolopoulos, I. D., Papathanasiou, N. D., Spyridonidis, T. & Apostolopoulos, D. J. Automatic characterization of myocardial perfusion imaging polar maps employing

deep learning and data augmentation. Hellenic J. Nucl. Medicine 23, 125–132, DOI: 10.1967/S002449912101 (2020).

31. Apostolopoulos, I. D., Apostolopoulos, D. I., Spyridonidis, T. I., Papathanasiou, N. D. & Panayiotakis, G. S. Multi-input deep learning approach for Cardiovascular Disease diagnosis using Myocardial Perfusion Imaging and clinical data. Phys. Medica 84, 168–177, DOI: 10.1016/J.EJMP.2021.04.011 (2021).
32. Spier, N., Nekolla, R., S. & C. Classification of polar maps from cardiac perfusion imaging with graph-convolutional neural networks. Sci. Rep. 9, 7569, DOI: https://doi.org/10.1038/s41598-019-43951-8 (2019).
33. Popescu, C. et al. PET-based artificial intelligence applications in cardiac nuclear medicine. Swiss Med. Wkly. 2022 :3 152, w30123, DOI: 10.4414/SMW.2022.W30123 (2022).
34. Juarez-Orozco, L. E. et al. Machine learning in the integration of simple variables for identifying patients with myocardial ischemia. J. Nucl. Cardiol. 27, 147–155, DOI: 10.1007/S12350-018-1304-X/FIGURES/3 (2020).
35. Wang, F. et al. Evaluation of the diagnostic value of joint PET myocardial perfusion and metabolic imaging for vascular stenosis in patients with obstructive coronary artery disease. J. Nucl. Cardiol. 28, 3070–3080, DOI: 10.1007/S12350-020-02160-X/FIGURES/6 (2021).
36. Yeung, M. W. et al. Multi-task Deep Learning of Myocardial Blood Flow and Cardiovascular Risk Traits from PET Myocardial Perfusion Imaging. J. Nucl. Cardiol. 2022 1–11, DOI: 10.1007/S12350-022-02920-X (2022).
37. Kwiecinski, J. et al. Machine Learning with 18F-Sodium Fluoride PET and Quantitative Plaque Analysis on CT Angiography for the Future Risk of Myocardial Infarction. J. Nucl. Medicine 63, 158–165, DOI: 10.2967/JNUMED.121. 262283 (2022).
38. Wang, X., Yang, B., Moody, J. B., Tang, J. & Wang, X. Improved myocardial perfusion PET imaging using artificial neural networks. Phys. Medicine & Biol. 65, 145010, DOI: 10.1088/1361-6560/AB8687 (2020).
39. Shi, L. et al. Automatic Inter-Frame Patient Motion Correction for Dynamic Cardiac PET Using Deep Learning. IEEE Transactions on Med. Imaging 40, 3293–3304, DOI: 10.1109/TMI.2021.3082578 (2021).
40. deKemp, R. A. et al. Multisoftware reproducibility study of stress and rest myocardial blood flow assessed with 3d dynamic pet/ct and a 1-tissue-compartment model of 82rb

kinetics. J. Nucl. Medicine 54, 571–577, DOI: https: //doi.org/10.2967/jnumed.112.112219 (2013).

41. Efseaff, M., Klein, R., Ziadi, M. C., Beanlands, R. S. & deKemp, R. A. Short-term repeatability of resting myocardial blood flow measurements using rubidium-82 pet imaging. J. Nucl. Cardiol. 19, 997–1006, DOI: https://doi.org/10.1007/ s12350-012-9600-3 (2012).
42. Hunter, C. R. R. N., Klein, R., Beanlands, R. S. & deKemp, R. A. Patient motion effects on the quantification of regional myocardial blood flow with dynamic pet imaging. Med. Phys. 43, 1829–1840, DOI: https://doi.org/10.1118/1.4943565 (2016).
43. Zou, H. & Hastie, T. Regularization and variable selection via the elastic net. J. Royal Stat. Soc. Ser. B (Statistical Methodol. 67, 301–320, DOI: https://doi.org/10.1111/j.1467-9868.2005.00503.x (2005).

TABLES

Table 1: Average test performance of the models computed across 100 stratified randomsplits. Boostrap-based 95% confidence intervals are reported for AUC. A LR model based on the 19 clinical features only achieves an AUC of 63.0 [61.5, 64.3], with a sensitivity of 70.6 and a specificity of 62.4.

		stress MBF			MFR			MFC radius		
model	# feat.	AUC	sens.	spec.	AUC	sens.	spec.	AUC	sens.	spec.
global	1	68.3 [67.0, 69.7]	80.4	62.4	69.7 [68.4, 71.2]	72.5	69.4	70.5 [69.4, 71.8]	77.4	66.0
regional	17	71.2 [69.6, 72.4]	78.1	65.3	71.6 [70.4, 72.9]	74.3	69.8	73.4 [72.3, 74.7]	74.8	**72.0**
radiomics full	93	67.4 [66.0, 69.0]	72.3	64.7	68.7 [67.2, 70.4]	73.1	67.5	71.6 [70.0, 73.0]	72.4	71.1
radiomics intensity	18	73.2 [71.6, 74.5]	77.1	70.2	68.4 [66.9, 69.8]	73.3	66.8	**73.8** [72.4, 75.1]	76.4	67.7
CNN 1	-	70.0 [68.5, 71.3]	80.1	64.3	70.3 [69.0, 71.8]	74.4	71.1	73.6 [72.4, 74.8]	74.8	71.0
CNN 2	-	71.3 [69.7, 72.8]	**81.4**	64.9	70.8 [69.4, 72.2]	77.3	66.4	**73.9** [72.5, 75.3]	77.5	69.0
clinical + global	20	67.6 [66.3, 68.9]	77.6	61.6	68.5 [67.2, 69.8]	75.2	64.6	69.1 [68.0, 70.3]	79.0	62.8
clinical + regional	36	70.9 [69.4, 72.1]	78.2	65.3	71.8 [70.6, 73.0]	76.9	68.4	72.5 [71.3, 73.8]	76.5	70.0
clin. + rad. full	112	69.1 [67.7, 70.5]	72.9	67.1	70.8 [69.1, 72.3]	78.0	67.1	72.8 [71.2, 74.1]	80.0	67.4
clin. + rad. intens.	37	71.5 [70.2, 72.8]	76.7	65.9	69.9 [68.5, 71.3]	77.9	64.5	72.7 [71.3, 73.8]	80.0	67.7

FIGURES

Figure 1: Right: Polar Map (PM) representation of the myocardial perfusion with 17-segment AHA parcellation. 3-segment parcellation is depicted with yellow (Right Coronary Artery, RCA), purple (Left CircumfleX artery, LCX) and cyan (Left Anterior Descending artery) colors. The mapping between the 16 × 36 MBF matrix S (left) and the MBF PM (right) is depicted.

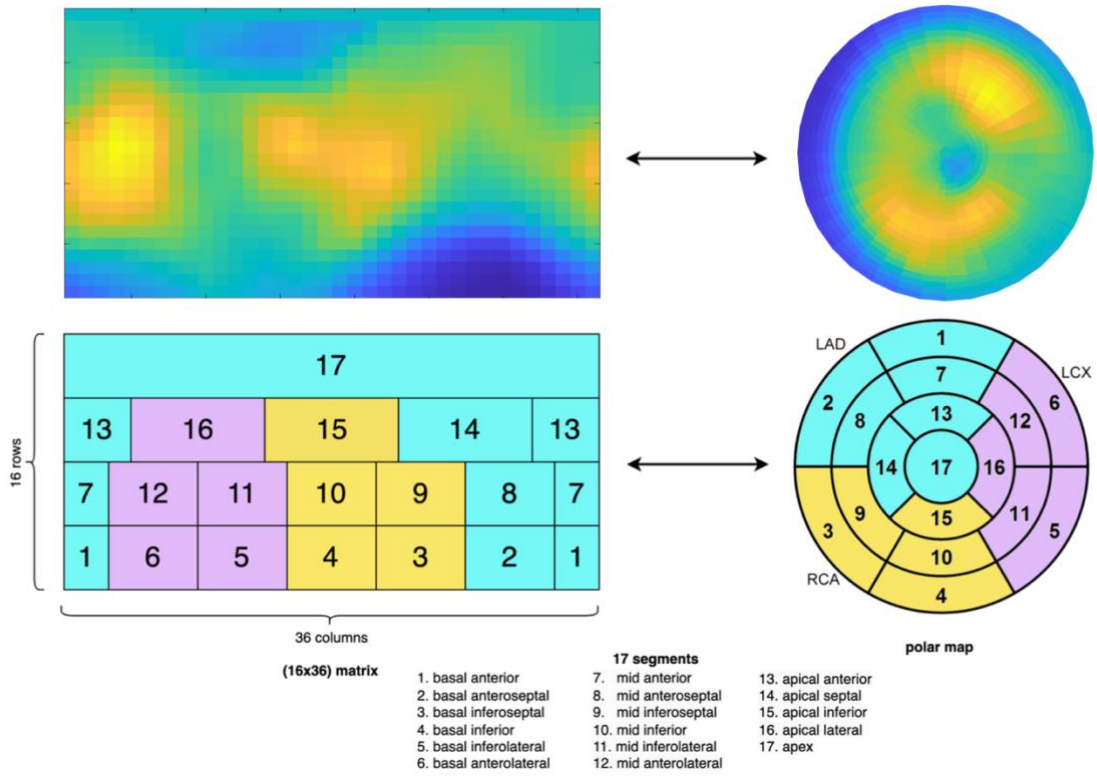

Figure 2: General pipeline for AI model validation.

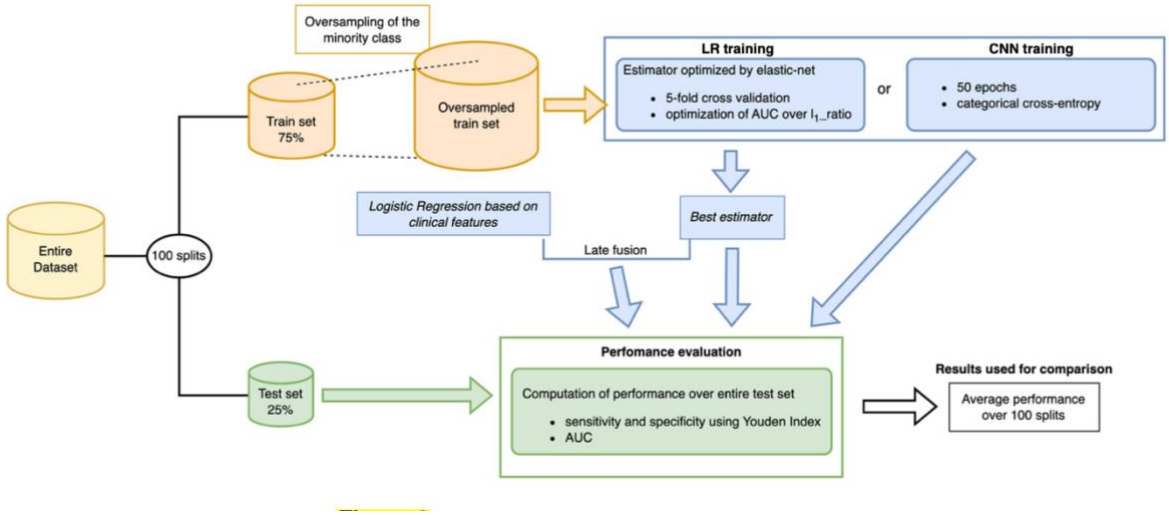

Figure 3: CNN architectures. CNN2 was proposed by Spier et al. for MPI analysis based on the MBF matrix S^{32}.

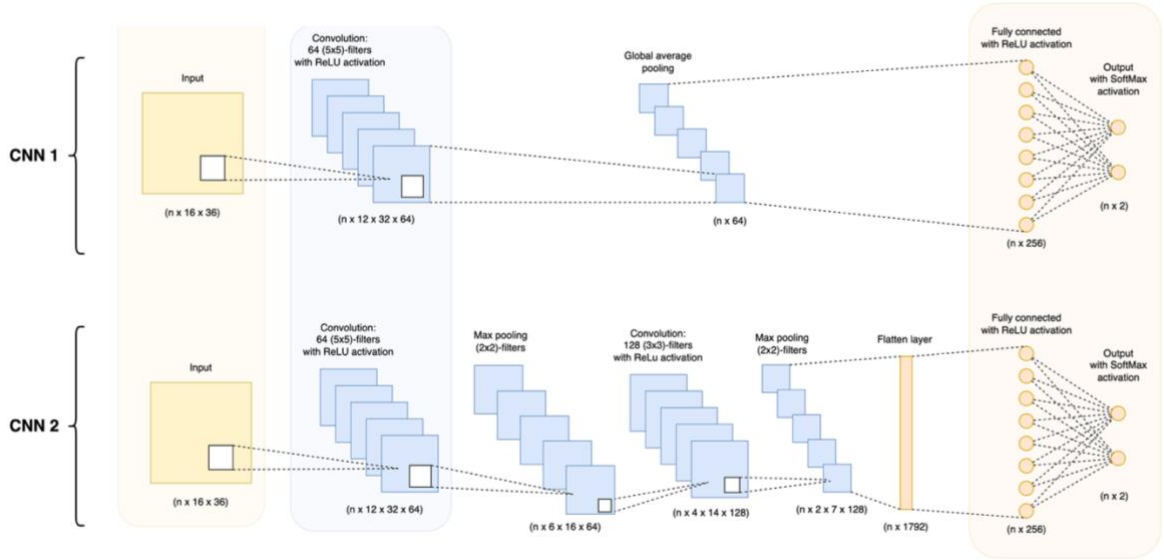

Figure 4: Kaplan-Meier analysis of the models. Low versus high risk groups are split based on the median score.

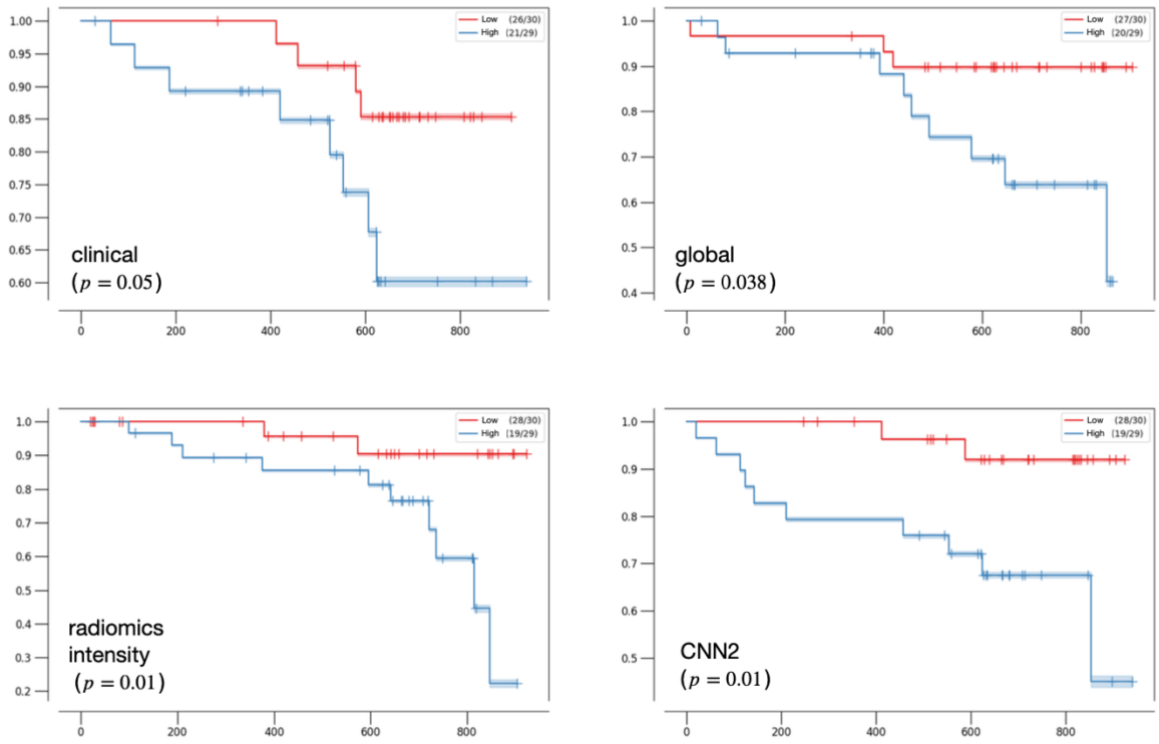

Figure 5: Features selection count for the MFC radius radiomics intensity model over the 100 repeated splits (see Fig. 2). Maximum number of times a feature can be selected is 100, i.e. at each split. The global average of the PM, referred to as "original_firstorder_Mean" is the one chosen least often.

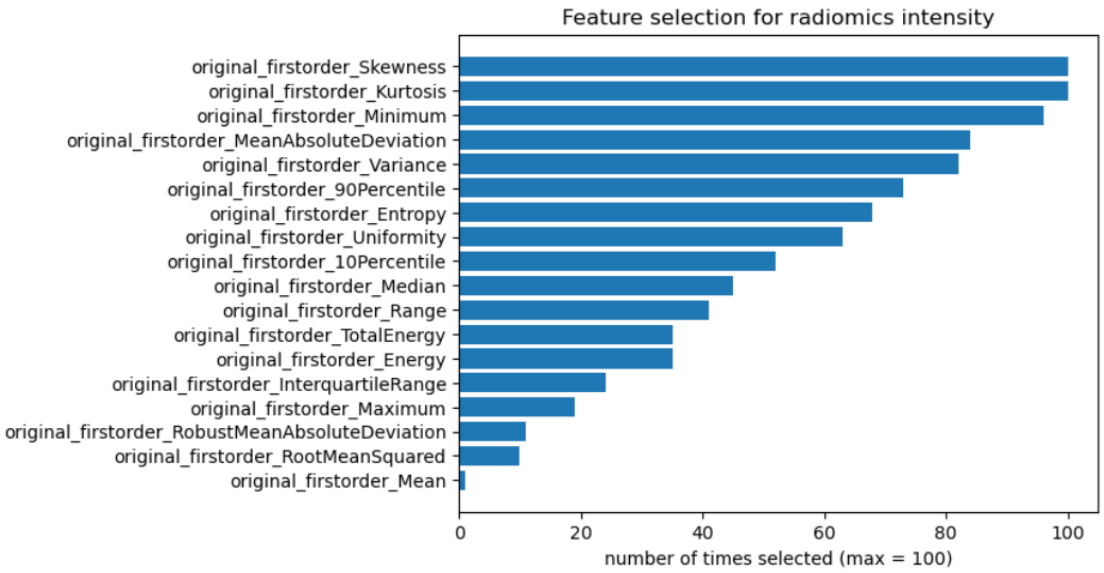

PART V

Annex studies

Chapter 11

Comparison of Integrin αvβ3 Expression with 68Ga-NODAGA-RGD PET/CT and Glucose Metabolism with 18F-FDG PET/CT in Esophageal or Gastroesophageal Junction Cancers

Eur J Hybrid Imaging. 2023 1;7:3. doi: 10.1186/s41824-023-00162-9

Matthieu Dietz, Vincent Dunet, Styliani Mantziari, Anastasia Pomoni, Ricardo Dias Correia, Nathalie Testart Dardel, Sarah Boughdad, Marie Nicod Lalonde, Giorgio Treglia, Markus Schafer, Niklaus Schaefer, and John O Prior

Abstract

Background

The primary aims of this study were to compare in patients with esophageal or esophagogastric junction cancers the potential of ^{68}Ga-NODAGA-RGD PET/ CT with that of ^{18}F-FDG PET/CT regarding tumoral uptake and distribution, as well as histopathologic examination.

Methods

Ten ^{68}Ga-NODAGA-RGD and ten ^{18}F-FDG PET/CT were performed in nine prospectively included participants (1 woman; aged 58±8.4 y, range 40–69 y). Maximum SUV (SUV_{max}) and metabolic tumor volumes (MTV) were calculated. The Mann-Whitney U test and Spearman correlation analysis (ρ) were used.

Results

^{68}Ga-NODAGA-RGD PET/CT detected positive uptake in 10 primary sites (8 for primary tumors and 2 for local relapse suspicion), 6 lymph nodes and 3 skeletal sites. ^{18}F-FDG PET/CT detected positive uptake in the same sites but also in 16 additional lymph nodes and 1 adrenal gland. On a lesion-based analysis, SUV_{max} of ^{18}F-FDG were significantly higher than those of ^{68}Ga-NODAGA-RGD (4.9 [3.7–11.3] vs. 3.2 [2.6–4.2] g/mL, $p = 0.014$). Only 1 participant showed a higher SUV_{max} in an osseous metastasis with ^{68}Ga-NODAGA-RGD as compared to ^{18}F-FDG (6.6 vs. 3.9 g/mL). Correlation analysis showed positive correlation between ^{18}F-FDG and ^{68}Ga-NODAGA-RGD PET parameters ($\rho = 0.56$, $p = 0.012$ for SUV_{max}, $\rho = 0.78$, $p < 0.001$ for lesion-to-background ratios and $\rho = 0.58$, $p = 0.024$ for MTV). We observed that ^{18}F-FDG uptake was homogenous inside all the confirmed primary sites (n = 9). In contrast, ^{68}Ga-NODAGA-RGD PET showed more heterogenous uptake in 6 out of the 9 confirmed primary sites (67%), seen mostly in the periphery of the tumor in 5 out of the 9 confirmed primary sites (56%), and showed slight extensions into perilesional structures in 5 out of the 9 confirmed primary sites (56%).

Conclusions

In conclusion, ^{68}Ga-NODAGA-RGD has lower potential in the detection of esophageal or esophagogastric junction malignancies compared to ^{18}F-FDG. However, the results suggest that PET imaging of integrin $\alpha_v\beta_3$ expression may provide complementary information and could aid in tumor diversity and delineation.

Introduction

Angiogenesis is defined as an active process, which regulates the growth of new blood vessels from a pre-existing vascular bed and exerts a prominent role in promoting tumor growth, progression, and metastasis. Integrin $\alpha_v\beta_3$ is highly expressed on activated endothelial cells of tumor neovasculature and has a key role in tumor angiogenesis (*31*). Arginine-glycine-aspartate (RGD) peptides have a high binding affinity and specificity with integrin $\alpha_v\beta_3$. As a result, a variety of RGD-based positron emission tomography (PET) imaging agents have been developed to visualize integrin $\alpha_v\beta_3$ expression (*32*,*33*). NODAGA-RGDyK, (cyclo[L-arginylglycyl-L-alpha-aspartyl-D-tyrosyl-N6-([4,7-bis(carboxymethyl)octahydro-1H-1,4,7-triazonin-1-yl]acetyl])-L-lysyl]), is a recently developed RGD peptide designed for PET imaging of $\alpha_v\beta_3$ integrin expression (*34*). The component NODAGA is a derivate of the NOTA system, which has no influence on receptor-specific binding and possesses high binding properties for radiometals with a ion radius like ^{68}Ga (*35*). ^{68}Ga-NODAGA-RGDyk has favorable biokinetics and safety profile (*36*,*37*).

Esophageal cancer is the seventh most common cancer worldwide and accounts for more than half a million deaths each year (*38*). The incidence of esophageal squamous-cell carcinoma (SCC), the most common histologic type, has been stable, whereas there is an increasing number of esophageal and esophagogastric junction (EGJ) adenocarcinomas in Western countries (*39*). Angiogenesis was identified as a poor prognosis marker in esophageal cancer (*40*). Ramucirumab, a vascular endothelial growth factor-receptor 2 (VEGFR-2) antibody, as a single agent or in combination with paclitaxel, is included as an option for second-line or subsequent therapy for patients with metastatic disease (*41*,*42*). However, more data are needed to ascertain whether the addition of such antiangiogenic therapy to other first-line chemotherapy regimens can improve overall survival (*41*,*43*,*44*). Currently, there are no validated biomarkers to select patients for antiangiogenic therapy. Thus, imaging angiogenesis could be crucial to prescreen patients who will benefit from antiangiogenic therapy.

We hypothesized that the molecular imaging visualization of integrin $\alpha_v\beta_3$ expression using ^{68}Ga-NODAGA-RGD PET/CT could be valuable in exploring esophageal or EGJ malignancies. The primary aims of this study were, first, to compare in patients with esophageal or EGJ cancers the potential of ^{68}Ga-NODAGA-RGD PET/ CT with that of ^{18}F-FDG PET/CT regarding tumoral uptake and distribution, as well as histopathologic examination, and second, to evaluate quantitative functional imaging parameters from ^{68}Ga-NODAGA-RGD PET/CT as potential prognostic markers for disease-free survival (DFS).

Methods

Participants

This study was approved by the ethics commission Vaud (protocol CER-VD #120/12) and registered at Clinical-Trials.gov (NCT02666547). Each participant signed a written informed consent form. Inclusion criteria consisted of biopsy-proven esophageal or EGJ cancer, age ≤ 85 years, Karnofsky index ≥ 80%, and signed consent form. Exclusion criteria consisted of pregnancy, lactation period, and age < 18 years.

TNMp or TNMyp (yp denotes the pathological stage after neoadjuvant therapy) stages and DFS (times from the date of scans to the first date of disease recurrence or death) were recorded, according to the criteria of the seventh edition of the Cancer Staging Manual of the American Joint Committee on Cancer. Recurrence was defined as the appearance of one or more new lesions confirmed by imaging or by cytologic or pathological evaluation. Pathology or follow-up examinations were assessed as ground truth in correlation with PET scans.

PET/CT acquisitions

All the enrolled participants underwent ^{68}Ga-NODAGA-RGD and ^{18}F-FDG PET/CT using a single dedicated PET/CT scanner (Discovery 690 TOF; GE Healthcare, Waukesha, WI, USA). The same procedure for both ^{68}Ga-NODAGA-RGD and ^{18}F-FDG PET/CT was used for data acquisition. A pregnancy test was done before the scan in women of childbearing age. Acquisitions were performed with 3 min per bed position. PET data were reconstructed using OSEM (3 iterations, 16 subsets). Vertex to mid-thigh unenhanced CT was acquired for attenuation correction (120 kV, 60 mA, 0.8 s/rotation, pitch 0.9, CTDI 4.54 mGy). The axial resolution was full width at half maximum of 4.7 mm, at 1 cm from the center of the field of view. The mean positron ranges of ^{18}F and of ^{68}Ga are 0.6 mm and 2.9 mm, respectively.

For ^{68}Ga-NODAGA-RGD PET/CT, participants were injected with ^{68}Ga-NODAGA-RGDyk. PET/CT images were acquired 59.6±3.5 (range 57–69) min after intravenous administration of 197.5±19.0 (range 165–218) MBq ^{68}Ga-NODAGA-RGDyk in an antecubital vein followed by 10 mL of 0.9% NaCl solution.

For ^{18}F-FDG PET/CT, participants fasted at least 6 h. Blood glucose levels were checked before ^{18}F-FDG administration and were confirmed to be < 8.3 mmol/L. PET/CT images were acquired 62.4±6.1 (range 55–72) min after intravenous injection of 243.5±54.8 (range 155–360) MBq ^{18}F-FDG in an antecubital vein followed by 10 mL of 0.9% NaCl solution. The time

interval between ^{68}Ga-NODAGA-RGD PET/CT and ^{18}F-FDG PET/CT was 4.9±2.6 (range 1–9) days.

Image analysis

PET images were analyzed based on standardized uptake value (SUV) measurements in both data sets (^{68}Ga-NODAGA-RGD and ^{18}F-FDG), using a workstation equipped with dedicated analysis software (Syngo.via, VB30, Siemens Healthineers, Erlangen, Germany). Scans were evaluated by two experienced nuclear medicine physicians (JOP and MD), blinded to participant's clinical and histological information. Any difference of opinion was resolved by a consensus. Through visual analysis, positive uptake was identified as areas of focal increase in contrast to the surrounding normal tissue. For the calculation of maximum SUV (SUV_{max}) and of metabolic tumor volumes (MTV), circular regions of interest were drawn around tumor lesions with focally increased uptakes in transaxial slices and automatically adapted to 3-D volumes of interest (VOI) delineated around lesions using 60% SUV_{max} thresholds. Lesion-to-background ratios were computed. For the definition of the background, 10-mm-radius circular volumes of interest were drawn in the right atrium (blood pool activity), and the SUV_{mean} was recorded.

The locations of the maximum uptake pixel within primary sites were visually identified in both data sets (^{68}Ga-NODAGA-RGD and ^{18}F-FDG), and the distance in millimeter (mm) between them was measured.

Histopathology

Histopathological analysis of tissues obtained from biopsies or resected surgical specimens were based on pathology reports.

Statistical analysis

The statistical analysis was performed using R version 4.0.3 (R Foundation for Statistical Computing, Vienna, Austria). We assessed the distribution of data with the Shapiro-Wilk test. Continuous parametric variables were expressed as mean ± SD. Nonparametric data were presented as median [interquartile range] and compared using the Mann-Whitney U test. Spearman correlation analysis (ρ) was used to evaluate potential interrelation between tracers uptake parameters. Cox's proportional hazards regression analysis was used to assess the effects of covariates on survival times. A p value of < 0.05 was considered statistically significant.

Results

Participants

In total, ten ^{68}Ga-NODAGA-RGD and ten ^{18}F-FDG PET/CT were performed in nine prospectively included participants (1 woman; aged 58±8.4 y, range 40–69 y). Participant's characteristics are summarized in Table 1. Six had adenocarcinoma, and three had squamous-cell carcinoma.

Previous therapies before the PET evaluation as well as following therapies after the PET evaluation are described in Table 2. One participant had an antiangiogenic therapy (ramucirumab) 44 days before the ^{68}Ga-NODAGA-RGD PET/CT.

Comparison of ^{68}Ga-NODAGA-RGD PET and ^{18}F-FDG PET data

^{68}Ga-NODAGA-RGD PET/CT detected positive uptake in 10 primary sites (8 for primary tumors and 2 for local relapse suspicion), 6 lymph nodes and 3 skeletal sites. ^{18}F-FDG PET/CT detected positive uptake in the same sites but also in 16 additional lymph nodes and 1 adrenal gland. Data from histology (n=17) or follow-up imaging (n=19) confirmed malignancies, except for a local relapse suspicion (histology proven esophageal candidiasis). An example of an intense ^{18}F-FDG uptake in a lymph node metastasis but without increased ^{68}Ga-NODAGA-RGD uptake is shown in Fig. 1.

The SUV_{max} measurements of ^{68}Ga-NODAGA-RGD and ^{18}F-FDG in confirmed lesions are shown in Table 3. On a lesion-based analysis, SUV_{max} of ^{18}F-FDG were significantly higher than those of ^{68}Ga-NODAGA-RGD (4.9 [3.7–11.3] vs. 3.2 [2.6–4.2] g/mL, $p = 0.014$). Only 1 participant showed a higher SUV_{max} in an osseous metastasis with ^{68}Ga-NODAGA-RGD compared with ^{18}F-FDG (SUV_{max} 6.6 vs. 3.9 g/mL, Fig. 2). Blood-pool activities of ^{18}F-FDG were significantly higher than those of ^{68}Ga-NODAGA-RGD (1.8 [1.7–2.2] vs. 1.2 [1.0–1.2] g/mL, $p = 0.001$). When lesion-to-background ratios were compared, no significant difference was found between ^{18}F-FDG and ^{68}Ga-NODAGA-RGD (2.6 [1.3–5.9] vs. 2.1 [1.9–4.0], $p = 0.9$). Correlation analysis showed moderate to good positive correlation between ^{18}F-FDG and ^{68}Ga-NODAGA-RGD PET parameters ($\rho = 0.56$, $p = 0.012$ for SUV_{max}, $\rho = 0.78$, $p < 0.001$ for lesion-to-background ratios and $\rho = 0.58$, $p = 0.024$ for MTV; Fig. 3).

Table 1 Baseline characteristics

N	9
Age, y	58 ± 8.4
Men	8 (89%)
Body mass index (kg/m^2)	29 ± 4.1
Tumor location at initial diagnosis—N (%)	
Esophagus	8 (89%)
Gastroesophageal junction	1 (11%)
Histologic type—N (%)	
Adenocarcinoma	6 (67%)
Squamous cell carcinoma	3 (33%)
Pathological lymph node status—N (%)	
ypN0	1 (11%)
≥ ypN1	3 (33%)
pN0	3 (33%)
≥ pN1	0
Not known	2 (22%)
Pathological tumor status—N (%)	
ypT0	1 (11%)
ypT1 or ypT2	0
ypT3 or ypT4	3 (33%)
pT0	0
pT1 or pT2	2 (22%)
pT3 or pT4	1 (11%)
Not known	2 (22%)
Histologic grade	
1 or 2	8 (89%)
3 or 4	1 (11%)
Not assessed	0
Tumor-cell PD-L1 expression—N (%)	
< 1%	0
≥ 1%	2 (22%)
Indeterminate or could not be evaluated	7 (78%)
HER2 status	
Positive	0
Negative	5 (56%)
Not reported	4 (44%)
*ECOG performance-status score—N (%) **	
0	6 (67%)
1	3 (33%)

***ECOG performance-status scores range from 0 to 5, with higher scores indicating greater disability**

We incidentally detected a focal increased uptake of ^{68}Ga-NODAGA-RGD in the thyroid, which was absent on the ^{18}F-FDG PET scan. No further investigation could have been done since the participant died 48 days after the ^{68}Ga-NODAGA-RGD PET/CT.

Table 2 Therapy

Participants who received concurrent chemoradiotherapy—*N* (%)	Prior scans	Subsequent scans†
Chemotherapy Neoadjuvant—N (%)		
Carboplatin/paclitaxel	1 (11%)	3 (33%)
Cisplatin/fluorouracil	0	1 (11%)
Other	0	0
Radiotherapy in concurrent chemoradiotherapy—N (%)	1 (11%)	4 (44%)
Radiotherapy dosage, Gray—N (%)		
< 41.4	0	2 (22%)
< 40	0	0
40– < 41.4	0	2 (22%)
41.4–50.4	1 (11%)	2 (22%)
> 50.4	0	0
Not reported	0	0
Participants with any therapies—N (%)		
Surgery	2 (22%)	5 (56%)
Interventional radiology	0	1 (11%)
Systematic therapy—N (%)		
Immunotherapy	0	2 (22%)
Targeted therapy—N (%)		
Anti-angiogenic therapy	1 (11%)	0
Other systemic anticancer therapy/chemotherapy	2 (22%)	1 (11%)

†Before first outcomes

Table 3 Measurements of ^{68}Ga-NODAGA-RGD or ^{18}F-FDG uptake in confirmed positive uptake

All	^{68} Ga-NODAGA-RGD				^{18}F-FDG			
	Median SUVmax (g/mL)	Median Tumor-to blood pool background ratio	Median MTV 60% (cm^3)	Confirmed Lesions (N)	Median SUVmax (g/mL)	Median Tumor-to blood pool background ratio	Median MTV 60% (cm^3)	Confirmed Lesions (N)
Primary sites	3.85	4.58	5.21	9	12.1	5.94	2.31	9
Involved lymph nodes								
Neck and supraclavicular	NA	NA	NA	NA	4.3	2.39	1.03	1
Mediastinum	3.2	1.93	1.07	5	3.75	1.99	0.73	14
Abdomen-Pelvis	2.33	1.94	1.88	1	5	2.78	0.95	7
All	2.85	1.94	1.47	6	3.96	2.17	0.94	22
Bone and visceral metastases								
Bone	3.5	2.85	2.77	3	3.9	1.4	3.5	3
Adrenal gland	NA	NA	NA	NA	5.61	3.38	12.18	1
All	3.5	2.85	2.77	3	4.76	2.39	6.43	4

NA not applicable

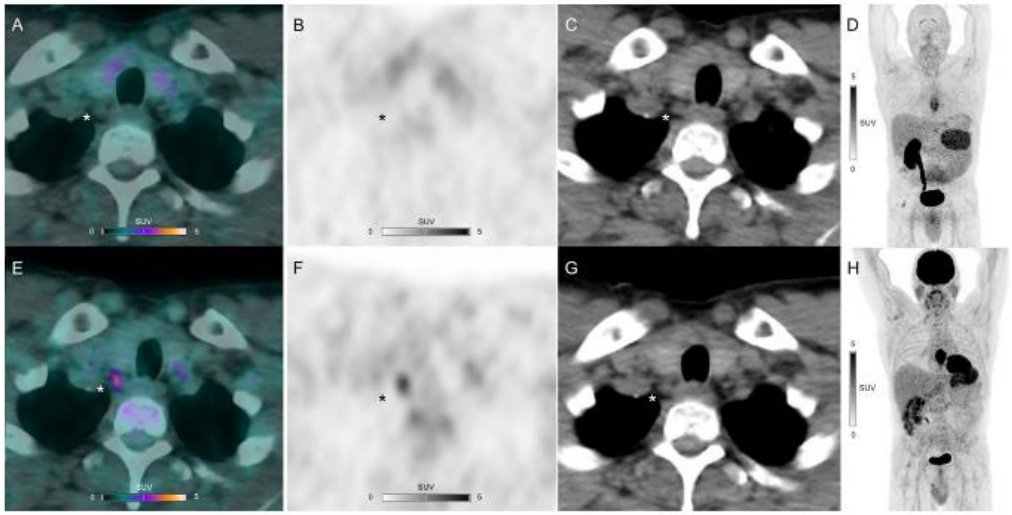

Fig. 1 ^{68}Ga-NODAGA-RGD PET/CT (**A**), PET (**B**, **D**) and CT (**C**) and ^{18}F-FDG PET/CT (**E**), PET (**F**, **H**) and CT (**G**) views of an upper paratracheal lymph node metastasis (asterisks) showing no increased ^{68}Ga-NODAGA-RGD uptake but intense ^{18}F-FDG uptake (SUV_{max} 3.9 g/mL) in a 59-year-old participant with esophageal squamous cell carcinoma

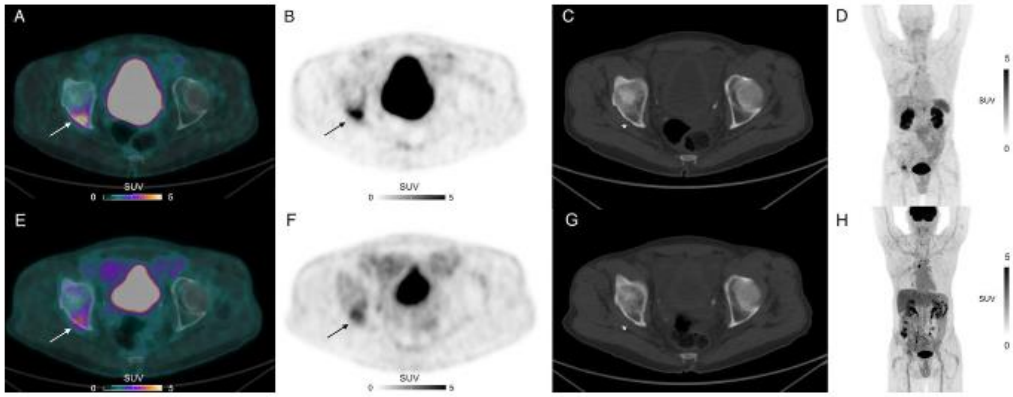

Fig. 2 ^{68}Ga-NODAGA-RGD PET CT (**A**), PET (**B**, **D**) and CT (**C**) and ^{18}F-FDG PET CT (**E**), PET (**F**, **H**) and CT (**G**) axial views showing more intense ^{68}Ga-NODAGA-RGD uptake compared with ^{18}F-FDG uptake (arrows) of an osteolytic lesion (asterisks) of a 63-year-old participant with a metastatic esophageal adenocarcinoma

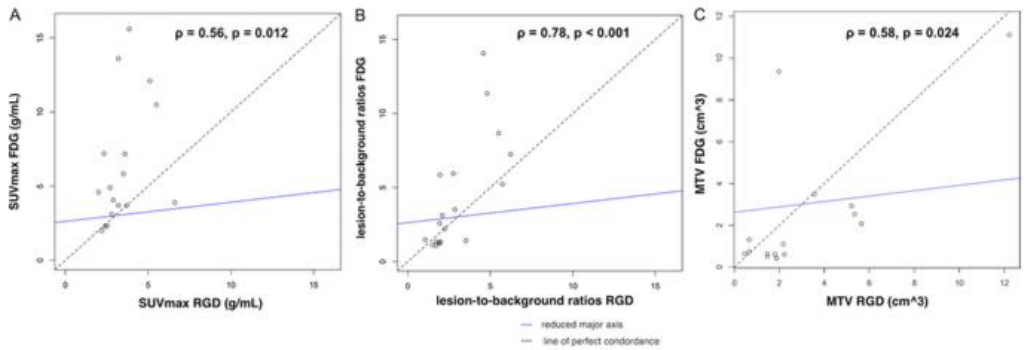

Fig. 3 Scatterplots showing positive correlation of SUV_{max} (**A**), lesion-to-background ratios (**B**) and metabolic tumor volumes (MTV) (**C**) of ^{18}F-FDG and ^{68}Ga-NODAGA-RGD uptake on per-lesion basis

Uptake patterns within primary lesions

The distribution of both tracers within primary sites was different. We observed that ^{18}F-FDG uptake was homogenous inside all the confirmed primary sites (n = 9). In contrast, ^{68}Ga-NODAGA-RGD PET showed more heterogenous uptake in 6 out of the 9 confirmed primary sites (67%), seen mostly in the periphery of the tumor in 5 out of the 9 confirmed primary sites (56%), and showed slight extensions into perilesional structures in 5 out of the 9 confirmed primary sites (56%). An example of these different uptake patterns is shown in Fig. 4.

The median distance between the maximum uptake locations of both scans was 6.5 [4.5–14] mm. This median distance was greater than the PET/CT scanner resolution and the mean positron ranges of ^{18}F and ^{68}Ga.

Effect of pathological tumor status and histologic grade

Both tracers' SUV_{max} in primary lesions did not correlate with pathological tumor status (dichotomized by status Tp or Typ ≤ 2 vs. Tp or Typ > 2; ^{68}Ga-NODAGA-RGD, 3.8 [3.2–5.1] vs. 4.6 [3.7–5.0] g/mL; ^{18}F-FDG, 12.1 [10.5–13.6] vs. 16.8 [10.0–17.0] g/mL, $p \geq 0.57$ for both).

Both tracers' SUV_{max} in primary lesions did not correlate with pathological tumor status (dichotomized by histologic grade 1 or 2 vs. histologic grade 3 or 4; ^{68}Ga-NODAGA-RGD, 3.9 [3.0–5.3] vs. 4.6 g/mL; ^{18}F-FDG, 12.1 [7.7–14.6] vs. 16.8 g/mL, $p \geq 0.5$ for both).

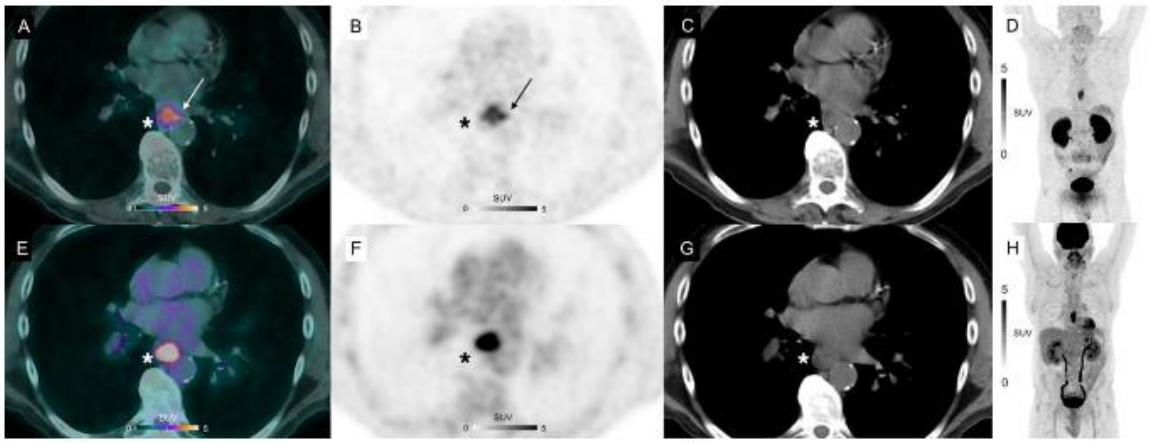

Fig. 4 ^{68}Ga-NODAGA-RGD PET/CT (**A**), PET (**B**, **D**) and CT (**C**) and ^{18}F-FDG PET/CT (**E**), PET (**F**, **H**) and CT (**G**) axial views of a primary lesion (asterisks) in a 53-year-old participant with esophageal squamous cell carcinoma. Note intense homogenous uptake in the primary lesion on ^{18}F-FDG PET/CT (SUV_{max} 12.1 g/mL, metabolic tumor volume 2.54 cm^3), whereas the primary lesion demonstrates a different uptake pattern in the corresponding ^{68}Ga-NODAGA-RGD PET/CT image: a weaker and more heterogeneous uptake (SUV_{max} 5.1 g/mL), seen mostly in the periphery of the tumor, with a slight extension in perilesional structures (arrows), and a larger metabolic tumor volume (metabolic tumor volume 5.35 cm^3)

Outcomes

Over the 825 ± 623 days [range 48-1786] of follow-up, 4 participants have experienced disease recurrence and 2 participants died. The median progression-free survival was 308 days. No ^{68}Ga-NODAGA-RGD uptake measurement in primary lesions turned out to be a prognostic factor for DFS on univariate analysis (SUV_{max}, HR 95% CI: 0.44 to 2.71, p = 0.8; Lesion-to-background ratio, HR 95% CI: 0.62 to 2.22, p = 0.6; MTV 60%, HR 95% CI: 0.83 to 1.59, p = 0.4). Interestingly, the only participant who showed a lesion with a higher SUV_{max} with ^{68}Ga-NODAGA-RGD compared with ^{18}F-FDG (Fig. 2) experienced disease recurrence 231 days after the ^{68}Ga-NODAGA-RGD PET/CT study and died 962 days after, during disease progression with fluorouracil, l-leucovorin, and irinotecan chemotherapy. Nevertheless, statistically, the presence of a lesion with higher SUV_{max} with ^{68}Ga-NODAGA-RGD compared with ^{18}F-FDG did not turn out to be a prognostic factor for DFS on univariate analysis in the current small cohort (HR 95% CI: 0.22 to 20.5, p = 0.5).

Discussion

We report several notable findings from this prospective preliminary study of ^{68}Ga-NODAGA-RGD PET imaging in esophageal or esophagogastric junction cancers. First, the molecular imaging visualization of integrin $\alpha_v\beta_3$ expression using ^{68}Ga-NODAGA-RGD PET/CT has lower potential in the detection of esophageal or esophagogastric junction malignancies compared to the visualization of glucose metabolism with ^{18}F-FDG PET/CT. However, ^{68}Ga-NODAGA-RGD PET/CT showed different uptake patterns in most primary lesions than ^{18}F-FDG PET/CT, and ^{68}Ga-NODAGA-RGD uptake was not systematically lower, suggesting that ^{68}Ga-NODAGA-RGD may provide complementary information.

The study of molecular imaging of integrin expression focused on esophageal or EGJ malignancies has not previously been well-established in the literature. To the best of our knowledge, the only previous study evaluating RGD imaging on the evaluation of esophageal cancer is a prospective study by Zheng et al., investigating the efficacy of [^{99m}Tc]3PRGD$_2$ on standard gamma cameras (*45*).

Our finding of a lower detection rate of ^{68}Ga-NODAGA-RGD than ^{18}F-FDG imaging in detecting malignancies is not unexpected and is consistent with previous other cancer studies in humans. Zheng et al. found a lower sensitivity than ^{18}F-FDG imaging for detecting small esophageal metastatic lesions in lymph nodes. Beer et al. found a lower sensitivity for lesion detection for ^{18}F-galacto-RGD PET as compared to ^{18}F-FDG PET in eighteen cancer patients,

mostly with non–small cell lung cancer (*46*). Haubner et al. demonstrated no increased uptake of ^{68}Ga-NODAGA-RGD in hepatocellular carcinoma compared with the background liver tissue (*47*). In contrast, ^{18}F-FPPRGD$_2$ showed higher sensitivity and specificity than ^{18}F-FDG in a preliminary PET study on breast cancer by Iagaru et al. (*48*).

The finding of a significantly higher uptake with ^{18}F-FDG than with ^{68}Ga-NODAGA-RGD in positive lesions is also not surprising, and consistent with previous studies in humans (*46*,*49*). To explain this difference in tracer uptake Beer et al. argued that ^{18}F-galacto-RGD binds predominantly to endothelial cells, with a substantially smaller number than the number of FDG-avid tumor cells (*46*). As both ^{18}F-Galacto-RGD and ^{68}Ga-NODAGA-RGD demonstrated similar preclinical results (*50*), this same theory could be applied to our study. However, a significantly lower tracer uptake does not necessarily mean a lower lesion-to-background ratio. In the present study when lesion-to-background ratios in positive lesions were compared, no significant difference was found between ^{18}F-FDG and ^{68}Ga-NODAGA-RGD. Same results were shown in a prospective study by Minamimoto et al. (*51*). By comparing ^{18}F-FPPRGD$_2$ and ^{18}F-FDG uptake values in various non-esophageal cancer patients, those authors showed no significant difference in tumor-to-background ratios between both tracers. The low RGD-based tracer uptake in several areas such as the lung, muscles, fat, the brain, or the myocardium could be an advantage for both qualitative and quantitative evaluation of thoracic, breast or brain lesions (*46*,*51*), or for non-oncological applications such as cardiovascular imaging or inflammatory diseases (Dietz et al. 2021; Ebenhan et al. 2021; Dietz et al. 2022; Zhu et al. 2014).

An encouraging finding is the fact that an osteolytic malignant lesion showed a clearly more intense ^{68}Ga-NODAGA-RGD uptake as compared to ^{18}F-FDG. This result is consistent with preclinical data, which supported that RGD-based PET tracer has the potential to effectively image bone metastases, especially in osteolytic metastases, by targeting of the $\alpha_v\beta_3$ integrin on osteoclasts and the proinflammatory cells involved at the bone metastatic site (*56*). In a pilot prospective study of ^{18}F-Alfatide II for detection of skeletal metastases in humans, Mi et al. showed high positive predictive value in the detection of bone metastases, with high lesion-to-background contrast (*57*). This observation is in alignment with the hypothesis that RGD-based imaging may provide complementary information in imaging cancer patients.

We strongly believe that the complementary information provided by molecular imaging of $\alpha_v\beta_3$ expression could be clinically relevant. Integrins, especially the $\alpha_v\beta_3$, are associated with tumor angiogenesis and the blockade of integrin signaling has been shown to inhibit tumor growth, angiogenesis, and early metastasis (Liu et al., 2008). Despite the intriguing concept of

anti-angiogenesis, initially described by Folkman et al. (Folkman et al., 1971), the real therapeutic breakthrough of this treatment never really held its promise and induced only very modest improvements in overall survival (Ribatti et al., 2019). One of the most prominent trials addressing $\alpha_v\beta_3/\alpha_v\beta_5$ inhibition was the CENTRIC trial [Celengitide, Merck KGaA, Darmstadt, Germany] in glioblastoma delivering negative results (Stupp et al., 2014).

The escape mechanisms of cancer against anti-angiogenic treatments are manifold but one key element of resistance is the heterogeneity of neoplastic endothelial cells (Montemagno et al., 2020). ^{68}Ga-NODAGA-RGD PET/CT is a noninvasive, holistic imaging of tumor angiogenesis and could play a pivotal role in identifying patients which have greatest benefit from anti-angiogenetic therapy. This hypothesis is supported by data from the CORE study, where glioblastoma patients with higher $\alpha_v\beta_3/\alpha_v\beta_5$ had significantly better outcomes (Nabors et al., 2015). This clearly demonstrates the need of biomarkers to select patients and find an optimal treatment window for patients receiving anti-angiogenic treatments. Especially functional imaging depicting angiogenic targets as $\alpha_v\beta_3$ could greatly help to select patients and an optimal time window for such treatments. ^{68}Ga-NODAGA-RGD might even serve as theranostic imaging marker followed by therapeutic beta-particle based radioligand therapy (Bozon-Petitprin et al., 2015).

Furthermore, $\alpha_v\beta_3$ integrin is involved in the epithelial–mesenchymal transition, which plays a pivotal role in the very early stages of tumorigenesis and tumor implantation (*58,59*). ^{18}F-FDG PET is widely accepted as preferred method for initial tumor staging in esophageal cancer. ^{68}Ga-NODAGA-RGD with its extensions of uptake into perilesional structures could help to delineate the pre-tumoral and pre-metastatic niche. In the near future, local procedures like surgical resection of radiotherapy in esophageal cancer might use ^{68}Ga-NODAGA-RGD uptake to optimally plan their resection margins or radiotherapy fields. Further investigations would be still required in the future to elucidate the potential role of ^{68}Ga-NODAGA-RGD in esophageal cancer management.

Limitations

There exist some limitations in our study. ^{68}Ga-NODAGA-RGD uptake was not prognostic for any of the investigated endpoints, but our number of participants is not large enough. The limited statistical power may also explain the absence of significant results in subgroup analysis for different pathological tumor status or histological grade. Immunohistochemistry tests were not performed to assess the correlation between integrin $\alpha_v\beta_3$ expression and ^{68}Ga-NODAGA-RGD uptake, which has been demonstrated in several animal and clinical studies (*32,34*).

Conclusion

In conclusion, ^{68}Ga-NODAGA-RGD has lower potential in the detection of esophageal or esophagogastric junction malignancies compared to ^{18}F-FDG. However, the results suggest that ^{68}Ga-NODAGA-RGD may provide complementary information, indicating that PET imaging of integrin $\alpha_v\beta_3$ expression could aid in tumor diversity and delineation.

References

1. Prabhu SD, Frangogiannis NG. The Biological Basis for Cardiac Repair After Myocardial Infarction: From Inflammation to Fibrosis. *Circ Res*. 2016;119:91-112.

2. Khurana R, Simons M, Martin JF, Zachary IC. Role of angiogenesis in cardiovascular disease: a critical appraisal. *Circulation*. 2005;112:1813-1824.

3. Meoli DF, Sadeghi MM, Krassilnikova S, et al. Noninvasive imaging of myocardial angiogenesis following experimental myocardial infarction. *J Clin Invest*. 2004;113:1684-1691.

4. Higuchi T, Bengel FM, Seidl S, et al. Assessment of alphavbeta3 integrin expression after myocardial infarction by positron emission tomography. *Cardiovasc Res*. 2008;78:395-403.

5. Brooks PC, Clark RA, Cheresh DA. Requirement of vascular integrin alpha v beta 3 for angiogenesis. *Science*. 1994;264:569-571.

6. van den Borne SWM, Isobe S, Verjans JW, et al. Molecular imaging of interstitial alterations in remodeling myocardium after myocardial infarction. *J Am Coll Cardiol*. 2008;52:2017-2028.

7. Dietz M, Kamani CH, Dunet V, et al. Overview of the RGD-Based PET Agents Use in Patients With Cardiovascular Diseases: A Systematic Review. *Front Med (Lausanne)*. 2022;9:887508.

8. Ebenhan T, Kleynhans J, Zeevaart JR, Jeong JM, Sathekge M. Non-oncological applications of RGD-based single-photon emission tomography and positron emission tomography agents. *Eur J Nucl Med Mol Imaging*. 2021;48:1414-1433.

9. Jenkins WSA, Vesey AT, Stirrat C, et al. Cardiac $\alpha_V\beta_3$ integrin expression following acute myocardial infarction in humans. *Heart*. 2017;103:607-615.

10. Knetsch PA, Petrik M, Griessinger CM, et al. [68Ga]NODAGA-RGD for imaging αvβ3 integrin expression. *Eur J Nucl Med Mol Imaging*. 2011;38:1303-1312.

11. Gould KL, Johnson NP, Bateman TM, et al. Anatomic Versus Physiologic Assessment of Coronary Artery Disease: Role of Coronary Flow Reserve, Fractional Flow Reserve, and Positron Emission Tomography Imaging in Revascularization Decision-Making. *Journal of the American College of Cardiology*. 2013;62:1639-1653.

12. Cerqueira MD, Weissman NJ, Dilsizian V, et al. Standardized myocardial segmentation and nomenclature for tomographic imaging of the heart. A statement for healthcare professionals from the Cardiac Imaging Committee of the Council on Clinical Cardiology of the American Heart Association. *Circulation*. 2002;105:539-542.

13. Lortie M, Beanlands RSB, Yoshinaga K, Klein R, Dasilva JN, DeKemp RA. Quantification of myocardial blood flow with 82Rb dynamic PET imaging. *Eur J Nucl Med Mol Imaging*. 2007;34:1765-1774.

14. Nesterov SV, Deshayes E, Sciagrà R, et al. Quantification of myocardial blood flow in absolute terms using (82)Rb PET imaging: the RUBY-10 Study. *JACC Cardiovasc Imaging*. 2014;7:1119-1127.

15. Sdringola S, Johnson NP, Kirkeeide RL, Cid E, Gould KL. Impact of Unexpected Factors on Quantitative Myocardial Perfusion and Coronary Flow Reserve in Young, Asymptomatic Volunteers. *JACC: Cardiovascular Imaging*. 2011;4:402-412.

16. Machac J, Bacharach SL, Bateman TM, et al. Positron emission tomography myocardial perfusion and glucose metabolism imaging. *J Nucl Cardiol*. 2006;13:e121-e151.

17. Ortiz-Pérez JT, Rodríguez J, Meyers SN, Lee DC, Davidson C, Wu E. Correspondence between the 17-segment model and coronary arterial anatomy using contrast-enhanced cardiac magnetic resonance imaging. *JACC Cardiovasc Imaging*. 2008;1:282-293.

18. Antonov AS, Kolodgie FD, Munn DH, Gerrity RG. Regulation of Macrophage Foam Cell Formation by αVβ3 Integrin. *Am J Pathol*. 2004;165:247-258.

19. Asano Y, Ihn H, Yamane K, Jinnin M, Mimura Y, Tamaki K. Increased expression of integrin alpha(v)beta3 contributes to the establishment of autocrine TGF-beta signaling in scleroderma fibroblasts. *J Immunol*. 2005;175:7708-7718.

20. de Haas HJ, Arbustini E, Fuster V, Kramer CM, Narula J. Molecular imaging of the cardiac extracellular matrix. *Circ Res*. 2014;114:903-915.

21. Verjans J, Wolters S, Laufer W, et al. Early molecular imaging of interstitial changes in patients after myocardial infarction: Comparison with delayed contrast-enhanced magnetic resonance imaging. *J Nucl Cardiol*. 2010;17:1065-1072.

22. Sherif HM, Saraste A, Nekolla SG, et al. Molecular imaging of early αvβ3 integrin expression predicts long-term left-ventricle remodeling after myocardial infarction in rats. *J Nucl Med*. 2012;53:318-323.

23. Meyer A, Auernheimer J, Modlinger A, Kessler H. Targeting RGD recognizing integrins: drug development, biomaterial research, tumor imaging and targeting. *Curr Pharm Des*. 2006;12:2723-2747.

24. Friedlander M, Brooks PC, Shaffer RW, Kincaid CM, Varner JA, Cheresh DA. Definition of two angiogenic pathways by distinct alpha v integrins. *Science*. 1995;270:1500-1502.

25. MacDonald TJ, Taga T, Shimada H, et al. Preferential susceptibility of brain tumors to the antiangiogenic effects of an alpha(v) integrin antagonist. *Neurosurgery*. 2001;48:151-157.

26. Bentsen S, Jensen JK, Christensen E, et al. [68Ga]Ga-NODAGA-E[(cRGDyK)]2 angiogenesis PET following myocardial infarction in an experimental rat model predicts cardiac functional parameters and development of heart failure. *J Nucl Cardiol*. May 2023.

27. Follin B, Hoeeg C, Hunter I, et al. [68Ga]Ga-NODAGA-E[(cRGDyK)]2 and [64Cu]Cu-DOTATATE PET Predict Improvement in Ischemic Cardiomyopathy. *Diagnostics (Basel)*. 2023;13:268.

28. Cleutjens JP, Blankesteijn WM, Daemen MJ, Smits JF. The infarcted myocardium: simply dead tissue, or a lively target for therapeutic interventions. *Cardiovasc Res*. 1999;44:232-241.

29. Sun M, Opavsky MA, Stewart DJ, et al. Temporal response and localization of integrins beta1 and beta3 in the heart after myocardial infarction: regulation by cytokines. *Circulation*. 2003;107:1046-1052.

30. van den Borne SWM, Isobe S, Zandbergen HR, et al. Molecular imaging for efficacy of pharmacologic intervention in myocardial remodeling. *JACC Cardiovasc Imaging*. 2009;2:187-198.

31. Hood JD, Cheresh DA. Role of integrins in cell invasion and migration. *Nat Rev Cancer*. 2002;2:91-100.

32. Chen H, Niu G, Wu H, Chen X. Clinical Application of Radiolabeled RGD Peptides for PET Imaging of Integrin αvβ3. *Theranostics*. 2016;6:78-92.

33. Dietz M, Kamani CH, Dunet V, et al. Overview of the RGD-Based PET Agents Use in Patients With Cardiovascular Diseases: A Systematic Review. *Front Med (Lausanne)*. 2022;9:887508.

34. Jeong JM, Hong MK, Chang YS, et al. Preparation of a promising angiogenesis PET imaging agent: 68Ga-labeled c(RGDyK)-isothiocyanatobenzyl-1,4,7-triazacyclononane-1,4,7-triacetic acid and feasibility studies in mice. *J Nucl Med*. 2008;49:830-836.

35. Knetsch PA, Petrik M, Griessinger CM, et al. [68Ga]NODAGA-RGD for imaging αvβ3 integrin expression. *Eur J Nucl Med Mol Imaging*. 2011;38:1303-1312.

36. Buchegger F, Viertl D, Baechler S, et al. 68Ga-NODAGA-RGDyK for αvβ3 integrin PET imaging. Preclinical investigation and dosimetry. *Nuklearmedizin*. 2011;50:225-233.

37. Gnesin S, Mitsakis P, Cicone F, et al. First in-human radiation dosimetry of 68Ga-NODAGA-RGDyK. *EJNMMI Res*. 2017;7:43.

38. Bray F, Ferlay J, Soerjomataram I, Siegel RL, Torre LA, Jemal A. Global cancer statistics 2018: GLOBOCAN estimates of incidence and mortality worldwide for 36 cancers in 185 countries. *CA Cancer J Clin*. 2018;68:394-424.

39. Arnold M, Ferlay J, Henegouwen MI van B, Soerjomataram I. Global burden of oesophageal and gastric cancer by histology and subsite in 2018. *Gut*. 2020;69:1564-1571.

40. Lurje G, Leers JM, Pohl A, et al. Genetic variations in angiogenesis pathway genes predict tumor recurrence in localized adenocarcinoma of the esophagus. *Ann Surg*. 2010;251:857-864.

41. Ajani JA, D'Amico TA, Bentrem DJ, et al. Esophageal and Esophagogastric Junction Cancers, Version 2.2019, NCCN Clinical Practice Guidelines in Oncology. *J Natl Compr Canc Netw*. 2019;17:855-883.

42. Fuchs CS, Tomasek J, Yong CJ, et al. Ramucirumab monotherapy for previously treated advanced gastric or gastro-oesophageal junction adenocarcinoma (REGARD): an international, randomised, multicentre, placebo-controlled, phase 3 trial. *Lancet*. 2014;383:31-39.

43. Wilke H, Muro K, Van Cutsem E, et al. Ramucirumab plus paclitaxel versus placebo plus paclitaxel in patients with previously treated advanced gastric or gastro-oesophageal junction adenocarcinoma (RAINBOW): a double-blind, randomised phase 3 trial. *Lancet Oncol*. 2014;15:1224-1235.

44. Fuchs CS, Shitara K, Bartolomeo MD, et al. Ramucirumab with cisplatin and fluoropyrimidine as first-line therapy in patients with metastatic gastric or junctional adenocarcinoma (RAINFALL): a double-blind, randomised, placebo-controlled, phase 3 trial. *The Lancet Oncology*. 2019;20:420-435.

45. Zheng S, Chen Z, Huang C, Chen Y, Miao W. [99mTc]3PRGD2 for integrin receptor imaging of esophageal cancer: a comparative study with [18F]FDG PET/CT. *Ann Nucl Med*. 2019;33:135-143.

46. Beer AJ, Lorenzen S, Metz S, et al. Comparison of integrin alphaVbeta3 expression and glucose metabolism in primary and metastatic lesions in cancer patients: a PET study using 18F-galacto-RGD and 18F-FDG. *J Nucl Med*. 2008;49:22-29.

47. Haubner R, Finkenstedt A, Stegmayr A, et al. [68Ga]NODAGA-RGD – Metabolic stability, biodistribution, and dosimetry data from patients with hepatocellular carcinoma and liver cirrhosis. *Eur J Nucl Med Mol Imaging*. 2016;43:2005-2013.

48. Iagaru A, Mosci C, Shen B, et al. 18F-FPPRGD2 PET/CT: Pilot Phase Evaluation of Breast Cancer Patients. *Radiology*. 2014;273:549-559.

49. Durante S, Dunet V, Gorostidi F, et al. Head and neck tumors angiogenesis imaging with 68Ga-NODAGA-RGD in comparison to 18F-FDG PET/CT: a pilot study. *EJNMMI Res*. 2020;10:47.

50. Pohle K, Notni J, Bussemer J, Kessler H, Schwaiger M, Beer AJ. 68Ga-NODAGA-RGD is a suitable substitute for (18)F-Galacto-RGD and can be produced with high specific activity in a cGMP/GRP compliant automated process. *Nucl Med Biol*. 2012;39:777-784.

51. Minamimoto R, Jamali M, Barkhodari A, et al. Biodistribution of the ^{18}F-FPPRGD$_2$ PET radiopharmaceutical in cancer patients: an atlas of SUV measurements. *Eur J Nucl Med Mol Imaging*. 2015;42:1850-1858.

52. Ebenhan T, Kleynhans J, Zeevaart JR, Jeong JM, Sathekge M. Non-oncological applications of RGD-based single-photon emission tomography and positron emission tomography agents. *Eur J Nucl Med Mol Imaging*. 2021;48:1414-1433.

53. Dietz M, Kamani CH, Deshayes E, et al. Imaging angiogenesis in atherosclerosis in large arteries with 68Ga-NODAGA-RGD PET/CT: relationship with clinical atherosclerotic cardiovascular disease. *EJNMMI Res*. 2021;11:71.

54. Zhu Z, Yin Y, Zheng K, et al. Evaluation of synovial angiogenesis in patients with rheumatoid arthritis using ^{68}Ga-PRGD2 PET/CT: a prospective proof-of-concept cohort study. *Ann Rheum Dis*. 2014;73:1269-1272.

55. Dietz M, Nicod Lalonde M, Omoumi P, Testart Dardel N, Hügle T, Prior JO. Imaging of αvβ3 integrin expression in rheumatoid arthritis with [68Ga]Ga-NODAGA-RGDyk PET/CT in comparison to [18F]FDG PET/CT. *Médecine Nucléaire*. 2021;45:293-295.

56. Wadas TJ, Deng H, Sprague JE, Zheleznyak A, Weilbaecher KN, Anderson CJ. Targeting the αvβ3 Integrin for Small-Animal PET/CT of Osteolytic Bone Metastases. *J Nucl Med*. 2009;50:1873-1880.

57. Mi B, Yu C, Pan D, et al. Pilot Prospective Evaluation of 18F-Alfatide II for Detection of Skeletal Metastases. *Theranostics*. 2015;5:1115-1121.

58. Kariya Y, Oyama M, Suzuki T, Kariya Y. αvβ3 Integrin induces partial EMT independent of TGF-β signaling. *Commun Biol*. 2021;4:1-11.

59. Liu Q, Zhang H, Jiang X, Qian C, Liu Z, Luo D. Factors involved in cancer metastasis: a better understanding to “seed and soil” hypothesis. *Molecular Cancer*. 2017;16:176.

Chapter 12

Imaging of αvβ3 Integrin Expression in Rheumatoid Arthritis with [68Ga]Ga-NODAGA-RGDyk PET/CT in comparison to [18F]FDG PET/CT

Med Nucl. 2021;45(5-6):293-295.

Matthieu Dietz, Marie Nicod Lalonde, Patrick Omoumi, Nathalie Testart Dardel, Thomas Hügle, John O Prior

Abstract

[^{68}Ga]Ga-NODAGA-RGDyk PET/CT and [^{18}F]FDG PET/CT were performed in a 65-year-old woman during the work-up of a squamous cell carcinoma of the tongue within a clinical study protocol. Images revealed both tracers' uptake in the primary tumor and cervical lymph nodes, but also bilaterally in the shoulders, elbows, wrists, metacarpophalangeal, interphalangeal, and hip joints. The patient had been diagnosed with rheumatoid arthritis 8 years prior to the examination. Images showed a significantly higher [^{18}F]FDG than [^{68}Ga]Ga-NODAGA-RGDyk uptake in primary tumor and cervical lymph nodes. However, the patient with moderately active rheumatoid arthritis had similar levels of [^{68}Ga]Ga-NODAGA-RGDyk and [^{18}F]FDG uptake in the involved joints, but with no [^{68}Ga]Ga-NODAGA-RGDyk uptake in the surrounding muscles, unlike with [^{18}F]FDG. Our case suggests that [^{68}Ga]Ga-NODAGA-RGDyk PET/CT allows imaging of integrins expression in rheumatoid arthritis, including integrins expressed in synovial angiogenesis, with potentially a better signal-to-noise ratio than on [^{18}F]FDG PET/CT.

We report the case of a 65-year-old woman who underwent [^{68}Ga]Ga-NODAGA-RGDyk PET/CT and [^{18}F]FDG PET/CT for imaging angiogenesis of a known squamous cell carcinoma of the tongue within a clinical study protocol. The patient was referred for baseline PET/CT scans for staging before receiving chemotherapy and radiotherapy. The protocol was approved by the Ethics Commission Vaud (CER-VD #120/12). A written informed consent was obtained. Images revealed both tracers' uptake in primary tumor and cervical lymph nodes, but also bilaterally in the shoulders, elbows, wrists, metacarpophalangeal, interphalangeal, and hip joints. The patient had been diagnosed with seronegative rheumatoid arthritis (RA) 8 years ago based on the presence of persistent symmetrical polyarthritis with an inflammatory reaction (C-reactive protein 12 mg/L), negativity for anti-cyclic citrullinated peptide antibody and rheumatoid factor, and excellent response after starting corticosteroid therapy. A combination therapy with corticosteroids, methotrexate, and salazopyrine had been initiated, followed later by adalimumab and tocilizumab. At the time of the study, the anti-rheumatic therapy had been suspended during chemotherapy. She presented moderately active rheumatoid arthritis with arthralgia and mild joint swelling of her metacarpophalangeal joints.

[^{68}Ga]Ga-NODAGA-RGDyk PET/CT images were acquired 86 min after intravenous administration of 197 MBq [^{68}Ga]Ga-NODAGA-RGDyk. [^{18}F]FDG PET/CT images were acquired 71 min after intravenous administration of 236 MBq [^{18}F]FDG. [^{68}Ga]Ga-NODAGA-RGDyk in comparison to [^{18}F]FDG PET/CT image demonstrated different distributions in the pathological regions. Compared to [^{68}Ga]Ga-NODAGA-RGDyk images, [^{18}F]FDG images demonstrated a very significantly higher uptake in primary tumor and cervical lymph nodes (Fig. 1). While the patient with moderately active RA had similar levels of [^{68}Ga]Ga-NODAGA-RGDyk and [^{18}F]FDG uptake in the involved joints (mean ± SD SUV_{max}: 2.00 ± 0.73 and 2.19 ± 0.66, respectively). However, [^{68}Ga]Ga-NODAGA-RGDyk uptake in surrounding muscles was lower than [^{18}F]FDG (SUV_{max} measured in a spherical 3 cm^3 volume of interest drawn in the gluteal muscle: 0.57 and 0.78, respectively); therefore, the mean [^{68}Ga]Ga-NODAGA-RGDyk joint-to-muscle background ratio was higher than [^{18}F]FDG (3.51 ± 0.73 and 2.80 ± 0.66, respectively). Movement disorder induced by pain in patients suffering from RA could potentially impair the evaluation of joint inflammation with [^{18}F]FDG PET/CT [1].

RA is an autoimmune disorder of unknown etiology. The disease is characterized by systematic, symmetric, and erosive synovitis. RA synovitis exhibits massive proliferative synovial membranes, leukocyte infiltration, and neovascularization. The formation of synovial

proliferative fibrovascular tissue known as pannus is directly responsible for cartilage and bone destruction, integrins playing a central role in triggering this proliferation [2,3].

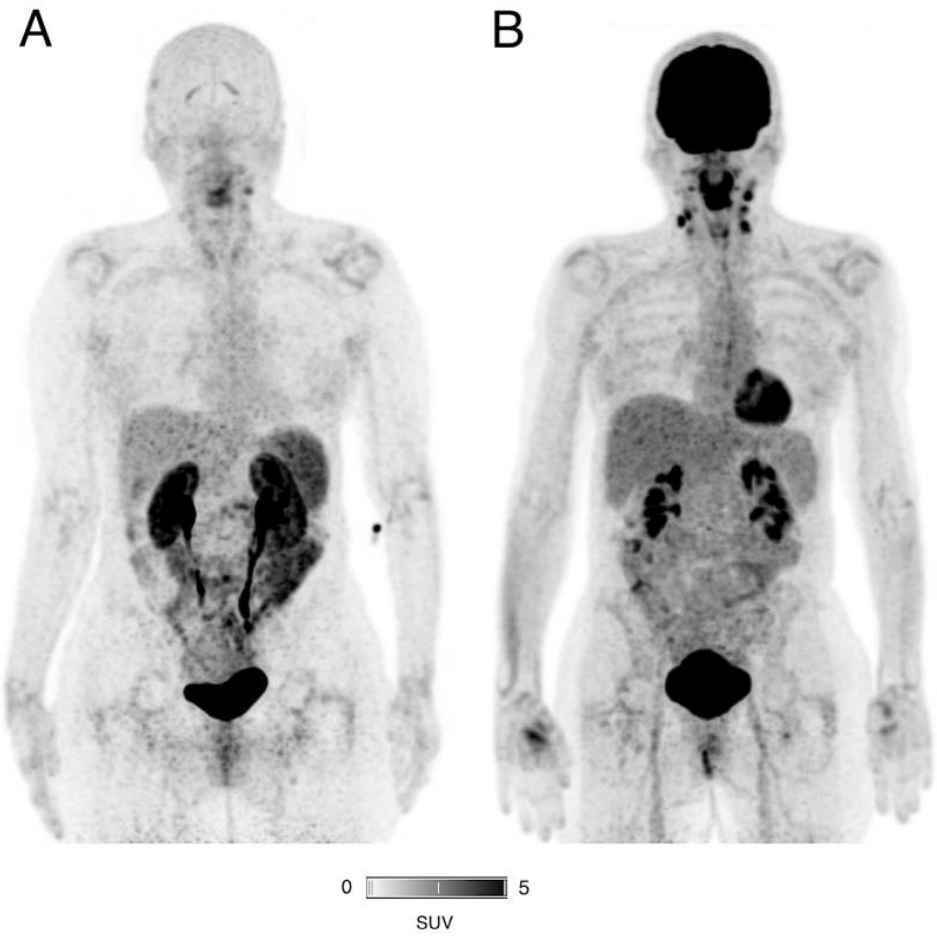

Fig. 1. A. [^{68}Ga]Ga-NODAGA- RGDyk PET/CT maximum intensity projection (MIP) view. B. [^{18}F]FDG PET/CT MIP view.
A. TEP/TDM au [^{68}Ga]Ga-NODAGA-RGDyk, vue maximum intensity projection (MIP). B. TEP/TDM au [^{18}F]FDG, vue MIP.

Various radiolabeled derivatives of arginine-glycine-aspartic acid (RGD)-peptides have been developed for imaging of αvβ3 integrin expression [4-7]. Increased αvβ3 expression has been observed in tumor angiogenesis, new blood vessels formed after myocardial infarction, or blood vessels in chronic inflammatory processes. Integrin αvβ3 is also expressed by some cancer cells, such as glioblastoma and melanoma, and in cells involved in extracellular matrix remodeling as well as fibroblasts and activated macrophages [6,7]. NODAGA-RGDyK, (cyclo[L-arginylglycyl-L-alpha-aspartyl-D-tyrosyl-N6-([4,7-bis(carboxymethyl)octahydro1H-1,4,7-triazonin- 1-yl]acetyl])-L-lysyl]), is a new RGD peptide designed for PET imaging of αvβ3 integrin expression. The compound c(RGDyK) showed high affinity for the integrin αvβ3 in vivo binding assays [8]. The component NODAGA is a derivate of the NOTA system which

has no influence on receptor-specific binding and possesses high binding properties for radiometals with an ion radius like ^{68}Ga [9]. [^{68}Ga]Ga-NODAGA- RGDyk has favorable biokinetics and safety profile [10,11].

The development of an extensive network of new blood vessels in the synovial membrane is typically found in the evolution of rheumatoid synovitis and evaluation of synovial angiogenesis using PET/CT could be of interest to improve the understanding of this disease [1,12]. Recently, Adipoe et al. showed, in a proof-of-concept study, a strong correlation between power Doppler ultrasound (US) in the joints of patients with RA and the uptake of [^{99m}Tc]Tc-maraciclatide, a radiolabelled tracer containing the RGD tripeptide motif with high affinity for integrin αvβ3 dedicated to scintigraphic imaging [13]. Their data are consistent with the previous study from Zhu et al, which preliminarily indicates the potential effectiveness of integrin imaging for evaluating RA joints [1]. Although patients with RA are typically monitored with US which detects synovitis, in a cheaper and non-invasive way, nuclear medicine techniques can provide whole body quantitative information in a single acquisition, with an easier interpretation of scans compared with US or MRI. Such new integrin imaging would mostly be interesting in a research setting, or to easily assess the global burden of the disease, which could potentially guide treatment decisions. Our case suggests that synovial angiogenesis in RA could be depicted using [^{68}Ga]Ga-NODAGA- RGDyk PET/CT, with potentially a higher signal-to-noise background ratio compared with [^{18}F]FDG PET/CT.

References

1. Zhu Z, Yin Y, Zheng K, et al. Evaluation of synovial angiogenesis in patients with rheumatoid arthritis using 68Ga-PRGD2 PET/CT: a prospective proof-of concept cohort study. Ann Rheum Dis. 2014;73:1269–72.
2. Leblond A, Allanore Y, Avouac J. Targeting synovial neoangiogenesis in rheumatoid arthritis. Autoimmun Rev. 2017;16:594-601.
3. Morshed A, Abbas AB, Hu J, et al. Shedding New Light on The Role of αvβ3 and α5β1 Integrins in Rheumatoid Arthritis. Molecules. 2019;18;24:1537.
4. Eo JS, Jeong JM. Angiogenesis imaging using Ga-68 RGD PET/CT: therapeutic implications. Semin Nucl Med. 2016;46:419–427.
5. Durante S, Dunet V, Gorostidi F, et al. Head and neck tumors angiogenesis imaging with ^{68}Ga-NODAGA-RGD in comparison to ^{18}F-FDG PET/CT: a pilot study. EJNMMI Res. 2020;10:47.
6. Ebenhan T, Kleynhans J, Zeevaart JR, et al. Non-oncological applications of RGD-based single-photon emission tomography and positron emission tomography agents. Eur J Nucl Med Mol Imaging. 2020. doi: 10.1007/s00259-020-04975-9.
7. N. Withofs, R. Hustinx. Integrin $\alpha_v\beta_3$ and RGD-based radiopharmaceuticals**.** Méd Nucl. 2016;40:41-54.
8. J. M. Jeong, M. K. Hong, Y. S. Chang et al. Preparation of a promising angiogenesis PET imaging agent: ^{68}Ga-labeled c(RGDyK)-isothiocyanatobenzyl-1,4,7-triazacyclononane-1, 4,7-triacetic acid and feasibility studies in mice. J Nucl Med. 2008;49:830-6.
9. Knetsch PA, Petrik M, Griessinger CM, et al. [68Ga]NODAGA-RGD for imaging αvβ3 integrin expression. Eur J Nucl Med Mol Imaging 2011;38:1303-12.
10. Buchegger F, Viertl D, Baechler S et al. 68Ga-NODAGA-RGDyK for αvβ3 integrin PET imaging. Nuklearmedizin 50:225–233.
11. Gnesin S, Mitsakis P, Cicone F et al. First in-human radiation dosimetry of 68Ga-NODAGA-RGDyK. EJNMMI Res. 2017;7:43.
12. Notni, J., Gassert, F.T., Steiger, K. et al. In vivo imaging of early stages of rheumatoid arthritis by α5β1-integrin-targeted positron emission tomography. EJNMMI Res. 2019;9,87.

13. Attipoe L, Chaabo K, Wajed J, ET AL. Imaging neoangiogenesis in rheumatoid arthritis (INIRA): whole-body synovial uptake of a ^{99m}Tc-labelled RGD peptide is highly correlated with power Doppler ultrasound. Ann Rheum Dis. 2020;79:1254-5.

Chapter 13

Summary and conclusions

Integrin $\alpha_v\beta_3$ expression in Cardiovascular PET/CT Imaging

Chapter 2

We evaluated recent studies using RGD-PET agents in cardiovascular diseases. Our systematic review provides an updated summary of the role of RGD-based PET agents in cardiovascular patients, aiming to guide future research. Original articles reporting on RGD-based PET agents in cardiovascular diseases were included from PubMed/MEDLINE and Cochrane library databases until October 26, 2021. Findings indicate an increasing role of RGD-based PET agents in cardiovascular diseases, particularly in the infarcted myocardium and atherosclerosis. RGD PET/CT scans effectively display $\alpha_v\beta_3$ integrin expression in the infarcted myocardium. The uptake of RGD-based PET radiotracers occurs early after myocardial infarction, peaking at 1–3 weeks post-infarction before declining. Limited research explores serial changes in RGD-based PET uptake post-ischemic events. Furthermore, RGD-based PET uptake in major vessels correlates with CT plaque burden, showing heightened signals in patients with previous cardiovascular events. Atherosclerotic carotid plaques reveal increased PET signals in stenotic versus non-stenotic areas, supported by MR or CT angiography data. Histopathological analysis validates tracer accumulation in regions expressing $\alpha_v\beta_3$. Promising applications emerge, including predicting infarcted myocardium remodeling and detecting active atherosclerosis, with potential clinical impact.

Chapter 3

In this prospective monocentric observational trial, we aimed to utilize the imaging biomarker ^{68}Ga-NODAGA-RGD to track angiogenic activity in the myocardium following reperfusion in patients who had experienced a ST-elevated myocardial infarction. A total of 20 patients with reperfused STEMI were enrolled in the study, and they underwent a series of 110 PET/CT scans at 1 week, 1 month, and 3 months after reperfusion. These scans included ^{68}Ga-NODAGA-RGD PET/CT and rest and stress ^{82}Rb-PET/CT. The results revealed that at 1 week after reperfusion, nearly all participants, except for one, exhibited increased ^{68}Ga-NODAGA-RGD uptake in the infarcted myocardium. Interestingly, the RGD SUV values in the infarcted

myocardium remained stable at 1 month after reperfusion, showing no significant difference from the 1-week measurement. However, at the 3-month mark, there was a partial but significant decrease in RGD SUV, indicating a decline in angiogenic activity. In conclusion, this study suggests that angiogenic activity in the infarcted myocardium persists for at least 1 month after reperfusion, followed by a partial decline by the 3-month mark, providing valuable insights into the dynamics of angiogenesis in the myocardium following ST-elevated myocardial infarction.

Chapter 4

We assessed ^{68}Ga-NODAGA-RGD, a PET tracer targeting $\alpha_v\beta_3$ integrin linked to angiogenesis post-acute myocardial infarction. In 31 patients after primary percutaneous coronary intervention, PET measured ^{68}Ga-NODAGA-RGD uptake and myocardial blood flow. Transthoracic echocardiography evaluated left ventricular function on the day of PET and at 6-month follow-up. Results showed increased ^{68}Ga-NODAGA-RGD uptake in the ischemic at-risk area, primarily in injured segments. The segment with highest uptake had higher SUVmax than mean SUV of remote myocardium (0.73±0.16 vs. 0.51±0.11, $p<0.001$). Predictors of ^{68}Ga-NODAGA-RGD uptake in the at-risk area included high peak NT-proBNP, low left ventricular ejection fraction, low global longitudinal strain ($p=0.01$), and low longitudinal strain in the at-risk area ($p=0.01$). Corrected ^{68}Ga-NODAGA-RGD uptake in the at-risk area predicted improved global longitudinal strain at follow-up ($p=0.002$), independent of troponin, NT-proBNP, and left ventricular ejection fraction. In conclusion, ^{68}Ga-NODAGA-RGD uptake early after AMI reflects increased $\alpha_v\beta_3$ integrin expression in the at-risk area, linked to regional/global systolic dysfunction and higher left ventricular filling pressure. Elevated ^{68}Ga-NODAGA-RGD uptake anticipates better global left ventricular function 6 months after acute myocardial infarction.

Chapter 5

We aimed to investigate the association between the accumulation of ^{68}Ga-NODAGA-RGD in arterial walls and various clinical factors in cardiovascular disease. We retrospectively analyzed data from 44 patients who underwent ^{68}Ga-NODAGA-RGD PET/CT scans. The results revealed that arterial uptake of ^{68}Ga-NODAGA-RGD was notably higher in patients with prior clinically documented atherosclerotic cardiovascular disease. The uptake also correlated with a

history of cardiovascular or cerebrovascular events, higher BMI, increased plaque burden, and hypercholesterolemia. These findings suggest that ^{68}Ga-NODAGA-RGD could serve as a promising non-invasive marker for assessing disease activity in atherosclerosis, offering insights into intraplaque angiogenesis.

Chapter 6

We explore the potential use of ^{177}Lu-DOTATATE therapy in coronary atherosclerotic plaque inflammation, employing a theranostic approach. ^{177}Lu-DOTATATE has demonstrated effectiveness in neuroendocrine tumor treatment. SST2-targeted peptide receptor radionuclide therapy using ^{177}Lu-DOTATATE delivers radioisotopes to cells expressing high SST2 levels. Inflammatory macrophages express SST2 and are implicated in atherosclerosis. The study evaluated 44 patients who underwent ^{177}Lu-DOTATATE PET/CT scans. Baseline and follow-up scans revealed a significant reduction in coronary uptake of ^{68}Ga-DOTATATE ligands after therapy, potentially indicating decreased plaque inflammation. While these findings suggest a therapeutic role, further prospective trials are required for confirmation.

Chapter 7

In this study, we investigated the effectiveness of a reliable quantitative variable in Rubidium-82 cardiac PET/CT for predicting major adverse cardiovascular events. We utilized low-dose silicon photomultipliers technology, enabling a reduction in injected activity and radiation dose, resulting in less than 1.0 mSv exposure for a 70-kg individual. We conducted a prospective study with 234 consecutive participants who had suspected myocardial ischemia. These participants underwent Rubidium-82 cardiac silicon photomultipliers PET/CT with an administered dose of 5 MBq/kg. Follow-up occurred over a median of 652 days (ranging from 559 to 751 days) to monitor major adverse cardiovascular events occurrence. For each participant, we measured global stress myocardial blood flow (stress MBF), global myocardial flow reserve (MFR), and the extent of severely reduced regional myocardial flow capacity (MFCsevere). We employed the Youden index to identify optimal threshold values. Through multivariate analysis, while considering clinical risk factors, we found that reduced global stress MBF (<1.94 ml/min/g), reduced global MFR (<1.98), and elevated regional MFCsevere (>3.2% of left ventricle) all emerged as independent predictors of MACE (with respective hazard ratios

of 4.5, 3.1, and 3.67, all p<0.001). However, when adjusting for clinical risk factors and accounting for the combined impact of global stress MBF, global MFR, and regional MFCsevere impairments, only reduced global stress MBF remained a statistically significant independent prognostic indicator for MACE (hazard ratio 2.81, p=0.027). In conclusion, we employed state-of-the-art silicon photomultipliers PET technology and administered low-dose Rubidium-82, halving the standard activity to achieve radiation exposure below 1 mSv for a 70-kg patient. Our findings indicated that impaired global stress MBF, global MFR, and regional MFC were robust predictors of cardiovascular events, surpassing the predictive capability of traditional cardiovascular risk factors. However, it was discerned that only reduced global stress MBF maintained its status as an independent predictor of MACE, exhibiting superior predictive performance compared to global MFR and regional MFC impairments.

Chapter 8

In this study, we investigated the correlation between small-vessel disease (SVD) affecting the heart and the brain using quantitative Rubidium-82 cardiac PET/CT and brain MRI. We analyzed 370 patients, including 38 with pure cardiac SVD and 176 with normal heart perfusion. Patients with cardiac SVD exhibited reduced stress LV-MBF and flow reserve, while brain MRI parameters were comparable between groups. Notably, increased resting LV-MBF in cardiac SVD patients correlated with specific brain region alterations, and decreased stress LV-MBF and LV-MFR were associated with other distinct brain changes. These findings indicate significant interrelations between cardiac and cerebral SVD markers, particularly concerning deep grey-matter variations, supporting the notion of SVD as a systemic disease.

Chapter 9

This study aimed to assess the suitability of ^{82}Rb PET/CT in pediatric patients by estimating dosimetry. Using both adult biokinetic data and data gathered from ten pediatric patients, the study found that ^{82}Rb PET/CT resulted in reasonably low radiation exposure in children, indicating its safety and tolerability. The most irradiated organs varied by age group but generally included the kidneys and heart wall in infants and newborns. These findings fill a

critical gap by providing original dosimetry data, potentially expanding the utility of this imaging technique in pediatric medical practice.

Chapter 10

The study focuses on assessing the individual risk of Major Adverse Cardiac Events, which are a significant concern due to cardiovascular diseases being the leading cause of death worldwide. The research utilizes Quantitative MPI based on [^{82}Rb] PET and employs scores derived from stress uptake and Myocardial Flow Capacity as a gold standard for prognosis assessment. The study explores the potential of Artificial Intelligence in predicting Major Adverse Cardiac Events using [^{82}Rb] SiPM PET MPI.

Researchers developed a systematic approach to validate Artificial Intelligence models and evaluate their performance by comparing global, segmental, radiomics, and Convolutional Neural Network models. These models leverage various MPI signals, such as stress MBF, MFR, or MFC radius, using data from 234 patients. The results indicate that regional Artificial Intelligence models significantly outperform the traditional global model, with the best Area Under the Curve of 73.9 obtained with a Convolutional Neural Network model. Interestingly, a radiomics model based on intensity features showed that the global average was the least important feature compared to other aggregations of the MPI signal across the myocardium.

In conclusion, the study demonstrates that Artificial Intelligence models can enhance personalized prognosis assessment for Major Adverse Cardiac Events, offering promising potential in improving risk prediction for cardiovascular events.

Chapter 11

In this study, we aimed to compare the effectiveness of ^{68}Ga-NODAGA-RGD PET/CT and ^{18}F-FDG PET/CT in patients with esophageal or esophagogastric junction cancers, focusing on tumor uptake and distribution, alongside histopathologic examination. A total of ten participants underwent both types of PET/CT scans. ^{68}Ga-NODAGA-RGD PET/CT identified positive uptake in primary sites (8 for primary tumors, 2 for local relapse suspicion), 6 lymph nodes, and 3 skeletal sites. ^{18}F-FDG PET/CT identified positive uptake in the same locations and additional lymph nodes and an adrenal gland. On analysis, ^{18}F-FDG SUVmax was significantly higher than ^{68}Ga-NODAGA-RGD SUVmax. Homogeneous ^{18}F-FDG uptake was observed within confirmed primary sites, while ^{68}Ga-NODAGA-RGD displayed heterogeneous

uptake in many cases, often at the tumor periphery or extending into perilesional structures. In conclusion, ^{68}Ga-NODAGA-RGD exhibited lower potential in detecting esophageal cancers compared to ^{18}F-FDG, but its imaging of integrin $\alpha_v\beta_3$ expression may offer complementary insights for tumor diversity and delineation.

Chapter 12

As part of a clinical study protocol, we presented here a 65-year-old woman with squamous cell carcinoma of the tongue who underwent both ^{68}Ga-NODAGA-RGD PET/CT and ^{18}F-FDG PET/CT. The scans revealed uptake of both tracers in the primary tumor, cervical lymph nodes, and bilaterally in various joints including shoulders, elbows, wrists, metacarpophalangeal, interphalangeal, and hip joints. The patient had a pre-existing diagnosis of rheumatoid arthritis for eight years. The PET/CT images demonstrated notably higher ^{18}F-FDG uptake compared to ^{68}Ga-NODAGA-RGD in the primary tumor and cervical lymph nodes. Interestingly, in the context of moderately active rheumatoid arthritis, the patient exhibited similar levels of uptake for ^{68}Ga-NODAGA-RGD and ^{18}F-FDG in the affected joints. However, it's worth noting that ^{68}Ga-NODAGA-RGD showed no uptake in the surrounding muscles, unlike ^{18}F-FDG. This case suggests the potential of ^{68}Ga-NODAGA-RGD PET/CT to depict synovial angiogenesis in rheumatoid arthritis, possibly offering a more favorable signal-to-noise ratio compared to ^{18}F-FDG PET/CT.

General discussion and future directions

Molecular cardiac imaging presents an innovative and emerging approach, holding significant potential for future advancements and enhancements prior to its integration into clinical practice. This thesis has specifically concentrated on molecular imaging of integrin $\alpha_v\beta_3$ concerning the remodeling of the heart following a myocardial infarction, a process often linked to the development of heart failure, as well as concerning angiogenesis in atherosclerosis. PET technology offers the ability to visualize the intricate molecular pathways active during these processes, enabling sequential imaging that illustrates the progression of the disease. Ultimately, this technology stands to be employed by medical practitioners to predict outcomes and tailor medications on an individual basis.

While the existing tracers have indeed undergone successful validation for targeting specific components, there remains room for refinement. Overcoming challenges in chemical engineering could involve enhancing the sensitivity and stability of the current tracers, thereby yielding higher-quality images. Additionally, there is an avenue for the creation of novel tracers to expand the repertoire of available options. This expansion would permit the examination of diverse molecular pathways, consequently deepening our understanding and facilitating a more personalized assessment and treatment approach for patients. Several potential targets that could significantly influence cardiac imaging include factors like tissue oxygenation, as well as specific cell populations like inflammatory or reparative monocytes/macrophages. However, the development of such tracers is a continual process that requires meticulous attention to detail and innovation.

Extensive literature delves into the intricate process of translating this research into clinical practice, a task known for its demands in terms of both expenses and time [1, 2, 3]. Numerous studies have centered on mice models, revealing distinct tracer behaviors between mice, pigs, and humans. This contrast becomes particularly pronounced in patients with co-morbidities and intricate cellular mechanisms [4, 5]. However, a recent development involves preliminary human trials for several of the described imaging techniques. While these trials are still in their initial phases, they have demonstrated the safety of tracers in humans and their effective visualization of intended targets. While additional human studies are imperative to assess safety and feasibility, the prospect of translating this innovation into clinical application is becoming more attainable than initially perceived.

Once these tracers secure a safety profile for human use, the subsequent phase will encompass extensive multi-center clinical trials. These trials will ascertain the tracers' capability to accurately image intended targets, offer prognostic insights to patients, and provide clinicians with evidence to personalize medication strategies. Adoption of these imaging techniques within clinical practice hinges on their proven safety, reliability, and their potential to yield clinically relevant outcomes that shape patient management. The confidence in the eventual integration of these techniques into patient care is underpinned by the conviction that they will enable disease progression and therapeutic response monitoring.

Moreover, these imaging techniques could complement emerging molecular therapeutics. Recent research has delved into therapies with anti-inflammatory and pro-angiogenic properties, among others [6, 7, 8]. The imaging methods outlined in this thesis could serve as guiding tools for these therapies, both in experimental settings and potential clinical applications.

In today's healthcare landscape, optimizing spending is of paramount importance. This prompts an exploration into the cost-effectiveness of this innovative technology. As imaging systems advance and scan durations shorten, the cost of a single scan diminishes. Given the substantial burden of heart failure on healthcare systems, any potential reduction in morbidity and mortality through these techniques might offset overall costs. As imaging systems continue to evolve, the techniques discussed in this thesis will naturally evolve as well. Notably, the emergence of PET/MRI hybrid systems, accessible at the Cardio-vascular Hospital Louis Pradel in Lyon, could fuel research in this domain, as these two modalities collectively dominate this field. With recent human trials marking a pivotal milestone, further evaluation and clinical testing remain pivotal. While considerable strides have been made, more groundwork is essential before molecular cardiac imaging becomes an integral tool for clinicians. Nevertheless, the recent progress underscores the promising trajectory towards clinical implementation.

Conclusion

The future application of radiotracer-based methods for angiogenesis-targeted imaging holds promise for advancing the assessment of conditions like myocardial ischemia/infarction

and atherosclerotic disease in clinical scenarios. Furthermore, the utilization of molecular imaging to observe angiogenesis could potentially enhance the non-invasive evaluation of how patients respond to medical interventions such as revascularization, exercise training, and novel treatments.

References

1. Jivraj N, Phinikaridou A, Shah AM, Botnar RM (2014) Molecu- lar imaging of myocardial infarction. Basic Res Cardiol 109:1– 16. https://doi.org/10.1007/s00395-013-0397-2
2. Majmudar MD, Nahrendorf M (2012) Cardiovascular molecular imaging: the road ahead. J Nucl Med 53:673–676. https://doi. org/10.2967/jnumed.111.099838
3. Sinusas AJ, Thomas JD, Mills G (2011) The future of molecu- lar imaging. JACC Cardiovasc Imaging 4:799–806. https://doi. org/10.1016/j.jcmg.2011.05.003
4. Chen IY, Wu JC (2011) Cardiovascular molecular imaging: focus on clinical translation. Circulation 123:425–443. https:// doi.org/10.1161/CIRCULATIONAHA.109.916338
5. Jivraj N, Phinikaridou A, Shah AM, Botnar RM (2014) Molecu- lar imaging of myocardial infarction. Basic Res Cardiol 109:1– 16. https://doi.org/10.1007/s00395-013-0397-2
6. Atluri P, Woo YJ (2008) Pro-angiogenic cytokines as car- diovascular therapeutics. BioDrugs 22:209–222. https://doi. org/10.2165/00063030-200822040-00001
7. Khan R, Spagnoli V, Tardif J, L'Allier PL (2015) Novel anti- inflammatory therapies for the treatment of atherosclerosis. Ath- erosclerosis 240:497–509. https://doi.org/10.1016/j.atherosclero sis.2015.04.783
8. Ridker PM, Lüscher TF (2014) Anti-inflammatory therapies for cardiovascular disease. Eur Heart J 35:1782–1791. https://doi. org/10.1093/eurheartj/ehu203

Chapter 14

List of publications

Articles in peer-reviewed journals

1. **Dietz M**, Kamani CH, Dunet V, Fournier S, Rubimbura V, Fournier S, Testart Dardel N, Schaefer A, Jreige M, Boughdad S, Nicod Lalonde M, Schaefer N, Mewton N, Prior JO, Treglia G. Overview of the RGD-based PET agents use in patients with cardiovascular diseases: a systematic review. Front Med (Lausanne). 2022;6;9:887508. doi:10.3389/fmed.2022.887508

2. **Dietz M**, Kamani C, Bousige C, Dunet V, Delage J, Rubimbura V, Nicod Lalonde M, Schaefer N, Nammas W, Saraste A, Knuuti J, Mewton N, Prior JO. Natural History of Myocardial αvβ3 Integrin Expression after Acute Myocardial Infarction: Correlation with Changes in Myocardial Blood Flow. J Nucl Med. 2024. (accepted with major revision)

3. Nammas W, Paunonen C, Teuho J, Siekkinen R, Luoto P, Käkelä M, Hietanen A, Viljanen T, **Dietz M**, Prior JO, Li WG, Roivainen A, Knuuti J, Saraste A. Imaging of myocardial αvβ3 integrin expression for evaluation of myocardial injury after acute myocardial infarction. J Nucl Med. 2024. doi:10.2967/jnumed.123.266148

4. **Dietz M**, Kamani CH, Deshayes H, Dunet V, Mitsakis P, Coukos G, Nicod Lalonde M, Schaefer N, Prior JO. Imaging Angiogenesis in Atherosclerosis in Large Arteries with 68Ga-NODAGA-RGD PET/CT: Relationship with Clinical Atherosclerotic Cardiovascular Disease. EJNMMI Res. 2021;11(1):71. doi:10.1186/s13550-021-00815-5

5. **Dietz M**, Boughdad S, Kamani CH, Prior JO, Schaefer N. Cardiac Theranostics: A Possible Role of 177Lu-DOTATATE Therapy in Coronary Atherosclerotic Plaque Inflammation. Med Nucl. 2022. 46(4), 201-203. doi:10.1016/j.mednuc.2022.04.003.

6. **Dietz M**, Kamani CH, Allenbach G, Rubimbura V, Fournier S, Dunet V, Treglia G, Nicod Lalonde M, Schaefer N, Eeckhout E, Muller O, Prior JO. Comparison of the Prognostic Value of Myocardial Flow Capacity and Global Myocardial Flow Reserve

and stress Myocardial Blood Flow on low-dose Rubidium-82 SiPM PET/CT. J Nucl Cardiol. 2022. doi:10.1007/s12350-022-03155-6.

7. Mazini B, **Dietz M**, Maréchal B, Corredor-Jerez R, Prior JO, Dunet V. The Interrelation between cardiac and brain small vessel disease: A pilot quantitative PET and MRI study. Eur J Hybrid Imaging. 2023. doi:10.1186/s41824-023-00180-7

8. Kamani C, Gnesin S, Di Bernardo S, **Dietz M**, Allenbach G, Dolan M, Nicod-Lalonde M, Schaefer N, Sekarski N, Prior JO. Human biodistribution and radiation dosimetry of [82Rb] at rest and during peak adenosine stress in a paediatric population. Radiology. 2023. (submitted)

9. Bors S, Abler D, Dietz M, Andrearczyk V, Fageot J, Nicod-Lalonde M, Schaefer N, DeKemp R, Kamani CH, Prior JO, Depeursinge A. Predicting MACE from [82Rb] PET: Can AI outperform more traditional quantitative assessment of the myocardial perfusion? Sci Rep. 2024. (accepted with major revision)

10. **Dietz M**, Dunet V, Mantziari S, Pomoni A, Dias Correia R, Testart Dardel N, Boughdad S, Nicod Lalonde M, Treglia G, Schafer M, Schaefer N, Prior JO. Comparison of Integrin αvβ3 Expression with 68Ga-NODAGA-RGD PET/CT and Glucose Metabolism with 18F-FDG PET/CT in Esophageal or Gastroesophageal Junction Cancers. Eur J Hybrid Imaging. 2023. doi:10.1186/s41824-023-00162-9.

11. **Dietz M**, Nicod Lalonde M, Omoumi P, Testart Dardel N, Hügle T, Prior JO. Imaging of αvβ3 Integrin Expression in Rheumatoid Arthritis with [68Ga]Ga-NODAGA-RGDyk PET/CT in comparison to [18F]FDG PET/CT. Med Nucl. 2021;45(5-6):293-295. doi:10.1016/j.mednuc.2021.09.002

Oral and poster presentations at international meetings

1. **Dietz M**, Kamani CH, Allenach G, Rubimbura V, Fournier S, Nicod Lalonde M, Schaefer N, Eeckhout E, Muller O, Prior JO. Prognostic Value of Myocardial Flow Capacity and Global Absolute Perfusion Measurements using Rubidium-82 with SiPM PET/CT
   Annual Congress of the European Association of Nuclear Medicine 2022, Barcelona, Spain.

2. Kamani CH, Ducchini M, **Dietz M**, Monney P, Prior JO. Assessment of the systolic left ventricular function from gated [Rb-82] Silicon-Photomultiplier (SiPM) PET/CT: A head-to-head comparison against two-dimensional planimetry transthoracic echocardiography
   Annual Congress of the European Association of Nuclear Medicine 2022, Barcelona, Spain.

3. Schaefer A, **Dietz M**, Nicod Lalonde M, Schaefer N, Prior JO, Kamani CH. Interrelation between cardiac and brain small vesse disease: a quantitative PET-MRI study
   Swiss Congress of Radiology 2022, Fribourg, Switzerland.

4. Mazini B, **Dietz M**, Maréchal B, Corredor-Jerez R, Prior JO, Dunet V. Interrelation between cardiac and brain atrophy in small vesse disease: a quantitative PET-MRI study
   Journées Francophones de Radiologie 2022, Paris, France.

5. **Dietz M**, Kamani CH, Rubimbura V, Fournier S, Allenbach G, Muller O, Prior JO. Valeur pronostique des réserves de flux myocardique ainsi que des flux myocardiques de stress globaux et territoriaux en TEP/TDM cardiaque au Rubidium82
   Journées Francophones de Médecine Nucléaire 2022, Paris, France.

6. **Dietz M**, Dunet V, Mantziari S, Jreige M, Nicod Lalonde M, Schafer M, Schaefer N, Prior JO. Comparison of Angiogenesis Imaging with 68Ga-NODAGA-RGD PET/CT

and Glucose Metabolism with 18F-FDG PET/CT in Esophageal or Gastroesophageal Junction Cancers: a pilot study
Swiss Congress of Radiology 2022, Fribourg, Switzerland (Poster).

7. Mazini B, **Dietz M**, Maréchal B, Corredor-Jerez R, Prior JO, Dunet V. Interrelation between cardiac and brain small vesse disease: a quantitative PET-MRI study
Swiss Congress of Radiology 2022, Fribourg, Switzerland.

8. Mazini B, **Dietz M**, Maréchal B, Corredor-Jerez R, Prior JO, Dunet V. Interrelation between cardiac and brain small vesse disease: a quantitative PET-MRI study
American Society of Neuroradiology Annual Meeting 2022, New York, USA.

9. **Dietz M**, Kamani CH, Mewton N, Prior JO. Study Protocol - Imaging of angiogenesis in cardiac lesions with 68Ga-NODAGA-RGD PET/CT.
Journée Scientifique de l'EDISS 2021, Lyon, France.

10. **Dietz M**. Étude de l'angiogenèse par PET cardiaque au 68Ga-NODAGA-RGD dans les lésions myocardiques aiguës
Journées Francophones de Radiologie 2020, Paris, France (Poster).

Chapter 15

Acknowledgements

I anticipated that writing this section would be simple, but it has proven to be challenging to condense three years of my life into a few pages. Reflecting on this period, it was a journey filled with hard work, encountering incredible individuals, acquiring new knowledge, experiencing enthusiasm (often), facing frustration (more frequently!), and most importantly, it was a transformative period that made me a stronger person and a better researcher.

Now, as this captivating journey comes to an end, it is time for me to express my heartfelt gratitude to all the people who contributed to this thesis and influenced my life in Switerland.

Dear Professor Prior, I am sincerely grateful for the opportunity to meet you. You are an exceptional doctor and researcher, an outstanding educator, and above all, a person worthy of admiration. Your ability to critically analyze research projects sometimes presented challenges for me, but it consistently led to improved outcomes. I extend my gratitude for providing me with the privilege of working in your department, which stands among the finest in Europe and worldwide. You granted us access to cutting-edge technology and the opportunity to showcase our work in prestigious international conferences—a privilege that should never be taken for granted.

Dear Professor Mewton, you had a huge impact on the main article of this thesis and your guidance throughout this research journey has been invaluable. Your insightful feedback and critical analysis have led to a more comprehensive and rigorous study. Your ability to encourage innovative thinking has been inspiring, and I am grateful for the opportunity to learn from you. As I embark on the next phase of my career, I will carry forward the lessons I've learned from you. Thank you for your belief in my potential and for pushing me to reach new heights in my academic pursuits.

Dear Professor Schaefer, I want to express my gratitude for the opportunity to work with you. Although I was not directly supervised by you, your keen attention to the clinical implications made a notable difference in our research papers.

I wish to extend my heartfelt gratitude to Dr. Marie Nicod Lalonde and Dr. Vincent Dunet. Your expertise and invaluable assistance have been a beacon of guidance, for which I am truly thankful.

Dear Moritz, my dear friend, words fail to convey my gratitude. During my time in Switerland, you became like family to me. Your unwavering dedication and kindness make you one of the most exceptional individuals I have encountered in my life—never forget that. I eagerly anticipate our reunion in France or Germany!

Dear Ricardo, I sincerely thank you for your friendship and the memorable international lunches we shared.

To my French friends Ana & Charles, the time we spent together holds a special place in my heart, as it brought a sense of home to me. I sincerely hope that happiness and success follow you throughout your life your new family (and by the way, what a wonderful name you've chosen for your son!).

To the radiopharmacists Kilian, Julien, and Judith, the moments we shared have woven themselves into a unique corner of my heart.

Dear Christel, we engaged in numerous brainstorming sessions and research endeavors—some flourished, while others remained unrealized. Such is the nature of research (and life). I wish you all the best!

I would also like to express my gratitude to all the individuals I encountered in the nuclear medicine department—Victor, Sarah, Katharina, Maria, Nathalie, Adriana, Patrick, Melanie, Ouafah, Marta, Paulo, Ljubinca, Chantal, Margarita, Stephane —who were always available to help. I apologize if I unintentionally omitted someone.

I hold a unique gratitude for Sandra and Christine. Your immeasurable support has been utterly invaluable. My heart is brimming with thanks!

Lastly, I dedicate this thesis to my family.

To my beloved wife Clothilde, you are my cherished partner and lifelong companion. You inspired me to push harder, overcome obstacles, and never surrender. Our time together in Switerland was a transformative experience that I am certain we will cherish in the years to come.

To my parents, who granted me the opportunity to become the person I am today. To my Mother and my Brothers, who supported me in every possible way. And to my Father, who may no longer be with me physically but will forever remain in my heart.

Chapter 16

Curriculum Vitae

Date prepared: 17.10.2023

Personal information

Matthieu DIETZ, MD, PhD student

Assistant Hospitalier Universitaire, Nuclear Medicine and Molecular Imaging, Hôpital Cardio-Vasculaire Louis Pradel, 28 avenue Doyen Lépine, BP Lyon-Monchat 69394, LYON Cedex 03, France

INSERM U1060, INRA U1397, CarMeN laboratory, University of Lyon, France Phone: +33 (0)6 11 90 59 93

Born September 16, 1991, in Munich, Germany

Nationality: French

Married (Clothilde BERGER, MD - Cardiology), 1 child

matthieu.dietz@chu-lyon.fr

Publications 23; ORCID 0000-0001-6041-2531; WOS ResearcherID AAQ-7986-2021; Scopus 57217073577; Loop 1362611.

Education

Institution	Degree	Date	Field
Université Claude Bernard Lyon 1	PhD student	2020–	Clinical Research, technological innovation
Université Claude Bernard Lyon 1	MPH	2020	Clinical Research
Université Paris Descartes	Inter University Diploma	2020	Cardio-vascular Imaging
Université Montpellier, Université Toulouse	Inter University Diploma	2019	Osteo-articular Imaging
Université Paris Descartes	University Diploma	2018	MRI
Université Claude Bernard Lyon 1	Specialization Diploma	2020	Medical Doctor/ Nuclear Medicine
Université Claude Bernard Lyon 1	Diploma	2016	Medicine

Experience

Institution, location	Title	Date	Field
Hospices Civils de Lyon, France	Assistant Hospitalier Universitaire	11/2022–	Nuclear Medicine
Lausanne University Hospital, Switzerland	Chef de clinique	11/2021–10/2022	Nuclear Medicine
Lausanne University Hospital, Switzerland	Research Fellow	11/2020–10/2021	Nuclear Medicine

Institution, location	Title	Date	Field
Hospices Civils de Lyon, France	Resident	11/2016–10/2020	Nuclear Medicine: 5 semesters Radiology: 3 semesters
Centre Hospitalier Princesse Grace, Monaco	Visiting Resident	11/2019–05/2020	Nuclear Medicine Clinical Research master s thesis on ^{18}F-sodium fluoride uptake in coronary plaques
Hôpital Bichat, Paris, France	Visiting Resident	05/2019–10/2019	Nuclear Medicine
Hôpital Edouard Herriot, Lyon, France	Willing on-call duty participation: Medical emergency imaging	07/2018–10/2018	Radiology

Approved research projects

1. Société Française de Radiologie, Collège des Enseignants en Radiologie de France (SFR-CERF, Paris) - Grant « Alain Rahmouni » of **€ 10.000** (2020-2021) for the project Study of Cardiac Lesions Angiogenesis by (68)Ga-NODAGA-RGD Cardiac PET
2. Agence régionale de santé (ARS) Auvergne-Rhône-Alpes, Université Claude Bernard Lyon 1 - Salary award « Année Recherche » of **€ 25.000** (2020-2021) for the project Study of Cardiac Lesions Angiogenesis by (68)Ga-NODAGA-RGD Cardiac PET

Peer-reviewed publications

1. **Dietz M**, Bochaton T, Al Mansour L, Tordo J, Flaus A. Identification of lipomatous metaplasia on CT images helps confirm prior silent myocardial infarction associated with equivocal perfusion abnormality on SPECT/CT imaging. J Nucl Cardiol. 2023 (accepted for publication)
2. Nammas W, Paunonen C, Teuho J, Siekkinen R, Luoto P, Käkelä M, Hietanen A, Viljanen T, **Dietz M**, Prior JO, Li XG, Roivainen A, Saraste A. Imaging of myocardial αvβ3 integrin expression for evaluation of myocardial injury after acute myocardial infarction. J Nucl Med. 2023. doi:10.2967/jnumed.123.266148
3. Mazini B, **Dietz M**, Maréchal B, Corredor-Jerez R, Prior JO, Dunet V. Interrelation between cardiac and brain in small vesse disease: a pilot quantitative PET and MRI study. Eur J Hybrid Imaging. 2023. doi:10.1186/s41824-023-00180-7
4. Jacquet-Francillon N, Dijoud F, Carlin L, **Dietz M**, Flaus A, Tordo J. Randall-Type Monoclonal Immunoglobulin Deposition Disease in bone scintigraphy. Clin Nucl Med. 2023. doi:10.1097/RLU.0000000000004927
5. Serrano B, Beaumont T, Hugonnet F, **Dietz M**, Berthier F, Garnier N, Villeneuve R, Nataf V, Mocquot F, Montemagno C, Faraggi M, Paulmier B. Quantitative Analysis of 99mTc-Pertechnetate Thyroid uptake with a large field CZT Gamma Camera: feasibility and comparison between SPECT/CT and Planar acquisitions Benjamin Serrano. EJNMMI Phys. 2023. doi:10.1186/s40658-023-00566-3.
6. Courlet P, Abler D, Guidi M, Girard P, Amato F, Vietti Violi N, **Dietz M**, Guignard N, Wicky A, Latifyan S, De Micheli R, Jreige M, Dromain C, Csajka C, Prior JO, Venkatakrishnan K, Michielin O, Cuendet MA, Terranova N. Modeling tumor size dynamics based on real-world electronic health records and image data in advanced melanoma patients receiving immunotherapy. CPT Pharmacometrics Syst Pharmacol. 2023. doi:10.1002/psp4.12983.
7. **Dietz M**, Jacquet-Francillon N, Bani Sadr A, Collette B, Mure PA, Demède D, Pina-Jomir G, Moreau-Triby C, Grégoire B, Mouriquand P, Janier M, Flaus A. Ultrafast cadmium-zinc-telluride-based renal single

photon emission computed tomography: clinical validation. Pediatr Radiol. 2023. doi:10.1007/s00247-023-05682-x

8. **Dietz M**, Jobbe-Duval A, Moreau-Triby C, Flaus A. Difference in cardiac uptake between ^{99m}Tc-HMDP and ^{99m}Tc-DPD for the non-invasive diagnosis of cardiac transthyretin amyloidosis. J Nucl Cardiol. 2023 doi:10.1007/s12350-023-03282-8
9. Abler D, Courlet P, **Dietz M**, Gatta R, Girard P, Munafo A, Wicky A, Jreige M, Guidi M, Latifyan S, De Micheli R, Csajka C, Prior JO, Michielin O, Terranova N, Cuendet M. A Semi-Automated Pipeline to Quantify Tumor Evolution From Real-World PET/CT Imaging. JCO Clin Cancer Inform. 2023 doi:10.1200/CCI.22.00126.
10. **Dietz M**, Dunet V, Mantziari S, Pomoni A, Dias Correia R, Testart Dardel N, Boughdad S, Nicod Lalonde M, Treglia G, Schafer M, Schaefer N, Prior JO. Comparison of Integrin αvβ3 Expression with ^{68}Ga-NODAGA-RGD PET/CT and Glucose Metabolism with ^{18}F-FDG PET/CT in Esophageal or Gastroesophageal Junction Cancers. Eur J Hybrid Imaging. 2023. doi:10.1186/s41824-023-00162-9.
11. **Dietz M**, Kamani CH, Allenbach G, Rubimbura V, Fournier S, Dunet V, Treglia G, Nicod Lalonde M, Schaefer N, Eeckhout E, Muller O, Prior JO. Comparison of the Prognostic Value of Myocardial Flow Capacity and Global Myocardial Flow Reserve and stress Myocardial Blood Flow on low-dose Rubidium-82 SiPM PET/CT. J Nucl Cardiol. 2023;30(4):1385-1395. doi:10.1007/s12350-022-03155-6.
12. Einstein AJ, Hirschfeld C, Williams MC, Vitola JV, Better N, Villines TC, Cerci R, Shaw LJ, Choi AD, Dorbala S, Karthikeyan G, Lu B, Sinitsyn V, Ansheles AA, Kudo T, Bucciarelli-Ducci C, Nørgaard BL, Maurovich-Horvat P, Campisi R, Milan E, Louw L, Allam AH, Bhatia M, Sewanan L, Malkovskiy E, Cohen Y, Randazzo M, Narula J, Morozova O, Pascual TNB, Pynda Y, Dondi M, Paez D. **INCAPS COVID 2 Investigators Group**. Worldwide Disparities in Recovery of Cardiac Testing 1 Year Into COVID-19. J Am Coll Cardiol. 2022;24;79:2001-2017. doi:10.1016/j.jacc.2022.03.348.
13. **Dietz M**, Kamani CH, Dunet V, Fournier S, Rubimbura V, Fournier S, Testart Dardel N, Schaefer A, Jreige M, Boughdad S, Nicod Lalonde M, Schaefer N, Mewton N, Prior JO, Treglia G. Overview of the RGD-based PET agents use in patients with cardiovascular diseases: a systematic review. Front Med (Lausanne). 2022;6;9:887508. doi:10.3389/fmed.2022.887508
14. **Dietz M**, Boughdad S, Kamani CH, Prior JO, Schaefer N. Cardiac Theranostics: A Possible Role of ^{177}Lu-DOTATATE Therapy in Coronary Atherosclerotic Plaque Inflammation. Med Nucl. 2022. 46(4), 201-203. doi:10.1016/j.mednuc.2022.04.003.
15. **Dietz M**, Nicod Lalonde M, Omoumi P, Testart Dardel N, Hügle T, Prior JO. Imaging of αvβ3 Integrin Expression in Rheumatoid Arthritis with [^{68}Ga]Ga-NODAGA-RGDyk PET/CT in comparison to [^{18}F]FDG PET/CT. Med Nucl. 2021;45(5-6):293-295. doi:10.1016/j.mednuc.2021.09.002
16. **Dietz M**, Kamani CH, Deshayes H, Dunet V, Mitsakis P, Coukos G, Nicod Lalonde M, Schaefer N, Prior JO. Imaging Angiogenesis in Atherosclerosis in Large Arteries with ^{68}Ga-NODAGA-RGD PET/CT: Relationship with Clinical Atherosclerotic Cardiovascular Disease. EJNMMI Res. 2021;11(1):71. doi: 10.1186/s13550-021-00815-5
17. **Dietz M**, Tordo J. Glucose Activity of Neurogenic Heterotopic Ossification with FDG PET/CT Matching with Ongoing Osteoblastic Activity on Bone Scan. Mol Imaging Radionucl Ther. 2022;31:166-168. doi:10.4274/mirt.galenos.2021.48243
18. **Dietz M**, Paulmier B, Berthier F, Civaia F, Mocquot F, Serrano B, Nataf V, Hugonnet F, Faraggi M. An intravenous 100mL lipid emulsion infusion dramatically improves myocardial glucose metabolism extinction in cardiac FDG PET clinical practice. Clin Nucl Med. 2021; 46(6):e317-e324. doi:10.1097/RLU.0000000000003556
19. **Dietz M**, Chironi G, Faraggi M. Reduced ^{18}F-sodium fluoride activity in coronary plaques after statin therapy. Eur Heart J Cardiovasc Imaging. 2021;22(8):e133. doi:10.1093/ehjci/jeab016
20. **Dietz M**, Si-Mohamed S, Deville A, Tordo J, Moreau-Triby C. Unexpected Vertebral Bodies Trapping of ^{99m}Tc Macroaggregated Albumin during Lung Perfusion Scintigraphy in a Patient with Collateral Paravertebral Venous System. Clin Nucl Med. 2021;46(5):e276-e278. doi:10.1097/RLU.0000000000003476
21. **Dietz M**, Debarbieux S, Righetti M, Harou O, Tordo J. Paraneoplastic Multicentric Reticulohistiocytosis on ^{18}F-FDG PET/CT Breast Carcinoma Follow-up. Clin Nucl Med. 2021;46(5):e253-e255. doi:10.1097/RLU.0000000000003417
22. **Dietz M**, Chironi G, Claessens YE, Farhad RL, Rouquette I, Serrano B, Nataf V, Hugonnet F, Paulmier B, Berthier F, Keita-Perse O, Giammarile F, Perrin C, Faraggi M, for the MONACOVID Group. COVID-19 Pneumonia: Relationship Between Inflammation Assessed by Whole-body FDG PET/CT and Short-term Clinical Outcome. Eur J Nucl Med Mol Imaging. 2021;48(1):260-268. doi:10.1007/s00259-020-04968-8
23. **Dietz M**, Neyrand S, Dhomps A, Decaussin-Petrucci M, Tordo J. ^{18}F-FDG PET/CT of a Rare Case of an Adenomatoid Tumor of the Adrenal Gland. Clin Nucl Med. 2020;45(7):e331-e333.

doi:10.1097/RLU.0000000000003097

Review activities

Reviewer for EJNMMI Research (3); Molecular Imaging and Biology (1); Journal of Cardiothoracic Surgery (1).

Clinical Trials

NCT04437927

Start Date: April 2020
Completion Date: November 2020
Recruitment Status: Terminated
Condition(s): Metabolic Preparation, Myocardial Inflammation

NCT04441489

Start Date: March 2020
Completion Date: May 2020
Recruitment Status: Terminated
Condition(s): COVID-19, FDG PET/CT, Inflammation

Certificate of good clinical practice (GCP) exam

Good Clinical Practice (GCP-E6(R2) 2016) of the TRREE training programme in research ethics evaluation.
Release Date: 16/11/2020.

Teaching experience

- Enseignements Dirigés de biophysique, 2nd year medical students, Université Lyon 1 (2023)
- Cardiologie Nucléaire - cardiology residents, Lyon (2020, 2023)
- Viabilité en médecine nucléaire - Continuing Medical Education, Service d'urgences cardiologiques et de soins intensifs, Hôpital Cardio-Vasculaire Louis Pradel, Lyon (2023)
- Apport de la TEP dans le cadre de l'endocardite infectieuse - cardiology residents, Lyon (2023)
- MOOC imagerie médicale, Médecine Nucléaire - 2nd year medical students, Université Lyon 1 (2018, 2022)
- TEP/CT dans la recherche de sarcoïdose cardiaque : Des nouveautés dans les récentes guidelines européennes ? Continuing Medical Education, Nuclear Medicine Physicians of the French-speaking part of Switzerland, Lausanne (2022)
- Détection d'une cardiopathie inflammatoire par PET-CT: live in a box - Continuing Medical Education, EduCardio (Cardiologists of the canton of Vaud), Lausanne (2022)
- Rôle des radio-traceurs RGD en PET chez les patients avec maladies cardiovasculaires - Continuing Medical Education, CHUV, Lausanne (2021)
- Radiomics potential application to PET Rb pronostic prospectively acquired data - CHUV Radiomics meeting, Lausanne (2021)
- Flux de perfusion myocardique - Continuing Medical Education, CHUV, Lausanne (2021)
- Médecine Nucléaire - radiology residents, Lyon (2020)
- School for radiology technicians - IFSI Esquirol, Lyon (2020)

- Introduction à l'imagerie nucléaire cardiologique - CarMeN laboratory Journal Club, Lyon (2020)
- Cardiologie Nucléaire - cardiology residents, Lyon (2020)
- Imagerie des arthropathies microcristallines - Continuing Medical Education, Hôpital Bichat, Paris (2019)
- Annual teaching presentations - Nuclear Medicine Rhône-Alpes interregional meetings (2016-2020)
- Innovations en médecine nucléaire - Master 2 Polytech Lyon (2018)

Oral and poster presentations at international conferences

1. Abler D, Courlet P, **Dietz M**, Jreige M, Guidi M, Amato F, Guignard N, Wicky A, Gatta R, Girard P, Munafo A, Vietti Violi N, Dromain C, Venkatakrishnan K, Latifyan S, De Micheli R, Csajka C, Prior JO, Michielin O, Terranova N, Cuendet M. Investigating response of advanced melanoma patients to ICI by assessing tumor burden dynamics from real-world data
   ISREC-SCCL Symposium 2023, Lausanne, Switzerland (Poster).
2. Jacquet-Francillon N, Morelec I, **Dietz M**, Clotagatide A, Tordo J, Al-Mansour L, Isal S, Flaus A. 18F-Fluorocholine PET/CT and scintigraphy detection rate stratified by PTH levels in parathyroid imaging
   Annual Congress of the European Association of Nuclear Medicine 2023, Vienna, Austria.
3. Abler D, Courlet P, **Dietz M**, Gatta R, Girard P, Munafo A, Wicky A, Jreige M, Guidi M, Csajka C, Prior JO, Michielin O, Terranova N, Cuendet M. Semi-automatic quantification of tumor evolution from real-world PET/CT imaging
   11th SCCL Faculty & Staff Retreat 2022 by SCCL, Geneva, Switzerland (Poster).
4. **Dietz M**, Kamani CH, Allenach G, Rubimbura V, Fournier S, Nicod Lalonde M, Schaefer N, Eeckhout E, Muller O, Prior JO. Prognostic Value of Myocardial Flow Capacity and Global Absolute Perfusion Measurements using Rubidium-82 with SiPM PET/CT
   Annual Congress of the European Association of Nuclear Medicine 2022, Barcelona, Spain.
5. Kamani CH, Ducchini M, **Dietz M**, Monney P, Prior JO. Assessment of the systolic left ventricular function from gated [Rb-82] Silicon-Photomultiplier (SiPM) PET/CT: A head-to-head comparison against two-dimensional planimetry transthoracic echocardiography
   Annual Congress of the European Association of Nuclear Medicine 2022, Barcelona, Spain.
6. Schaefer A, **Dietz M**, Nicod Lalonde M, Schaefer N, Prior JO, Kamani CH. Interrelation between cardiac and brain small vesse disease: a quantitative PET-MRI study
   Swiss Congress of Radiology 2022, Fribourg, Switzerland.
7. Mazini B, **Dietz M**, Maréchal B, Corredor-Jerez R, Prior JO, Dunet V. Interrelation between cardiac and brain atrophy in small vesse disease: a quantitative PET-MRI study
   Journées Francophones de Radiologie 2022, Paris, France.
8. **Dietz M**, Kamani CH, Rubimbura V, Fournier S, Allenbach G, Muller O, Prior JO. Valeur pronostique des réserves de flux myocardique ainsi que des flux myocardiques de stress globaux et territoriaux en TEP/TDM cardiaque au Rubidium82
   Journées Francophones de Médecine Nucléaire 2022, Paris, France.
9. **Dietz M**, Dunet V, Mantziari S, Jreige M, Nicod Lalonde M, Schafer M, Schaefer N, Prior JO. Comparison of Angiogenesis Imaging with ^{68}Ga-NODAGA-RGD PET/CT and Glucose Metabolism with ^{18}F-FDG PET/CT in Esophageal or Gastroesophageal Junction Cancers: a pilot study
   Swiss Congress of Radiology 2022, Fribourg, Switzerland (Poster).
10. Mazini B, **Dietz M**, Maréchal B, Corredor-Jerez R, Prior JO, Dunet V. Interrelation between cardiac and brain small vesse disease: a quantitative PET-MRI study
    Swiss Congress of Radiology 2022, Fribourg, Switzerland.
11. Mazini B, **Dietz M**, Maréchal B, Corredor-Jerez R, Prior JO, Dunet V. Interrelation between cardiac and brain small vesse disease: a quantitative PET-MRI study
    American Society of Neuroradiology Annual Meeting 2022, New York, USA.
12. **Dietz M**, Kamani CH, Mewton N, Prior JO. Study Protocol - Imaging of angiogenesis in cardiac lesions with ^{68}Ga-NODAGA-RGD PET/CT.
    Journée Scientifique de l'EDISS 2021, Lyon, France.
13. **Dietz M**. Étude de l'angiogenèse par PET cardiaque au ^{68}Ga-NODAGA-RGD dans les lésions myocardiques aiguës
    Journées Francophones de Radiologie 2020, Paris, France (Poster).

14. **Dietz M**. Imagerie de l'amylose : approche multimodale
    Les Rencontres Lyonnaises de Rythmologie 2020, Lyon, France (invited speaker).
15. Moreau A, Giraudet AL, Parisse S, Bahri H, **Dietz M**, Foret T, Mognetti T, Isnardi V. Découverte fortuite d'un hibernome et d'une NEM1 grâce aux explorations isotopiques
    Journées Francophones de Médecine Nucléaire 2017, Paris, France (Poster)
16. Moreau A, Parisse S, Bahri H, Isnardi V, Foret T, **Dietz M**, Mognetti T, Giraudet AL. Lésion pulmonaire fixant l'iode 131 en rapport avec une séquestration pulmonaire chez une patiente suivie pour carcinome thyroïdien : attention au faux-positif
    Journées Francophones de Médecine Nucléaire 2017, Paris, France (Poster)
17. Foret T, **Dietz M**, Parisse S, Bahri H, Giraudet AL, Mognetti T, Moreau A. Disparition sous antibiothérapie de lésions de « carcinose péritonéale » évaluées en TEP/TDM FDG
    Journées Francophones de Médecine Nucléaire 2017, Paris, France (Poster)

Honours and Awards

- Short-listed for the 2022 EANM Young Author Award's selection
- Médaille d'Or 2020 des hôpitaux de Lyon

Lyon (France), October 17, 2023

ORCID